Multiphysical and Multi Scale Modelling of Composite Materials for Aircraft De-Icing

Dissertation
zur Erlangung des akademischen Grades

Doktoringenieur
(Dr.-Ing.)

von **Maximilian Otto Heinrich Schutzeichel, M.Sc.**
geb. am 15.10.1992 in Menden (Sauerland)

genehmigt durch die Fakultät für Maschinenbau
der Otto-von-Guericke-Universität Magdeburg

Gutachter:

Prof. Dr.-Ing. Hans Peter Monner

Prof. Dr.-Ing. habil. Thomas Kletschkowski

Prof. Dr.-Ing. Peter Wierach

Promotionskolloquium am 24. April 2023

Kurzfassung

Multifunktionale Komposite können strukturgebend und mindestens für eine oder mehrere weitere Funktionen genutzt werden, um ein System aus monofunktionalen Komponenten in einem Fahr- oder Flugzeug zu ersetzen. Ein Beispiel für ein solches Material ist die Strukturbatterie. Ihre Fähigkeit, Energie zu speichern, wird durch die eingebetteten Kohlefasern ermöglicht, die in der Lage sind, den Kunststoff zu verstärken und die Möglichkeit besitzen, Lithium Ionen einzulagern. Eine speziell entwickelte, strukturelle Elektrolytbeschichtung der Kohlefasern isoliert die Faser elektrisch und ermöglicht zudem den Ionenfluss und eine signifikante Lastübertragung. Wenn die strukturgebenden Materialien eines Fahr- oder Flugzeuges durch diesen multifunktionalen Verbund ersetzt werden, kann eine hohe Energiespeicherkapazität bei gleichzeitiger Gewichtsersparnis auf der Systemebene erreicht werden, da keine konventionellen Energiespeicher mehr benötigt werden.

Während im multifunktionalen Verbundmaterial Strom geleitet wird, entsteht Joulesche Wärme, die einen bedeutsamen Temperaturanstieg zur Folge hat. Ein Industriepatent hat vorgeschlagen, diese Wärme zur Enteisung von Flugzeugstrukturen zu nutzen, indem die Struktur selbst aus dem multifunktionalen Faserverbund gefertigt und aktiv erwärmt wird. Traditionelle Enteisungssysteme fügen einem Flugzeug eine signifikante, zusätzliche Masse hinzu und sind mechanisch sowie thermisch monofunktional konzipiert, sodass sie wenig Energieeffizient sind. Durch den Einsatz multifunktionaler Komposite wird eine bedeutsame Massenreduktion bei gleichzeitiger Energieeinsparung erwartet, da sie teil der bestehenden, lasttragenden Primärstruktur sein können und ihre funktionale Leistungsfähigkeit den Anwendungsbedingungen ideal angepasst werden kann.

Der Einfluss der Elektrolytbeschichtung auf das Verhalten des Verbundmaterials, sowie die physikalischen Kopplungseffekte, die bei multifunktionaler Nutzung entstehen, sind bislang nicht hinreichend analysiert worden, wodurch ein signifikanter Bedarf besteht, die erwartete Leistungsfähigkeit mit quantitativen Ergebnissen zu untermauern. Ferner ist auch zu prüfen, welche möglichen Einschränkungen gegenüber klassischen Faserverbundmaterialien bestehen, sodass sie bei der Auslegung berücksichtigt werden können. Um diesen Herausforderungen zu begegnen, wird in dieser Arbeit das Prinzip der modellbasierten Entwicklung und Optimierung auf den multifunktionalen Verbund angewendet. Dazu werden die elektro-thermischen sowie die mechanischen Eigenschaften der beschichteten Kohlefasern experimentell ermittelt. Ferner, wird ein neues elektro-thermo-mechanisch gekoppeltes, Multiskalenmodell aufgebaut, welches das gemessene Materialverhalten wiedergibt und weitere virtuelle Charakterisierungen erstmals ermöglicht. Das Modell wird letztlich durch Messungen an einer Versuchsstruktur in einem Enteisungsprüfstand erfolgreich validiert.

Die Modellierung der temperaturinduzierten Reduktion der effektiven Steifigkeit und die Optimierung der Energieversorgung unter Berücksichtigung konvektiver Wärmedis-

sipation sind wichtige, neue Ansätze dieser Arbeit. Zudem werden Effekte der inneren Wärmeleitung und der konvektiven Wärmedissipation in Bezug auf die modellbasierte Optimierung und die daraus abgeleiteten Innovationen diskutiert. Schließlich kann die Leistungsfähigkeit des multifunktionalen Verbundes zum Zwecke der Enteisung mit der der traditionellen Heizmattensysteme zum ersten mal verglichen werden. Auf Basis der quantitativen Ergebnisse ist zu erwarten, dass die zusätzliche Masse eines Enteisungssystems durch die Anwendung des multifunktionalen Materials eingespart werden kann und gleichzeitig eine signifikante Effizienzsteigerung bei der Wärmeleistung möglich ist.

Zukünftige Untersuchungen können auf den entwickelten Modellen und Schlussfolgerungen aufbauen, indem sie die Modelldefinition verfeinern und Schlussfolgerungen dieser Arbeit im Kontext anderer Anwendungsfälle, wie etwa der Strukturbatterie, diskutieren.

Abstract

Multifunctional composite materials provide structural integrity and at least one or more functions which can be applied beneficially in vehicle systems. One example of a multifunctional material is the structural battery. The energy storage function of this material is given by the carbon fibre that reinforces the plastic matrix and provides a lithium ion intercalation function. A tailored polymer electrolyte coating on the fibre's surface is electrically insulating, ion conducting and significantly load bearing simultaneously so that the energy storage function is supported. The multifunctional use for structural integrity and energy storage enables a significant weight saving potential when monofunctional components and their assemblies are replaced.

During operation, the Joule heat effect provides a significant temperature rise of the multifunctional composite material. An industry patent suggested the use of the polymer electrolyte coated carbon fibres for the De-Icing of aircraft structures. Traditional systems provide a significant additional mass to the primary structure due to a low level of optimisation and their monofunctional concept. A significant weight reduction could contribute to the reduction of fossil fuel burn in a next generation aircraft. It is expected that the existing monofunctional primary structure can be replaced by a multifunctional structure, so that no additional mass is needed to provide the De-Icing function. In addition, it is expected that the structure can be optimised for an ideal functional performance which can lead to a reduced energy consumption for De-Icing.

The influence of the polymer electrolyte coating on the characteristics of the composite material as well as the effects resulting from physical couplings during operation are not sufficiently analysed. In addition, possible constraints of the multifunctional application need to be quantified, in order to take them into account for future system development. In order to face these challenges, this thesis builds on the basic principle of a model based, optimised application of multifunctional composite materials that comprise polymer electrolyte coated carbon fibres and a polymer matrix. Therefore, the electro-thermal and mechanical properties of the coated carbon fibres are examined experimentally to conclude suitable model assumptions in a first approach. Furthermore, an electro-thermo-mechanically coupled multi scale model is introduced which covers the multifunctional material behaviour under operational conditions for the first time. The model is successfully validated by measurements in a De-Icing test bed with a flat plate type specimen structure.

Significant physical couplings like a temperature induced stiffness change and an optimisation of heat transfer towards a minimum energy supply are important results of this thesis. In addition, conclusions from thermal heat transfer within the multifunctional composite material as well as the convective heat dissipation are discussed with respect to model based innovation. Finally, a new benchmark compares the optimised multifunctional

material performance for De-Icing with traditional De-Icing systems like the bleed-air system or the heater mat system. Based on the optimisation results, a complete removal of the De-Icing system's mass is expected and a significant increase of energy efficiency can be enabled.

Future research can build on the derived conclusions towards a refinement of the coupled multiphysics model and towards further application scenarios like the structural battery.

Contents

List of Figures

List of Tables

Notation and Lists of Symbols

Remarks on Notation

For this thesis a general notation for physical properties of materials is defined. The following table provides the basic symbols and related explanation. The comment indicates to which condition or theory these quantities are related. Exceptions from this notation are explained in the text if necessary.

Property	Symbol	Comment
Density	ρ	Mass per volume
Young's modulus	E	Static loads
Storage modulus	E'	Real part of complex modulus
Poisson's ratio	ν	Ratio of transversal contraction
Mechanical strength	S	Longitudinal, isotropic
Thermal expansion coeff.	α	Linear theory
Glass transition temperature	θ_g	For polymers
Mass specific heat	c_p	At constant pressure
Heat conductivity	λ	Temperature invariant
Electrical conductivity	σ	Temperature invariant
Electrical capacity	c_i	At given charge rate
Charge rate	C	Multiple of 1 h charge

It is typical for composite material constituents that it's properties can be either isotropic or transversal isotropic. For the latter, the indices $||$ and $\perp$ indicate longitudinal (e.g. in fibre direction) and transversal (across fibre direction) properties, respectively. Further indices provide the relation to the single constituents, e.g. index f for carbon fibres and m for matrix materials as well as c for coating materials. If no indication to a direction is indicatd, this is an isotropic property.

Apart from material property related notation, a general notation for tensor calculus is defined as follows: Bold italic capital letters like $\boldsymbol{C}$ denote 4^{th} rank tensors, bold roman capital letters like $\mathbf{T}$ denote 2^{nd} rank tensors and bold roman small letters like $\mathbf{q}$ denote vectors (1^{st} rank tensors). It should be noted that "roman" means "non-italicised" letters. This also applies for Greek letters. Scalars are written in italic capital or small letters like A, d. There is one exception in this work: The italic capital letter "C" is related to

tensor elements of 4^{th} rank. Roman capital letters like "T" denote tensor elements of 2^{nd} rank, roman small letters like "q" are related to vector elments (1^{st} rank tensor). This distinction applies also for Greek letters. Further, single exceptions are mentioned in the text if necessary.

Indices are roman for tensor indices and italic for further info on related conditions. All indices are distinguished by commas, e.g. $\mathrm{T}_{\mathrm{ij},th,\mu}$ denotes stress tensor elements with tensor indices ij, with additional info that these stresses are related to thermal heat (th) on the microscale μ. For good readability, no double index is used. If symbols like x_1 are used as index, the second level index is pulled to the first level (e.g. Γ^{+}_{x1}). Triangle brackets $\langle\rangle$ are used to indicate volume averaged quantities and overlines (e.g. $\overline{C}$) are used to indicate effective quantities. In addition tilde is used to indicate unit strains (e.g. $\widetilde{\mathbf{E}}$ with $|\mathbf{E}| = 1$).

Moreover, mathematical operators are defined. The nabla operator $\nabla = \left[\frac{\partial}{\partial x1}\ \frac{\partial}{\partial x2}\ \frac{\partial}{\partial x3}\right]^T$ combines the partial derivatives related to the x_1, x_2 and x_3 coordinates or any other orthonormal basis. The operator $\partial_x = \frac{\partial}{\partial x}$ indicates the partial derivative towards x, which could also be related to time: $\partial_t = \frac{\partial}{\partial t}$. Finally the Kronecker delta is defined as:

$$\delta_{\mathrm{ij}} = 1 \quad \text{for} \quad \mathrm{i} = \mathrm{j} \quad \text{and}$$
$$\delta_{\mathrm{ij}} = 0 \quad \text{for} \quad \mathrm{i} \neq \mathrm{j}.$$

Subsequently, all symbols and acronyms defined and used in this thesis are presented in the following lists. Within the arabic symbols list sub headings are provided to sort for the topical relation. All symbols and acronyms are sorted alphabetically.

Arabic Symbols

Symbol	Explanation	Unit	Page of Definition
	Geometry and Mathematical Constants		
A_c	Cross section area	[m^2]	49
A_s	Surface area	[m^2]	28
A_m	Measured (captured) surface area	[m^2]	80
a_h	Altitude above mean sea level	[m]	19
a, b, c	Edge length of RVE on micro scale	[m]	29
b_p	Width of flat plate laminate	[mm]	93
b_r	Width of the active PeCCF roving	[mm]	93

c_b	Break up criterion for iterative optimisation	[K]	85
d_f	Carbon fibre diameter	[µm]	8
d_p	Filler particle diameter	[m]	40
d_a	Equivalent thickness in third direction for 2D heat transfer	[m]	69
d_e	Equivalent thickness in third direction for 2D Joule heat	[m]	69
l	Length	[m]	43
l_c	Coated length	[m]	43
l_i	Length of the distance between active PeCCF rovings	[mm]	93
l_p	Filler particle length	[m]	40
l_c	Cord position of measurement window	[mm]	80
n_f	Number of fibres	[-]	85
n_r	Number of rovings	[-]	85
p	Correction factor for measured elongation	[-]	44
R	Linear regression coefficient	[−]	45
t	Time	[s]	49
t_s	Point in time with indicated stationary heat transfer	[s]	49
t_c	Polymer electrolyte coating thickness	[nm]	14
t_m	Heater element thickness of electrical heater mat system	[mm]	21
t_g	Glass fibre fabric thickness	[mm]	XII
t_p	Thickness of flat plate specimen	[mm]	80
t_{pl}	Single ply thickness	[mm]	96
V	Domain volume	[m^3]	33
w_p	Length of flat plate laminate	[mm]	93
	Material Properties		
c_p	Mass specific heat at constant pressure	$\left[\frac{J}{kgK}\right]$	xiv
$c_{p,f}$	Mass specific heat at constant pressure of carbon fibre	$\left[\frac{J}{kgK}\right]$	xiv
$c_{p,c/m}$	Mass specific heat at constant pressure of coating or matrix material	$\left[\frac{J}{kgK}\right]$	15
c_i	Electrical capacity (related to ion intercalation)	$\left[\frac{mAh}{g}\right]$	xiv

$c_{i,f}$	Carbon fibre electrical capacity (related to ion intercalation)	$\left[\frac{\mathrm{mAh}}{\mathrm{g}}\right]$	10
c_w	Volume specific total water content in air	$\left[\frac{\mathrm{g}}{\mathrm{m}^3}\right]$	19
$\overline{E}_{\mathrm{i}}$	Effective Youngs' modulus related to direction i	$\left[\frac{\mathrm{N}}{\mathrm{m}^2}\right]$	38
$E_{\mathrm{i,j}}$	Young's modulus in direction i of constituent j	$\left[\frac{\mathrm{N}}{\mathrm{m}^2}\right]$	38
$v_{p,max}$	(Geometrical) Maximum particle volume fraction	[-]	40
E	Young's modulus	$\left[\frac{\mathrm{N}}{\mathrm{m}^2}\right]$	xiv
$E_{\|\|,f}$	Carbon fibres Young's modulus in longitudinal direction	$\left[\frac{\mathrm{N}}{\mathrm{m}^2}\right]$	10
$E_{\perp,f}$	Carbon fibres Young's modulus in transversal direction	$\left[\frac{\mathrm{N}}{\mathrm{m}^2}\right]$	10
E_p	Particle's transversal Young's modulus	$\left[\frac{\mathrm{N}}{\mathrm{m}^2}\right]$	40
$E'_{c/m}$	Storage modulus of coating or matrix material	$\left[\frac{\mathrm{N}}{\mathrm{mm}^2}\right]$	15
E_{s}	Young's modulus of specimen	$\left[\frac{\mathrm{N}}{\mathrm{m}^2}\right]$	46
E_m	Matrix' transversal Young's modulus	$\left[\frac{\mathrm{N}}{\mathrm{m}^2}\right]$	40
$\overline{E}_{\mathrm{PeCCF}}$	PeCCF averaged Young's modulus	$\left[\frac{\mathrm{N}}{\mathrm{m}^2}\right]$	47
$\overline{G}_{12}$	Effective shear stiffness in x_1x_2 plane	$\left[\frac{\mathrm{N}}{\mathrm{m}^2}\right]$	39
$G_{\|\|,f}$	Shear stiffness of carbon fibres parallel to longitudinal direction	$\left[\frac{\mathrm{N}}{\mathrm{m}^2}\right]$	10
$G_{\perp,f}$	Shear stiffness of carbon fibres perpendicular to longitudinal direction	$\left[\frac{\mathrm{N}}{\mathrm{m}^2}\right]$	11
s	Stefan Boltzmann constant	$\left[\frac{\mathrm{W}}{\mathrm{m}^2\mathrm{K}^4}\right]$	28
S	Strength	$\left[\frac{\mathrm{N}}{\mathrm{m}^2}\right]$	xiv
S_f	Carbon fibre strength in longitudinal direction	$\left[\frac{\mathrm{N}}{\mathrm{m}^2}\right]$	10
v_{j}	Volume fraction of constituent j	[-]	38
v_f	Fibre volume fraction	[-]	22
$v_{f,\Omega\mathrm{i}}$	Fibre volume fraction of related domain	[-]	96
v_{cf}	Carbon fibre volume fraction	[-]	81
v_{gf}	Glass fibre volume fraction	[-]	81
v_m	Matrix fibre volume fraction	[-]	81
V_{j}	Volume of constituent j	$[\mathrm{m}^3]$	38

	Process Parameter		
C	Charging rate (1 C corresponds to fully charge in one h)	[-]	xiv
F_t	Tensile force	[N]	44
m_d	Length specific mass of ice protection system	$\left[\frac{\mathrm{kg}}{\mathrm{m}}\right]$	20
	Coordinates		
$\mathbf{x}$	Spatial coordinates on micro scale	[m]	31
$\mathbf{x}_{\mathrm{n}}$	Spatial coordinates of subdomain n on micro scale	[m]	31
$\mathbf{x}_{\mathrm{i}}$	Unit base vector on micro scale in direction i	[m]	37
$\mathbf{x}$	Micro scale coordinate base vector	[m]	29
x_{i}	Micro scale coordinate elements	[m]	29
$\mathbf{y}$	Meso scale coordinate base vector	[m]	29
y_{i}	Meso scale coordinate elements	[m]	29
$\mathbf{y}$	Spatial coordinates on meso scale	[m]	30
$\mathbf{n}_{\mathrm{x1}}$	Unit vector in x_1 direction	[m]	64
	Mechanical Domain		
$\boldsymbol{C}$	Stiffness tetrade (4^{th} rank tensor)	$\left[\frac{\mathrm{N}}{\mathrm{m}^2}\right]$	26
C_{ijkl}	Elements of the stiffness tetrade with 4^{th} rank indices	$\left[\frac{\mathrm{N}}{\mathrm{m}^2}\right]$	26
$\{C_{\mathrm{ij},T}\}$	Transversal isotropic stiffness tetrade in Voigt index notation	$\left[\frac{\mathrm{N}}{\mathrm{m}^2}\right]$	26
$C_{\mathrm{ijkl},m}$	Stiffness tetrade elements on meso scale	$\left[\frac{\mathrm{N}}{\mathrm{m}^2}\right]$	30
$C_{\mathrm{ijkl},\mu}$	Stiffness tetrade elements on micro scale	$\left[\frac{\mathrm{N}}{\mathrm{m}^2}\right]$	31
$\overline{C}_{\mathrm{ijkl},\mu}$	Effective stiffness tensor elements, derived from microscale	$\left[\frac{\mathrm{N}}{\mathrm{m}^2}\right]$	31
$\overline{C}_{\mathrm{ij},\mu}$	Effective stiffness tensor elements, derived from microscale, Voigt notation	$\left[\frac{\mathrm{N}}{\mathrm{m}^2}\right]$	31
$\mathbf{E}$	Linearised Cauchy strain tensor	[-]	24
E_{ij}	Elements of the strain tensor with 2^{nd} rank indices	[-]	26
$\mathrm{E}_{\mathrm{kl},m}$	Strain tensor elements on meso scale	[-]	30
$\mathrm{E}_{\mathrm{kl},\mu}$	Strain tensor elements on meso scale	[-]	31
$\widetilde{\mathrm{E}}_{\mathrm{ij,kl}}$	Unit strain for computational homogenisation	[-]	31

$\widetilde{\mathbf{E}}$	Unit strain tensor	[-]	33
E_m	Measured strain	[-]	44
$\overline{\mathrm{E}}_m$	Arithmetic mean of measured strain	[-]	45
S_{jilk}	Compliance tensor with 4^{th} rank indices	$\left[\frac{\mathrm{m}^2}{\mathrm{N}}\right]$	34
$\mathbf{T}$	Linearised Cauchy stress tensor	$\left[\frac{\mathrm{N}}{\mathrm{m}^2}\right]$	26
T_{ij}	Elements of the stress tensor with 2^{nd} rank indices	$\left[\frac{\mathrm{N}}{\mathrm{m}^2}\right]$	26
$\mathrm{T}_{\mathrm{ij},m}$	Stress tensor elements on meso scale	$\left[\frac{\mathrm{N}}{\mathrm{m}^2}\right]$	30
$\mathrm{T}_{\mathrm{ij},\mu}$	Stress tensor elements on micro scale	$\left[\frac{\mathrm{N}}{\mathrm{m}^2}\right]$	31
$\langle \mathbf{T}_\mu \rangle$	Volume averaged stress tensor at the micro scale	$\left[\frac{\mathrm{N}}{\mathrm{m}^2}\right]$	33
$\mathbf{T}_{th}$	Thermal stress tensor	$\left[\frac{\mathrm{N}}{\mathrm{m}^2}\right]$	34
$\mathrm{T}_{\mathrm{ij},th,m}$	Thermal stress tensor elements on meso scale with 2^{nd} rank indices	$\left[\frac{\mathrm{N}}{\mathrm{m}^2}\right]$	34
$\mathrm{T}_{\mathrm{ij},th,\mu}$	Thermal stress tensor elements on micro scale with 2^{nd} rank indices	$\left[\frac{\mathrm{N}}{\mathrm{m}^2}\right]$	34
T_m	Technical stress related to measured tensile force	$\left[\frac{\mathrm{N}}{\mathrm{m}^2}\right]$	44
$\overline{\mathrm{T}}_m$	Arithmetic mean of technical stress related to measured tensile force	$\left[\frac{\mathrm{N}}{\mathrm{m}^2}\right]$	45
$\mathbf{u}(\Gamma_{\mathrm{xi}}^{-,+})$	Boundary surface discplacement vector on positive $(+)$ or negative $(-)$ surface related to base coordinate $\mathbf{x}_{\mathrm{i}}$	[m]	32
$\mathbf{u}$	Displacement vector	[m]	24
$\mathbf{u}(-)$	Displacement vector as a function of $(-)$	[m]	35
	Thermo-Mechanical Domain		
$\mathbf{A}$	Thermal expansion tensor	$\left[\frac{1}{\mathrm{K}}\right]$	26
A_{ij}	Elements of the thermal expansion tensor with 2^{nd} rank indices	$\left[\frac{1}{\mathrm{K}}\right]$	26
$\{\mathrm{A}_{\mathrm{i},T}\}$	Transversal isotropic thermal expansion tensor in Voigt index notation	$\left[\frac{1}{\mathrm{K}}\right]$	27
$\overline{\mathrm{A}}_{\mathrm{kl},\mu}$	Effective thermal expansion tensor elements on the micro scale with 2^{nd} rank indices	$\left[\frac{1}{\mathrm{K}}\right]$	34
$\mathrm{A}_{\mathrm{kl},\mu}$	Thermal expansion tensor elements on the micro scale with 2^{nd} rank indices	$\left[\frac{1}{\mathrm{K}}\right]$	34
A_{ji}	Thermal expansion tensor elements with 2^{nd} rank indices	$\left[\frac{1}{\mathrm{K}}\right]$	34

$\mathrm{A}_{\mathrm{j},\mu}$	Thermal expansion tensor elements on the micro scale with 2nd rank indices in Voigt notation	$\left[\frac{1}{\mathrm{K}}\right]$	35
$\mathbf{M}$	Temperature stress tensor	$\left[\frac{\mathrm{N}}{\mathrm{m^2K}}\right]$	26
M_{ij}	Elements of the temperature stress tensor with 2nd rank indices	$\left[\frac{\mathrm{N}}{\mathrm{m^2K}}\right]$	26
$\mathrm{M}_{\mathrm{ij},m}$	Elements of the temperature stress tensor on meso scale with 2nd rank indices	$\left[\frac{\mathrm{N}}{\mathrm{m^2K}}\right]$	34
$\mathrm{M}_{\mathrm{ij},\mu}$	Elements of the temperature stress tensor on micro scale with 2nd rank indices	$\left[\frac{\mathrm{N}}{\mathrm{m^2K}}\right]$	34
	Thermal Domain		
h	Heat transfer coefficient	$\left[\frac{\mathrm{W}}{\mathrm{m^2K}}\right]$	24
R_{th}	Thermal resistance	$\left[\frac{\mathrm{K}}{\mathrm{W}}\right]$	49
$\mathbf{q}$	Heat flux vector	$\left[\frac{\mathrm{W}}{\mathrm{m^2}}\right]$	24
$\mathrm{q}_{\mathrm{i},m}$	Heat flux vector elements on meso scale	$\left[\frac{\mathrm{W}}{\mathrm{m^2}}\right]$	35
$\mathrm{q}_{\mathrm{i},\mu}$	Heat flux vector elements on micro scale	$\left[\frac{\mathrm{W}}{\mathrm{m^2}}\right]$	36
Q	Sum of volumetric heat sources and sinks	$\left[\frac{\mathrm{W}}{\mathrm{m^3}}\right]$	27
Q_g	Generated volumetric heat	$\left[\frac{\mathrm{W}}{\mathrm{m^3}}\right]$	27
Q_r	Radiated heat	$\left[\frac{\mathrm{W}}{\mathrm{m^3}}\right]$	27
Q_c	Convectively dissipated heat	$\left[\frac{\mathrm{W}}{\mathrm{m^3}}\right]$	27
Q_m	Sum of volumetric heat sources and sinks on meso scale	$\left[\frac{\mathrm{W}}{\mathrm{m^3}}\right]$	35
Q_μ	Sum of volumetric heat sources and sinks on micro scale	$\left[\frac{\mathrm{W}}{\mathrm{m^3}}\right]$	36
$Q_{\mathrm{i},f}$	Total forced heat for virtual material testing	[W]	36
	Energy		
p_d	Area specific energy consumption of an ice protection system	$\left[\frac{\mathrm{kW}}{\mathrm{m^2}}\right]$	20
p_{max}	Area specific maximum energy consumption of an ice protection system	$\left[\frac{\mathrm{kW}}{\mathrm{m^2}}\right]$	20
P_d	Absolute energy consumption of an ice protection system	[kW]	21
P_{max}	Absolute maximum energy consumption of an ice protection system	[kW]	21
	Electrical Domain		
$\boldsymbol{e}$	Electrical field vector	$\left[\frac{\mathrm{V}}{\mathrm{m}}\right]$	24
I	Electrical current	[A]	47

I_f	Forced current	[A]	48
I_s	Prescribed, optimised current	[A]	96
$\overline{I}$	Mean current applied to flat plate specimen	[A]	80
$\mathbf{j}$	Vector of electrical current density	$\left[\frac{\mathrm{A}}{\mathrm{m}^2}\right]$	24
$\mathbf{j}_{2D}$	Vector of electrical current density for a 2D model	$\left[\frac{\mathrm{A}}{\mathrm{m}^2}\right]$	69
K	Resistance	[Ohm]	49
P	Power	[W]	49
	General Effective Parameter		
$\overline{k}$	Effective scalar quantity (unit depends on input)		37
$\langle k \rangle$	Volume averaged scalar quantity (unit depends on input)		37
$k_{\mathrm{i,j}}$	Scalar quantitiy in direction i of constituent j (unit depends on input)		38

Greek Symbols

Symbol	**Explanation**	**Unit**	**Page of Definition**
α	Coefficient of thermal expansion	$\left[\frac{1}{\mathrm{K}}\right]$	xiv
$\alpha_{\|\|,f}$	Carbon fibre coefficient of thermal expansion in longitudinal direction	$\left[\frac{1}{\mathrm{K}}\right]$	10
$\alpha_{\perp,f}$	Carbon fibre coefficient of thermal expansion in transversal direction	$\left[\frac{1}{\mathrm{K}}\right]$	10
$\alpha_{c/m}$	Coating or matrix coefficient of thermal expansion	$\left[\frac{1}{\mathrm{K}}\right]$	15
α_l	Ply orientation angle with respect to longitudinal directions	[°]	93
α_a	Angle of attack	[°]	82
Γ	Boundary surface	[m^2]	29
$\Gamma_{\mathrm{xi}}^{+,-}$	Boundary surface in x_{i} direction on micro scale	[m^2]	29

$\Gamma^{+,-}_{\mathrm{yi}}$	Boundary surface in y_i direction on meso scale	[m^2]	83
$\Gamma^{-}_{\mathrm{x1,j}}$	Boundary surface area for current density application to conductors (micro scale)	[m^2]	65
$\Gamma^{-}_{\mathrm{y1,j}}$	Boundary surface area for current density application to conductors (meso scale)	[m^2]	85
$\Gamma^{+}_{\mathrm{x1},\phi}$	Boundary surface area for ground application to conductors (micro scale)	[m^2]	65
$\Gamma^{+}_{\mathrm{y1},\phi}$	Boundary surface area for ground application to conductors (meso scale)	[m^2]	85
γ_{xixj}	Complete glide angle	[rad]	32
γ_{xi}	Glide angle of body edge related to coordinate x_i	[rad]	32
Δ_t	Total elongation	[m]	44
Δ_r	Resin related elongation	[m]	44
Δ_s	Specimen elongation	[m]	44
$\Delta\theta^0_{\mathrm{xi}}$	Periodic thermal boundary condition related to direction x_i		36
$\Delta\theta$	Temperature change	[K]	24
Δ_C	Drop of effective stiffness	[%]	57
Δ_A	Drop of thermal expansion coefficient	[%]	57
Δ_θ	Temperature drop in thickness direction	[K]	73
$\Delta_{\theta c}$	Computed temperature drop in thickness direction	[K]	XIII
δ_θ	Specific temperature drop in thickness direction	$\left[\frac{\mathrm{K}}{\mathrm{mm}}\right]$	73
$\delta_{\theta,2D}$	Specific temperature drop in thickness direction of 2D representation	$\left[\frac{\mathrm{K}}{\mathrm{mm}}\right]$	76
ε	Emissivity	[-]	28
ζ	Ratio of volume fractions in Lewis-Nielsen method	[-]	40
η	Weight function in Lewis-Nielsen method	[-]	40
θ	Local temperature	[K]	24
$\langle\theta\rangle$	Volume averaged temperature	[K]	74
θ_0	Reference temperature	[K]	24
θ_a	Ambient temperature	[K]	37
θ_r	Room temperature	[K]	XIII

$\theta(\Gamma_{\mathrm{xi}}^{+,-})$	Temperature at positive or negative boundary surface related to direction x_{i}	[K]	36
$\theta_{g,c/m}$	Glass transition temperature of coating or matrix polymer	[K]	15
θ_b	Bleed air temperature taken from engine	[K]	20
θ_s	Surface temperature	[K]	21
θ_m	Temperature measured by thermographic camera	[K]	87
θ_p	Prescribed ambient temperature in De-Icing test bed	[K]	87
θ_c	Computed temperature	[K]	91
$\overline{\theta}_{m,max}$	Arithmetic average of maximum measured temperature	[K]	86
$\theta_{m,max}$	Maximum measured temperature	[K]	86
θ_{min}	Minimum temperature	[K]	96
θ_{max}	Maximum temperature	[K]	96
ϑ_{k}	Empirical variance	$\left[\mathrm{K}^2\right]$	86
κ	Isotropic, specific electrical resistance	[Ωcm]	28
κ_f	Isotropic, specific electrical resistance of carbon fibre	[Ωcm]	10
$\kappa_{c/m}$	Isotropic, specific electrical resistance of coating or matrix polymer	[Ωcm]	15
κ_s	Isotropic, specific electrical resistance of semiconductors	[Ωcm]	42
κ_g	Isotropic, specific electrical resistance of glass fibre fabric	[Ωcm]	XII
λ	Heat conductivity	$\left[\frac{\mathrm{W}}{\mathrm{mK}}\right]$	xiv
$\lambda_{\parallel,f}$	Carbon fibre heat conductivity in longitudinal direction	$\left[\frac{\mathrm{W}}{\mathrm{mK}}\right]$	10
$\lambda_{c/m}$	Coating or matrix material heat conductivity	$\left[\frac{\mathrm{W}}{\mathrm{mK}}\right]$	15
$\lambda_{\perp,f}$	Carbon fibre heat conductivity in transversal direction	$\left[\frac{\mathrm{W}}{\mathrm{mK}}\right]$	10
λ_g	Glass fibre fabric heat conductivity (quasi-isotropic)	$\left[\frac{\mathrm{W}}{\mathrm{mK}}\right]$	XII
$\Lambda_{\mathrm{ij},m}$	Heat conductivity tensor on meso scale with 2$^{\mathrm{nd}}$ rank indices	$\left[\frac{\mathrm{W}}{\mathrm{mK}}\right]$	35

$\overline{\Lambda}_{\mathrm{ij},\mu}$	Effective heat conductivity tensor on micro scale with 2nd rank indices	$\left[\frac{\mathrm{W}}{\mathrm{mK}}\right]$	35
$\mathbf{\Lambda}$	Heat conductivity tensor	$\left[\frac{\mathrm{W}}{\mathrm{mK}}\right]$	27
$\Lambda_{\mathrm{ij},\mu}$	Heat conductivity tensor elements on micro scale with 2nd rank indices	$\left[\frac{\mathrm{W}}{\mathrm{mK}}\right]$	36
Λ_{i}	Heat conductivity tensor element in Voigt's notation	$\left[\frac{\mathrm{W}}{\mathrm{mK}}\right]$	28
μ	Marks micro scale as index	[-]	29
ν	Poisson's ratio	[-]	xiv
$\nu_{\parallel,f}$	Carbon fibre Poisson's ratio in longitudinal direction	[-]	10
$\nu_{\perp,f}$	Carbon fibre Poisson's ratio in transversal direction	[-]	10
ν_j	Isotropic Poisson's ratio of constituent j	[-]	39
$\nu_{c/m}$	Coating or matrix Poisson's ratio	[-]	15
ν_a	Air velocity	$\left[\frac{\mathrm{m}}{\mathrm{sm}}\right]$	82
ξ	Particle shape factor in Lewis-Nielsen method	[-]	40
ρ	Density	$\left[\frac{\mathrm{kg}}{\mathrm{m}^3}\right]$	xiv
ρ_f	Carbon fibre density	$\left[\frac{\mathrm{kg}}{\mathrm{m}^3}\right]$	10
$\rho_{c/m}$	Matrix or coating density	$\left[\frac{\mathrm{kg}}{\mathrm{m}^3}\right]$	15
$\rho_{s,h}$	Surface weight of heater element in heater mat system	$\left[\frac{\mathrm{g}}{\mathrm{m}^2}\right]$	22
$\rho_{s,g}$	Surface weight of glass fibre fabric	$\left[\frac{\mathrm{g}}{\mathrm{m}^2}\right]$	22
$\rho_{s,hm}$	Estimated surface weight of heater mat system	$\left[\frac{\mathrm{g}}{\mathrm{m}^2}\right]$	22
ρ_m	Surface weight of matrix material	$\left[\frac{\mathrm{g}}{\mathrm{m}^2}\right]$	22
ρ_g	Glass fibre fabric density	$\left[\frac{\mathrm{g}}{\mathrm{cm}^3}\right]$	XII
σ	Isotropic, specific electrical conductivity	$\left[\frac{\mathrm{S}}{\mathrm{m}}\right]$	xiv
ϕ	Electric potential	[V]	24
$\chi_{\mathrm{xi}}^{+,-}$	Boundary edge in x_{i} direction	[m]	68
$\chi_{\mathrm{x1,j}}^{-}$	Boundary edge for 2D current density application to conductors	[m]	69
$\chi_{\mathrm{x1},\phi}^{+}$	Boundary edge for 2D ground application to conductors	[m]	69
$\psi_{c/m}$	Ionic conductivity of coating or matrix material	$\left[\frac{\mathrm{S}\cdot 10^{-8}}{\mathrm{cm}}\right]$	15
Ψ	Stress interval related to linear regression	$\left[\frac{\mathrm{N}}{\mathrm{m}^2}\right]$	47

Ω	Spatial domain	$[m^3]$	29
Ω_m	Spatial domain on meso scale	$[m^3]$	29
Ω_μ	Spatial domain on meso scale	$[m^3]$	29

Operators

Symbol	Explanation	Unit	Definition
∇	Nabla operator	$[\frac{1}{m}]$	24
∇_{2D}	2D Nabla operator	$[\frac{1}{m}]$	69
∂_t	Time derivative	$[\frac{1}{s}]$	27
δ	Kronecker delta	[-]	31

Acronyms

Acronym	Explanation	Page of Definition
APU	Auxiliary Power Unit	19
CFRP	Carbon fibre reinforced plastic	1
DC	Direct current	48
DMF	Dimetylformamide	14
EIDI	Electro-Impulse De-Icing	23
EMEDS	Electro-Mechanical Expulsion De-Icing System	23
FEM	Finite element method	8
HTC	Heat transfer coefficient	28
MCM	Multifunctional composite material	1
MC	Micro controller	81
NTC	Negative temperature coefficient	42
ONB	Orthonormal basis	25
PDE	Partial differential equation	38
PeCCF	Polymer electrolyte coated carbon fibre	3
PeCCFC	Polymer electrolyte coated carbon fibre based composite	95
PE	Polymer electrolyte	17
PTC	Positive temperature coefficient	42

ROM	Rule of mixtures	38
RVE	Representative volume element	8
SBE	Structural battery electrolyte	3
SEM	Scanning electron microscope	48
SPE	Structural polymer electrolyte	3
TEC	Thermal expansion coefficient	27
TGA	Thermogravimetric analysis	38
TLLN	Two-Level Lewis-Nielsen	66
TPLN	Three-Phase Lewis-Nielsen	41
UC	Unit cell	8
WAI	Wing anti-ice system	20
VA	Volume average	74

1 Introduction

1.1 Background of Multifunctional Composites and Applications

Multifunctional composite materials (MCM) aroused high research interest during the last decade. The basic benefit of MCM is their ability to provide electrical, thermal or mechanical functions simultaneously, aiming at a reduction of the resulting system's weight. This weight reduction potential is enabled by decreasing the amount of several monofunctional system components, their installation material as well as the overall complexity (see figure 1.1).

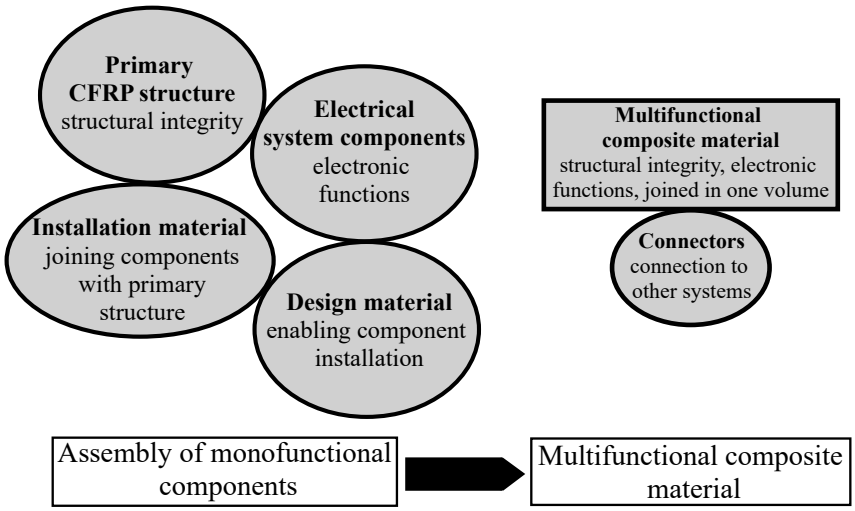

Figure 1.1: Principle of weight saving by MCMs; the bubble area symbolises material weight

This general principle can be applied in the area of mechanical, electrical and thermal systems of future mobility solutions. The basic principle of an energy efficiency increase by a vehicle's weight reduction is well known. The discipline of aeronautical engineering brings this principle to perfection, since incremental as well as disruptive weight savings provide an important contribution to the reduction of emissions from fossil fuel burn. Although a perspective of fossil fuel free air transport is under development for future air transport, the efficient use of alternative propulsion power sources will be an ever demanding objective.

A standard composite material which offers high mechanical performance while being light weight is the carbon fibre reinforced plastic (CFRP) that has a material share of over 50 % in modern passenger aircraft like the Airbus A350 [1]. One approach to use this material in a multifunctional manner is the *structural battery* concept, made from

a composite of carbon fibres, structural battery electrolytes and filler materials [2]. The structural battery aims at storing energy in form of a chemical potential which is the internally stored energy related to the presence of particles. For the structural battery, this is enabled by the ability to intercalate lithium ions within the carbon fibres. Accordingly, the carbon fibres act both as a reinforcement and as a battery electrode. The replacement of monofunctional CFRPs in the body of an aircraft by structural batteries could offer a high energy storage capacity while reducing the need for standard energy storage systems within the aircraft [3].

Joule heat has a significant influence on the multifunctional performance of the structural battery which is generated by ion and electron movement throughout the conducting materials. An industry patent considers the application of the Joule heat effect in MCM for an energy efficient De-Icing of aircraft surfaces [4]. Since traditional systems are designed to fulfill only one function (e.g. De-Icing), the system components are typically monofunctional which results in a substantial aircraft mass increase when the system is installed on the primary structure. Accordingly, the potential for a general mass reduction of the De-Icing system is expected to be high. Furthermore, the MCM architecture could be optimised by a computational model of the material behaviour in order to increase the energy efficiency.

The application of the MCM in the area of De-Icing is enabled by a suitable material model which considers the coupled electro-thermo-mechanical behaviour that is pertinent for multifunctional applications. This thesis aims at the development of an accurate *electro-thermo-mechanically coupled multi scale model* which covers the material behaviour under operational conditions and enables a model based optimisation. A proper model can pave the way for an innovation towards aircraft De-Icing systems and their industry adoption. The choice of the De-Icing application is motivated by the fact that the thermal load case is expected to be the most severe for the MCM. Conclusions derived from this thermo-mechanical load case under operational conditions can be transferred to other application scenarios of MCM, e.g. the structural battery.

Based on the state of research, the following subsection introduces the details of this approach and summarises the scope by three research hypotheses that are under investigation throughout this thesis.

1.2 Research Hypotheses on Modelling and De-Icing Application

Multifunctional composite materials, comprising constituents like carbon fibres, structural electrolytes and (particle filled) matrix polymers, hold potential for a new lightweight design on a system's level (e.g. vehicle's battery system or aircraft De-Icing systems [4, 5]). Traditionally, lightweight design is related to monofunctional structures which are optimised

towards their load bearing function. Any additional function is then provided by system components installed on top of the structure, e.g. a battery and cables which are attached to the lightweight structure. Structures made from MCM aim at providing such functions by a beneficial application of their intrinsic material (constituent) properties. Accordingly, the MCM is imbued with structural integrity and further functions which facilitates less system components and less installation material, thus enabling by now unknown mass reduction potential. One example is the structural battery [2,6] which combines the energy storage function with the structural integrity of a vehicle's structure. Especially in the area of energy efficient, low emission transport, this completely new approach can be of high value to decrease emissions as well as costs throughout the vehicle's life-cycle.

Research towards applications of MCM was enabled by the field of electro-chemistry, which led to the development of tailored polymer systems for structural energy storage and morphing composites. This resulted in a number of coating materials for carbon fibres, opening new design windows for MCM [7–9]. These types of structural battery electrolyte (SBE, [2]; frequently also denoted as structural polymer electrolyte, SPE) are coatings that represent a new material phase within the CFRP which changes the mechanical behaviour compared to two-phase classical CFRPs. It is expected that the influence on the mechanical behaviour can be significant if the stiffness of the coating is much lower compared to the remaining constituents. Furthermore, the polymeric coatings show significant stiffness drops with rising temperature which indicates a direct coupling of the thermal and mechanical domain [10]. Accordingly, for the application of MCMs the thermo-mechanically coupled material behaviour should be considered.

The material based multifunctional approach is a new challenge for lightweight design of structures which needs to overcome the monofunctional design to release the potential for a system level mass reduction. Apart from the original application scenarios (structural power and morphing [6, 10]), the polymer electrolyte coated carbon fibres (PeCCF) are beneficial for thermal management purposes. As already indicated for existing applications, carbon fibres emit significant Joule heat during electrical current conduction. The resulting temperature rise usually needs to be limited to prevent damage or a decrease in mechanical performance. A new application scenario, in which such emitted heat is desired, is the De-Icing of aerodynamic surfaces like wing leading edges. One of the classical, certified De-Icing systems in today's commercial passenger aircraft is the *bleed air* system, taking hot air from the engine which is distributed via a pipe system to the iced airframe structures [11, 12]. A second approach, are *electrical heater mats* which are installed on top of the load bearing structure [13, 14]. The electrical heater mats gain heat by electrical energy applied to a metallic mat.

A new approach based on MCM is considered in this work, in which the PeCCFs are utilised for heat generation within the structure [4]. Compared to earlier approaches

by standard CFRP which was functionalised for De-Icing [15], the polymer electrolyte coating enables an electrical insulation of the carbon fibre and prevents short-circuits with other carbon fibres or plies of the laminate. Consequently, it is expected that the De-Icing function is provided by the constituents of the MCM laminate, reducing the system components to the load bearing structure and the energy source. The installation of further system components, like pipes or electrical heater mats in the classical systems, is not necessary. Moreover, it is expected that the heat emitting, but insulated PeCCFs can be distributed in a way that the De-Icing function is realised with less material effort and that the needed energy consumption can be reduced to a minimum.

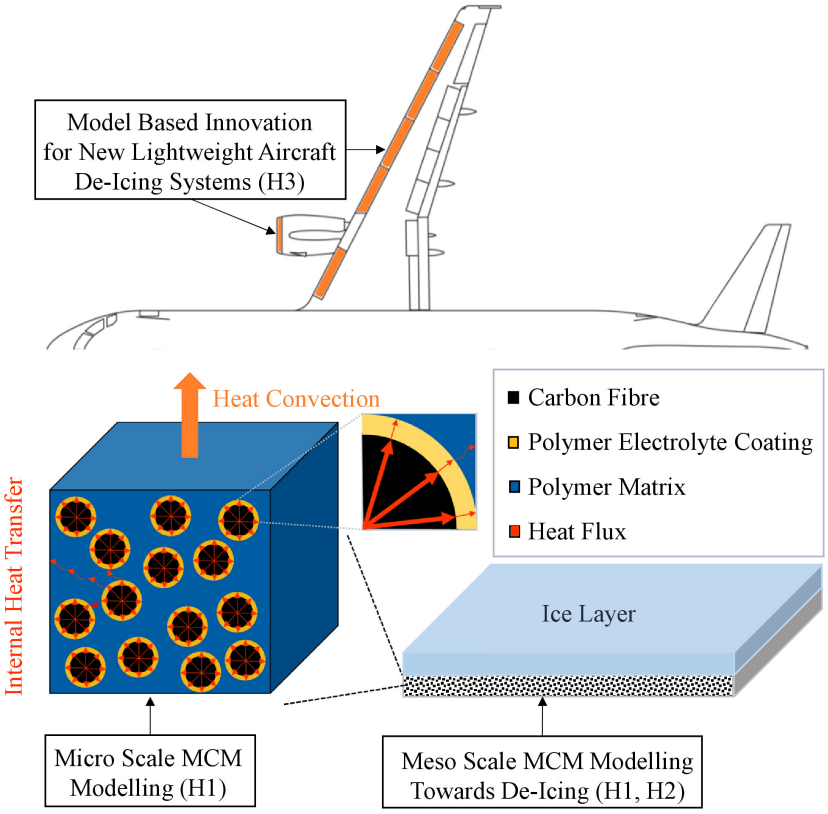

Figure 1.2: Relation of the hypotheses to the MCM and to the De-Icing application scenario

In general, the challenge of MCM is to develop a good understanding of the multiphysical coupling and its effect on the material behaviour to define related design requirements. The optimisation potential towards applications will be mainly driven and finally limited by the composite material properties. From this viewpoint, the application for De-Icing represents a maximum thermal load case. The thermal field and especially the influence of Joule heat are expected to have significant influence on the mechanical behaviour. Compared with investigations towards thermal effects of the structural energy storage [16, 17], this can be understood as an upper thermal boundary. However, the influence of thermal loads, especially those related to Joule heat and forced heat convection, on the mechanical behaviour of the MCM are negligible or assumed to be minor so far. The analysis of the

De-Icing case will contribute to the understanding of thermal effects under application related conditions. It is expected that the superior lightweight design potential of MCM can only be released if the coupled material behaviour can be described with sufficient resolution and accuracy while beeing computationally efficient.

The described expectations and potentials are summarised in three specific research hypotheses, providing the scope of this work:

H1 It is expected that an electro-thermo-mechanically coupled model, embedded in a multiscale material representation, is able to cover the major properties of MCMs made from PeCCF.

H2 It is expected that PeCCF based MCM are able to provide a proper De-Icing function for aircraft structures under operation conditions, enabling a significant mass and energy consumption reduction in the future.

H3 It is expected that requirements for functional optimisation can be derived from computational analysis, leading to model based innovation towards furture MCM based lightweight design structures.

This thesis aims at developing and validating the needed electro-thermo-mechanically coupled material model on multiple scales. The model provides the basis for application related MCM analysis (hypothesis H1) which is focused on different material scales (e.g. micro and meso scale, see figure 1.2). New strategies for the optimisation of the model towards computational efficiency will be introduced and discussed. Furthermore, the ability of the MCM to provide a proper De-Icing functionality is evaluated based on the modelling framework for the first time, which is mainly related to a coupon scale (meso scale, see figure 1.2). The results are discussed with an emphasis on the comparison with classical solutions towards mass reduction and energy efficiency (hypothesis H2). Finally, it is analysed which new requirements for a system level optimisation of the MCM towards best lightweight design solutions can be derived (hypothesis H3), aiming at future applications for aircraft De-Icing systems (see figure 1.2). It should be noted that the proof of hypotheses H2 and H3 is enabled after H1 is successfully demonstrated.

For the modelling framework and the focused application for De-Icing, this work builds on the state of the art which is presented in the next chapter (see chapter 2). Furthermore, chapter 3 introduces the theoretical fundament for the development of the micro and meso scale model of PeCCF based MCM and related means of experimental validation given in chapter 4. The model is further used for the evaluation of the De-Icing application, presented in chapter 5. Important results concerning structural behaviour under application related boundary conditions are discussed. Finally, chapter 6 summarises the major conclusions of the thesis, rates the results versus the hypotheses and provides an outlook on future research activities around multifunctional materials and structures.

2 Actual Multifunctional PeCCF Materials and De-Icing Systems

2.1 Definition of Multifunctionality

The term *multifunctional* is frequently used with very different definitions in the context of MCMs and multifunctional structures. The following three definitions are distinguished:

(1) *Multifunctional material*: E.g. (a) A carbon fibre which provides structural reinforcement and is able to intercalate lithium ions or (b) A shape memory alloys which return into a geometric state with temperature increase (see [18, 19])

(2) *Multifunctional composite material*: Carbon fibre electrodes embedded in a solid polymer electrolyte, serving as load bearing structural energy storage (see [6])

(3) *Multifunctional structure*: A structure like a sandwich panel in which a standard battery is embedded (see [20, 21])

As described by (3) the term multifunctional structure is used for structures which are composed by one or more monofunctional subcomponents, e.g. a structure with integrated standard batteries is frequently called a multifunctional structure. Accordingly, monofunctional subcomponents like the standard battery and a CFRP laminate are combined to provide the energy storage function and structural integrity (see e.g. [20, 21]).

For multifunctional material composites (2), the multifunctionality is provided by the constituents that are multifunctional materials (1). Accordingly, the MCM (2) can be understood as an assembly of an amount of multifunctional materials (1). Multifunctional materials are able to provide several functions due to their physical properties. One example for such constituents is the carbon fibre providing the functions structural integrity, Joule heating and ion intercalation. These functions are enabled by its structural stiffness and strength, its intermediate electrical conductivity and its graphitic nanotexture respectively. Consequently, *multifunctional* is related to the single functions provided by the composite constituents which are combined so that their multifunctionality can be applied for weight saving. This is the case for the MCM based De-Icing in which the material's functions Joule heating and structural integrity are applied [4]. Another example is the popular structural (massless) energy storage that provides structural integrity and energy storage functionality [2, 3, 22].

Definitions (1) and (2) are used in this thesis with respect to the level of resolution which is subject of discussion. Assemblies of monofunctional subcomponents or structures (3) are not examined in this thesis. With this understanding it is defined that a MCM combines several multifunctional constituents on the micro scale in order to apply these functions in a beneficial way on structure or system scale. With respect to the term *smart material*, this definition is not related to materials that are able to auto adapt to the environment like an intelligent subject (as described e.g. in [23]). However, the materials described in this thesis can adapt their performance (e.g. the stiffness) by the influence of a controlled actuation (e.g. by a temperature change) which corresponds to the definition of a temperature active smart material [24]. Such functionalities related to electro-thermo-mechanical coupling effects are discussed within this thesis.

Since this definition of multifunctionality implies the demand for examination on different scale levels, the next subsection introduces a comprehensive scale level definition used in this thesis.

2.2 Scale Levels Related to Application

MCMs under investigation in this work are composed by three or more constituents. These constituents are either thin fibres (e.g. carbon or glass fibres), polymeric matrix materials (e.g. epoxy resin) and interphase materials. In terms of interphase materials, SPEs are focussed. Depending on their application, several further constituents like $LiFePo_4$ particles or glass fibre fabrics can be part of the MCM. Traditionally, composite materials and structures are described on different scale levels to resolve the geometry of the internal architecture of the composed material in a model. This is especially defined for structural design and test, when it comes to airworthiness certification procedures in the aviation industry (see e.g. the building block test pyramid [25]). The application of the MCM in the area of De-Icing is focused in this thesis. Respectively, figure 2.1 illustrates the scale levels with respect to a composite structure in an aircraft wing leading edge. Starting with the nano scale of the single constituents of a composite, the texture of a carbon fibre is presented here [26]. In earlier works, the texture was identified to define the intrinsic properties of the constituents (e.g. stiffness, strength, or ion intercalation capacity). The desired functions, e.g. mechanical stiffness, depend on the nano-structure of the constituents [27–29]. This highlights that the multifunctional properties of the constituents are intrinsically given by their individual physical composition. In combination with other constituents, a composite material can be formed on the micro scale. This basic micro scale architecture is then reproduced by manufacturing processes on the macro scale to build structural elements. Those structural elements can be of coupon or part scale which is equivalent to the dimension of an aircraft part [25]. In this example it is represented

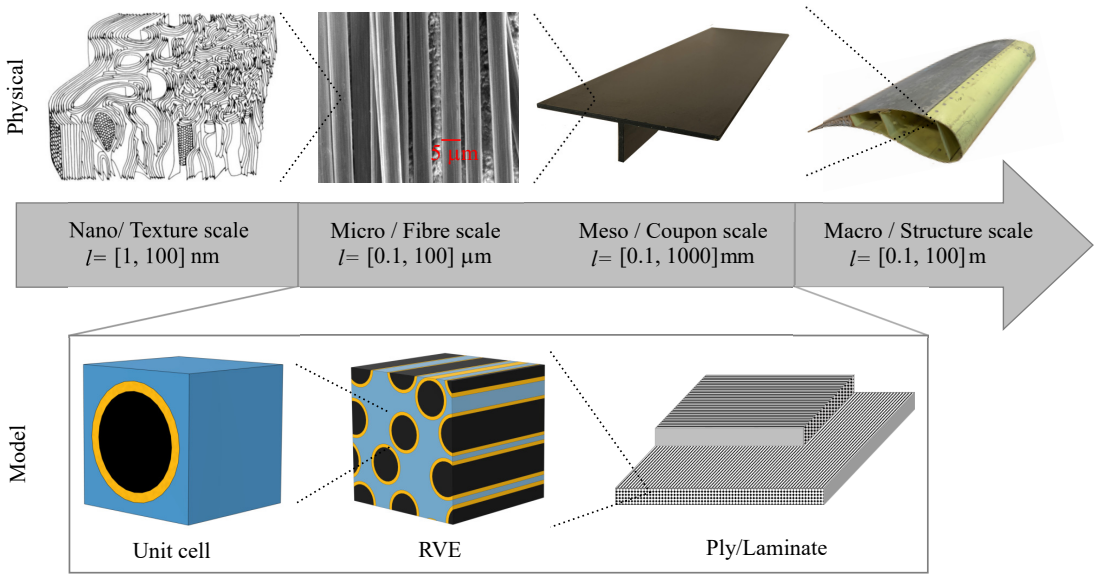

Figure 2.1: Overview of scale levels, nano scale illustration taken from [26]

by an aicraft leading edge slat which is one of the aerodynamic surfaces exposed to ice accumulation during flight.

In between nano and macro scale, several intermediate scale levels can be defined. For this work, the definition is based on the single constituents and laminate level structures made from it. Accordingly, the micro scale is considered to be related to the typical carbon fibre diameter ($d_f = 5$ µm). The meso scale is related to a single composite ply or several plies stacked to a laminate. For model development the focus lies on these two scale levels, since they can be well described by the continuum mechanics theory for elastic bodies and related theories like continuum thermodynamics. Furthermore, in the theory of continuum mechanics it is assumed that each spatial point in the domain is considered to be continous [30]. However, this sometimes is not the case on the nano scale. The micro scale is resolved based on unit cells (UC) or representative volume elements (RVE) and the meso scale geometry is usually represented as homogenised solid volumes (compare figure 2.1). Most computational work is done by the help of the finite element method (FEM), combined with analytical equations. Consequently, the separation from the nano scale is motivated further by the fact that the physical properties of the constituents used for the analysis are known. In addition, this work concentrates on the identification of MCM related physical effects and coupling effects resulting from the combination of material constituents on the micro scale up to the meso scale. Higher-level modelling on sub-component or component scale is excluded, since structural design related considerations are not part of this work.

The next subsection presents multifunctional constituent materials and the related state of research, followed by the different application areas and the theoretical fundament

related to continuum mechanics theory. The theoretical fundament will build on this micro and meso scale (later referred to as *multiscale*) definition.

2.3 Multifunctional Constituents and Composites

2.3.1 Carbon Fibres

As introduced in foregoing sections, the multifunctionality is related to the single constituents of the MCM. One of those multifunctional constituents is the carbon fibre which is classically used as a reinforcement in plastics. Such CFRPs benefit from high stiffness and strength of the fibre combined with it's low density. Since at least three decades, CFRPs enable superior lightweight design resulting in more than 50 % CFRP material share in modern commercial aircraft [1].

In most applications, the carbon fibres are applied as reinforcement only which is understood here as a monofunctional application [31]. Therefore, research towards carbon fibres was focussed on optimising the structural properties of the fibres resulting in a wide range of mechanical properties for structural design [32]. Carbon fibres based on polyacrylonitrile (PAN) are usually known for high strength, whereas pitch based carbon fibres are known for high Young's moduli and increased thermal conductivity [33, 34]. However, carbon fibres show in general intermediate electrical conductivity compared to standard conductor materials like copper. This provides either the ability to conduct electrical energy but also to induce Joule heat [35–38]. In addition, the carbon fibre is able to intercalate lithium ions what in turn is interesting for electrode applications inside a battery [18, 27, 39, 40]. Huge efforts in the area of structural batteries, also known as structural batteries, already lead to successfull demonstrations (see also subsection 2.3.3). Accordingly, some conclusions towards carbon fibres' multifunctional performance are provided here from energy storage research.

Table 2.1 provides an overview on properties of typical carbon fibre types which are under consideration for multifunctional use. The existing literature provides a wide range of mechanical, thermal and electrical material properties. Some properties, e.g. related to the transversal isotropic plane, are not given in literature. Therefore, estimates indicated by intervals (shown in brackets with lower and upper bound), which are given in calculation guidelines like [32], are used instead. However, the interest to determine more than the standard properties of carbon fibres increases, since they are of high interest for the modelling of MCM. The given examples are focussed in structural battery research, since these show superior energy storage capacity c_i^* [18, 38, 44, 45]. It should be noted that the numbers for IMS65 are chosen, since this carbon fibre was extensively applied in structural battery research due to its best reversible energy storage capacity, which is the research background of this thesis (see subsection 1.1). Accordingly, the bold numbers are

Table 2.1: Properties of some carbon fibre types, under consideration for multifunctional use; Intervals indicated by brackets are chosen, since no exact data is given in literature; References: [18, 32, 41–46]

Property	IMS65	T800	UMS45	M60J	Unit
$E_{\|\|,f}$	**290**	294	425	588	$\left[\frac{\text{kN}}{\text{mm}^2}\right]$
$E_{\perp,f}$	**21.8**	14.0	-	17.0	$\left[\frac{\text{kN}}{\text{mm}^2}\right]$
$G_{\|\|,f}$	**12.50**	8.78	-	5.84	$\left[\frac{\text{kN}}{\text{mm}^2}\right]$
$\nu_{\|\|,f}$		[**0.30**, 0.41]			$[-]$
$\nu_{\perp,f}$		[**0.35**, 0.45]			$[-]$
S_f	**6000**	5490	4600	3820	$\left[\frac{\text{N}}{\text{mm}^2}\right]$
$\alpha_{\|\|,f}$	-	**-0.56**	-	-1.10	$\left[\frac{10^{-6}}{\text{K}}\right]$
$\alpha_{\perp,f}$		[**7.0**, 9.7]			$\left[\frac{10^{-6}}{\text{K}}\right]$
ρ_f	**1.78**	1.81	1.83	1.93	$\left[\frac{\text{g}}{\text{cm}^3}\right]$
$c_{p,f}$	-	**752**	-	732	$\left[\frac{\text{J}}{\text{kg K}}\right]$
$\lambda_{\|\|,f}$		[**9**, 640]			$\left[\frac{\text{W}}{\text{m K}}\right]$
$\lambda_{\perp,f}$		[**1.1**, 1.7]			$\left[\frac{\text{W}}{\text{m K}}\right]$
κ_f	**1.45**	1.40	0.97	0.70	$[\Omega\text{cm} \cdot 10^{-3}]$
d_f	**5.0**	5.0	4.7	5.0	[µm]
$c^*_{i,f}$	317	243	33	154	$\left[\frac{\text{mAh}}{\text{g}}\right]$
C	0.1	0.1	≈0.3	0.1	$[-]$

*unsized, related to charging rate C in the line below

used as a fundament for numerical analysis in this thesis, especially for the evaluation of micro scale homogenisation methods. In addition, figure 2.2 indicates the chosen numbers in the typical CF property range normalised to the individual maximum. Results from material models can be discussed towards these ranges in order to choose ideal composite constituents. It should be noted that in most cases, carbon fibre's mechanical properties can be assumed to be transversal isotropic. Therefore, only five mechanical constants are needed to describe the stiffnesses in all directions properly. The remaining shear stiffness $G_{\perp,f}$ can be computed due to isotropy in the transversal plane by

$$G_{\perp,f} = \frac{E_{\perp,f}}{2 \cdot (\nu_{\perp,f} + 1)}. \tag{2.1}$$

In addition, the fibre diameter $d_f = 5$ µm is indicated, since it is used for the geometry definition of the CF within simulation models. Therefore, the diameter of specimens was verified by scanning electron microscopy (see also figure 2.3 (b) in the follwing subsection) for this thesis. However, also different magnitudes for the given properties can be considered, corresponding to the indicated typical magnitude ranges [32].

Related to these physical properties it is plausible that multiple functions can be provided, e.g.:

1. Reinforcement (increasing stiffness and strength),
2. Electrical current conduction,
3. Joule heating,
4. Ion intercalation (electrode function).

In classical lightweight design, only the monofunctional application as a reinforcement of plastics is considered. Energy transmission, Joule heating and ion intercalation (related to energy storage) are usually provided by further systems, subsystems or components which are installed on top of the CFRP structure, e.g. a battery attached to the primary structure of a vehicle. Related to hypothesis H2 (see subsection 1.2), the carbon fibre provides beneficial properties for the De-Icing function which is based on Joule heating. This results in a multifunctional use case, combining structural integrity and thermal heating based on the existing CFRP structure. As explained in hypothesis H2, it is expected that a multifunctional use of carbon fibres is beneficial in terms of weight saving and reduction of energy consumption on system level. Therefore, the subsections 2.3.3 and 2.4 present existing multifunctional application scenarios of carbon fibres and benachmarking De-Icing systems of commercial aircraft, respectively.

As already mentioned, the ability to coat the carbon fibres with a polymer (electrolyte) enables electrical insulation towards the remeining material domain and thereby, directed

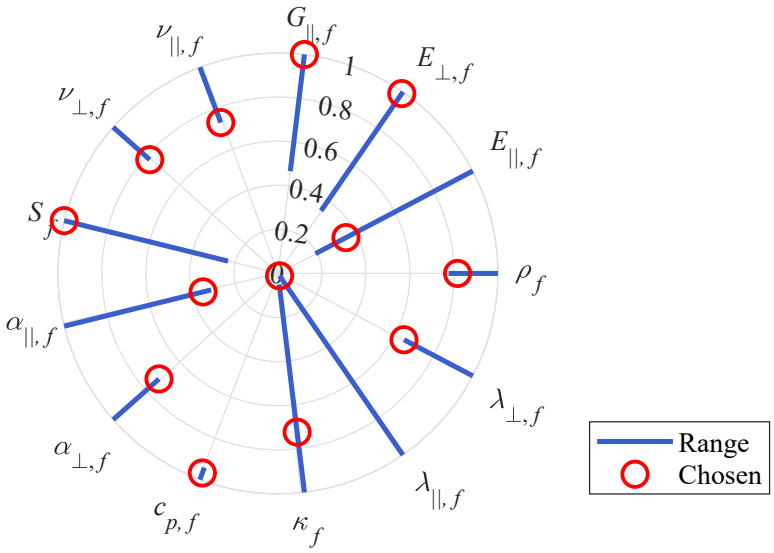

Figure 2.2: Overview on chosen CF properties (bold numbers in table 2.1) related to typical ranges of general CF properties (see [32, 43, 47, 48]); each normalised to related maximum

electrical power conduction. The properties of the polymer electrolyte coating and subsequently the properties of typical matrix materials are mentioned in the next subsection.

2.3.2 Polymer Electrolyte Coating and Matrix Materials

In the field of structural battery research, the 3D Battery approach is based on the idea to coat carbon fibres with a polymer electrolyte (SBE), which covers the fibre completely. The polymer elctrolyte coating should provide ion conductivity and electrical insulation, in order to make the carbon fibre function as an electrode in the structural battery composite [2, 6, 8, 27, 49].

The coating technology is based on the electro-chemical process *electro-polymerisation* (frequently also called *electrografting* or *electrocoating*) in which the carbon fibre is covered by a homogeneous polymer electrolyte coating [8, 9, 27, 50, 51]. Therefore, the carbon fibres are placed in a mold which is filled with a liquid mixture of the desired monomers, solvent and lithium salt. By tailoring the composition of this mixture, the desired properties of the resulting coating polymer can be adjusted. During the coating process, the lithium salt acts as supporting electrolyte and the coating process is enabled by setting a voltage between the active electrode and the passive electrode, both made from carbon fibre rovings (see figure 2.3 a)). It should be noted that the active electrode is the carbon fibre bundle which is coated and the passive electrode is a bundle of carbon fibres which is only applied as counter electrode to provide a full circuit. The polymerisation is initiated at the surface of the active electrode (bundle of carbon fibres). The coating process is finished when the complete surface area of each individual fibre within the bundle is coated,

since then, no electric current can be transferred anymore. Accordingly, the coating acts as an electrical insulator. After the process is finished, the active electrode represents a bundle (roving) of individually PE coated carbon fibres which can be embedded in a composite laminate. The volume of the monomer mixture is reduced by the amount that is electrografted as a polymer on the surface of the fibres. The excess monomer mixture remains liquid and the second CF bundle which was used as a counter electrode remains uncoated. Accordingly, these materials can be reused for another coating process.

Figures 2.3 b) and c) indicate examples of uncoated and coated IMS65 carbon fibres, respectively. The bare carbon fibres shows a diameter of $d_f = 5.02$ µm, which supports the data in table 2.1. It is mentioned that the coating process has similarities with cathodic dip painting of component surfaces [52].

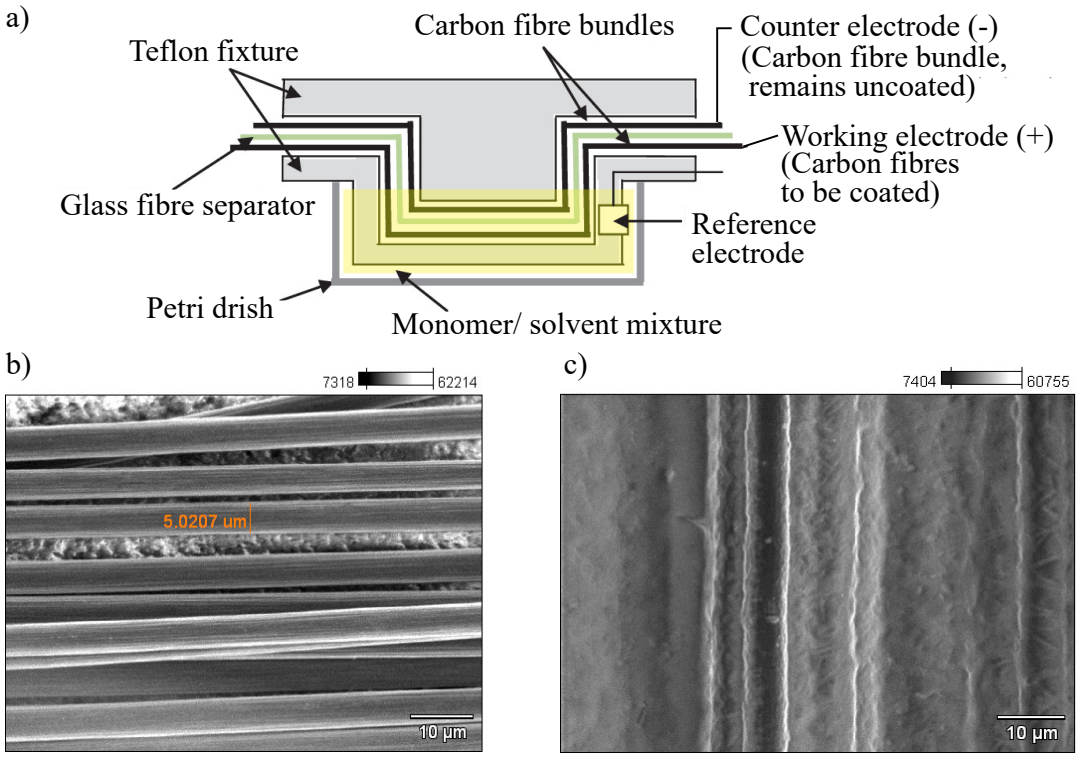

Figure 2.3: Polymer electrolyte coating: a) Coating setup (figure taken and adapted with permission from [8]), b) Bare IMS65 carbon fibre, c) Polymer electrolyte coated IMS65 carbon fibre

The resulting coating quality depends on the applied monomer mixture which is a composition of monomers resulting in either stiff or soft polymers [8]. Stiff polymers are sensitive to deformation, form cracks and show detachements from the fibre while handling after coating. The soft polymer provides a stiffness below 1 MPa, which is not suitable for a structural application. Accordingly both monomers are combined so that proper coatings in the form of a pinhole free cover of the carbon fibre result. The example shown in figure 2.3 c) is made with a monomer mixture containing monomer A and B in a 50:50 by weight ratio [methoxy polyethylene glycol (350) monomethacrylate (SR550) and tetraethylene

glycol dimethacrylate(SR209), respectively] with 8 % lithium trifluoromethanesulfonate (Li-triflate) solved in Dimetylformamide (DMF). The mixture is electro-polymerised and coated onto the carbon fibre according to the procedure given in [8]. The resulting coating thickness is indicated as $t_c = 500$ nm which is applied for geometric representations in this work's numerical analysis [6, 8].

The described monomer system is also given in table 2.2 which indicates the physical properties of the resulting polymers, after the related monomer was polymerised/coated. Comparing the different combinations of monomers A and B one finds that an intermediate storage modulus at 293.15 K of about 800 MPa comes with intermediate ion conductivity $\psi_{c/m} \approx 5 \cdot 10^{-8} \frac{\mathrm{S}}{\mathrm{cm}}$. As reported by Asp and co-workers [6], the multifunctional performance of a MCM is often a compromise between the different desired properties (here ion conductivity and structural stiffness).

Related to these properties, it is plausible that the following functions can be provided by the polymer electrolyte coating:

1. Electrical insulation,
2. Mechanical load bearing,
3. Stiffness adaption (related to temperature change),
4. Ion intercalation (related to battery function).

The desired functions for the De-Icing application are the ability to insulate the current conducting carbon fibres from the remaining composite and to bear mechanical loads between fibre and matrix, in order to maintain the reinforcment function of the carbon fibre. Therefore, the coating needs to be pinhole free, which is given for the presented monomer mixture of A and B. Furthermore, an intermediate storage modulus must be accepted since brittle and non-dense coatings can not be applied due to the risk for short circuits within the material. With this compromise in mind, the comparison with the epoxy resin in table 2.2 highlights that new challenges arise with the thermo-mechanical behaviour of the coating phase. At increased temperature, e.g. for $\hat{\theta} = 393.15$ K, the coating's storage modulus drops by 94 %. This is also indicated by the glass transition temperature $\theta_{g,c/m}$ being much smaller compared e.g. to typical maximum operating temperatures of aircraft $\hat{\theta} \approx 375$ (see also definitions in subsection 2.4). It is expected that the resulting effect on the composite performance is significant, which needs to be analysed by representing this behaviour in a suitable material model. This is also given by hypothesis H1 which provides the assumption that the given material behaviour can be implemented in a multiphysically coupled material model and that coupling effects can be analysed (compare subsection 1.2).

Table 2.2: Properties of some monomer mixture types in polymerised condition in comparison with epoxy resin; A: methoxy polyethylene glycol (350) monomethacrylate (SR550), B: tetraethylene glycol dimethacrylate(SR209), Li-salt: lithium trifluoromethanesulfonate (Li-triflate); References: [8, 32, 53–57]

Prop.	A	B	A+B	A+B	Epoxy	Unit
Ratio*	-	-	(50:50)	(50:50)	-	
Li cont.	12	-	8	12	-	[%]
$E'_{c/m}(\theta_a)$	1417	1	**820**	770	[1, **3000**]	$\left[\frac{\mathrm{N}}{\mathrm{mm}^2}\right]$
$E'_{c/m}(\hat{\theta})$	-	1	**49**	51	[1, **3000**]	$\left[\frac{\mathrm{N}}{\mathrm{mm}^2}\right]$
$\theta_{g,c/m}$	-	247	**332**	328	>**373**	[K]
$c_{p,c/m}$	-	-	**2090**	2090	**1050**	$\left[\frac{\mathrm{J}}{\mathrm{kg\ K}}\right]$
$\lambda_{c/m}$	-	-	**0.21**	0.21	**0.19**	$\left[\frac{\mathrm{W}}{\mathrm{m\ K}}\right]$
$\psi_{c/m}$	150	0.002	**5**	5.5	-	$\left[\frac{\mathrm{S}\cdot 10^{-8}}{\mathrm{cm}}\right]$
$\rho_{c/m}$			[**0.96**, 1.64]			$\left[\frac{\mathrm{g}}{\mathrm{cm}^3}\right]$
$\nu_{c/m}$			[**0.30**, 0.40]			[−]
$\alpha_{c/m}$			[**20**, 100]			$\left[\frac{10^{-6}}{\mathrm{K}}\right]$
$\kappa_{c/m}$			$\to \infty$			[Ωcm]

$\theta_a = 293.15$ K, $\hat{\theta} = 393.15$ K, *by weight

The aim of interface control or adaption was already formulated by Bismarck et al. [7], who imagined to provide a carbon fibre coating with the aim to adjust the composite's stiffness. This resulted in a MCM application related to adjustable stiffness which is discussed in the next subsection. In any case, the effects related to the modification of the composite by interface or interphase control between carbon fibre and matrix was not analysed in detail. Since the standard epoxy matrix material shows a temperature stable storage modulus until $\hat{\theta} = 393.15$ K [56], the thermo-mechanical coupling is reduced to the coating phase of the composite material. This recognition highlights the demand for the analysis of the thermo-mechanical coupling towards the composite's behaviour which is covered in this thesis.

In table 2.2 the bold numbers are chosen for numerical simulations in this thesis. To indicate these choices compared to typical PE property ranges, figure 2.4 indicates the relevant numbers graphically, in which each quantity is normalised by its maximum. Even though the choice depends on electro-chemical manufacturability, numerical results based on these choices can be discussed towards optimisation potential in the coating composition. Apart from the thermo-mechanical coupling, the polymer electrolyte coating

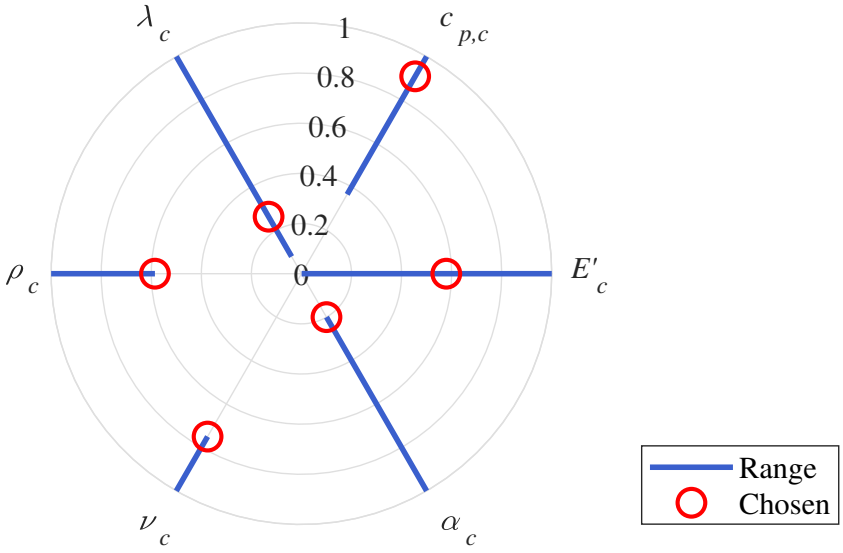

Figure 2.4: Overview of chosen polymer electrolyte properties (bold numbers in table 2.2) related to given ranges (see [8, 53, 54]); each normalised to related maximum

and the epoxy resin matrix are assumed to provide similar thermal properties, e.g. specific heat and thermal conductivity. Since no specialised analysis of these properties is given in literature, standard ranges from similar polymer types are assumed [32, 56, 57]. All bold numbers in table 2.2 are used as standard material properties for numerical analysis if not specified differently.

The following subsection will introduce an overview of existing multifunctional applications of carbon fibres equipped with polymer electrolyte coatings. Based on the recognition of the state of research for MCMs, existing De-Icing technology applied in

today's aircraft is presented subsequently to form a benchmark for the new concept of PeCCF supported De-Icing.

2.3.3 Multifunctional Composite Materials and Applications

The multifunctional constituents are combined to form a MCM which is similar to classical fibre reinforced plastics. Such multifunctional CFRPs are highly specialised towards their application scenario. As described in the previous section, the PeCCF is under investigation for structural battery. This application combines the structural integrity with the function of energy storage and energy supply. The carbon fibres act as one electrode of the energy storage (e.g. as anode) and the polymer electrolyte acts as electrical insulator of the electrode and as ion conductor between the electrodes [2, 6, 8, 49].

Besides the structural battery application, the coated carbon fibres are in addition considered for a fibre-matrix interface control, e.g. in the area of active stiffness adaption. This concept applies suitable polymer coating systems with a glass transition temperature slightly above room temperature ($\hat{\theta}_g > \theta_a = 293.15$ K). This enables an active control of the interphase stiffness and thereby, the effective stiffness of the composite material, since the load transfer between matrix material and reinforcing carbon fibres is influenced. This is enabled by heating the material via Joule heating of the carbon fibres [7, 10, 58, 59].

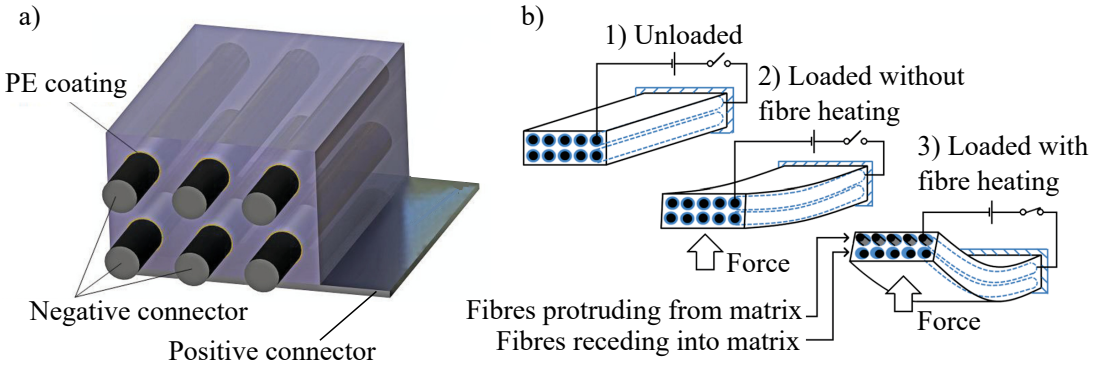

Figure 2.5: Applications of polymer (electrolyte) coated carbon fibres: a) 3D structural battery (taken and adapted with permission from [27]), b) Composite with adaptive stiffness (Reprinted and adapted with permission from [10]. Copyright 2013 American Chemical Society)

Figure 2.5 shows schematics of a) a structural battery half cell (polymer elctrolyte (PE) coating in yellow) and b) a stiffness controllable composite material in a beam configuration (coating in blue). In both application scenarios, the materials are exposed to Joule heat induction due to current conduction along the carbon fibres. On one hand, the heat generation in the structural battery is desired to reach the ideal operating temperature. For the adaptive stiffness case, the temperature rise is necessary to soften the interphase. On the other hand, the temperature needs to be limited to avoid degradation of the polymers and subsequent damage of the device. Especially with respect to operational

conditions, in which heat is generated and transferred to the environment, this can lead to complex electro-thermo-mechanical couplings for the material behaviour.

In the area of structural batteries, Carlstedt, Asp and co-workes developed a simulation framework for structural batteries and studied the effects of the 3D structural battery approach towards chemo-electro-thermo-mechanical couplings [2, 5, 6, 16, 60]. The emphasis was on identifying heat generation related to the energy storage function (e.g. due to ion intercalation). Joule heating was omitted for these studies. A new study related to a different, so called "laminated structural battery" or "2D structural battery", case revealed that significant heat generation and temperature distributions need to be considered during structural battery operation [17, 61]. However, a thermo-mechanical coupling of the PE coating is not part of this analysis. Especially the coupling of the effective composite material stiffness with the thermal field and generated temperature and stress fields under operational conditions are not covered in previous studies.

In this work, hypthesis H1 (see subsection 1.2) comprises the expectation that the desired effects and couplings can be analysed based on a model with a full electro-thermo-mechanical coupling. Therefore, it should be mentioned that the De-Icing application scenario is one of the most severe thermal load cases for a multifunctional composite, due to low ambient temperatures and high temperature gradients within the material during heat generation. Results from a detailed analysis of this application scenario will provide conclusions which are also of interest for PeCCF based structural batteries and composites with adaptive stiffness.

The next section introduces actual De-Icing technologies from industrial application and new concepts considered in the research field. The main characteristics as well as operational conditions will be summarised as a benchmark for the new concept based on MCM, which is analysed and discussed in the following main chapters of this thesis.

2.4 De-icing Technologies for Aircraft Wing Leading Edges

2.4.1 Icing Conditions During Aircraft Operation

During aircraft operation, e.g. after take-off and during decent for landing, the aircraft is frequently exposed to cold air with supercooled water or mixed phase conditions, in which liquid and iced water occurs. This leads to ice accumulation at the airframe outer surface, especially in the area of wing or stabiliser leading edges, engine inlets and measurement probes. Such icing of the aircraft surface is dangerous during aircraft flight, since aerodynamic lift, engine operation and measurements from the probes can be affected by increasing ice layer thickness [62]. Consequently, aircraft certification specifications demand for sufficient de- or anti-icing systems to prevent failures during operation [63].

Icing conditions occur in a specific ambient temperature range of $\theta_a = [243, 273]$ K

with volume specific total water contents of $c_w > 0.24\ \frac{\mathrm{g}}{\mathrm{m}^3}$. Such total water contents can occur in altitudes of $a_h = [0, 8000]$ m, which is related to the corresponding temperature and pressure of air [64, 65]. Civil aircraft are usually operated at flight altitudes around $a_{h,c} = [9000, 13000]$ m during cruise. This means that icing conditions occur only during climb and decent through wet air conditions. For 1.5 h total flight time, this flight phase makes 43 % of the total flight time, which corresponds to a short distance flight [66]. On long distance flights this portion decreases, since the absolute time for climb and decent remain similar, whereas the time for cruise increases. For instance, for a flight distance of 9300 km from Frankfurt am Main to Los Angeles, the flight time is about 12 h. Thus the corresponding portion of climb and decent is less than 6 % of the flight time.

The time fraction of the critical flight phases indicates that a de- or anti-icing system is usually only operated during minor time proportions of the flight when cold wet air conditions appear. Accordingly, the systems which prevent icing (anti-ice systems) or which remove ice from the surface of the aircraft (de-ice systems) should be light weight. Increased light weight design on a system level enables an additional reduction of fuel consumption, especially since the system represents parasitic (not needed) mass in most flight cases. Hypotheses H2 and H3 are motivated and supported by this recognition, since it is expected that a new MCM based De-Icing system offers increased weight saving potential compared to traditional systems (compare subsection 1.2).

Besides the system mass aspect, energy consumption during anti- or De-Icing operation is an important factor that should be considered for optimisation. Most active systems realise ice removal by thermal heat or by mechanical deformation of the surface. The energy is provided in form of hot air, pneumatic or electrical energy, all beeing produced from the engines. Thus, the less energy is needed, the more efficient is the aircraft in terms of fuel consumption.

For these aspects a benchmark is provided by indicating relavant quantitative measures in the following subsections, based on existing certified de- or anti-ice systems and related concepts from the research field.

2.4.2 Bleed Air System

The “bleed air“ De-Icing system operates with hot air taken from the compressor section of the aircraft's engine, being distributed to the ice critical airframe structures, e.g. the wing leading edges [62, 67–69]. This system is a certified standard for most commercial passenger aircraft from Boeing and Airbus [12, 70–72]. The hot air is distributed via a movable pipe system to the wing leading edges and a number of valves control the airflow. Figure 2.6 shows the air distribution system and a cut view of a wing leading edge with indicated hot air stream. The centrally controlled system directs hot air from either the main engine or the auxiliary power unit (APU) to the critical surfaces of the wing leading

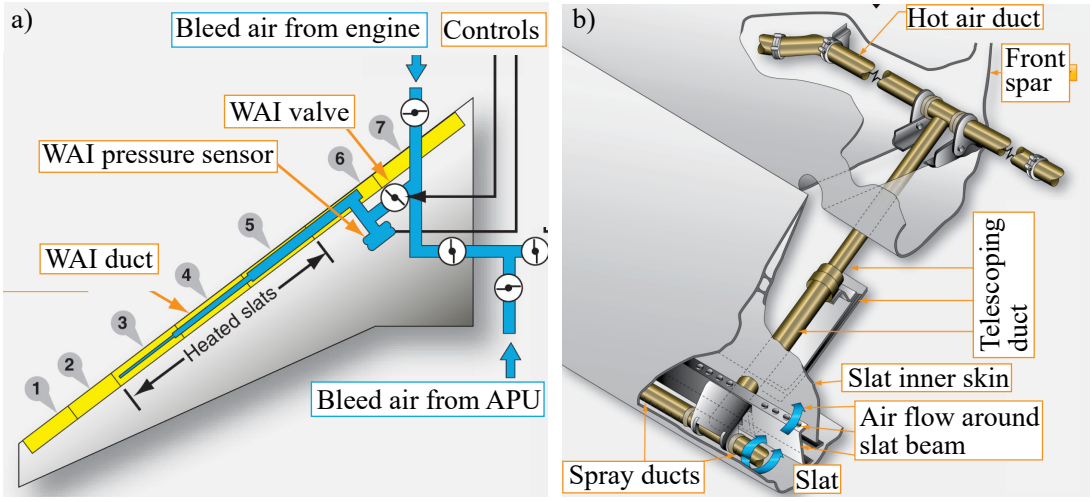

Figure 2.6: Bleed air enabled wing anti-icing (WAI) system: a) Hot air distribution system in a wing, b) Movable pipe system and air flow in leading edge slat (both adapted from [62])

edge/slat (see 2.6 a)). Since the slats are movable, the pipe system is designed so that the movement is supported by telescope ducts (see figure 2.6 b). The air is then distributed by a spray duct inside the leading edge and is exhausted at the lower back edge of the slat. The whole system adds a lot of necessary pipe and installation material to the primary structure of the wing. Related to the heated leading edge length, this adds $m_d = 3.6\ \frac{\text{kg}}{\text{m}}$ in case of the Boeing 767 [73, 74].

Besides added mass, the system takes hot air from the thermodynamic cycle of the engine at a temperature of $\theta_b \approx 500$ K. This heats the leading edge to a surface temperature of $\theta_s = 323$ K, which is more than needed to de-ice the surface of the wing [75]. To limit the energy consumption, a reduced operation mode called “running-wet“ anti-icing can be distinguished from “full evaporative“ mode. In the first case, the water is heated just enough to stay liquid so that it can flow downstream and in the second case, the water is directly evaporated as soon as it contacts the surface [76]. This leads to an approximated energy consumption related to the heated surface of $p_d = [16.0,\ 25.0]\ \frac{\text{kW}}{\text{m}^2}$ at running-wet anti-icing operation and $p_{max} = [46.0,\ 62.0]\ \frac{\text{kW}}{\text{m}^2}$ at evaporative anti-icing operation, as calculated in [73, 77].

The indicated measures of the bleed-air system support the expectation that new De-Icing systems made from MCM could improve the mass and energy consumption on a systems level (see hypothesis H2 in subsection 1.2). Besides the expectation of less system mass, the new system is expected to be more energy efficient and can be optimised towards an ideal energy input - heat up effectiveness, without such excessive over heat. However, it should be mentioned that the classical primary wing structure is made from metallic materials. This enables proper heat conduction from the inner area, in which hot air is spread, to the outer skin. The heat conductivity of CFRP made wing structures is

reduced a lot compared to its metallic twin which led to the development of an alternative approach, the heater mat system [73]. The next subsection introduces the heater mat system and its system measures.

2.4.3 Electrical Heater Mats

The heater meats represent a thermo-electrical De-Icing system, operating without bleed air from the engine. This system is invented and made by GKN Aerospace [78] and is used e.g. on the Boeing 787 wing leading edge slats [13, 14]. The advantage of this system is a thin metallic heater element in form of a thin patterned plate which enables Joule heating. Both are integrated in a composite structure which forms the heater mat. Especially new aircraft types, of which the leading edge is made from fibre reinforced plastics with low heat conductivity, the heater mat system provides an adaptable solution for De-Icing, which is integrated in the structure. In case of the Boeing 787, the laminate consists of two layers glass fibre fabric that cover the metallic heat element. The glass fibre fabrics insulate the electro-thermal heater element electrically from surrounding material layers. This core is sandwiched by 15 layers of carbon fibre fabrics on each side for structural integrity [14]. The whole component is covered by a high impact erosion shield as a top layer. The composite structure is then installed at the primary structure of the leading edge [14].

In case of the 787 De-Icing system, the energy need is $P_d = [45.0,\ 75.0]$ kW. Compared to the bleed air system, the heater mat is able to reduce the resulting temperature to the needed minimum, thus reducing the total energy consumption. This configuration heats the surface of the wing leading edge to at least $\theta_s = [280.0,\ 294.0]$ K. However, the system provides also an evaporative anti-icing operation mode which results in an energy consumption of $P_{max} = [150.0,\ 200.0]$ kW, indicating the increased energy need for this operation mode [14].

To enable a proper comparison of the different De-Icing systems, the de-iced surface area specific energy consumption and added specific mass per de-iced slat length are of interest. Due to lack of data about the heater mat system in literature, some estimated quantities are provided hereinafter.

A surface area of approximately 5 m x 1 m=5 m^2 for each slat is assumed based on the dimensions provided in [79] with 5 slats at each wing [80]. With a total of eight ice protected slats of the Boeing 787 [14], this results in an ice protected surface area of about 40 m^2. Related to this surface area, the specific energy consumption in De-Icing mode is approximated as $p_d = [1.1,\ 1.9]\ \frac{\text{kW}}{\text{m}^2}$ and in evaporation mode as $p_{max} = [3.75,\ 5.0]\ \frac{\text{kW}}{\text{m}^2}$.

The metallic heater element is made from copper [78] and has a thickness of about $t_m = 0.05$ mm. It is assumed, that a specific pattern is applied as heating element, which covers only 30 % of the surface area. This yields an estimated surface weight of

$\rho_{s,h} = 132\ \frac{\mathrm{g}}{\mathrm{m}^2}$ for the heater element layer. Taking this into account for a 1 m^2 heater mat with two additional layers of glass fibre fabric (lamina surface weight of $\rho_{s,g} = 291\ \frac{\mathrm{g}}{\mathrm{m}^2}$, [81]) a total surface weight of $\rho_{s,hm} = 714\ \frac{\mathrm{g}}{\mathrm{m}^2}$ is assumed for the heater mat system (without wiring). It should be noted that a fibre volume fraction of $v_f = 0.35$ with a matrix surface weight of $\rho_m = 112\ \frac{\mathrm{g}}{\mathrm{m}^2}$ was assumed for this calculation. Related to the heated leading edge length, the functional layers of the heater mat add roughly $m_d = 0.71\ \frac{\mathrm{kg}}{\mathrm{m}}$ to the slat's weight.

Compared to the traditional bleed air system, the heater mat system reduces the necessary system mass and energy consumption for the De-Icing and anti-icing function. The bleed-air and the heater mat system are certified and used for large aircraft. Beside these large aircraft solutions, several additional approaches are applied for small aircraft types and in the research field. The following subsection summarises the relevant approaches and identifies a benchmark for performance analysis of the newly proposed De-Icing system based on MCM.

2.4.4 De-Icing System Benchmark

Besides the bleed air and heater mat systems which are applied in actual large transport aircrafts' ice protection strategies, several alternative approaches are used for smaller aircraft types or are under investigation in the research field. Table 2.3 provides an overview of these approaches with related specific system mass and specific energy consumption.

The pneumatic boot system is a mechanical De-Icing system based on elastic boots made from rubber. Such boots are expanded as soon as an ice layer has formed on the surface so that the ice layer is bursted off. This system can be applied to small and large aircraft types, but is usually only considered for aircraft with small flight hour duties which is caused by its intense demand for inspection and maintenance [69, 73]. Chemical wet De-Icing is based on glycol which is stored in a tank and distibuted to the leading edge. The glycol is then led to the surface by small pores in the leading edge material which lowers the freezing point of the impinging water droplets. This system is usually not applicable to large aeroplanes, since it requires a huge volume of glycol to be carried during flight and the operation time is limited by the glycol volume. Due to the glycol volume, the specific mass for De-Icing is much larger compared to other solutions (see table 2.3).

The *Electro Impulse De-Icing (EIDI)* is a electro-mechanical De-Icing system which is operated by an electro-magnetic shock actor. The actor provides a mechanical impulse to the leading edge structure causing the surface to deform elastically with high velocity resulting in bursting off the ice-layer. An evolved system called *Electro-Mechanical Expulsion De-Icing System (EMEDS)* comprises the EIDI system and a thermal heating layer embedded in the leading edge structure. The EMEDS combines the benefits of both

Table 2.3: Comparison of typical ice protection systems with data from literature

System	p in $\left[\frac{\mathrm{W}}{\mathrm{m}}\right]$	m_d in $\left[\frac{\mathrm{kg}}{\mathrm{m}}\right]$	Ref.
Pneumatic Boots	≈ 62	≈ 2	[69, 73, 82]
Chemical De- Icing by Glycol	≈ 5	$\approx > 5$	[69, 73, 83]
Electro-Impulse De-Icing (EIDI)	≈ 23	1.8	[73, 74, 82]
Elec.-Mech. Expulsion De-Icing (EMEDS)	$*54.3 \cdot 10^3$	N.A.	[73, 84, 85]
Bleed Air	$*[16,\ 62] \cdot 10^3$	3.6	[73, 74]
Heater Mats	$**\mathbf{[1.1,\ 5] \cdot 10^3}$	**0.71**	[14, 73, 78–80]

*related to 1 m ice protected cord length

**as estimated in subsection 2.4.3

systems. It introduces thermal heating to lower the ice adherence and uses the mechanical removal of the ice layer. This reduces the needed total energy for a thermal-heat-only system and assures proper De-Icing by mechanical actuation [85]. However, also the EIDI as well as the EMEDS systems introduce further actuation mechanism which results in increased weight (compare table 2.3).

Accordingly, all alternative systems show much higher specific weight m_d and partly higher specific energy consumption $\left[\frac{\mathrm{W}}{\mathrm{m}}\right]$ compared to the actual heater mat system. In addition, most of the systems are intended for small or medium size aircraft which is not the main focus in this work. Consequently, the heater mat system is identified here as the base line system, representing a benchmark in terms of energy efficiency and light weight design potential (see bold measures in table 2.3). Within this work, the benchmark is used for analysis and discussions towards benefits of the MCM based De-Icing approach in chapter 5. Since the research design is based on the analysis of the intrinsic material constituents' and MCM functions, a physically motivated material model is needed, of which the theoretical fundament is provided in the following section.

3 Theoretical Fundament for Material Modelling

3.1 General Field equations

3.1.1 Multiphysical Coupling

For the mathematical description of the material and structural behaviour related to the different scales (see subsection 2.2), the framework of continuum physics, that is applied in this thesis, is presented. Related generator systems and assumptions for the electro-thermo-mechanical coupled model are provided in a general format which enables the description of specific models and the understanding of related results in the following chapters.

For all calculations, the basic assumption of linear thermoelasticity for small deformations is applied [30]. Classically, linearised Cauchy stresses $\mathbf{T}$ are assumed to depend on Greens' linearised strain tensor $\mathbf{E}$ and on the temperature difference $\Delta\theta = (\theta - \theta_0)$ related to a reference temperature θ_0 and local temperature θ

$$\mathbf{T} = T(\mathbf{E}, \Delta\theta) \quad \text{with} \tag{3.1}$$

$$\mathbf{E} = E(\mathbf{u}) = \frac{1}{2}\left(\nabla\mathbf{u} + \mathbf{u}\nabla\right) \quad . \tag{3.2}$$

The mechanical strain tensor depends on the displacmeent vector $\mathbf{u}$, which is usually the independent variable in the mechanical problem. Additional temperature induced strains can contribute to the stress field due to thermal expansion (see equation 3.5). In a thermo-mechanical problem, the temperature θ is covered as independent variable in the heat equation

$$\mathbf{q} = q(\theta, \nabla\theta, \mathbf{j}, \mathbf{E}) \tag{3.3}$$

that is further dependent on the temperature gradient $\nabla\theta$, the strain tensor (e.g. via friction) and the electric current vector $\mathbf{j}$. The latter couples the thermal field with the electrical field :

$$\mathbf{j} = j(\mathbf{e}, \theta, \mathbf{E}), \tag{3.4}$$

where $\mathbf{e}$ represents the electrical field. Equations 3.1-3.4 represent the general physical fields of mechanics, thermodynamics and electricity, that are subject to a direct coupling, since some of the independent variables act on other physics fields. This multiphysics framework is denoted as the electro-thermo-mechanical coupling in this work. Physical

variables leading to the coupling in this framework are the mechanical strains **E**, the temperature θ, the electrical field vector **e** and the electrical current density vector **j** (see figure 3.1).

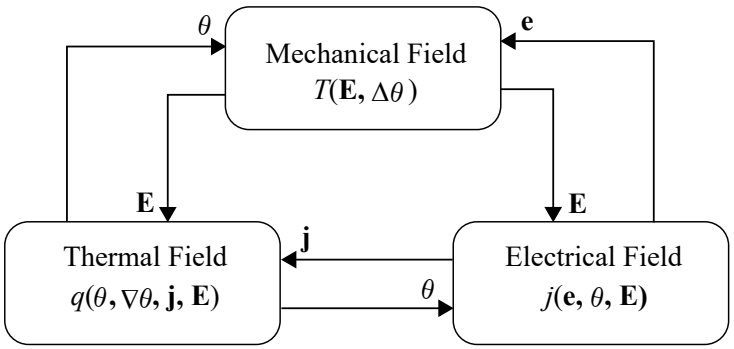

Figure 3.1: Illustration of physical couplings, inspired by [61]

All physical fields are computed with respect to global or local coordinates. As a reference generator system, a 3D kartesian orthonormal basis system (ONB) is used, as defined in [30] (if nothing else is indicated). In tensor calculus for continuum mechanics, for which a kartesian ONB is chosen, tensors up to the 4^{th} rank appear and are related to at least four indices. The tensors used in this thesis show multiple symmetries leading to the use of Voigt's notation. This reduces the number of required tensor indices at the 4^{th} rank from four to two. Identical tensor elements are then summarised by one elment with a Voigt index (see table 3.1). Voigt's notation is usually applied for engineering

Table 3.1: Voigt indices (see [30])

Tensor indices:	11	22	33	23	13	12
Voigt indices:	1	2	3	4	5	6

applications, especially in the area of composite materials and related structural mechanics. Accordingly, tetrades (4^{th} order tensors, e.g. stiffness tetrade) are displayed as matrices. Second order tensors are displayed as vectors (e.g. stress tensor).

The following sections introduce the different physics such as the mechanical, thermal and electrical field, with related basic equations and assumptions.

3.1.2 Structural Mechanics

As part of the mechanical field the thermoelastic stress field is considered. Therefore, the linearised Cauchy stress tensor **T** depends on Green's linearised strain tensor **E** and the local temperature difference $\Delta\theta$ [30]. These independent variables are coupled with the stress field via the material related stiffness tetrade $\boldsymbol{C}$ and the temperature stress tensor

M as follows:

$$\mathbf{T} = \boldsymbol{C} \cdot\cdot \mathbf{E} + \Delta\theta \mathbf{M} \quad \text{with} \tag{3.5}$$

$$\mathbf{M} = -\boldsymbol{C} \cdot\cdot \mathbf{A}. \tag{3.6}$$

The temperature stress tensor is the double scalar product of the stiffness tetrade and the thermal expansion tensor **A**, which is also a material dependent property. The double scalar product for $\boldsymbol{C}$ and **E** as well as for $\boldsymbol{C}$ and **A** represents a double contraction with respect to the tensor rank. The exact definition of the douple scalar product with respect to a kartesian ONB is defined in appendix A.1. These tensors show typical symmetries that are given in index notation:

$$\begin{aligned} &C_{\mathrm{ijkl}} = C_{\mathrm{klij}}, \quad C_{\mathrm{ijkl}} = C_{\mathrm{jikl}} = C_{\mathrm{ijlk}} = C_{\mathrm{jilk}}, \\ &\mathrm{T_{ij}} = \mathrm{T_{ji}}, \qquad \mathrm{E_{ij}} = \mathrm{E_{ji}}, \qquad \mathrm{M_{ij}} = \mathrm{M_{ji}}, \qquad \mathrm{A_{ij}} = \mathrm{A_{ji}}. \end{aligned} \tag{3.7}$$

These symmetries enable the application of Voigt's notation, halving the number of required indices (compare table 3.1 in subsection 3.1.1). This results for the stiffness tetrade $\boldsymbol{C}$ in the following matrix representation

$$\{C_{\mathrm{ij}}\} = \begin{Bmatrix} C_{11} & C_{12} & C_{13} & \sqrt{2}C_{14} & \sqrt{2}C_{15} & \sqrt{2}C_{16} \\ C_{21} & C_{22} & C_{23} & \sqrt{2}C_{24} & \sqrt{2}C_{25} & \sqrt{2}C_{26} \\ C_{31} & C_{32} & C_{33} & \sqrt{2}C_{34} & \sqrt{2}C_{35} & \sqrt{2}C_{36} \\ \sqrt{2}C_{41} & \sqrt{2}C_{42} & \sqrt{2}C_{43} & 2C_{44} & 2C_{45} & 2C_{46} \\ \sqrt{2}C_{51} & \sqrt{2}C_{52} & \sqrt{2}C_{53} & 2C_{54} & 2C_{55} & 2C_{56} \\ \sqrt{2}C_{61} & \sqrt{2}C_{62} & \sqrt{2}C_{63} & 2C_{64} & 2C_{65} & 2C_{66} \end{Bmatrix}. \tag{3.8}$$

The factors 2 and $\sqrt{2}$ are normalisation factors related to the ONB [30]. In most cases examined in this work, the material shows transversal isotropy. For this special case of material symmetry, the transversal stiffness tetrade is given:

$$\{C_{\mathrm{ij},T}\} = \begin{Bmatrix} C_{11} & C_{12} & C_{12} & 0 & 0 & 0 \\ C_{12} & C_{22} & C_{12} & 0 & 0 & 0 \\ C_{12} & C_{12} & C_{22} & 0 & 0 & 0 \\ 0 & 0 & 0 & 2C_{44} & 0 & 0 \\ 0 & 0 & 0 & 0 & 2C_{44} & 0 \\ 0 & 0 & 0 & 0 & 0 & C_{11} - C_{22} \end{Bmatrix}. \tag{3.9}$$

This reduces the number of independent stiffness tensor elements from 21 for anisotropic materials down to 5 for transversal isotropic materials. This is the case e.g. for the stiffness of a long fibre reinforced plastic in an unidirectional lamina.

Since the temperature stress tensor $\mathbf{M}$ depends on the thermal expansion tensor $\mathbf{A}$, the appearance for anisotropic and transversal isotropic materials is given as:

$$\{\mathrm{A_i}\} = \begin{Bmatrix} \mathrm{A}_1 \\ \mathrm{A}_2 \\ \mathrm{A}_3 \\ 0 \\ 0 \\ 0 \end{Bmatrix}, \quad \{\mathrm{A}_{\mathrm{i},T}\} = \begin{Bmatrix} \mathrm{A}_1 \\ \mathrm{A}_2 \\ \mathrm{A}_2 \\ 0 \\ 0 \\ 0 \end{Bmatrix}, \tag{3.10}$$

respectively. The anisotropic case considers three independent thermal expansion coefficients (TECs)(one in each spatial direction). For the transversal isotropic case, two independent TECs remain, since the thermal expansion in the transversal plane is direction invariant. It should be noted that the transversal isotropic plane is related to the plane defined by the ONB base vectors $\mathbf{x}_2$ and $\mathbf{x}_3$ (compare figure 3.2 in subsection 3.1.4).

3.1.3 Thermal Heat Transfer and Joule Heating

The thermal field is governed by the heat (transfer) equation that is given in the transient (time dependent) case as

$$c_p \cdot \rho \cdot \partial_t \theta = \nabla \cdot \mathbf{q} + Q \quad \text{with} \tag{3.11}$$

$$Q = Q_g + Q_r + Q_c, \tag{3.12}$$

where Q is the sum of all volumetric heat sources and heat sinks [86]. In particular, the heat sink related to convective heat dissipation Q_c is highlighted, since this can be one of the main influencing factor for heat transfer at MCMs [87]. Furthermore, radiative heat dissipation Q_r is usually present at heated surfaces. The generated heat Q_g represents all heat sources, e.g. Joule heat. The constant pressure related specific heat c_p and the density ρ (homogeneous material) in equation 3.11 are omitted for the stationary case

$$-\nabla \cdot \mathbf{q} = Q_g + Q_r + Q_c \quad . \tag{3.13}$$

The heat flux vector is given by Fourier's law

$$\mathbf{q} = -\mathbf{\Lambda} \cdot \nabla \theta, \tag{3.14}$$

where $\mathbf{\Lambda}$ represents the second rank tensor of anisotropic thermal conductivity [86]. The heat conductivity tensor provides three independent thermal conductivities in case of anisotropy, in which two independent variables remain in case of transversal isotropy.

Similar to the transversal isotropic stiffness, the properties in the transversal plane are equal ($\Lambda_2 = \Lambda_3$) related to the plane defined by the ONB base vectors $\mathbf{x}_2$ and $\mathbf{x}_3$ (compare figure 3.2 in subsection 3.1.4).

With the set of equations 3.11-3.14, the thermal heat transfer can be described properly. Besides the material constants (ρ, c_p, Λ_i), the main influencing factors on heat transfer are the heat sources and sinks (Q_g, Q_r, Q_c). One of the main heat sources is Joule heat, that couples the electrical field with the thermal field. Based on Ohm's law, the electrical field vector $\mathbf{e}$ is proportional to the current density vector $\mathbf{j}$

$$\mathbf{j} = \sigma \mathbf{e} \quad \text{with} \tag{3.15}$$

$$\mathbf{e} = -\nabla \phi, \tag{3.16}$$

where the proportionality constant σ represents the isotropic electrical conductivity of the material and ϕ is the electrical potential [88]. The assumption of isotropic conductivity holds for all conductors under examination in this work. Physical conductors are in general not ideal which means that resistive losses occur in the form of Joule heat. The generated heat is defined as

$$Q_g = \mathbf{j} \cdot \mathbf{e} = \kappa |\mathbf{j}^2|, \quad \text{with} \tag{3.17}$$

$$\kappa = \frac{1}{\sigma}, \tag{3.18}$$

where κ provides the specific electrical resistivity, that is the inverse of the electrical conductivity σ [88]. Accordingly, the heat source is provided by the same material that is subject to heat transfer, described by equation 3.11. This highlights the electro-thermo-mechanical coupling, since all three physical fields are acting on the material during multifunctional operation. A second important influence is given by heat sinks of which two important heat sinks are

$$Q_c = A_\mathrm{s} \cdot h \cdot (\theta - \theta_a) \quad \text{and} \tag{3.19}$$

$$Q_r = s \cdot \varepsilon \cdot A_s \cdot (\theta^4 - \theta_a^4) \tag{3.20}$$

where the convective heat transfer to the environment Q_c is porportional to the surface area A_s and the heat transfer coefficient (HTC) h. In addition, heat energy is dissipated by thermal radiation Q_r at the surface, which is proportional to the Stefan-Boltzmann constant s and the emissivity of the material ε. Both heat sinks are present at the boundary of the material, at which heat is transferred from the material domain to the environment. Both conditions are assumed to depend on the relation of material temperature θ and the ambient temperature θ_a. Besides these heat sources and sinks, further heat transfer

conditions are relevant, especially in the area of virtual material testing of MCM that is introduced in subsection 3.2.3.

The next subsection introduces the framework of multiscale material modelling, in which a geometrical fundament is provided for the spatial (three dimensional) description of the presented physical fields.

3.1.4 Micro-Meso Scale Interaction

The physical fields act on the meso and micro scales of the material (as introduced in subsection 2.2). To distinguish calculations on the different length scales and to define the interaction across the length scales, the following framework is introduced.

The two scales are distinguished since some assumptions towards the material properties and the information transfer from one scale to the other need to be considered. All physical quantities and associated tensors are related to the ONB generator system. The notation is displayed in figure 3.2: The spatial coordinates for the micro scale are defined as $\mathbf{x} = [x_1\ x_2\ x_3]^T$ whereas the spatial coordinates for the meso scale are defined as $\mathbf{y} = [y_1\ y_2\ y_3]^T$. Domains are denoted by Ω, in which indices μ and m are associated with micro and meso scale respectively. This holds also for equation symbols related to a specific scale in subsequent sections. In addition, boundary surfaces are denoted by Γ, in which the lower index indicates the surface normal related to the ONB and the upper index indicates if it is the positive (+) or negative (-) surface related to the surface normal (see figure 3.2).

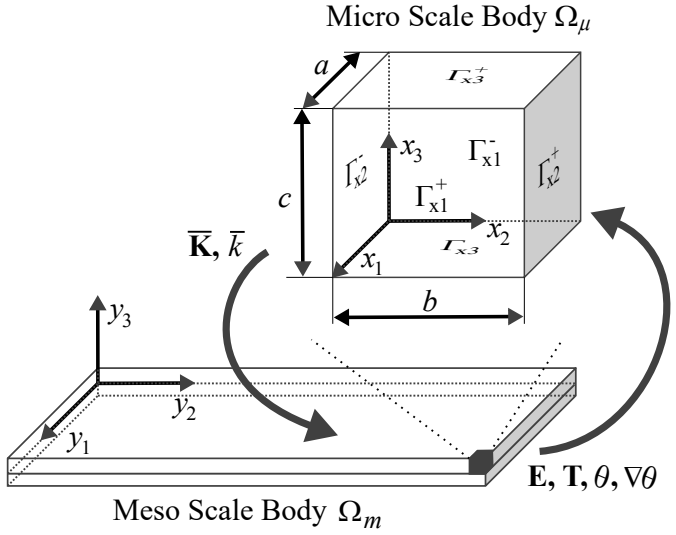

Figure 3.2: Formal representation of micro and meso scale levels with related domains, boundaries and generator system as well as interaction scheme

The micro scale models are built based on RVEs or UCs, which can be used for virtual material testing and homogenisation. The lengths a, b and c are related to the edge length of the RVE/UC. Homogenisation leads to effective material parameter in scalar or tensor

representation, $\overline{k}$ and $\overline{\mathbf{K}}$ respectively. Here the symbols $\overline{k}$ and $\overline{\mathbf{K}}$ are representatives for any effective material property. These effective material properties depend on the MCM's micro scale architecture and on the properties of the constituents. To reduce the model resolution on the meso scale, the effective material properties are transferred to the meso scale model (see figure 3.2) that is then subject to external load cases for material and structural analysis. Areas, in which electro-thermo-mechanical loads are critical, can be resolved again by subsequent micro scale analysis, in which actual loads like temperature θ, temperature gradient $\nabla\theta$ and deformations $\mathbf{E}$ or mechanical stresses $\mathbf{T}$ are transferred to the micro scale model again. This enables high resolution analysis on the micro scale if required. It should be noted that the meso scale body can be a laminate of several plies, each formed by the material composition on the micro scale. Accordingly, similar to the classical laminate theory, the effective properties derived on the micro scale are then transferred to the single layers on the meso scale and direction related transformations are applied.

The homogenisation of the microscale is underpinned by some numerical and analytical methods that are only specifically applicable to related material properties, e.g. the effective mechanical stiffness or the efffective thermal heat conductivity. The considered methods for this work are given in the following subsections.

3.2 Numerical Methods for Microscale Homogenisation

3.2.1 Effective Stiffness

Effective material properties, e.g. effective stiffness, are always averaged quantities that are calculated on the micro scale and are applied on the meso scale. Consequently, the definitions are given with an introduction to the field equation on the meso scale and then the effective quantity is defined by field equations on the micro scale.

Therefore, Hook's law for linear elasticity on the meso scale is defined in tensor index notation

$$\mathbf{T}(\mathbf{y}) = \{\mathrm{T}_{\mathrm{ij},m}\} = \{C_{\mathrm{ijkl},m}\} \cdot\cdot \{\mathrm{E}_{\mathrm{kl},m}\} \quad \text{with} \tag{3.21}$$

$$\mathbf{y} \in \Omega_m, \tag{3.22}$$

where $\mathrm{T}_{\mathrm{ij},m}$ are the stress tensor elements with second rank tensor indices, $C_{\mathrm{ijkl},m}$ are the stiffness tetrade elements with fourth rank tensor indices and $\mathrm{E}_{\mathrm{kl},m}$ are the elements of the strain tensor with second rank tensor indices. To simplify the notation, the reference to the ONB ($\mathbf{y}$) is omitted for the index notation. The index m provides the relation to the meso scale. It should be noted that the spatial coordinate vector $\mathbf{y}$ is related to the meso scale (see subsection 3.1.4). For efficient calculations, the micro structure of the material

is not resolved on the meso scale. Therefore, the stiffness tetrade is given by effective stiffnesses from the micro scale $\overline{C}_{\mathrm{ijkl},\mu}$

$$\{C_{\mathrm{ijkl},m}\} = \{\overline{C}_{\mathrm{ijkl},\mu}\}. \tag{3.23}$$

In this equation, the index μ provides the relation to the micro scale. The elements of the effective stiffness tetrade $\{\overline{C}_{\mathrm{ijkl},\mu}\}$ are computed on the micro scale on which the architecture of the composite material, including all material phases, is resolved. Linear elasticity is also assumed on the micro scale, defining Hook's law (equation 3.21) with index μ

$$\mathbf{T}(\mathbf{x}_\mathrm{n}) = \{\mathrm{T}_{\mathrm{ij},\mu}\} = \{C_{\mathrm{ijkl},\mu}\} \cdot \cdot \{\mathrm{E}_{\mathrm{kl},\mu}\} \quad \text{with} \tag{3.24}$$

$$\mathbf{x}_\mathrm{n} \subseteq \mathbf{x} \in \Omega_\mu. \tag{3.25}$$

It should be noted that the spatial coordinate vector $\mathbf{x}_\mathrm{n}$ is related to the micro scale, in which n indicates the different material phases (e.g. carbon fibre, coating and matrix phase in this thesis). All material phases are part of the spatial domain on the micro scale Ω_μ. For the calculation of averaged stiffness elements of the stiffness tetrade, the RVE is testet virtually. This means, unit strains are applied to the control volume and the resulting stress distribution inside the domain is understood to be representative for the related strain condition. To match the resulting stress state with direction related stiffnesses, the applied unit strains are defined in a way that the ONB base directions $\mathbf{x} = [x_1\ x_2\ x_3]^T$ are related to tensile and shear deformations [89]:

$$\widetilde{\mathrm{E}}_{\mathrm{ij,kl}} = \frac{1}{2}(\delta_{\mathrm{ik}}\delta_{\mathrm{jl}} + \delta_{\mathrm{il}}\delta_{\mathrm{jk}}). \tag{3.26}$$

The indices ij are the tensor indices of the strain element and the indices kl indicate the corresponding unit strain mode, e.g. kl=11 is related to the tensile deformation in x_1 direction and kl=12 is the shear deformation in the x_1x_2 plane. The formulation in equation 3.26 related to the kronecker symbol δ leads to the following unit strain modes

$$[\widetilde{\mathbf{E}}_1 ... \widetilde{\mathbf{E}}_6] = [\{\widetilde{\mathrm{E}}_\mathrm{j}\}_1 ... \{\widetilde{\mathrm{E}}_\mathrm{j}\}_6] = ...$$
$$\left[\begin{Bmatrix}1\\0\\0\\0\\0\\0\end{Bmatrix};\begin{Bmatrix}0\\1\\0\\0\\0\\0\end{Bmatrix};\begin{Bmatrix}0\\0\\1\\0\\0\\0\end{Bmatrix};\begin{Bmatrix}0\\0\\0\\0.5\\0\\0\end{Bmatrix};\begin{Bmatrix}0\\0\\0\\0\\0.5\\0\end{Bmatrix};\begin{Bmatrix}0\\0\\0\\0\\0\\0.5\end{Bmatrix}\right] \tag{3.27}$$

These strain modes define a tensile deformation of magnitude 1 and pure shear deformations of magnitude 0.5 which is accounting for the normalisation factors for shear stiffnesses in the stiffness tetrade (see subsection 3.1.2, equation 3.8). The shear strain magnitude corresponds to the *complete* glide angle γ_{xixj} which is defined as

$$\gamma_{\mathrm{xixj}} = \gamma_{\mathrm{xi}} + \gamma_{\mathrm{xj}}, \tag{3.28}$$

where the angles γ_{xi} and γ_{xj} are measured between the deformed body edges and the related coordinates x_{i} and x_{j}. Consequently, for a magnitude of 0.5, the edge rotates by $\gamma_{\mathrm{xi}} = \gamma_{\mathrm{xj}} = \gamma_{\mathrm{xixj}} \cdot 0.5 = 14.3\ °$.

While applying these unit strains to the RVE, full compatibility with neighbouring cells needs to be assured. Accordingly, the deformation of the RVE is constrained by periodic boundary conditions (as defined in [89]):

$$\mathbf{u}(\Gamma^{-}_{\mathrm{xi}}) = \mathbf{u}(\Gamma^{+}_{\mathrm{xi}}) + \mathbf{u}(\widetilde{\mathbf{E}}). \tag{3.29}$$

This formulation shows that the deformation needs to be equal at opposite boundary surfaces $\mathbf{u}(\Gamma^{+,-}_{\mathrm{xi}})$. This definition results in the following deformation modes, generally illustrated in figure 3.3. The equality of the resulting effective stress state inside the micro

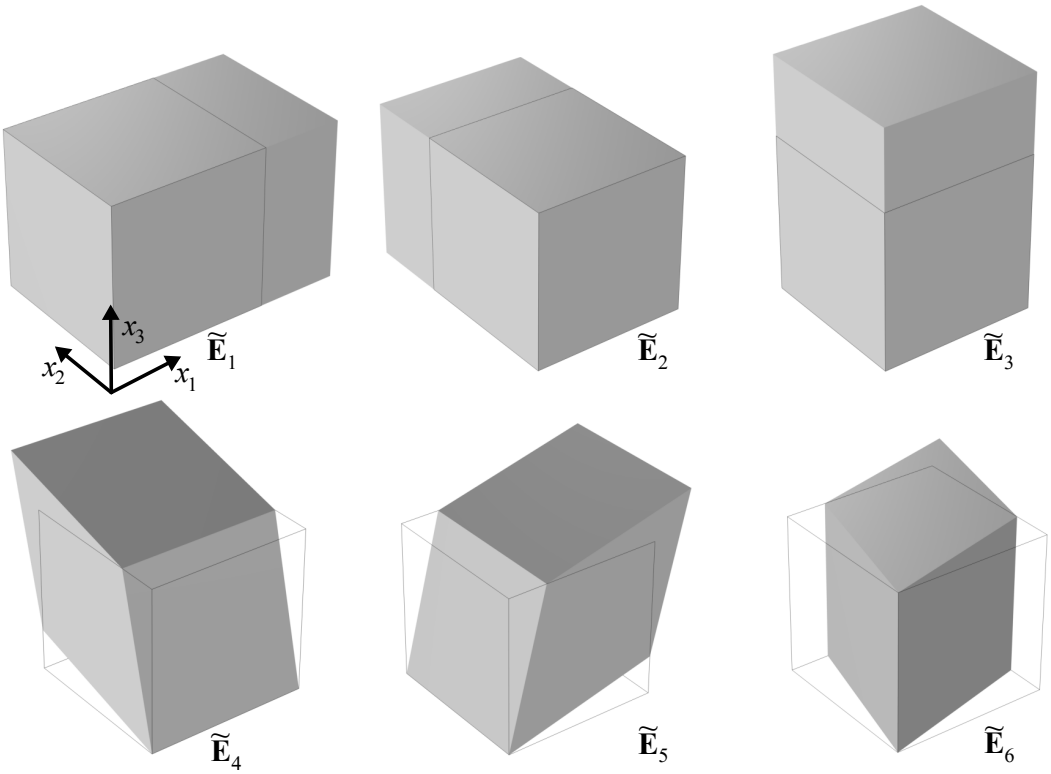

Figure 3.3: Representation of unit deformation modes on a cubic UC, compare [89]

scale domain $\overline{\mathbf{T}}_{\mu}(\widetilde{\mathbf{E}})$ and the volume averaged stress state which would act on the meso

scale $\langle \mathbf{T}_m(\mathbf{E}) \rangle$ is then postulated by the Hill-Mandel equality condition [89–91]

$$\overline{\mathbf{T}}_\mu(\widetilde{\mathbf{E}}) = \langle \mathbf{T}_m(\mathbf{E}) \rangle. \tag{3.30}$$

Accordingly, the actual stress state within the RVE can be understood to be representative for the material behaviour. The stiffness tetrade is therefore computed as volume average of the stress tensor that resulted from the unit strains:

$$\langle \mathbf{T}_\mu(\widetilde{\mathbf{E}}) \rangle = \frac{1}{V} \int_V \mathbf{T}(\mathbf{x}, \widetilde{\mathbf{E}}) \, dV, \quad \text{with} \tag{3.31}$$

$$V = V(\Omega_\mu) \quad \textit{and} \quad \mathbf{x} \in \Omega_\mu, \tag{3.32}$$

where V is the volume of the micro scale domain and $\mathbf{T}(\mathbf{x}, \overline{\mathbf{E}})$ is the actual stress state on the micro scale in domain Ω_μ. In Voigt's notation, the stiffness tetrade is then assembled by the resulting volume averaged stress states

$$\{\overline{C}_{\mathrm{ij},\mu}\} = \{\langle \mathbf{T}_{1,\mu}(\widetilde{\mathbf{E}}_1) \rangle; ...; \langle \mathbf{T}_{6,\mu}(\widetilde{\mathbf{E}}_6) \rangle\}. \tag{3.33}$$

It is assumed that only rhombic or more simple elasticity is present in all material configurations in this thesis, since the composite material constituents are at least transversal isotropic or isotropic. This assumption leads to the following orthotropic representation of the stiffness tetrade, in which all elements given as zero are expected to be near zero in the numerical analysis (compare [30]):

$$\{\overline{C}_{\mathrm{ij},\mu}\} = ...$$

$$\begin{Bmatrix} \overline{C}_{11,\mu} & \overline{C}_{12,\mu} & \overline{C}_{13,\mu} & 0 & 0 & 0 \\ \overline{C}_{21,\mu} & \overline{C}_{22,\mu} & \overline{C}_{23,\mu} & 0 & 0 & 0 \\ \overline{C}_{31,\mu} & \overline{C}_{32,\mu} & \overline{C}_{33,\mu} & 0 & 0 & 0 \\ 0 & 0 & 0 & \overline{C}_{44,\mu} & 0 & 0 \\ 0 & 0 & 0 & 0 & \overline{C}_{55,\mu} & 0 \\ 0 & 0 & 0 & 0 & 0 & \overline{C}_{66,\mu} \end{Bmatrix}. \tag{3.34}$$

The orthotropy shows no coupling between shear deformation and tensile stress. It is noteworthy that, due to the symmetry of the stiffness tetrade, not all elements are independent (e.g. $C_{12} = C_{21}$). However, these equal elements are computed from different stress tensors. Accordingly, this can be used as a control mechanism to assure correct calculations or to reduce computational effort, once verified [89].

The resulting stiffness tetrade is then used as effective stiffness on the meso scale. This enables the assumption of a homogenised domain Ω_μ that is not resolved on the meso scale anymore. On the one hand, the representation of the mechanical behaviour on the

meso scale will be efficient due to the reduction of spatial resolution. On the other hand, local stress distributions which could be caused by discrete material phase distributions are omitted by this approach. Accordingly, a local load condition from the meso scale can be transferred to the micro scale again to analyse local, non-homogeneous stress distributions (see e.g. figure 3.2).

The next subsection provides a similar approach for the calculation of effective TECs that are relevant for the complete linear thermoelastic problem on the meso scale.

3.2.2 Effective Thermal Expansion Coefficients

For the linear thermoelastic material behaviour, the TECs of the material are needed to compute temperature related stresses. Since the thermal expansion can be anisotropic due to anisotropic expansion behaviour of the constituents, the problem needs to be resolved in three dimensions. The coupling of temperature and thermal stresses $\mathbf{T}_{th}(\mathbf{y})$ on the meso scale of the material is given by the temperature stress tensor $\{\mathrm{M}_{\mathrm{ij},m}\}$ in

$$\mathbf{T}_{th}(\mathbf{y}) = \{\mathrm{T}_{\mathrm{ij},th,m}\} = \Delta\theta\{\mathrm{M}_{\mathrm{ij},m}\} \quad \text{with} \tag{3.35}$$

$$\{\mathrm{M}_{\mathrm{ij},m}\} = -\{\overline{C}_{\mathrm{ijkl},\mu}\} \cdot\cdot \{\overline{\mathrm{A}}_{\mathrm{kl},\mu}\} \quad \text{and} \tag{3.36}$$

$$\mathbf{y} \in \Omega_m. \tag{3.37}$$

Similar to the stiffness definition on the meso scale, the temperature stress tensor depends on the effective values of stiffness tetrade $\{\overline{C}_{\mathrm{ijkl},\mu}\}$ and thermal expansion tensor $\{\overline{\mathrm{A}}_{\mathrm{kl},\mu}\}$, which are derived on the micro scale. This quantity is informed by the linear thermoelastic problem, defined with respect to index μ

$$\mathbf{T}_{th}(\mathbf{x}_\mathrm{n}) = \{\mathrm{T}_{\mathrm{ij},th,\mu}\} = \Delta\theta\{\mathrm{M}_{\mathrm{ij},\mu}\} \quad \text{with} \tag{3.38}$$

$$\{\mathrm{M}_{\mathrm{ij},\mu}\} = -\{C_{\mathrm{ijkl},\mu}\} \cdot\cdot \{\mathrm{A}_{\mathrm{kl},\mu}\} \quad \text{and} \tag{3.39}$$

$$\mathbf{x}_\mathrm{n} \subseteq \mathbf{x} \in \Omega_\mu. \tag{3.40}$$

The effective thermal expansion tensor elements $\overline{\mathrm{A}}_{\mathrm{ji},\mu}$ can be computed with respect to the compliance tensor $\{S_{\mathrm{jilk}}\}$ under consideration of a unit temperature change of $\Delta\theta$ [92]

$$\{\overline{\mathrm{A}}_{\mathrm{ji},\mu}\} = -\frac{1}{\Delta\theta} \cdot \{S_{\mathrm{jilk}}\} \cdot\cdot \{\langle \mathrm{T}_{\mathrm{lk},th,\mu}\rangle\} \quad \text{with} \tag{3.41}$$

$$\{S_{\mathrm{jilk}}\} = \{C_{\mathrm{ijkl}}\}^{-1} \text{ and } \Delta\theta = \theta - \theta_0 = 1 \text{ K}. \tag{3.42}$$

The internal volume averaged stress state $\{\langle \mathrm{T}_{\mathrm{lk},th,\mu}\rangle\}$ on the micro scale is representative if the body is constrained by periodic boundary conditions to assure geometric compatibility [92]. All remaining deformations are related to temperature change and therefore to free

expansion:

$$\mathbf{u}(\Gamma^{-}_{\mathrm{xi}}) = \mathbf{u}(\Gamma^{+}_{\mathrm{xi}}) + \mathbf{u}(\Delta\theta). \tag{3.43}$$

For the computation of the effective thermal expansion tensor on the micro scale $\{\langle A_{\mathrm{j},\mu}\rangle\}$, the volume averaged stresses induced by the unit temperature change are calculated by

$$\{\langle \mathrm{T}_{\mathrm{lk},th,\mu}\rangle\} = \frac{1}{V}\int_V \mathbf{T}(\Delta\theta, \mathbf{x})\; dV, \quad \text{with} \tag{3.44}$$

$$V = V(\Omega_\mu) \quad \text{and} \quad \mathbf{x} \in \Omega_\mu. \tag{3.45}$$

The resulting effective thermal expansion tensor is then present as

$$\{\overline{\mathrm{A}}_{\mathrm{j},\mu}\} = \left\{ \begin{array}{cccccc} \overline{\mathrm{A}}_1 & \overline{\mathrm{A}}_2 & \overline{\mathrm{A}}_3 & 0 & 0 & 0 \end{array} \right\}^T. \tag{3.46}$$

This definition holds for an anisotropic thermal expansion behaviour. Depending on the material composition on the micro scale, the number of independent TECs $\mathrm{A_i}$ can be reduced to 2, e.g. in case of transversal isotropy, which is considered for some applications in this work. The volume average based effective TEC computation is assumed to be suitable with respect to experimental results which was already approved in foregoing studies [93, 94].

Besides the mechanical field, the thermal and electrical field related effective material properties can be defined by homogenisation on the microscale. The next subsection provides the methodology for the computation of effective thermal heat conductivities of the composite.

3.2.3 Effective Heat Conductivity

Heat conductivity can be an anisotropic material property, resulting from anisotropic material constituents or the ansiotropic combination of isotropic constituents on the micro scale. Similar to mechanical homogenisation, the heat transfer behaviour on the meso scale can be defined with respect to material properties derived on the micro scale. The meso scale stationary heat transfer problem is given as

$$-\nabla\mathbf{q}(\mathbf{y}) = Q_m \quad \text{with} \tag{3.47}$$

$$\mathbf{q}(\mathbf{y}) = \{\mathrm{q}_{\mathrm{i},m}\} = -\{\Lambda_{\mathrm{ij},m}\} \cdot \nabla\theta(\mathbf{y}), \tag{3.48}$$

$$\{\Lambda_{\mathrm{ij},m}\} = \{\overline{\Lambda}_{\mathrm{ij},\mu}\} \quad \text{and} \tag{3.49}$$

$$\mathbf{y} \in \Omega_m, \tag{3.50}$$

where Q_m is the sum of the heat sources and sinks, $\{\mathrm{q}_{\mathrm{i},m}\}$ provides the heat flux vector, $\{\Lambda_{\mathrm{ij},m}\}$ is the heat conductivity tensor and $\nabla\theta(\mathbf{y})$ is the temperature gradient. The heat

conductivity is important for the heat transfer problem since it has an effect on both, the transient and the stationary heat transfer problem. The stationary case is used for homogenisation since no other material properties are present. Heat transfer takes place between the spatial distribution of heat sources and sinks Q_m. Therefore, direction dependent heat conductivities are of important interest in the area of multifunctional composites. The challenge of the coupling between micro and meso scale for the thermal problem is that the heat sources and sinks, for example convective heat transfer at a boundary surface, are usually given on the meso scale. Accordingly, a meso scale model can be informed by effective material properties such as effective heat conductivity $\{\overline{\Lambda}_{\mathrm{ij},\mu}\}$ being derived on the micro scale based on artificial boundary conditions. For high resolution analysis, the micro scale model then needs to deal with local temperature gradients $\nabla\theta(\mathbf{x}_\mathrm{n})$ informed by a meso scale load scenario (compare figure 3.2, subsection 3.1.4).

The micro scale stationary heat transfer problem is given as

$$-\nabla\mathbf{q}(\mathbf{x}_\mathrm{n}) = Q_\mu \quad \text{with} \tag{3.51}$$

$$\mathbf{q}(\mathbf{x}_\mathrm{n}) = \{\mathrm{q}_{\mathrm{i},\mu}\} = -\{\Lambda_{\mathrm{ij},\mu}\} \cdot \nabla\theta(\mathbf{x}_\mathrm{n}) \quad \text{and} \tag{3.52}$$

$$\mathbf{x}_\mathrm{n} \subseteq \mathbf{x} \in \Omega_\mu, \tag{3.53}$$

where $\{\Lambda_{\mathrm{ij},\mu}\}$ is the heat conductivity tensor of the single constituents on the micro scale and $\mathbf{q}(\mathbf{x}_\mathrm{n})$ represents the heat flux vector in that constituent domain. The computation of the effective heat conductivity $\{\overline{\Lambda}_{\mathrm{ij},\mu}\}$ is enabled by a virtual measurement of the composite's heat conductivity $\{\Lambda_{\mathrm{ij},\mu}\}$ on the micro scale. The virtual measurement is defined here by reducing the continous problem to a discrete problem at the RVE body (compare [95]). As illustrated in figure 3.2, the micro scale body provides discrete dimensions a, b, c that can be used to decompose the heat flux through the body as

$$\frac{Q_{1,f}}{bc} = \overline{\Lambda}_{11}\frac{\theta(\Gamma^+_{\mathrm{x1}}) - \theta(\Gamma^-_{\mathrm{x1}})}{a}. \tag{3.54}$$

In this representation, $\overline{\Lambda}_{11}$ is the effective heat conductivity, $\theta(\Gamma^+_{\mathrm{x1}}) - \theta(\Gamma^+_{\mathrm{x1}})$ provides the temperature drop between two opposite surfaces of the body and $\frac{Q_{1,f}}{bc}$ is the resulting total heat flux across the surface normal to x_1 direction [95]. The heat flux in other directions can be suppressed so that only the heat flux along x_1 direction remains. These conditions are related to an RVE representation and applied by periodic boundary conditions for the temperature at the remaining surfaces, for which a zero temperature drop is set:

$$\theta(\Gamma^+_{\mathrm{x2}}) - \theta(\Gamma^-_{\mathrm{x2}}) = 0, \tag{3.55}$$

$$\theta(\Gamma^+_{\mathrm{x3}}) - \theta(\Gamma^-_{\mathrm{x3}}) = 0. \tag{3.56}$$

To solve the problem, the remaining quantities in equation 3.54 need to be defined so that the resulting temperature distribution can be solved. For instance, this is given by an inward heat flux (heat source) $\mathbf{q}(\Gamma^-_{\mathrm{x1}})$ and a constant temperature at the opposite surface $\theta(\Gamma^+_{\mathrm{x1}})$ (heat sink):

$$\theta(\Gamma^+_{\mathrm{x1}}) = \theta_a, \tag{3.57}$$

$$\mathbf{q}(\Gamma^-_{\mathrm{x1}}) = \mathbf{x}_1 \cdot \frac{Q_{1,f}}{bc} \quad \text{with,} \tag{3.58}$$

$$Q_{1,f} = 1 \text{ W}, \tag{3.59}$$

where the defined total heat flux $Q_{1,f}$ is set to 1 W and θ_a can be ambient temperature. The temperature field is computed and the temperature at the remaining surface $\theta(\Gamma^-_{\mathrm{x1}})$ can be identified. The corresponding effective heat conductivity $\overline{\Lambda}_{11}$ is then solved by equation 3.54. This method is independent from the internal heat conductivity distribution or dimension of the RVE. It assumes that any resulting temperature solution is related to a corresponding heat conductivity in heat flux direction. By applying these conditions to all three ONB directions, the single effective heat conductivity elements $\overline{\Lambda}_{11}$ can be predicted.

The resulting effective heat conductivity tensor can be applied on the meso scale $\{\Lambda_{\mathrm{ij},m}\} = \{\overline{\Lambda}_{\mathrm{ij},\mu}\}$ for homogenised structural domains. In addition, meso scale related heat flux or temperature distributions can be transferred to the micro scale model, setup by suitable boundary conditions, and can be used for local thermal analysis with high resolution. This is especially interesting for the electro-thermo-mechanically coupled analysis.

All homogenisation procedures presented in the foregoing subsections were related to direction dependent material properties. The next section presents the brief approach for volume related, isotropic homogenisation.

3.2.4 Volume Related Homogenisation

The volume related homogenisation is applied for all material properties that are in general volume specific and do not represent an anisotropic property. Such properties are e.g. the density ρ and the volume specific heat at constant pressure c_p. These material properties are computed by a simple volume average:

$$\langle k \rangle = \frac{1}{V} \int_V k(\mathbf{x})\, dV \quad \text{with} \tag{3.60}$$

$$V = V(\Omega_\mu) \quad \text{and} \quad \mathbf{x} \in \Omega_\mu. \tag{3.61}$$

where $\langle k \rangle$ represents the volume averaged quantity, $k(\mathbf{x})$ is the quantity within the single domains or material constituents. This volume average is related to the micro scale RVE volume which results in a volumetric average, weighted for the single volume fractions of each constituent. It should be noted that this results in the simple rule of mixtures (ROM, Voigt's solution) which assumes that the effective quantity $\overline{k}$ only depends on the volume fraction of each contributor (compare equation 3.63 in the following subsection, [96]).

It is mentioned that, for this thesis, all field problems are solved by the help of the FEM in the commercially available software Comsol Multiphysics (v5.5). The software is capable of computing various physical fields with respect to the underlaying partially differential equations (PDEs) and to couple the single physics in a multiphysics approach. Since the physical fields in the MCM are coupled as given in section 3.1.1, this selection appeared to be beneficial. Concerning FEM theory, one is referred to the standard literature (e.g. [97, 98]).

The next section summarises classical analytical solutions for anisotropic or isotropic effective material properties. These solutions are most frequently used as a benchmark for computationally derived solutions from foregoing equations and fields.

3.3 Classical Analytical Solutions for Homogenisation

3.3.1 Rule of Mixtures (Voigt's and Reuss' Solutions)

The classical ROM is based on the assumption that all constituents of a body contribute with the proportion of their volume fraction to an effective material property. All solutions are related to the following definition of the volume fraction

$$v_{\mathrm{j}} = \frac{V_{\mathrm{j}}}{V} \quad \text{with } V = V(\Omega_\mu), \tag{3.62}$$

where V_j is the absolute volume of a constituent and V is the total volume of the sample. This quantity is either defined by the geometric representation of the material on the micro scale (RVE/UC) or is measured by thermogravimetric analysis (TGA) of a material sample from a specimen. Details about TGA can be found in [99].

For the calculation of isotropic quantities, the rule of mixture holds

$$\overline{k}_1 = \sum_{\mathrm{j}}^{n} k_{1,\mathrm{j}} \cdot v_{\mathrm{j}}, \tag{3.63}$$

where $\overline{k}_1$ is the effective material property, $k_{1,\mathrm{j}}$ is the related property of the single material phase j and v_{j} the corresponding volume fraction [96]. Typically, it is used for all volume related (isotropic) material properties like density ρ and specific heat c_p. At the same time, this method provides a result for the effective longitudinal stiffnesses (Young's modulus) $\overline{E}_1$

(e.g. in x_1 direction) of long fibre reinforced composite materials. This is also called Voigt's solution [90], which assumes equal strains for parallel arranged material constituents and represents the upper boundary of the effective stiffness.

In addition, the lower bound is given by the Reuss' solution [90], which assumes equal stresses in all material constituents and is usually valid for the fibre arrangement along the transversal directions (e.g. x_2 and x_3 direction). The transversal stiffness of the constituents is inversely related to the fibre volume fraction:

$$\overline{k}_2 = \overline{k}_3 = \left(\sum_{\mathrm{j}=1}^{n} \frac{v_{\mathrm{j}}}{k_{2,\mathrm{j}}} \right)^{-1} . \tag{3.64}$$

Here, $\overline{k}_2$ and $\overline{k}_3$ indicate the direction dependent, effective solutions in the transversal directions and $k_{2,\mathrm{j}}$ is the transversal property of constituent j. This solution is especially used for the effective transversal stiffnesses (Young's modulus) $\overline{E}_2 = \overline{E}_3$ of long fibre reinforced composite materials and the corresponding shear stiffnesses $\overline{G}_{12}$ [96], also known as Reuss' solution for materials arranged in a row.

However, Reuss' solution neglects any influence of transversal contraction, described by Poisson's ratio. The consideration of the isotropic Poissons' ratios leads to a more exact solution for the transversal effective stiffness in case of standard two phase composite materials as

$$\overline{E}_2 = \overline{E}_3 = \left(\frac{v_1}{E_{2,1}} + \frac{v_2}{E_{2,2}} + \frac{v_1 v_2 (E_{2,1}\nu_2 - E_{2,2}\nu_1)^2}{E_{2,1}E_{2,2}(E_{2,2}v_1 + E_{2,2}v_2)} \right)^{-1} , \tag{3.65}$$

where $E_{\mathrm{i},j}$ is Young's modulus in direction x_{i} of constituent j and ν_j represents the Poisson's ratio of constituent j [96]. The ROM is the most frequently applied method to estimate effective material properties, especially stiffnesses of composites. However, the results are suitable only as upper and lower boundaries only and represent an ideal case that is usually truncated by inaccuracies in the constituent's arrangement on the micro scale.

The next subsection introduces another, empirically motivated analytical solution for transversal, in series aligned material properties that is more accurate compared to measured effective stiffnesses.

3.3.2 Halpin-Tsai and Lewis-Nielsen Methods

The Halpin-Tsai and Lewis-Nielsen equations are based on the same set of equations, reaching back to Einstein's theory of particles dissolved in viscous media. The Halpin-Tsai method is a semi-empirically derived solution for the computation of effective material properties of composites with two constituents. The concept assumes that a homogeneous, isotropic matrix material is filled by particles, whose geometry, volume fraction and

stiffness have an influence on the effective stiffness of the composite. The Halpin-Tsai equations [100, 101] improve the solution compared to Reuss' solution and are given as

$$\frac{\overline{E}}{E_1} = \frac{1 + \xi\eta v_2}{1 - \eta v_2} \quad \text{with} \tag{3.66}$$

$$\eta = \frac{(\frac{E_2}{E_1}) - 1}{\frac{E_2}{E_1} + \xi}, \tag{3.67}$$

where E, E_1 and E_2 denote the effective modulus as well as the matrix and filler particle moduli, respectively. Moreover, ξ includes geometrical characteristics. In addition, η describes the influence of the Young's moduli and v_2 indicates the volume fraction of the filler. Originally, Einstein had derived the geometry factor ξ related to a suspension of spheres [102] and Burgers developed an enlarged choice for different geometries like elipsoidal or fibre like geometries [101, 103]. For the computation of effective thermal properties, Nielsen dervied the following equations:

$$\overline{k}_2 = \overline{k}_3 = k_m \frac{1 + \xi\eta v_\mathrm{p}}{1 - \zeta\eta v_\mathrm{p}} \quad \text{with} \tag{3.68}$$

$$\eta = \frac{k_p - k_m}{k_p + \xi k_m}, \tag{3.69}$$

$$\zeta = 1 + \frac{(1 - v_{p,max})}{v_{p,max}^2} v_p \quad \text{and} \tag{3.70}$$

$$\xi = 2\frac{l_p}{d_p} \quad , \tag{3.71}$$

where ξ is given as a continous function of the particle shape with diameter d_p and particle length l_p [104]. The parameter ζ is a function of the particles' volume fraction and maximum volume fraction $v_{p,max}$. This provides an additional recognition of the particle packaging. As reported in [101, 104], this approach provides suitable solutions for two phase composites without a main fibre alignment direction. Accordingly, with respect to long fibre reinforced carbon fibre composites, these results can only be compared with respect to the transversal isotropic plane.

Kochetov et al. [105] introduced a ROM-based three phase solution for the prediction of effective thermal conductivities for composite comprising three constituents. This approach is based on the classical Lewis-Nielsen equations for the heat conductivity of a two-phase composite that are identical to the Nielsen method for effective stiffness (equations 3.68-3.71). The third phase, which was assumed to be a thin coating covering the particle completely, was included by adding a homogenisation rule for the coated particle. This was done by Reuss' solution (compare equation 3.64) and holds for the two

phase particle

$$\overline{k}_p = \left(\frac{v_p}{k_p} + \frac{v_c}{k_c} \right)^{-1} . \tag{3.72}$$

Here the index p indicates the particle related and c the coating related quantities. Similar to the two phase approach presented previously, the *Three-Phase Lewis-Nielsen* (TPLN) model can only be applied to predict effective quantities in the transversal plane (e.g. x_2 and x_3) [104].

Similar to the rule of mixture, the Lewis-Nielsen and also extended Lewis-Nielsen methods can be applied to mechanical as well as thermal related, direction dependent material properties. In this thesis, the TPLN approach will be discussed towards effective thermal conductivities of coated carbon fibre composites. Results will be compared with solutions obtained from numerical homogenisation. In addition, a new approach will be introduced later on that applies the Lewis-Nielsen approach for the homogenisation of the coated particle.

The next chapter will introduce first experimental and numerical investigations on coated carbon fibre composites on the micro scale. The micro scale simulations are underpinned by first observations from experimental evaluation of coated carbon fibre specimens.

4 Micro Scale Material Characterisation and Modelling

4.1 Experimental Examination of PeCCF

4.1.1 Derivation of Characterisation Demand

In advance, it should be noted that parts of section 4.2 have been published earlier by Maximilian Schutzeichel in [38]. This original research is displayed in a greater context of this thesis to contribute to the research hypotheses.

A basic characterisation of the PeCCFs in terms of mechanical and thermal behaviour is motivated by the described polymer electrolyte coating material (see subsection 2.3.2). The PeCCF represents a two phase composite material which is dedicated to be embedded into a typical matrix polymer like epoxy resin. Before introducing numerical approaches for the analysis of the composites' behaviour, initial experimental characterisations are conducted to evaluate the material behaviour with respect to constant, linear and non-linear measures. This enables the identification of suitable models for numerical studies.

Based on extensive research reported in literature, it is expected that the PE coating, despite its small thickness of $t_c = 500$ nm, has a significant influence on the effective stiffness of the PeCCF compared to the uncoated carbon fibre [106–109]. To characterise this influence in case of the presented polymer electrolyte coating system, tensile tests are conducted and results are reported in the following subsection.

In addition, the electrical conductivity of the IMS65 carbon fibre $\kappa_f = 3.45 \cdot 10^{-3}$ Ωcm lies in the range of semiconductors $\kappa_s = [10^{-3}, 10^{6}]$ Ωcm, even though it is at the border to conductors [110]. This resistor type can develop non-constant electrical resistances with rising temperature. Therefore, four different types of resistors are distinguished: Constant (ohmic, invariant resistance), a negative temperature coefficient (NTC) resistor with decreasing resistance during temperature rise, a positive temperature coefficient (PTC) resistor with increasing resistance during temperature rise and a varistor which shows variant thermo-resistive behaviour [110]. In order to define the type of resistor, also electro-thermal investigations are conducted and results are reported in subsection 4.1.3.

4.1.2 Mechanical Characterisation of PeCCF

The mechanical characterisation of PeCCF is challenging, since the measurement of mechanical properties related to a micro scale specimen (carbon fibre and coating) is not compatible with typical tensile or bending test cases. Furthermore, it is expected that the

transversal stiffness and the shear stiffness of the PeCCF are influenced significantly by the coating material. This is also motivated by the spatial parallel arrangement of both materials related to the longitudinal direction. Accordingly, Reuss' solution for effective stiffness indicates that the carbon fibre's stiffness is dominant, thus the influence of the coating material in longitudinal direction is small (see subsection 3.3.1).

However, clamping a bundle of PeCCF for tensile tests will result in a load path from the clamping support via the PEC coating to the carbon fibre, which provides a shear load for the polymer electrolyte coating. Therefore, a tensile test setup is introduced, which enables a first characterisation of the PeCCF compound in terms of strain-stress relation and effective stiffness. For experimental characterisation, 22 PeCCF specimens are prepared according to the coating procedure described in subsection 2.3.2 related to [8]. Table 4.1 presents data of all specimens after the coating process.

Table 4.1: Properties of PeCCF specimens: total length l, coated length l_c and number of fibres n_f; Coating system: 50:50 (A:B) monomer mixture with 8 % Li salt content solved in DMF (see subsection 2.3.2)

Nr.	l [mm]	l_c [mm]	n_f [-]	Nr.	l [mm]	l_c [mm]	n_f [-]
Spec 1	85	30	856	Spec 12	100	40	1632
Spec 2	85	30	403	Spec 13	100	25	2771
Spec 3	95	20	1132	Spec 14	120	80	9821
Spec 4	105	20	1528	Spec 15	120	80	3545
Spec 5	75	20	372	Spec 16	100	20	1636
Spec 6	80	20	614	Spec 17	100	20	2137
Spec 7	55	40	419	Spec 18	100	20	2118
Spec 8	75	40	1364	Spec 19	100	40	699
Spec 9	107	25	1218	Spec 20	100	25	1840
Spec 10	120	40	4385	Spec 21	120	25	1467
Spec 11	120	25	3973	Spec 22	120	40	957
Ref	150	-	24,000				

The different lengths l, coating lengths l_c and numbers of fibres n_f are related to different production charges and different coating moulds which provide different coating lengths. It should be noted that the specimen bundles were taken by hand from an unsized IMS65 carbon fibre roving with a total of $n_f = 24,000$ fibres. The number of fibres was calculated from electrical measurements, according to the procedure given in [38]. However, all specimens are coated by the same coating material, resulting from electropolymerisation of monomers A:B in a 50:50 mixture ratio with 8 % Li salt solved

in DMF. Specimens *Spec 1* to *Spec 9* are used for tensile tests. The test procedure is related to the standard of ASTM D4018-11 [111] but is adapted to the individual needs for the given specimens. The specimens are glued with epoxy resin in an aluminium clamp support at both ends. A schematic of the cross section is given in the detailed view in figure 4.1. As already mentioned, the load transfer is given from the clamp support via the epoxy resin to the PeCCF specimen. This results in an elastic chain in which the epoxy resin, the PE coating and the carbon fibre are elastically deformed during tensile test. The 50 mm x 10 mm x 6 mm Aluminum support is considered to be rigid compared to the specimen and resin in this setup. Consequently, the total deformation in a tensile test is given by the sum of the resin deformation $2 \cdot \Delta_r$ and the specimen elongation Δ_s:

$$\Delta_t = 2 \cdot \Delta_r + \Delta_s \quad . \tag{4.1}$$

Since the strain-stress relation of the specimen is desired without any influences of the clamp support and the epoxy resin connection, a standard carbon fibre sample is used to identify a correction factor p:

$$p = \frac{\Delta_t}{\Delta_{IMS65}}, \tag{4.2}$$

where Δ_{IMS65} is the calculated elongation of the specimen related to its theoretical tensile deformation. In order to identify the measured total displacement, a reference specimen of uncoated carbon fibres *Ref* (see table 4.1) is tested in a TIRAtest 2810 testing maschine (see figure 4.1). The test maschine is able to measure the tensile force F_t by a 1000 N load cell and the lifting beam displacement. In order to avoid any influences from the maschine setup within displacement data, the optical correlation system Q400 is used to track the clamp support's displacements (see figure 4.1). The tensile test is strain controlled by a total strain of $\mathrm{E}_m = 2$ %.

Figure 4.2 (a) shows a tensile test of the reference specimen. Here the tensile strain E_m is related to the lifting beam displacement and the clear length of the specimen and the stress T_m is related to the total cross section of the specimen *Ref*, which is given by the number of fibres n_f and the cross section of one fibre A_f. All maesurements are taken at an ambient temperature of $\theta_a = 297$ K.

First a non-linear stress-strain relation is indicated in the area of $\mathrm{E}_m = [0.0,\ 1.3]$ % that is related to a non-ideal clamping of several fibres with slightly different clear length. As soon as all fibres are loaded, the curve becomes linear-elastic. Accordingly, the stiffness calculation is reduced to the linear-elastic part that is displayed in detail in figure 4.2 (b).

Besides the original curve from (a), the respective curve related to the Q400 displacement measurement *Q400* and the theoretical stress-strain relation calculated from Hook's law (indicated as *Calculated*) are given. The curves of Q400 and the direct measurement from Tira are nearly identical. However, the Q400 curve shows a slightly stiffer strain-stress

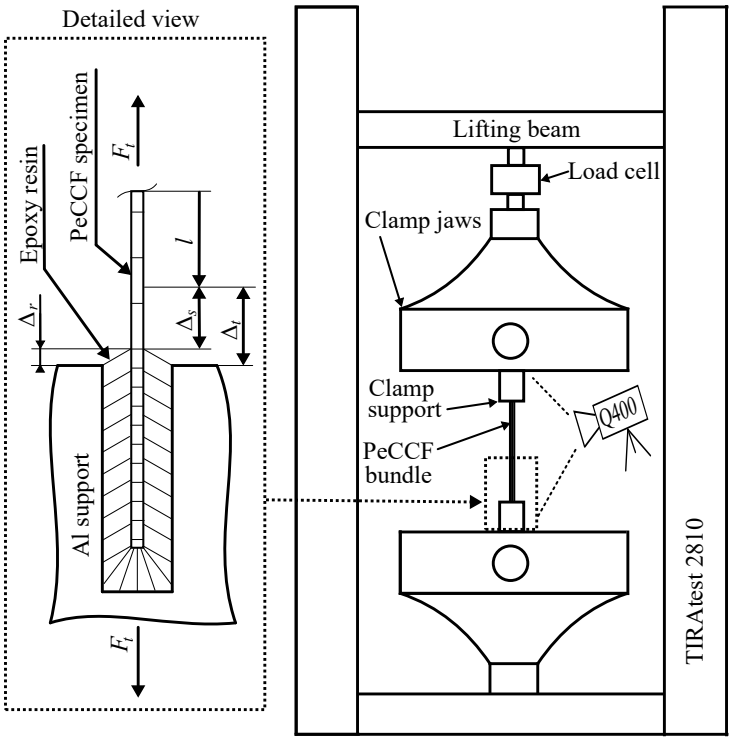

Figure 4.1: Schematic of the tensile test setup; Figure taken and modified with permission from [38]

curve which is plausible since this measurement does not include deformations within the maschine setup. Accordingly, displacement measurements from Q400 are considered for stiffness calculation. In addition, the curve related to the theoretical stiffness IMS65 (calculated) illustrates a significant influence by the resin. The measured total elongation and the theoretical elongation are used to calculate the correction factor for this type of clamping to $p = 0.33$, which indicates that only 33 % of the nominal stiffness of IMS65 are measured. Accordingly, the loss of 67 % is related to the resin deformation.

With this information, the influence of the clamp support can be vanished from measurements on the PeCCF specimens. In a next step, the specimens *Spec 1* to *Spec 9* are tested similar to the reference specimen. Figure 4.2 (c) and (d) indicate a choice of the resulting curves from these measurements, related to the displacement measurement from Tira test system. It should be noted that the strain of $\mathrm{E}_m = 0$ is artificially defined by the starting point for a linear elastic deformation in order to highlight the behaviour in a case of ideal loading of all fibres (compare figure 4.2 (b)). It is found that all specimens show similar stress-strain relations. For a calculation of the resulting stiffness, the linear-elastic area was identified by calculating the linear regression coefficient R

$$R = \frac{\sum_{\mathrm{j}=1}^{\mathrm{n}} \mathrm{E}_{m,\mathrm{j}} \mathrm{T}_{m,\mathrm{j}} - \mathrm{n}\ \overline{\mathrm{E}}_{m,\mathrm{j}}\ \overline{\mathrm{T}}_{m,\mathrm{j}}}{\sqrt{\left(\sum_{\mathrm{j}=1}^{\mathrm{n}} \mathrm{E}_{m,\mathrm{j}}^2 - \mathrm{n}\overline{\mathrm{E}}_{m,\mathrm{j}}^2\right)\left(\sum_{\mathrm{j}=1}^{\mathrm{n}} \mathrm{T}_{m,\mathrm{j}}^2 - \mathrm{n}\overline{\mathrm{T}}_{m,\mathrm{j}}^2\right)}}, \tag{4.3}$$

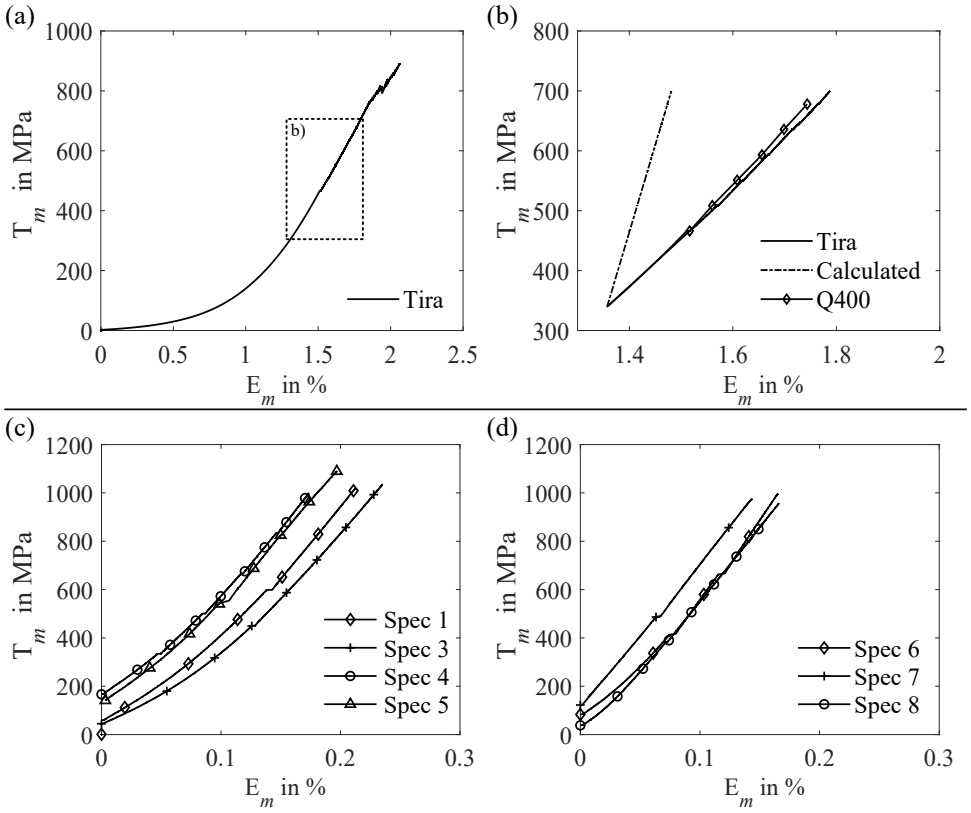

Figure 4.2: Results of tensile tests: (a) Reference measurement on specimen R1 (uncoated), (b) Comparison of Tira and Q400 strain measurement with calculated stiffness, (c) Overiew of stress-strain relation of PeCCF specimens, (d) Continued overview of stress-strain relation of PeCCF specimens

for intervals of each curve. The interval was set when values of R>0.995 are supported. The identified data interval is then applied for linear regression of the curve and the corresponding slope (Young's modulus) is calculated as

$$E_{\mathrm{s}} = \frac{\mathrm{n} \cdot \sum_{\mathrm{j}=1}^{\mathrm{n}} \mathrm{E}_{m,\mathrm{j}} \mathrm{T}_{m,\mathrm{j}} - \left(\sum_{\mathrm{j}=1}^{\mathrm{n}} \mathrm{E}_{m,\mathrm{j}}\right) \cdot \sum_{\mathrm{j}=1}^{\mathrm{n}} \mathrm{T}_{m,\mathrm{j}}}{\Delta} \,, \tag{4.4}$$

with

$$\Delta = \mathrm{n} \cdot \sum_{\mathrm{j}=1}^{\mathrm{n}} \mathrm{E}_{m,\mathrm{j}}^2 - \left(\sum_{\mathrm{j}=1}^{\mathrm{n}} \mathrm{E}_{m,\mathrm{j}}\right)^2 . \tag{4.5}$$

To correct the results from influence of the resin deformation, the measured total strain is reduced by the correction factor p:

$$\mathrm{E}_{m,\mathrm{j}} = p \cdot \mathrm{E}_{m,\mathrm{j}}. \tag{4.6}$$

The resulting Young's moduli E_s and related linear regression intervals Ψ are provided in table 4.2 (data previously published in [38]). The results indicate a significant reduction in effective stiffness compared to the nominal stiffness of bare IMS65 carbon fibres. The

averaged longitudinal stiffness is calculated here to $\overline{E}_{\mathrm{PeCCF}} = 250$ GPa, which represents a stiffness drop of ≈ 14 %. As a first conclusion, the expectation that the PEC coating has a signficiant influence on the stiffness of the PeCCF, also in longitudinal direction, is proved.

Table 4.2: Results from stiffness analysis of *Spec 1* - *Spec 9*

Nr.	E_s [GPa]	R [−]	Ψ [MPa]		
Spec 1	219	0.9962	1.08	$< T_m <$	1016
Spec 2	226	0.9950	466	$< T_m <$	1011
Spec 3	238	0.9950	126	$< T_m <$	1035
Spec 4	248	0.9958	166	$< T_m <$	1000
Spec 5	256	0.9963	141	$< T_m <$	1090
Spec 6	291	0.9956	83	$< T_m <$	995
Spec 7	304	0.9996	122	$< T_m <$	975
Spec 8	294	0.9990	38	$< T_m <$	957
Spec 9	180	0.9950	98	$< T_m <$	877
	$\overline{E}_s$	250			

Apart from this quantitative recognition, a linear elastic material behaviour of the PeCCF was identified by very narrow ranges of the linear regression coefficient for the first time (see table 4.2). This contributes directly to the model definition with respect to hypothesis H1. Accordingly, a linear elastic material model can be considered for PeCCF and MCM modelling and virtual characterisation in this thesis. This recognition is important for considering the linear thermo-elastic theory, which was already described in chapter 3 as a fundament for material modelling. Although the quantitative results are subject to a number of uncertainties related to stress-strain measurements (e.g. actual resin influence and the assumption of an ideal loading of all fibres), a subsequent numerical analysis of the PeCCF based compound is expected to be reasonable and to provide a more reliable insight into the PeCCF characteristics. This is also taken into account for PeCCF micro scale modelling described in subsection 4.2.

Some specimens from tensile tests as well as specimens *Spec 10* - *Spec 22* are used further for thermal characterisations. The next subsection provides a thermo-electrical characterisation of the PeCCF specimen with an emphasis on the effects from the PEC coating compared to bare IMS65.

4.1.3 Electro-Thermal Characterisation of PeCCF

For the electro-thermal characterisation of PeCCF specimens, the measurement setup described in [38] is used. The setup comprises two Tektronix DMM4020 digital multimeter for the measurement of electrical current I and electrical potential ϕ at the specimens. Furthermore, a high definition thermographic camera system Jenoptik VarioCam HD is

used for temperature mesaurements. The specimens are connected to an external power source and related current, potential and temperature measures are recorded. Figure 4.3 (a) shows an exemplary thermographic image of specimen *Spec 14* under investigation. The specimen is contacted by micro clamps, those being connected to the measurement circuit. Depending on the measurement scenario, a DC force current I_f is applied to the specimen, causing it to heat up due to the Joule effect.

Within the captured area, two different surface points are indicated for a temperature measurement. The areas indicated by R1 and R5 are related to a coated carbon fibre surface and an uncoated carbon fibre surface, respectively. Scanning electron microscope (SEM) images given in (a) verifiy the surface condition of the specimen at positions R1 and R5. For the temperature measurement, an emissivity for carbon fibre filaments of $\varepsilon = 0.77$ is set in the thermographic camera. Figure 4.3 (b) shows the temperature rise over time as well as the related, calculated temperature time derivative $\partial_t\theta$ with respect to an applied forced current of $I_f = 0.29$ A. The maesurements are performaed at an ambient temperature of $\theta_a = 297$ K.

It is found that the coated surface shows an increased temperature compared to the uncoated surface during the whole time interval. In addition, the temperature time derivative for the coated surface drops slower compared to the uncoated surface. Similar indications were made for other specimens (see Appendix A.2). This already indicates a reduced ability to transfer heat from the fibre to the environment, which can only be explained by the coating material. It should be noted that these results should be treated as *qualitative*, since their reliability depends highly on the emissivity of the material surface. It is expected that the coated and the bare surface have different emissivities. With the given setup it was not possible to support different emissivities within one measurement of the thermographic camera system, nor to verify them. Although the measured temperatures may be affected by different emissivities, this first indication is an important support for further model based investigations towards the heat transfer within the PeCCF composite.

Apart from the heat transfer behaviour, the electrical performance related to Joule heating is measured. Therefore, the potential is applied in a range of $\phi = [0.0,\ 8.0]$ V and the resulting current as well as the resulting temperature at the surface are recorded. The curve in Figure 4.3 (c) indicates for specimen *Spec 5* a linear current increase while the temperature rises. An important indication is that the current vs. potential curve is linear. This identifies the PeCCF specimen as a constant ohmic resistor within the indicated temperature interval of $\theta_s = [293.0,\ 375.0]$ K. Related to the modelling of the electro-thermally coupled behaviour of the PeCCF, a constant ohmic resistivity is beneficial since no temperature dependency needs to be modelled. In addition, the temperature interval corresponds to the typical aircraft system operating temperatures, e.g. for De-Icing

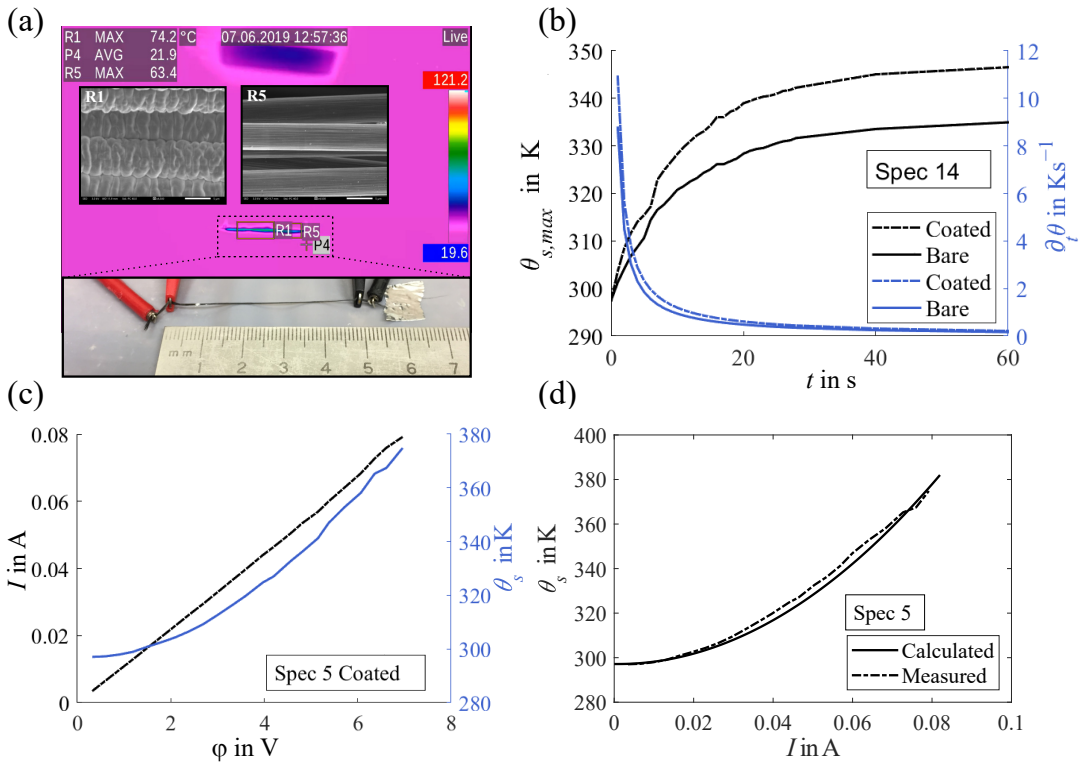

Figure 4.3: Results of thermal investigations: (a) Measurement setup, (b) Temperature and temperature time derivative of coated and uncoated surface at specimen 14, (c) Overview on current and temperature rise at specimen 5, (d) Current vs. temperature rise of specimen 5 - taken and modified with permission from [38]

(see subsection 2.4). Especially application related in-situ simulations will benefit from this recognition.

In order to support this finding, a simple 1D model is setup to calculate the temperature rise related to the applied current. Therefore, the heat transfer to the environment is assumed to be proportional to the thermal resistance R_{th} of the material

$$R_{th} = \frac{\Delta\theta}{Q_\mathrm{h}} = \frac{\theta_\mathrm{s} - \theta_\mathrm{a}}{P} = \frac{\theta_\mathrm{s} - \theta_\mathrm{a}}{I^2 \cdot K} \ , \tag{4.7}$$

where Δ_θ represents the temperature change, Q_h represents the heating rate, P is the heating power which is related to the applied current and the specimen's total resistance K. The individual electrical resistances K are given in Appendix A.2 in table A.1. Once the thermal resistance is known, the temperature rise can be computed. For the given case of specimen *Spec 5*, the thermal resistance is calculated based on the measured data to $R_{th} = 142.77\ \frac{\mathrm{K}}{\mathrm{W}}$ for an ambient temperature of $\theta_a = 297$ K. Accordingly, the function of temperature rise holds

$$\theta_\mathrm{s} = \frac{R_{th} I^2 \kappa l}{A_c} + \theta_a \ , \tag{4.8}$$

where K is replaced by the individual dimensions of the specimen: length l, cross section

of the bundle A_c and the IMS65' specific resistance κ_f as $K = \kappa l / A_c$ (see subsection 2.3.1). The resulting temperature rise related to current increase is given in figure 4.3 (d), in which the measured and the predicted curves almost coincide. Consequently, it has been demonstrated for the first time that the Joule heating can be considered to be constant ohmic with a free convective heat transfer to the environment. This is an important contribution to the model assumptions with respect to hypothesis H1. It is expected further that the heat transfer behaviour can be predictd by an electro-thermally coupled model based on the partial differential heat equation, as indicated in chapter 3.

These electro-thermal characteristics of the PeCCF provide the fundament for the introduction of a coupled model for PeCCF on the micro scale that is introduced in the following chapters. The model is then used for the analysis of the PE coating's influence on mechanical properties, Joule heating and heat transfer..

4.2 Micromechanical Model and Homogenisation

4.2.1 Model Assumptions and Theory Application

It should be noted that parts of section 4.2 have been published earlier by Maximilian Schutzeichel in [112]. This original research is displayed in a greater context of this thesis to contribute to the research hypotheses.

The PE coating shows significiant influences on the effective properties of the PeCCF compared to standard carbon fibres, as indicated in the prior section. Accordingly, the coating's influence on the resulting MCM is of special interest since the coating represents a third material phase once the PeCCF is embedded in a polymeric matrix material. The micro mechanical description of the resulting MCM is done here based on a numerical FEM approach. Therefore, a UC which represents the three material phases is introduced and used for the prediction of the effective stiffness tensor $\boldsymbol{C}$ as well as the thermal expansion tensor $\mathbf{A}$. Subsequently, the micro mechanical UC approach is utilised for multi scale simulations in which micro scale information is transferred to the meso scale and vice versa (compare figure 3.1 in subsection 3.1.1).

The polymer electrolyte coating shows a significant thermo-mechanical behaviour which results in a 94 % drop of the storage modulus E_c' in a temperature range of $\theta = [273.0,\ 393.0]$ K (see table 2.2 in subsection 2.3.2). Since the PEC represents an interphase material, separating the reinforcing carbon fibre and the matrix material, significant influences by the temperature variant stiffness of the PEC are expected. The expectation is also related to similar cases in which significant influences of composite interphases on the transversal properties of composite materials were reported [113–117]. As indicated in subsections 3.2.1 and 3.2.2, the effective material properties of a representative material volume can be computed by unit strains and resulting volume

averaged stresses. The representative material volume needs to fulfill the periodicity requirement, stating geometrical compatibility with neighbouring cells in all mechanical states. In order to contribute to research hypthesis H1 of this thesis, a cubic UC is chosen, comprising the carbon fibre (domain Ω_1), the PE coating (domain Ω_2) and the matrix material (domain Ω_3, see figure 4.4 (a)) with indicated microscale ONB coordinates. Such material representations have been applied in several earlier works in literature [118–120]. Consequently, the illustrated UC is considered to be representative and reliable for the MCM on the micro scale in accordance with hypothesis H1.

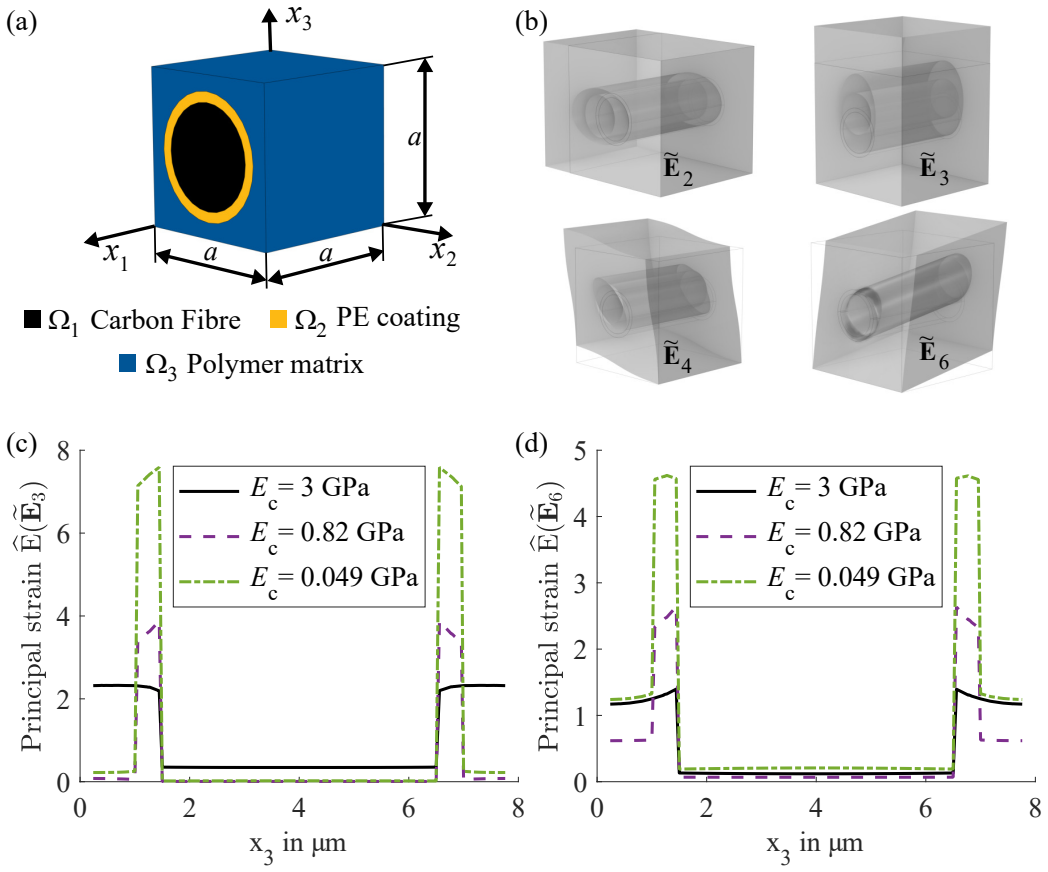

Figure 4.4: (a) Definition of UC, (b) Exemplary illustration of unit strain deformation, (c) First principal strain distribution for unit strain case $\widetilde{\mathbf{E}}_3(x_1 = x_2 = a/2,\, v_f = 0.5)$, (d) First principal strain distribution for unit strain case $\widetilde{\mathbf{E}}_6(x_1 = x_2 = a/2,\, v_f = 0.5)$

It should be noted that hexagonal UCs are frequently preferred due to their direction invariant properties in the transversal plane [121, 122]. However, it is assumed that transversal properties, predicted by the cubic UC approach along x_2 and x_3 directions, are reliable and can be considered as direction invariant in the transversal $x_2,\ x_3$ plane for the application as effective properties on the meso scale. This was also demonstrated in literature [118–120].

To enable a first exploration of the effective material behaviour, viscoelasticity is not considered for the micro scale model. The objective is to evaluate the general effect of

the coating towards the elastic properties of the MCM. Consequently, fatigue and damage are also not considered. As described in section 4.1, a linear elastic material behaviour was indicated for the PeCCF compound. Accordingly, the linear thermo-elastic continuum theory is applied and considered to enable a proper prediction of effective mechanical properties of the MCM (supporting hypothesis H1). For the material composition, an ideal bond between material phases is assumed. This is motivated by the electroplymerisation process, grafting the PE coating directly onto the surface of the carbon fibre (as described in subsection 2.3.2). An ideal bond between the PEC and the polymeric matrix material is considered based on studies from literature, stating a good bond quality between polymeric fibre coatings and matrix materials [123]. Furthermore, isotropy of the coating is assumed. Literature reports on ultra thin composite interphases which only show property gradients for interphase thicknesses of $t_c < 200$ nm [124, 125]. The thickness of the considered coating is identified as $t_c = 500$ nm as a result of the PEC choice and the coating process (see subsection 2.3.2) so that isotropy of the interphase is a justified assumption. The assumptions are summarised as follows:

1. Linear thermo-elastic continuum theory
   (limit case of viscoelasticity),
2. Fatigue and damage induction are not considered,
3. Ideal bond at interfaces of material phases,
4. Isotropic interphase (PEC) properties.

Based on this fundament, the continuum theory for effective material stiffnesses and TECs (as described in subsections 3.2.1 and 3.2.2) is used. The characterisation and prediction of effective material properties is needed to enable a meso scale description of the material. Accordingly, the micro scale representation is an important fundament for a multi scale approach (supporting hypothesis H1). Therefore, the unit strain modes and periodic boundary conditions (equations 3.27 and 3.29) are applied to the UC. The transversal isotropic properties of the carbon fibre and the isotropic properties of the PEC as well as of the matrix are applied (compare tables 2.1 and 2.2 in section 2.3, respectively).

Figure 4.4 (b) illustrates examples of the deformations from unit strains $\widetilde{\mathbf{E}}_\mathrm{j}$ applied to the UC. In (c) and (d) the resulting principal strain states are demonstrated for $\widetilde{\mathbf{E}}_3$ and $\widetilde{\mathbf{E}}_6$, respectively. The different strain distributions are related to the x_3 direction of the coordinate system, as defined in (a). Three interphase Young's modulus cases are distinguished for this investigation:

C1 *Standard carbon fibre composite* $E_c = E_m = 3000$ MPa

C2 *PE coating at room temperature* $E_c(\theta = 293\ \mathrm{K}) = 850$ MPa

C3 *PE coating above glass transition temperature*
$E_c(\theta_g < \theta = 393\ \text{K}) = 49\ \text{MPa}$

Consequently, the curves illustrate the strain distribution of the PeCCF based MCM (case C2 and C3) in comparison to a standard carbon fibre composite (case C1) for which the interphase properties are equal to the matrix material properties. The two Young's moduli of the PE coating are considered as boundary values related to the considered temperature range in operation.

In figure 4.4 (c) and (d) it is indicated that the introduction of the coating phase has a significant effect on the strain distribution. Compared to the standard carbon fibre composite, the coating interphase shows a strain increase of factor two and four in these two configurations. This quantitative observation indicates for the first time that the inclusion of a low stiffness PE coating, as considered here, has an important impact on the internal compliance distibution. Although the indicated numbers are related to unit strains without relation to an external load condition, the strain distribution highlights a significant influence compared to a standard carbon fibre composite, especially for load cases in transversal directions. The quantitative increase in compliance of the coating phase is in agreement of qualitative demonstrations of Tridech et al. [10]. This demonstrates the ability to represent the elastic behaviour of the material compound in this material model as well as the quantitative influence of the interphase for the first time (hypothesis H1).

In addition, it is mentioned that this first linear elastic analysis is only a limit case of the actual viscoelastic behaviour of the interphase. With respect to creep effects, the interphase will develop further strain with time. Although viscoelasticity is not considered here, the investigation of viscoelastic effects towards fatigue and damage initiation should be part of future work.

This first indication of the internal strain distribution reinforces the expectation of significant influences of the coating on the effective stiffness of the MCM. The next subsection presents the predicted effective stiffnesses and TECs with a discussion of the interphase influences.

4.2.2 Effective Stiffness and Thermal Expansion

The effective stiffness tensor elements of the MCM are computed based on the volume averaged stresses obtained from the application of the unit strain modes on the UC (see equation 3.31). As mentioned during theory description, this method provides options for the verification of results. Especially the stiffness tensor elements with indices i≠j are computed repeatedly by different unit strain modes. In addition, the results related to tensor indices i=j of the standard carbon fibre composite (case C1, $E_c = E_m = 3000$ GPa) can be compared to results obtained from the ROM. Therefore, the longitudinal effective Young's modulus $\overline{E}_1$ is obtained from Voigt's solution (equation 3.63) and the transversal

effective Young's moduli $\overline{E}_2$, $\overline{E}_3$ are obtained from the advanced Reuss solution, considering transversal contraction with respect to the Poisson's ratio (equation 3.65).

Figure 4.5 (a) and (b) show the specific effective stiffnesses of the standard carbon fibre composite related to the Young's modulus of the matrix. Both results are computed for fibre volume fractions of $v_f = [0.1,\ 0.7]$. The longitudinal stiffness C_{11} shows identical results for both methods. The transversal stiffness C_{22} shows similar magnitudes with a slight offset between FEM and ROM solutions. This offset is related to the assumption of Reuss' solution that all materials contribute equally to the stress distribution. This is not the case for the discrete material distribution in the UC. Accordingly, the effective stiffness obtained from the linear elastic 3D UC model is assumed to provide a more exact solution. Related to the fact of similar results' magnitude, a good reliablity of the FEM approach is identified. In addition, transversal isotropy stating $C_{22} = C_{33}$ and $C_{44} = 0.5 \cdot (C_{22} - C_{23})$ is found for the predicted results (see appendix A.4, figures A.4 - A.6). Therefore, the expected material symmetry as well as the proper prediction of effective material properties is considered to be reliable (supporting hypothesis H1).

With respect to FEM theory, different mesh definitions are studied for the UC. Appendix A.4 figure A.7 and table A.2 show two different mesh definitions with a *standard* and a *refined* mesh. The results presented here are computed by the standard mesh, since no significant benefits from a refined mesh definition are found. In order to save computational cost, the fine mesh was only used for verification purposes.

Based on this verification of the computational approach by FEM, the effect of the coating on the effective stiffnesses is studied. Therefore, the coating stiffness cases C2 and C3 (as descried in subsection 4.2.2) are applied to the interphase and the effective stiffness tensor elements are computed. As an example, figure 4.5 (c) indicates the results for the transversal stiffness C_{22} and (d) for the shear stiffness C_{66}. For the coating stiffness of $E_c = 820$ MPa the curves indicate a significant stiffness drop which is associated here with room temperature. Another significant drop is indicated for $E_c = 49$ MPa which is associated with an increased operating temperature of $\theta = 393$ K. This effect is even more pronounced for an increased fibre volume fraction. Even though the reinforcement of the carbon fibre is maintained for the room temperature case C2, the reinforcement is neutralised when the stiffness of the coating drops with temperature (case C3). For the first time this important indication for a multifunctional applications of the PeCCF compound was underpinned by computational results (supporting hypotheses H2 and H3), since the material is exposed to significant temperature increase during multifunctional use.

Besides these examples, all effective stiffness tensor elements $\overline{C}_{\mathrm{ij}}$ associated with the transversal plane show similar effective stiffness drops (see appendix A.4, figures A.4-A.5). The only exception is the effective stiffness in longitudinal direction which is

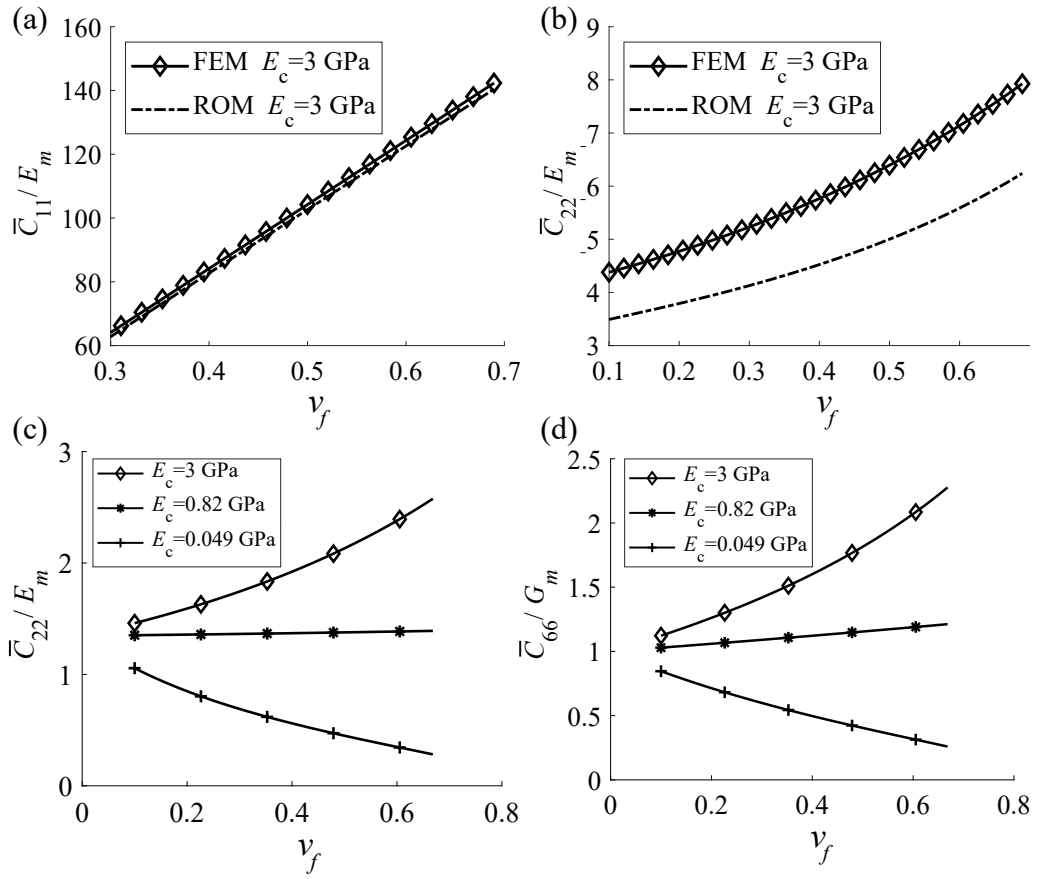

Figure 4.5: (a) and (b): Effective stiffnesses $\overline{C}_{11}$ and $\overline{C}_{22}$ computed by FEM and ROM, (c) and (d): Specific effective stiffness $\overline{C}_{22}$ and $\overline{C}_{66}$ computed by FEM for different coating moduli E_c

nearly unaffected by the coating's Young's modulus (see appendix A.4, figure A.4 (a)). This can be explained by the assumption that all material phases are loaded by an equal strain in longitudinal direction (Voigt's solution). Correspondingly, the stiffness of the carbon fibre dominates the parallel arrangement in longitudinal direction. However, tensile tests described in section 4.1 already indicated that also longitudinal load cases can be affected by the coating, as soon as the load tansfer is provided by shear forces from the outer matrix material to the carbon fibre. This is plausible with respect to the unit shear strains analysed here and can occur when forces act on the material's outer boundary surface.

It can be summarised that the analysis of the micro scale effective transversal stiffness as well as shear stiffness elements are signifcantly affected by the coating's stiffness. This recognition in combination with the effect of temperature induced stiffness reduction of the coating phase are important conclusions towards multifunctional applciations like De-Icing (supporting hypothesis H2).

Apart from the analysis of the effective stiffness of the MCM, the elements of the effective thermal expansion tensor $\overline{\mathbf{A}}$ are computed. Therefore, the assumptions and

definitions described in subsection 4.2.2 are applied again. In order to compute the effective thermal expansion, the periodic boundary conditions are applied but the UC is allowed to expand freely as described by theory in subsection 3.2.2. In addition a unit temperature change of $\Delta\theta = 1$ K is applied to force the material constituents to develop thermo-mechanical strains. As described by equations 3.41 and 3.44, the resulting effective TECs can be obtained from the effective stiffness tensor $\overline{\boldsymbol{C}}$ and the volume averaged thermal stresses $\{\langle \mathrm{T}_{\mathrm{lk},th,\mu} \rangle\}$.

The thermal expansion coefficient of the PE coating is not characterised experimentally yet. To enable the analysis of it's possible effect on the effective TEC of the MCM, a typical range of $\alpha_c = [20.0,\ 100.0]\ \frac{10^{-6}}{\mathrm{K}}$ for this PE polymer type was assumed (compare table 2.2). Figures 4.7 (a)-(c) indicate the single elements of the effective transversal

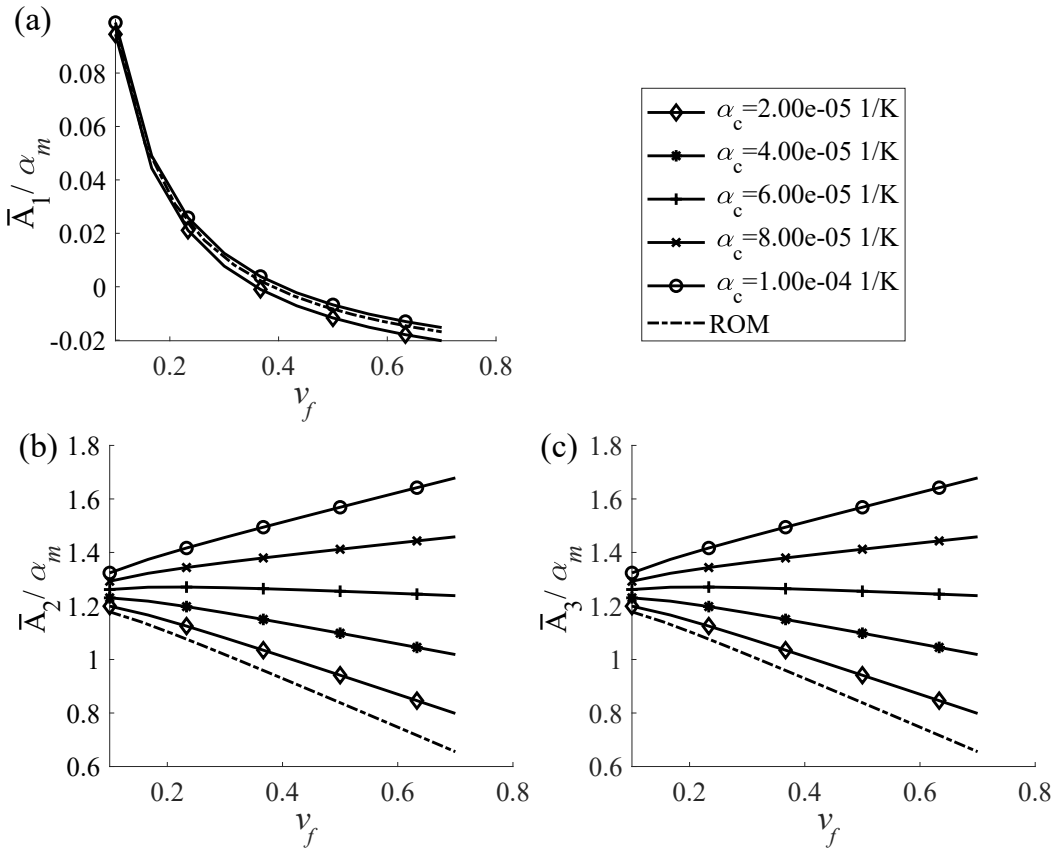

Figure 4.6: Elements of the specific transversal isotropic thermal expansion tensor: (a) for $\overline{\mathrm{A}}_1$,(b) for $\overline{\mathrm{A}}_2$, (c) for $\overline{\mathrm{A}}_3$

isotropic thermal expansion tensor $\overline{\mathbf{A}}$ with respect to the chosen fibre volume fraction. All curves are computed from FEM calculations except the ROM solution (dotted line). The ROM result (equations 3.63 and 3.64) for the standard carbon fibre composite with $\alpha_c = \alpha_m = 2 \cdot 10^{-5}\ \frac{1}{\mathrm{K}}$ is used for verification by comparison with the corresponding FEM solution. Similar to the observations for the effective stiffness, the results match perfectly for the longitudinal TEC, whereas the TEC in transversal direction is slightly

underestimated by the ROM. This is again reduced to the geometrical effects, which are not considered in the ROM. However, the computational results are found to have a reasonable magnitude which indicates appropriate computational results (supporting hypothesis H1).

The comparison with curves related to the coating's TEC range indicate only a minor influence on the effective longitudinal thermal expansion coefficient $\overline{\mathrm{A}}_1$. Contrarily, the transversal TECs $\overline{\mathrm{A}}_2$ and $\overline{\mathrm{A}}_3$ are found to be highly affected by the coating's TEC. This effect is more pronounced with increasing fibre volume fraction. It is mentioned that transversal isotropy is verified again by the equality of results of $\overline{\mathrm{A}}_2$ and $\overline{\mathrm{A}}_3$ (compare figure 4.7 (b) and (c)). Besides the effective stiffness tensor elements $\{\overline{C}_{\mathrm{ij}}\}$ also the effective TECs are identified to be sensitive to the corresponding coating properties in the transversal isotropic plane. The longitudinal direction is also affected but in a much lower magnitude.

To summarise the effect of the coating's elastic properties on the effective properties of the MCM, the following relative drops are computed:

$$\Delta_A = \frac{\max[\overline{\mathrm{A}}_{\mathrm{i}}(v_f)] - \min[\overline{\mathrm{A}}_{\mathrm{i}}(v_f)]}{\min[\overline{\mathrm{A}}_{\mathrm{i}}(v_f) - \overline{\mathrm{A}}_{\mathrm{i}}(v_f)]} \cdot 100 \quad \text{and} \tag{4.9}$$

$$\Delta_C = \left(1 - \frac{\overline{C}_{\mathrm{ij}}(E_{\mathrm{c}} = 0.049 \text{ GPa})}{\overline{C}_{\mathrm{ij}}(E_{\mathrm{c}} = 0.82 \text{ GPa})}\right) \cdot 100. \tag{4.10}$$

Therefore, the drop Δ_A indicates the TEC difference of the maximum and minimum TEC normalised by it's minimum difference. In a similar way, the drop Δ_C indicates the relative change in effective stiffness related to the two PEC Young's modulus cases (2) and (3). The results are plotted in figure 4.7. All elements of the effective stiffnes tensor

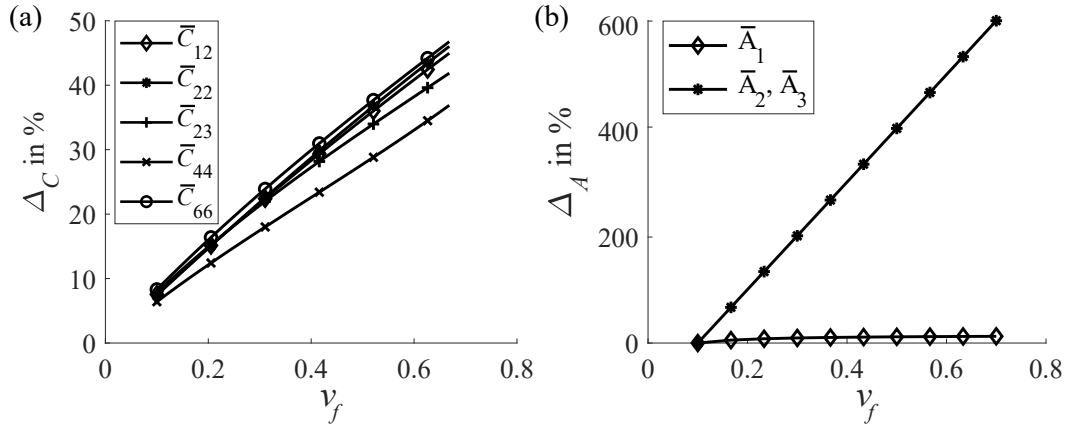

Figure 4.7: Drop of (a) Effective stiffness and (b) Effective TEC related to equations 4.9 and 4.10

$\{\overline{C}_{\mathrm{ij}}\}$, except the longitudinal stiffness $\overline{C}_{11}$, show significant drops for the two coating stiffness cases (2) and (3). The drop starts with about 8 % for $v_f = 0.1$ and increases up to 48 % at $v_f = 0.7$ which highlights the significant influence of a temperature related

drop of the coating's Young's modulus in a quantitative magnitude for the first time. The shear stiffness $\overline{C}_{66}$ shows the highest drop, but $\overline{C}_{44}$ is still highly affected, even when the drop is slightly smaller. For the effective TEC tensor elements, the longitudinal thermal expansion shows only a minor drop which appears constant over the fibre volume fraction. However, the transversal TEC $\overline{\mathrm{A}}_{22}$, $\overline{\mathrm{A}}_{33}$ shows a high sensitivity to the TEC range of the coating which was chosen here. Since the TEC range was defined to exhibit one order of magnitude, the effective TEC was even more increased by up to 600 % for the maximum fibre volume fraction $v_f = 0.7$.

Correspondingly, future work should concentrate on a TEC characterisation of the PE coating material in order to support the computation of the effective thermo-elastic properties. In addition, the effective TEC can be controlled by the coating phase, which could be used for the definition of new, tailored polymer electrolyte coating systems. The micro scale modelling of the thermo-elastic behaviour of the MCM is identified to be necessary and successfull for the electro-themo-mechanically coupled multi scale model approach of this thesis (supporting hypothesis H1).

Summarising, the polymer electrolyte coating has a high influence on the effective elastic properties of the MCM which is demonstrated in this investigation for the first time by quantitative results. Especially the parameter associated with the transversal isotropic plane as well as shear stiffness parameter show high drops, once the associated property of the coating drops. Accordingly, the meso scale model neeeds to be informed by the actual state on the micro scale which provides the effective material properties. Since the micro scale can not be resolved for meso scale calculations, actual effective properties are obtained from the micro scale model and applied on the meso scale in a coupled multi scale approach. This recoginition underpins the aim for a multiscale approach for the meso scale modelling of MCM (supporting hypothesis H1). With respect to ROM solutions for standard carbon fibre composites, the demonstrated mechanical model was found to be accurate in terms of magnitude and behaviour. It is assumed that the results obtained from the mechanical model are more precise, since the influence of the geometric architecture is included which is not the case for the ROM.

Related to these recognitions, the interphase must be understood as an important material phase which can be adapted towards mechanical and multifuntional requirements. If the stiffness drop initiated by temperature increase is desired (e.g. for stiffness adaptive structures [59]) the meso or macro scale structure can be designed so that the adaptable stiffness modes are addressed. If the stiffness drop is not desired (e.g. for a structural battery [17] or for a De-Icing application of the MCM [4]) the structure requirements must account for the stiffness drop in terms of ply and laminate architecture. Considering this perspective, the thermo-mechanical model on the micro scale provides the foundation for the investigations towards De-Icing capabilities and model based innovation (supporting

hypotheses H2 and H3).

However, a direct coupling to the thermal field was not introduced in models reported in literature. The next section will introduce a corresponding model of the thermal field on the micro scale. Similar to the evaluation in this section, the influence of the coating on the effective thermal properties of the composite is discussed and new methods for the representation of the thermal problem are introduced and analysed towards efficiency and reliability.

4.3 Modelling and Analysis of MCM Heat Transfer

4.3.1 RVE Definition, Generation and Modelling Strategies

It should be noted that parts of section 4.3 have been published earlier by Maximilian Schutzeichel in [87]. This original research is displayed in a greater context of this thesis to contribute to the research hypotheses.

The representation and modelling of the thermal heat transfer characteristics as well as the prediction of effective thermal properties is based on the choice of a RVE. The RVE is able to represent a number of randomly distributed PeCCFs in a cubic cell, which enables a realistic representation of the expected material architecture. Compared to the UC which was used for mechanical property prediction (see section 4.2), the RVE approach is necessary for spatial analysis of heat transfer inside the RVE with respect to the random PeCCF distribution and the influence of a homogenised representation in a direct comparison. The detailed analysis of the heat transfer behaviour on the micro scale is important for the prediction of the overall electro-thermo-mechanical behaviour, since the temperature as well as the temperature gradient directly act on the mechanical behaviour (see theory description in subscetion 3.1.1). Therefore, a unique RVE definition will be introduced in this section to enable an appropriate heat transfer analysis of the MCM for the first time.

The RVE needs to fulfill the requirements for geometric compatibility with neighbouring cells. This is necessary for the computation of effective heat transfer related properties based on periodic boundary conditions as well as for the use in a multi scale approach (see subsections 3.2.3 and 3.1.4, respectively). To assure the periodicity requirement, a cubic base geometry is chosen which provides equal surface areas on opposite surfaces. An edge length of $a = 20$ µm is chosen and random PeCCF positions are defined in the $x_2,\ x_3$ base plane. With this edge length, a sufficient number of fibres can be included in order to investigate fibre distribution related effects on the thermal behaviour. Therefore, the outer radius of the coated fibre of $r_{cf} = r_f + t_c = 3$ µm is used. In order to avoid overlapping fibres as well as to assure the periodicity requirement, an algorithm for the generation of adequate fibre positions with random distribution is introduced and implemented in Matlab.

Figure 4.8 provides a schematic overview of the single algorithm steps and related conditions. In a first step, random PeCCF positions are created within the 20 µm x 20 µm base area by the definition of $x_2,\ x_3$ coordinate pairs. The generation stops, as soon as the actual fibre volume fraction of the PE coated carbon fibre v_{cf} reached the prescribed fibre volume fraction v_r. In a next step, the algorithm checks if some of the PeCCFs are located so that they reach over edges or corners of the base area. For all *edge fibres* (PeCCF overlapping with an edge) a corresponding fibre coordinate on the opposite edge

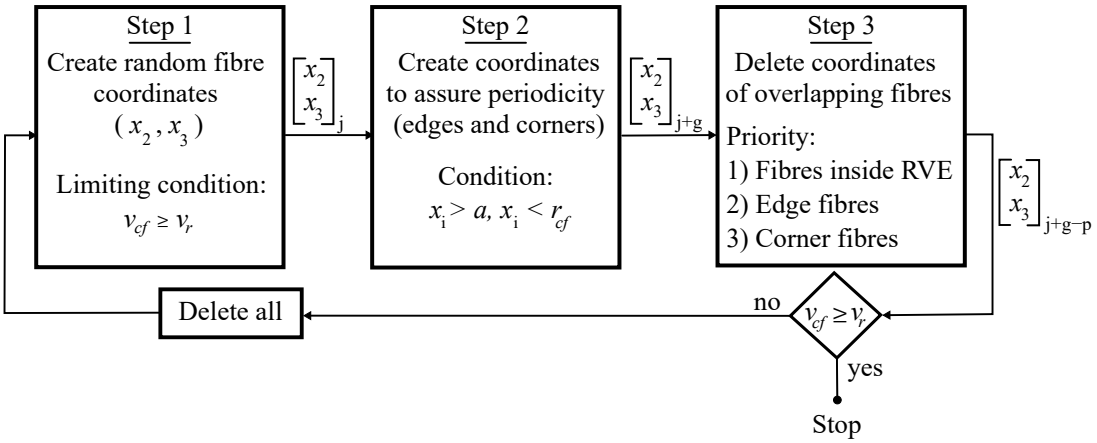

Figure 4.8: Overview of algorithm steps for the genertion of a random fibre distribution with reference fibre volume fraction v_r, taken with changes from the author's publication in [87]

is generated. The same is done for *corner fibres* (PeCCF overlapping with two edges) whereas the corner fibre is repeated at all 4 corners. In a postprocessing step, the edge and corner fibres will be cut with the cubic boundary surfaces in order to create the corresponding cut areas on opposite RVE surfaces. In a third step, the algorithm checks for overlapping fibres and deletes fibres by priority: 1) Fibres which are inside the RVE, 2) Edge fibres and 3) Corner fibres. After the removal of overlaps, the fibre volume fraction is checked again based on the remaining set of fibre coordinates. If the desired fibre volume fraction is provided, the algorithm stops. Otherwise, the algorithm deletes all generated coordinates and starts again with step 1. The algorithm is very efficient for fibre volume fractions $v_{cf} < 0.5$, since the chance vor many overlaps is low. With further increasing fibre volume fractions, the likelyhood for overlaps increases which leads to an increased number of iterations. However, the algorithm provides suitable results with acceptable computational time.

Figure 4.9 (a) shows the resulting fibre distribution after Step 2 of the algorithm and (b) after Step 3. Overlapping fibres are removed by the given strategy and the geometric compatibility is assured by corresponding opposite fibres on all edges and corners. The set of fibre coordinates is then transferred to the geometry definition in Comsol Multiphysics (V6) and is expanded in x_1 direction. Finally, edge and corner fibres are cut by the outer surfaces of the cubic base cell, resulting in a periodic RVE. Figure 4.9 (c) shows an example with respect to the defined ONB and to the related boundary surfaces which were defined for the theoretical fundament (compare figure 3.2).

Based on this RVE representation of the MCM on the micro scale, a discrete heat transfer from the Joule heating carbon fibres to the surrounding materials and to the environment can be analysed. Due to the fact that carbon fibres show intermediate thermal properties and the PE coating as well as the epoxy matrix material show poor

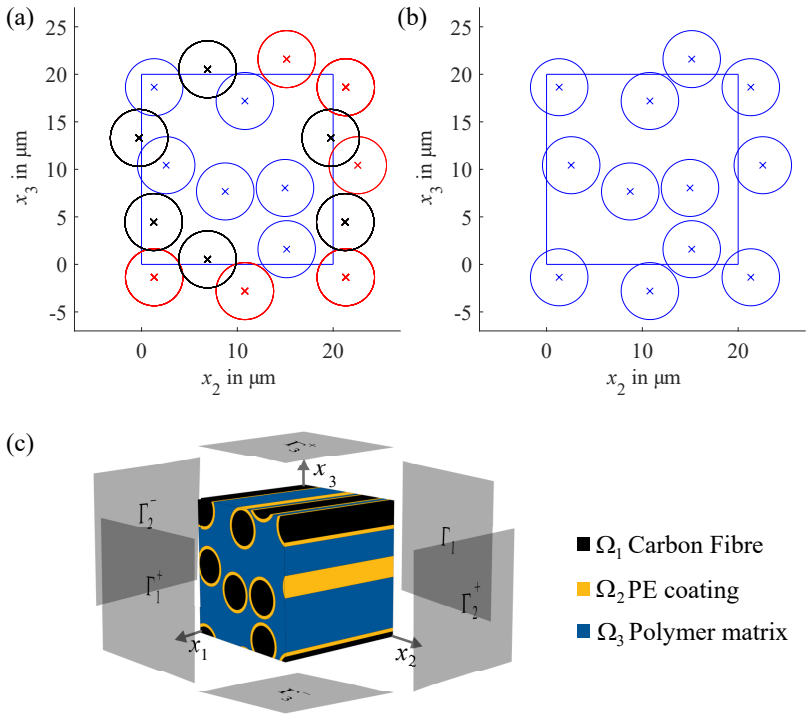

Figure 4.9: RVE geometry generation: (a) Fibre distribution after Step 2 of the algorithm, (b) Final fibre distribution after Step 3 of the algorithm, (c) 3D representation of RVE with indicated ONB and boundary surfaces

thermal properties [32,126], the effect of the internal fibre distribution is of special interest. Furthermore, the influence of the PE coating in comparison to a standard carbon fibre composite is examined here for the first time by a numerical approach. Related to this ambition, the analysis is motivated by geometric properties of the MCM on the meso scale. Figure 4.10 introduces a schematic, how the RVE could be located within an UD ply of a laminate. With respect to the meso scale geometry, the RVE can be defined to represent longitudinal and transversal directions which are given by the fibre orientation. The transversal plane can be distinguished into the thickness and the width direction. The transversal thickness direction plays an emphasised role for heat transfer, since heat convection to the environment is usually present at the surface of the structure. This is in conjunction with the application scenario of De-Icing in which the architecture of a heating MCM ply on the surface of a laminate is considered (see figure 1.2 in section 1.2). Accordingly, the main heat transfer path starts at the heat source (Joule heating carbon fibres) and is directed towards the outer surface area in x_3 direction. Consequently, the investigation will focus on the temperature gradient in thickness direction. Besides this general strategy for heat tansfer analysis, physical assumptions are motivated based on the material constituents. An ideal material contact between all constituents is assumed as already motivated in subsection 4.2 for the mechanical domain and is applied here again. Concerning heat transfer at composite constituent's interfaces, an effect called *Kapista*

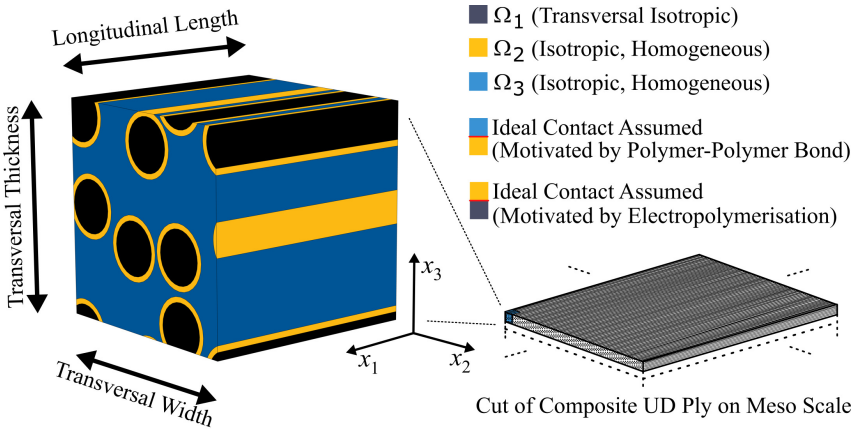

Figure 4.10: Definitions and assumptions on the micro scale with relation to the meso scale

resistance can lead to a significant reduction of the thermal conductivity [126–129]. In this examination of the PeCCF based MCM, Kapista resistance is nigligible due to the following conclusions from literature: First, the Kapista resistance is indicated to be significant only for filler particle sizes on the nano scale ($l \approx 1$ nm) which is not given for the present micro scale ($l = [0.1,\ 100.0]$ µm, see figure 2.1) MCM architecture [130, 131]. Second, the main cause for interface thermal resistance was identified to be caused by a highly disordered textures at the interface and imperfect adhesion [128, 132]. This assumption is further supported by a numerical study of Kaminski and Ostrowski, investigating the effect of interface defects on the resulting Kapista resistance [133]. Third, the effect of Kapista resistance is found to be most significant near cryogenic temperatures of $\theta = 30$ K. With respect to operating temperatures of the MCM in an interval of $\theta_a = [243, 373]$ K (e.g. with application in the area of De-Icing, compare section 2.4), the assumption of negligible Kapista resistance is further supported [128, 129].

Concerning the thermal properties of the material constituents, the carbon fibre (domain Ω_1) is assumed to be transversal isotropic with respect to thermal conductivity. The PE coating (domain Ω_2) and the matrix material (domain Ω_3) are defined to be isotropic, since no preferred material orientation is present (see legend in figure 4.10).

For the examination of the thermal behaviour of the MCM on the micro scale, two modelling cases are distinguished for the subsequent investigation:

C1 Virtual measurement of the effective heat conductivity

C2 Thermal heat transfer with free convection at surface Γ^{+}_{x3}

Modelling case C1 represents a numerical virtual test case for the identification of the effective thermal conductivity of the MCM related to the RVE micro scale representation. This is mainly used for the verification of results obtained from analytic methods. Modelling case C2 is then used to analyse the heat transfer behaviour considering free convection at the surface of the RVE. Thereby, the influences of homogenisation techniques on this

behaviour and the related computational performance can be analysed. Subsequently, the two cases are defined in terms of boundary conditions and theoretical considerations.

Modelling case C1

For the virtual measurement of effective heat conductivities, a number of boundary conditions are defined related to the surfaces of the RVE. These conditions comprise suitable periodicity conditions and the needed temperature and heat source definitions. All conditions are related to the boundary surface areas and corresponding domains indicated in figure 4.10. Exemplary for the calculation of the effective transversal heat conductivity $\overline{\Lambda}_{11}$, the following conditions are set (related to equations 3.54-3.59 in subsection 3.2.3):

$$\theta(\Gamma^{+}_{\mathrm{x2}}) = \theta(\Gamma^{-}_{\mathrm{x2}}), \tag{4.11}$$

$$\theta(\Gamma^{+}_{\mathrm{x3}}) = \theta(\Gamma^{-}_{\mathrm{x3}}), \tag{4.12}$$

$$\theta(\Gamma^{+}_{\mathrm{x1}}) = 500 \text{ K}, \tag{4.13}$$

$$\mathbf{q}(\Gamma^{-}_{\mathrm{x1}}) = \mathbf{n}_{\mathrm{x1}} \cdot \frac{Q_{1,f}}{a^2} \quad \text{with} \tag{4.14}$$

$$Q_{1,f} = 1 \cdot 10^{-4} \text{ W}. \tag{4.15}$$

Equations 4.11 and 4.12 define thermal periodicity in directions perpendicular to the measurement direction x_1. Equations 4.13 and 4.14 indicate an isotemperature and an inward directed heat flux at the normal surfaces to the measurement direction. The vector $\mathbf{n}_{\mathrm{x1}}$ is a unit vector pointing in x_1 direction which is simultaneously the inwart pointing surface normal. Since the heat conductivity directly acts on the temperature gradient, but not on the temperature, the chosen temperature and heat source conditions are arbitrary. Accordingly, the resulting effective heat conductivity is invariant of conditions defined in equations 4.13-4.15. The resulting thermal field can be calculated by FEM and the desired surface temperature $\theta(\Gamma^{-}_{\mathrm{x1}})$ can be used for the calculation of the effective heat conductivity $\overline{\Lambda}_{11}$. For the computation of the remaining effective thermal conductivities in other directions, the boundary conditions need to be exchanged in a circular manner. The corresponding results of this virtual measurement as well as predictions from analytical solutions are presented in subsection 4.3.4.

Modelling case C2

For the prediction of the temperature field including the related temperature gradient, the special case of a surface heat convection is investigated. Therefore, the carbon fibre related Joule heat emission is applied and a convective heat transfer (Newton/Robbin) boundary condition is defined on the top surface Γ^{+}_{x3} in thickness direction. At the opposite surface Γ^{-}_{x3} an adiabatic condition is defined (no heat transfer), which is motivated by the

assumption of isothermal sub-plies of MCM uderneath the considered ply. The remaining boundaries are subject to periodic thermal boundary conditions which do not allow for a temperature drop. Summarised, the following BC apply:

$$\theta(\Gamma^{+}_{\mathrm{x2}}) = \theta(\Gamma^{-}_{\mathrm{x2}}), \tag{4.16}$$

$$\theta(\Gamma^{+}_{\mathrm{x1}}) = \theta(\Gamma^{-}_{\mathrm{x1}}), \tag{4.17}$$

$$\mathbf{q}(\Gamma^{-}_{\mathrm{x3}}) = 0 \ \frac{\mathrm{W}}{\mathrm{m}^2}, \tag{4.18}$$

$$Q(\Gamma^{+}_{\mathrm{x1}}) = A_{\mathrm{s}}(\Gamma^{+}_{\mathrm{x1}}) \cdot h \cdot (\theta - \theta_a) \quad \text{with} \tag{4.19}$$

$$\theta_a = 293 \text{ K}. \tag{4.20}$$

With these thermal boundary conditions, the heat flux inside the material domain can be analysed with respect to the transversal isotropic plane x_2, x_3. The choice of the convective heat transfer condition is related to room temperature and the convective HTC is chosen for all individual cases. Since the resulting stationary heat transfer behaviour is invariant to the magnitude of heat dissipation, this condition was chosen arbitrary. However, the overall temperature level is determined thereby. For the thermal energy source, the following electrical boundary conditions are defined to apply the Joule heat source as:

$$Q_{\mathrm{p}} = \kappa_f |\mathbf{j} \cdot \mathbf{j}| \qquad \text{with} \tag{4.21}$$

$$\mathbf{j}(\Gamma^{-}_{\mathrm{x1,j}}) = j \cdot \mathbf{n}_{\mathrm{x1}} \qquad \text{for } \Gamma^{-}_{\mathrm{x1,j}} \in \Omega_1 \text{ and} \tag{4.22}$$

$$\phi(\Gamma^{+}_{\mathrm{x1},\phi}) = 0 \text{ V} \qquad \text{for } \Gamma^{+}_{\mathrm{x1},\phi} \in \Omega_1 \tag{4.23}$$

With this set of boundary conditions, the thermal heat transfer behaviour in x_3 direction can be calculated and analysed. In addition, the internal temperature distribution, which is expected to be sensitive to the PeCCF distribution, can be analysed.

For both modelling cases the single constituents of the RVE are defined based on the material properties in tables 2.1 and 2.2 (bold numbers). In order to investigate the effect of different homogenisation methods, the single domain properties will be exchanged with the related effective properties. The classical, analytical homogenisation methods are summarised in the following subsection along with a newly proposed approach.

4.3.2 Analytical Homogenisation of Thermal Properties

For the computation of effective thermal material properties, a number of analytical methods is considered. The single effective properties are applied to modelling case C2 in order to compare the effects on the predicted heat transfer behaviour. The ideal analytical approach is identified by comparison with the discrete FEM solution. For the heat transfer

problem, the three thermal material properties *Heat conductivity* Λ, *Specific heat* c_p and *density* ρ are discussed towards influences by homogenisation. Special emphasis is on the heat conductivity, since it acts on both, the transient and stationary heat transfer case and is a direction dependent, transversal isotropic qantity. Specific heat and density act on the transient thermal heat problem only and are isotropic properties. Therefore, these properties can be homogenised by the ROM (Voigt's solution) or by a RVE volume average (see equation 3.60).

All analytic solutions for effective material properties rely on the volume fractions of the materials. Table 4.3 introduces the volume fractions related to the RVE under investigation (see figure 4.9).

Table 4.3: Material constituent volume fractions with indicated reference volume, taken with changes from the author's publication in [87]

Volume fractions	Symbol	Value	Reference volume
Fibre volume fraction	v_f	0.29	RVE
Coating volume fraction	v_c	0.13	RVE
Matrix volume fraction	v_m	0.58	RVE
Coated fibre volume fraction	v_cf	0.42	RVE
Particle fibre volume fraction	v_pf	0.69	PeCCF
Particle coating volume fraction	v_pc	0.31	PeCCF

Some analytical homogenisation methods consider a first application on particle level which corresponds to the PeCCF. Accordingly, the particle related fractions indicate the volume fractions related to one PE coated carbon fibre.

For the investigation of effects on the predicted heat transfer behaviour, the following homogenisation methods are considered:

1. Rule of Mixture || (Voigt's solution, equation 3.63)
2. Rule of Mixture $\perp$ (Reuss' solution, equation 3.64)
3. Three Phase Lewis-Nielsen Method
   (after [105], equations 3.64 and 3.68-3.71)
4. New Two-Level Lewis-Nielsen Method (TLLN)
   (equations 3.68-3.71 and 4.24-4.27)

All methods are applied in order to compare the relative quality of the resulting effective heat conductivity. Furthermore, the results of modelling case C1, which represents a virtual measurement of the thermal conductivity, are used for a comparison in order to identify the most suitable method.

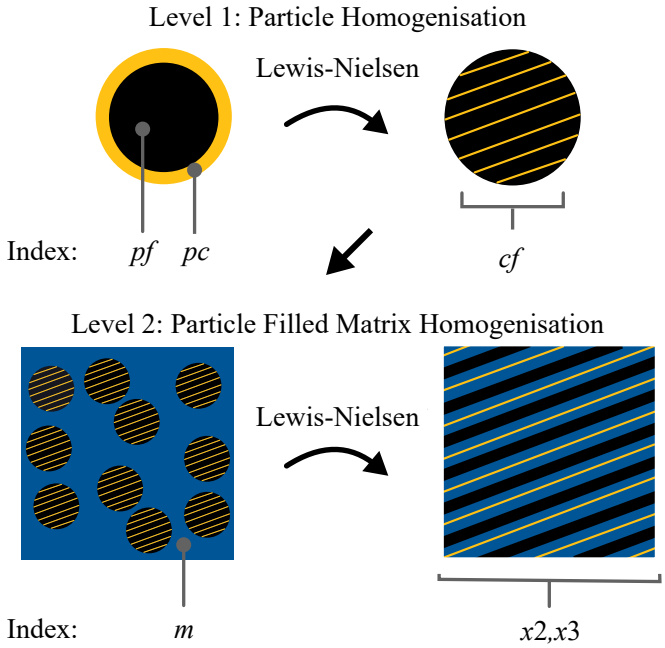

Figure 4.11: Schematic of TLLN method, taken with changes from the author's publication in [87]

The new *Two-Level Lewis-Nielsen* method was first published in [87] and was originally developed by the author during investigations of the MCM heat transfer behaviour. Referring to the TPLN method of Kochetov et al., a two step homogenisation is applied. Therefore, the particle homogenisation is now done by applying the Lewis-Nielsen method on a first level: the particle with coating phase (compare figure 4.11). In a second step, the Lewis-Nielsen method is applied again based on the input from level 1 homogenisation and applies then the two-phase particle volume fraction and the corresponding matrix fraction. For the homogenisation on level one, the particle related Lewis-Nielsen eqution are written as follows:

$$\overline{k}_{cf} = k_{\mathrm{pc}} \frac{1 + \xi_{pf}\eta_{pf}v_{pf}}{1 - \Phi_{pf}\eta_{p}v_{pf}} \quad \text{with} \tag{4.24}$$

$$\eta_{pf} = \frac{k_{pf} - k_{pc}}{k_{pf} + \xi_{pf}k_{pm}}, \tag{4.25}$$

$$\Phi_{pf} = 1 + \frac{(1 - v_{pf,max})}{v_{pf,max}^2} v_{pf} \quad \text{and} \tag{4.26}$$

$$\xi_{pf} = 2\frac{l_{pf}}{d_{pf}} \quad . \tag{4.27}$$

The homogenisation on level 2 is done with the standard equations 3.68-3.71 with $k_p = \overline{k}_{cf}$. Accordingly, the new TLLN approach is distinguished from Kochetov et al. (method 3, [105]) by the method which is applied on level 1. The presentation of results related to modelling case C2 will discuss the paramter choice and benefits of the new method (see

subsection 4.3.4).

The ambition for reliable analytical solutions for the prediction of effective thermal material properties is driven by the aim for computational efficient modelling. Apart from the homogenisation of the material representation on the micro scale, another option for an increase in computational efficiency by a model order reduction is introduced. The next subsection presents an approach to reduce the 3D RVE of the MCM to a plane 2D representation. All results predicted by the different methods are presented in subsection 4.3.4.

4.3.3 Model Reduction Strategy

For the computation of the transversal heat transfer problem on the micro scale, two general conditions need to be met: 1) The heat source and the related material domain need to be separated from the passive (non heating) material domains. 2) The boundaries for the electrical and thermal boundary conditions need to be present. To meet these conditions, the removal of the x_2 direction in the 3D model is considered, since periodicity is considered in this direction (modelling case 2) and no significant heat source or sink is related to this direction.

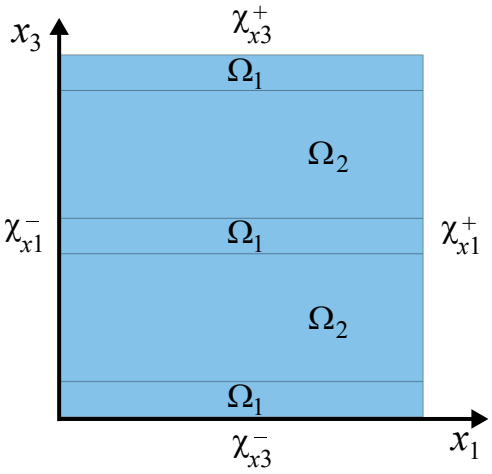

Figure 4.12: 2D representation of the heat transfer within the RVE in x_3 direction

Figure 4.12 shows the 2D geometry for the plane representation of the heat transfer problem. The quadratic plane representation of the RVE is divided into two domains which represent the area of the carbon fibre volume fraction Ω_1 and the remaining volume fraction Ω_2 (including coating and matrix phase). The boundaries are now reduced to the edges and are denoted by $\chi^{+,-}_{xi}$, similar to the notation in the 3D case by Γ. The actual separation of all three phases is not needed anymore, since the homogenised material properties $\overline{\mathbf{\Lambda}}$ (TLLN Method), $\overline{\rho}$ and $\overline{c_p}$ (both ROM Voigt's solution) are applied to both domains Ω_1 and Ω_2.

It should be noted that the carbon fibre area is divided into three parts and distributed

equally over the surface area in order to emulate the non-centered heat source distribution similar to the original discrete fibre distribution. Due to the fact that the heating power is dependent on the specific electrical resistance κ, the volume of the Joule heating material needs to be covered in a plane representation by equivalent constant thickness in the (removed) third direction. The same condition is needed for the equivalent volume of material which is heated in a transient case. Therefore, the transient heat transfer problem and the Joule heat equation are redefined for the 2D case and two representative thickness definitions are introduced

$$d_a \bar{c}_p \bar{\rho} \partial_t \theta = d_a \nabla_{2D} \overline{\mathbf{\Lambda}} (\nabla_{2D} \theta) + Q_g \qquad \text{with} \tag{4.28}$$

$$d_a = a \qquad \text{and} \tag{4.29}$$

$$Q_g = d_{eq} \kappa |\mathbf{j}_{2D}^2| \qquad \text{with} \tag{4.30}$$

$$d_{eq} = \frac{v_\mathrm{f} \cdot a^3}{a^2} = v_f \cdot a, \tag{4.31}$$

where d_a is the thickness of the heated volume in the third direction and d_{eq} is the equivalent thickness of the Joule heating carbon fibres. The index $2D$ indicates that the nabla operator and the current density vector are only two dimensional in this equation. Similar to modelling case C2, the adiabatic condition is set for boundary χ_{x3}^- and the convective heat transfer is defined on boundary χ_{x3}^+. The periodicity condition in x_1 concerning a zero temperature change across boundaries $\chi_{x1}^{-,+}$ remains. The applied heating current density j is applied again for domain Ω_1 and a corresponding ground condition is set. Thereby, an equivalent material volume is subject to Joule heating resulting in an equivalent heat source compared to the discrete 3D RVE representaiton. Summarised, the following set of boundary conditions is applied:

$$\mathbf{q}(\chi_{\mathrm{x3}}^-) = 0 \ \frac{\mathrm{W}}{\mathrm{m}^2}, \tag{4.32}$$

$$Q(\chi_{\mathrm{x1}}^+) = d \cdot l_b(\chi_{\mathrm{x1}}^+) \cdot h \cdot (\theta - \theta_a) \qquad \text{with} \tag{4.33}$$

$$\theta_a = 293 \text{ K} \qquad \text{as well as} \tag{4.34}$$

$$\mathbf{j}(\chi_{\mathrm{x1},j}^-) = d_{eq} \cdot j \cdot \mathbf{n}_{\mathrm{x1}} \qquad \text{for } \chi_{\mathrm{x1},j}^- \in \Omega_1 \text{ and} \tag{4.35}$$

$$\phi(\chi_{\mathrm{x1},\phi}^+) = 0 \text{ V} \qquad \text{for } \chi_{\mathrm{x1},\phi}^+ \in \Omega_1 \tag{4.36}$$

Ultimately, the FEM representation of the 2D case is able to reduce the total number of elements needed to discretise the thermal problem and is expected to be much more efficient (see mesh comparison in the appendix, figure A.8).

The following subsection presents the results from modelling and homogenisation approaches considered for the 3D modelling cases C1 and C2 as well as for the 2D reduced representation.

4.3.4 Discussion of Effective Heat Transfer

The presentation of results of the stationary thermal heat transfer modelling is divided into two main parts. First, the analytical results for material property homogenisation are presented and second, the influences of the different effective media are discussed based on modelling case C2. Subsequently, the transient heat transfer behaviour will be characterised for both, the discrete and the homogenised case.

In order to provide an overview of the discrete solution of the stationary thermal field in modelling case C2, figure 4.13 shows isotemperature planes along the x_3 direction with respect to the RVE. For this solution, the convective HTC $h = 40\ \frac{\mathrm{K}}{\mathrm{m^2K}}$ was chosen.

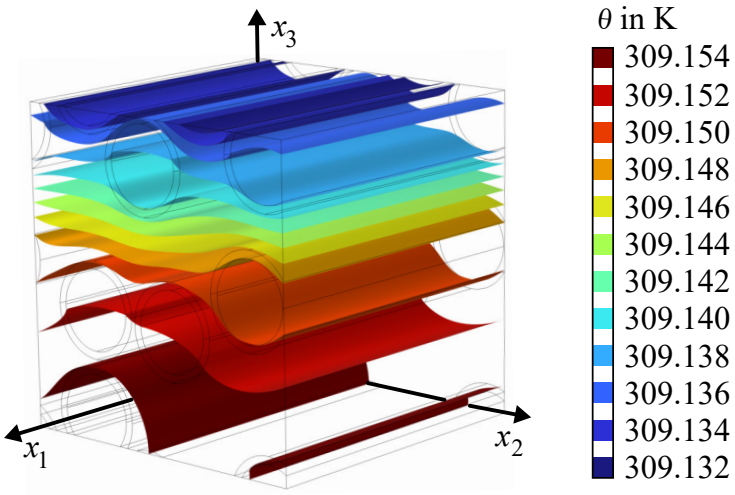

Figure 4.13: Isosurfaces for stationary heat transfer with convective heat transfer at the surface ($h = 40\ \frac{\mathrm{K}}{\mathrm{m^2K}}$)

Besides the condition of a clear temperature decrease along the thickness direction, an increased temperature gradient is indicated in areas with less carbon fibre density. This is marked by narrow distances between the iso surfaces. This clearly indicates the differences in thermal heat conductivity of the material constituents. In general, the temperature gradient increases in thickness direction that can be related to the adiabatic condition on the lower surface Γ^{-}_{x3}. The discussion of effects from homogenisation on the heat transfer behaviour is based on a comparison with this discrete FEM solution. However, the small overall temperature intervall found within the RVE enables an assumption of a constant temperature for computations on the micro scale. This assumption is further applied in coupled meso-micro scale simulations, as presented in section 5.2.

Table 4.4 introduces the results of the effective heat conductivity and the chosen parameter for the single methods. In addition, the results of modelling case C1 are indicated.

It should be recognised that Voigt's solution of the ROM is only suitable for the longitudinal effective heat conductivity $\overline{\Lambda}_1$. Accordingly, the longitudinal heat conductivity

Table 4.4: Predicted, effective thermal conductivities

Method	$\overline{\Lambda}$ in $[\frac{\mathrm{W}}{\mathrm{mK}}]$	Input parameters	Equations
ROM (Voigt)	2.79	$\lambda_{\|\|,f} = 9\ \frac{\mathrm{W}}{\mathrm{mK}}$	3.63
ROM (Voigt)		$\lambda_{\perp,f} = 1.1\ \frac{\mathrm{W}}{\mathrm{mK}}$	3.63
ROM (Reuss)	0.25	$\lambda_{\perp,f} = 1.1\ \frac{\mathrm{W}}{\mathrm{mK}}$	3.64
Three-Phase	0.30	$\lambda_{\perp,f} = 1.1\ \frac{\mathrm{W}}{\mathrm{mK}}$	3.64 and
Lewis-Nielsen		$\xi = 6.6$	3.68
		$v_{\max} = 0.79$	
Two-Level	0.29	$\lambda_{\perp,f} = 1.1\ \frac{\mathrm{W}}{\mathrm{mK}}$	3.68 and
Lewis-Nielsen		$\xi = 0.01$	4.24
		$v_{\max} = 0.79$	
		$\xi_{\mathrm{pf}} = 6.6$	
		$v_{\mathrm{pf,max}} = 1$	
Modelling case C1	$\overline{\mathbf{\Lambda}} = \left[\overline{\Lambda}_1, \overline{\Lambda}_2, \overline{\Lambda}_3\right]^T = [2.76, 0.29, 0.29]^T\ [\frac{\mathrm{W}}{\mathrm{mK}}]$;		

of the carbon fibre $\lambda_{||,f}$ is used for the calculation. For the remaining heat conductivities, the heat conductivity of the carbon fibre in transversal direction $\lambda_{\perp,f}$ is used. Apart from the method related parameters (as indicated in table 4.4), the volume fractions in table 4.3 as well as the isotropic heat conductivities of the PE coating and the matrix material are applied as indicated in table 2.2.

The solution of the ROM (Voigt) is identical to the virtual measurement of the longitudinal effective heat conductivity by modelling case C1. Furthermore, the Results of ROM (Reuss) and the TPLN approach show an under- or overestimation of the measured transversal effective heat conductivity. However, these two predictions can be understood as narrow upper and lower bounds of the transversal effective heat conductivity. In addition, the newly introduced TLLN approach directly fits to the results of the virtual measurement. With this first recognition, the representation of the stationary heat transfer of the RVE in a homogenised medium is expected to be very accurate. The effects of the different effective heat conductivity measures on the prediction of the thermal field are further discussed related to modelling case C2.

For modelling case C2 two different convective heat coefficients are chosen $h = 5\ \frac{\mathrm{W}}{\mathrm{m^2K}}$ and $h = 40\ \frac{\mathrm{W}}{\mathrm{m^2K}}$ which are indicated in figure 4.14 (a) and (b) respectively. For both choices, the different thermal field solutions area indicated as temperature plots over the x_3 coordinate, corresponding to the thickness direction. The applied homogenisation methods are indicated in the legend. A clear temperature drop over the thickness of the RVE is present. The discrete solution enables a recognition of the fibre and matrix related phases

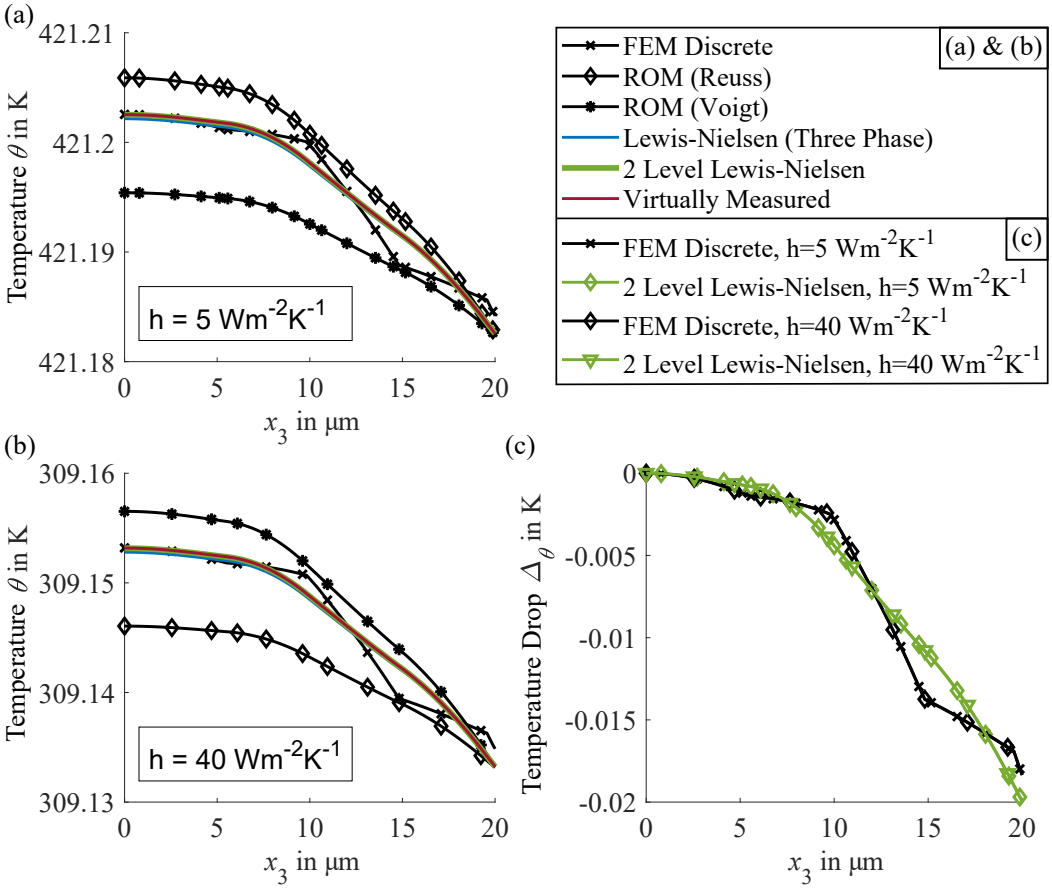

Figure 4.14: Overview on stationary temperature distribution over thickness x_3 (at $x_1 = x_2 = 10$ µm): (a) Result for $h = 5\ \frac{\mathrm{W}}{\mathrm{m^2K}}$, (b) Result for $h = 40\ \frac{\mathrm{W}}{\mathrm{m^2K}}$, (c) Temperature drop comparison for different heat convection coefficients; taken with changes from the author's publication in [87]

which are distinguished by different temperature gradients. The decrease in temperature is much larger in the matrix domain. The coating phase is not directly indicated by the temperature gradient. This leads to the conclusion that the influence of the coating material on the internal heat transfer is small compared to the influence of the matrix material. This is also associated with the much smaller volume fraction of the coating phase. Accordingly, the measured temperature difference on coated and uncoated carbon fibres (as presented in subsection 4.1.3) is plausible but the effect on the effective heat transfer of the MCM is negligible when the PeCCF is embedded in a matrix polymer.

The comparison of the two convective HTCs highlights that only the stationary temperature level, but not the internal temperature distribution is influenced. With respect to the different homogenisation methods, the ROM (Voigt) and ROM (Reuss) indicate overall upper and lower bounds with respect to the temperature gradient. The remaining solutions, especially the measured effective thermal conductivity, represent a smooth average of the discrete curve. However, the temperature gradient is represented very well by the analytical TPLN as well as the TLLN methods. This highlights its

reliablity for the accurate prediction of the effective heat conductivity of the three phase MCM.

It should be noted that the results of the Three-Phase and the TLLN method are very close in this case which is related to the choice of input heat conductivities. The heat conductivities of all three material phases are chosen to be of similar magnitude (compare table 2.2). In the assignet publication of this method in [87], a more pronounced suitablity of the TLLN was indicated. Concluding, the TLLN method is even better in case of very different heat conductivity magnitudes of the constituents.

For the quantification of the temperature drop over thickness, the difference

$$\Delta_\theta = max\left[\theta(x_3)\right] - \theta(x_3) \tag{4.37}$$

is shown in figure 4.14 (c) for the discrete and for the TLLN solution with respect to $h = 5\ \frac{\mathrm{W}}{\mathrm{m^2K}}$ and $h = 40\ \frac{\mathrm{W}}{\mathrm{m^2K}}$. As expected, the convective HTC has no influence on the temperature drop within the material. This is clear, since the heat conductivity only acts on the temperature gradient. Despite the fact that the discrete solution shows different slopes over the single domains, the homogenised TLLN solution is able to represent the overall temperature drop of $\Delta_\theta \approx 0.02$ K. For the correct interpretation of the drop magnitude, the number is related to the distance in thickness direction, which results in a specific drop of $\Delta_\theta = 1\ \frac{\mathrm{K}}{\mathrm{mm}}$. This magnitude indicates for the first time a significant temperature drop of the MCM in thickness direction that could be relevant for the mechanical behaviour of the MCM due to the thermo-mechanical coupling (supporting hypothesis H1 and H2).

Summarising, a good representation of the heat transfer behaviour was indicated for the homogenised 3D representation. In addition, the solution quality was checked based on two different FEM meshes (see appendix, figure A.8). No infleunces of mesh fineness are found so that all results presented here are computed by the coarse mesh for maintaining a high computational efficiency.

Besides the stationary heat transfer case, the transient temperature evolution over time is investigated. Here the homogenisation of specific heat c_p and density ρ are discussed towards influences of the heat up process. Since both quantities only act on the time derivative of the temperature, the stationary heat transfer is not affected. However, the accurate prediction of dynamic heat up processes is of special interest, since several application scenarios like De-Icing as well as structural energy storage are exposed to non stationary energy transfer. This results in permanent electrical energy load changes over time which in turn is relevant for the heat generation change.

Table 4.5 shows the results of homogenised specific heat and density by a volume average related to the RVE and the ROM (Voigt's solution).

As expected, these volume specific quantities show identical results for the volume

Table 4.5: Homogenised specific heat and density parameter with respect to method and input parameter

Method	$\overline{c}_p$ $[\frac{\mathrm{J}}{\mathrm{kgK}}]$	$\overline{\rho}$ $[\frac{\mathrm{kg}}{\mathrm{cm}^3}]$	Input parameters	Equation
Volume Average (VA)	997	1110	Table 2.1 & 2.2 bold numbers	3.60
ROM (Voigt)	997	1110	Table 2.1 & 2.2 bold numbers	3.63

average and the ROM (Voigt's solution). However, compared to the specific heat and density numbers of the single constituents, the effective numbers show significant differences, especially with respect to the carbon fibre and the coating material (compare with tables 2.1 and 2.2). For the discrete representation and the homogenisation input, the coating's specific heat was assumed to be $c_{p,c} = 2090\ \frac{\mathrm{J}}{\mathrm{kgK}}$, which is a literature value related to the polymer type of the PE coating. However, the influences of lithium salt fraction as well as the general combination of monomers A and B for the coating material are not yet characterised. In order to discuss the influence of the coating material on the heat up process, another discrete configuration was chosen with $c_{p,c} = c_{p,m} = 1050\ \frac{\mathrm{J}}{\mathrm{kgK}}$. The remaining parameter are equal to the discrete representation. Accordingly, three different configurations are presented:

1. Discrete,
2. Discrete with $c_{p,c} = c_{p,m} = 1050\ \frac{\mathrm{J}}{\mathrm{kgK}}$,
3. Homogenised by ROM/VA.

Figure 4.15 (a) shows the volume averaged temperature $\langle\theta\rangle$ rise over time and (b) indicates the temperature distribution over x_3 for the different configurations. The changes related to specific heat and density changes are visible in the time interval of $t = [0.0,\ 20.0]$ s which corresponds to their action on the temperature time derivative. However, during the heat up phase, significant differences in predicted temperatures are visible in (b). This corresponds to the fact that the homogenisation leads to a significantly decreased specific heat capacity which leads again to a slightly faster heat up in the homogenised representation. The influence of the coating material on the heat up process can be characterised as minor, although it provides a much higher heat capacity compared to the remaining constituents. Especially the fact that the curves of configurations 2 and 3 are similar, the influence of the coating lies in the range of the expected accuracy loss due to homogenisation.

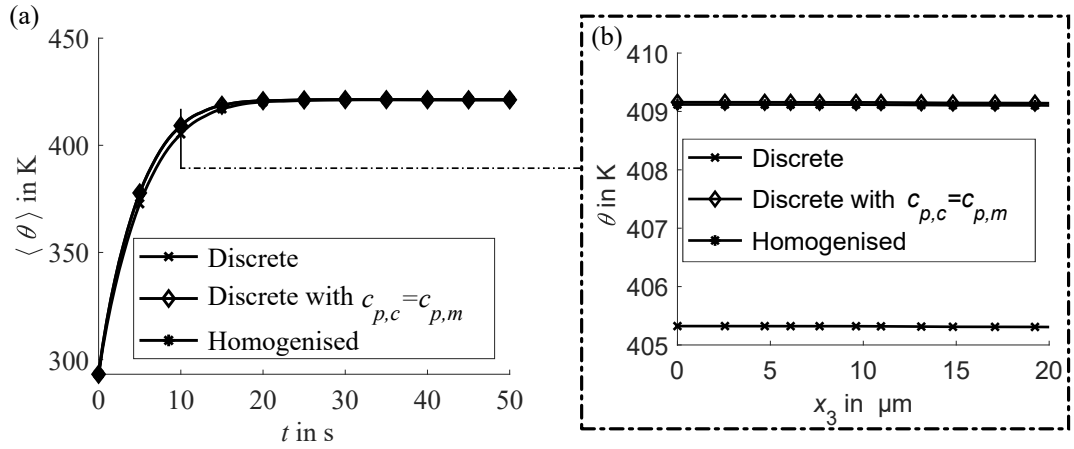

Figure 4.15: (a) Transient rise of volume averaged temperature over time, (b) Detailed view on Temperature distribution in x_3 direction (for $x_1 = x_2 = 10$ µm)

Apart from the influence of the coating properties, it was demonstrated that the homogenisation of specific heat and density is suitable for an appropriate prediction of the transient heat up process of the MCM. Although small differences of absolute temperatures are indicated in the heat up period, the overall behaviour is similar to the discrete result.

Based on these results, the accurate representation of the heat transfer behaviour of the MCM by an RVE and a homogenised representation are demonstrated for the first time (contributing to hypothesis H1). In addition, it should be recognised that the influence of the material properties on the heat up rate is small. This is relevant for considerations of a fast (e.g. for De-Icing) or a slow heat up (e.g. for structural batteries) which in turn needs to be established by other measures as the choice of different matrix or coating materials in the MCM. One approach is the transient adoption of the current density to adapt the heat up rate which can be considered in a future application related development of e.g. a MCM based De-Icing system.

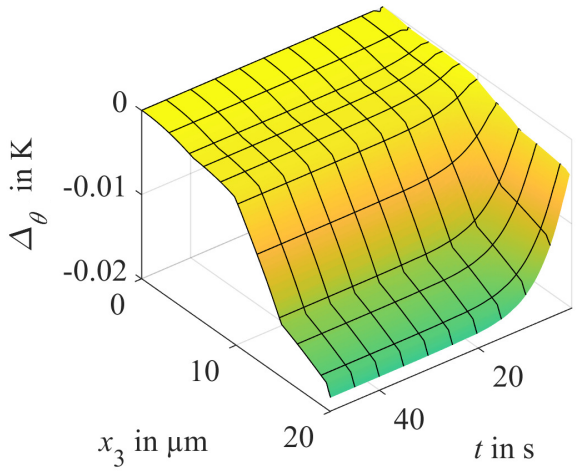

Figure 4.16: Temperature drop in thickness direction, evolution with time

Figure 4.16 presents the temperature drop over the thickness direction as a 3D plot over time. It is clearly visible that the increase in temperature drop is proportional with time. This highlights that the maximum temperature drop is related to the stationary heat transfer case. With respect to the thermo-mechancial interaction, the stationary case can be considered as the relevant case for temperature induced mechanical loads on the material. This conclusion is important again for model based innovation, since mechanical design of a MCM laminate can build on the stationary case, which is less computational expensive compared to the transient case.

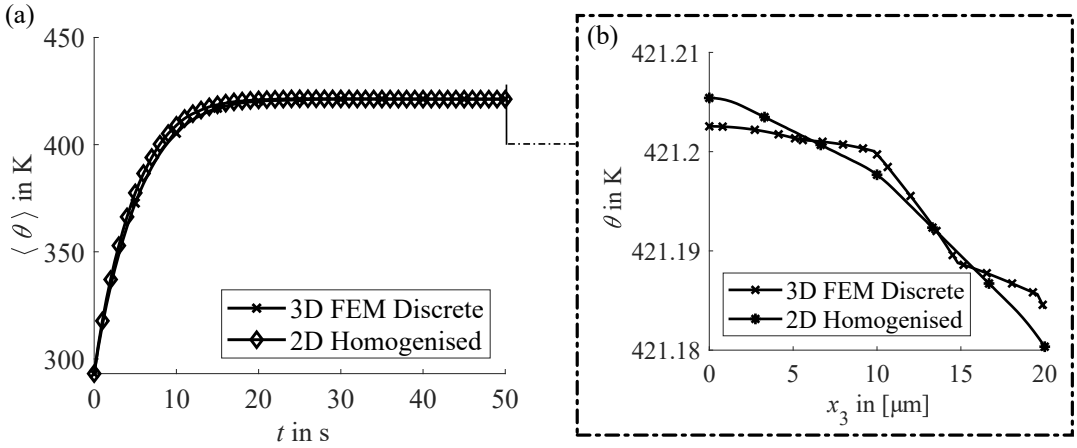

Figure 4.17: Comparison of 3D discrete and 2D homogenised approach: (a) Transient rise of volume averaged temperature over time, (b) Detailed view on Temperature distribution in x_3 direction (for $x_1 = x_2 = 10$ µm)

In general, computational efficiency is important for the use of the micro scale model in a multiscale modelling framework. Consequently, another approach for the increase of computational efficiency is introduced by the plane 2D representation of the homogenised RVE (see subsection 4.3.3). Figure 4.17 shows the results of the 2D homogenised representation in comparison with the 3D discrete representation. The curves indicate for the first time an accurate prediction of the heat transfer behaviour by the reduced 2D model. The transient heat up process is nearly identical to the discrete result and the temperature distribtion in thickness direction is also very similar. The effective specific temperature drop computed by the 2D approach is slightly increased compared to the discrete result $\Delta_{\theta,2D}(x_3) = 1.25\ \frac{\mathrm{K}}{\mathrm{mm}} > \Delta_{\theta,3D}(x_3) = 1\ \frac{\mathrm{K}}{\mathrm{mm}}$, but is considered to be appropriate with respect to the efficiency increase of the 2D representation (supporting the multi scale approach considered in hypothesis H1).

Table 4.6 indicates the single computation times for the transient and stationary solutions related to the FEM meshes (a) 3D refined, (b) 3D coarse and (c) 2D plane. The reduction of the model to the 2D representation provides an increase in computational efficiency by 98 % for both, the transient and the stationary case. This significant increase in efficiency is beneficial for a coupled multiscale simulation, in which the meso scale model

Table 4.6: Computational effort for 3D RVE representation in (a) Refined, (b) Coarse and (c) 2D plane configurations (related to appendix, figure A.8)

	Computation time in [s]	
Model	Transient problem	Stationary problem
3D Refined	1518	263
3D Coarse	364	60
2D Homogenised	7	6
Relative Reduction of Computational Cost	≈ 99 %	≈ 98 %

is underpinned by effective heat transfer information from the micro scale. Especially in cases in which a meso scale case needs to be analysed in detail on the micro scale in each single study step, the fast computation of the micro scale case is of high importance (contributing to hypothesis H1).

Based on the characterisation of the mechanical and thermal properties on the micro scale, the meso scale model is introduced in the following chapter with respect to hypothesis H1. Therefore, the meso scale model applies the homogenised material properties in order to model an experimental heat transfer case related to De-Icing conditions (contributing to hypothesis H2). In a subsequent part of the next chapter, model based innovation options are presented with respect to hypothesis H3.

5 Meso Scale Modelling and Engineering Application

5.1 Convection Modelling and Validation Under Icing Conditions

5.1.1 Experimental Measurement of Heat Convection

In advance, it should be noted that parts of section 5.1 have been published earlier by Maximilian Schutzeichel in [134]. This original research is displayed in a greater context of this thesis to contribute to the research hypotheses. Therefore, it is mentioned that the complete modelling work as well as specimen preparation were carried out by the author of this thesis. Additional, highly valued work was done by the co-authors of [134] in the area of measurement technology and De-Icing test bed operation.

The use of MCM for De-Icing or other multifunctional application scenarios depends directly on the thermal behaviour under operational conditions. Especially the temperature field acts significantly on the mechanical stiffness and thermal expansion, as demonstrated within micro scale investigations (see section 4). However, the prediction of the in-situ temperature field depends further on the environmental and system (boundary) conditions. Specifically, the heat transfer to the environment was identified to have a significant influence on the resulting temperature level within the material domain. Considering a model driven innovation towards e.g. De-Icing (as indicated by hypothesis H3), the heat transfer behaviour under related conditions needs to be characterised and covered accurately in a meso scale model (hypothesis H2). Once this behaviour is covered, the prediction of the system's electro-thermo-mechanical performance is enabled and measures for functional optimisation can be introduced. Besides this specific De-Icing application, the results of convective HTC will have an impact on model based innovation for structural energy storages and morphing materials as well, since their behaviour is as strong influenced as the behaviour of the MCM considered for De-Icing (see chapters 1 and 2). In addition, aircraft icing conditions are considered to be the most severe thermal load conditions for structural elements in a multifunctional use. Accordingly, the thermal characteristics and the coupled mechanical behaviour resulting from this investigation can be considered as upper boundaries also for other application scenarios.

In order to determine the heat transfer behaviour, an experimental investigation of a meso scale MCM specimen under aircraft icing conditions is introduced in this subsection. In addition, a numerical representation of the meso scale specimen is developed, underpinned by the micro scale thermal representation of the MCM (as presented in section

4). The combined experimental and numerical approach enables the identification of the model related convective HTC and the verification of the model's accuracy for the first time (supporting hypothesis H1 and H2 and enabling the proof of hypothesis H3). Since the main driver for technology maturation is a proper virtual representation of the application scenario, this investigation provides a signifcant contribution towards modelling accuracy and validation.

The most important aspect of the experimental approach is the ability to measure the temperature evolution with respect to Joule heating under aircraft icing conditions, as they are expected during aircraft operation. As already introduced in subsection 2.4.1, the relevant temperature range in which icing occurs, lies in the range of $\theta_a = [243,\ 273]$ K while the aircraft's outer skin is exposed to a steady air flow [135]. Besides the low temperature, a significant influence related to forced convection is expected with respect to the heat transfer behaviour. Accordingly, the magnitude of De-Icing energy needed can be directly related to the environmental conditions which in turn enables the system's optimisation towards realistic operational conditions.

The convective heat transfer behaviour is most commonly estimated based on standard parameter ranges from literature (e.g. [136]) or semi-empirical surrogate models of free and forced convection conditions which are always related to the specific air flow, material surface and environmental conditions of the single test case (see e.g. [86, 137]). However, the lack of suitable convective HTC characterisations for MCM was already highlighted in previous investigations [17, 87]. Hypothesis H2 states that the actual electro-thermo-mechanical behaviour of a MCM De-Icing application can be predicted by a numerical model. Accordingly, the expected environmental conditions are set up in a suitable De-Icing test bed which is available at the Institute of Mechanics and Adaptronics at the Technical University of Braunschweig. The measured heat transfer behaviour of a specimen can then be modelled and the model accuracy can be validated. The MCM specimen as well as the experimental setup within the De-Icing test bed are introduced hereinafter.

As a specimen for the convective HTC, a flat plate type specimen is considered that was frequently used for free and forced convective heat transfer characterisations before, as presented in literature [138–140]. In addition, this geometric configuration is similar to the state of the art MCM specimens under investigation (see e.g. [141]). The flat plate specimen is made from nine layers glass fibre fabric Interglas (nr. 92110) [81] and one top layer made from 4 IMS65 CF rovings, each providing 24000 fibres [41]. The remaining surface area is filled with further glass fibre fabric in order to establish an even surface. The number of glass fibre plies is chosen to establish a stiff plate with a minimum thickness of 2 mm. The whole laminate is produced in a hand laminating process with epoxy resin made from L20 resin and W300 hardener supplied by R&G Composite Technology [142]. After hand lamination, the specimen is cured in a sealed bag under vaccuum at room

temperature $\theta_a = 293$ K.

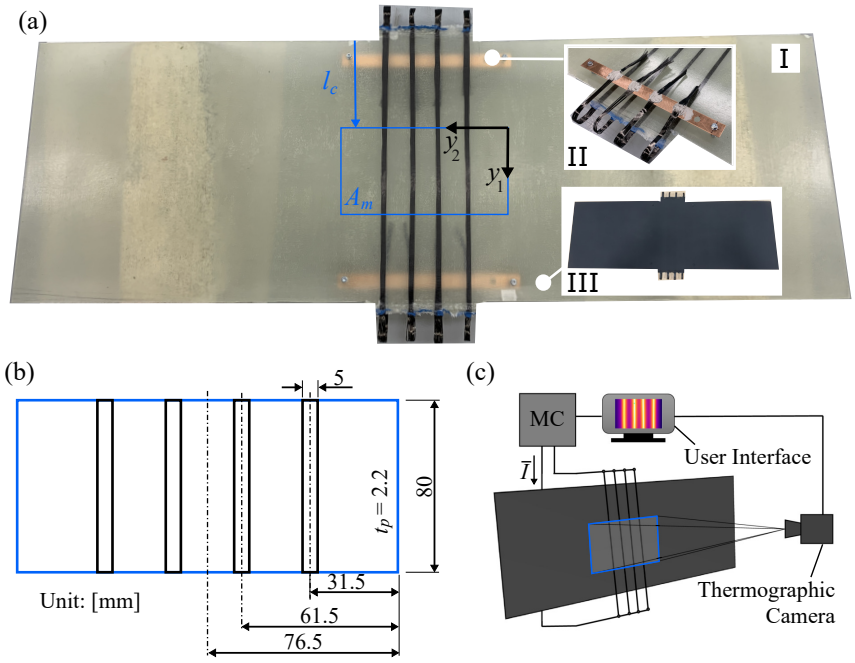

Figure 5.1: Flat plate specimen: (a) Production steps, (b) Dimensions of the measured surface Area, (c) Thermal measurement and control setup

The resulting 900 mm x 300 mm x 2.2 mm flat plate is shown in figure 5.1 (a) and the described result from the production process is marked by step I. The rovings are visible in the middle of the plate and are hanging over the longer edge. In step II, the roving ends are turned to the back side and are attached to a copper current collector bar. The copper bar is mounted on the back of the flat plate. The rovings are connected by conductive epoxy resin TDS CW2460 from Chemtronics [143]. In step III, the surface is coated by a matt black paint that assures a homogeneous emissivity of the surface (see figure 5.1 (a)). For the temperature measurement, a thermographic camera (Flir E60) is considered. Consequently, the correct indication of the surface temperature requires that the surface radiates homogeneously with known emissivity. The emissivity for this surface was characterised to hold $\varepsilon = 0.972 \pm 0.012$ [134]. This approach was proposed by Cardenas Garcia [144] and is assumed to have a minor influence on the heat transfer behaviour. The glass fibre, carbon fibre and matrix volume fractions are measured by a TGA post investigation and are given in table 5.1 to complete the specimen property description.

The single volume fractions are related to the volumetric domains of the carbon fibre rovings Ω_1 and Ω_2 (top layer) and to the glass fibre layers Ω_3 (compare figure 5.3). In the middle of the flat plate, a measurement surface area A_m is defined at a distance from the leading edge of $l_c = 110$ mm. The dimensions of this area, as well as the exact position of the carbon fibre rovings are indicated in figure 5.1 (b). This surface area is considered to

Table 5.1: Volume fractions of carbon fibre and glass fibre composite material domains, measured by TGA

Domain	Volume fraction	Symbol	Value	Reference volume
(1)	Carbon fibre	v_{cf}	0.58	$V_{\Omega_1} + V_{\Omega_2}$
	Epoxy Matrix	v_m	0.42	$V_{\Omega_1} + V_{\Omega_2}$
(2)	Glass fibre	v_{gf}	0.37	V_{Ω_3}
	Epoxy Matrix	v_m	0.63	V_{Ω_3}

be captured by the thermographic camera in order to provide a high resolution, transient record of the temperature rise and the stationary temperature field conditions (see figure 5.1 (c)). A micro controller (MC) based, tailored measurement and control system was developed for this test setup which is able to provide and control a constant average DC current $\overline{I}$ for Joule heating and is able to record the temperature data from the camera simultaneously. A detailed description of the system's setup and measurement verifiction can be found in [134].

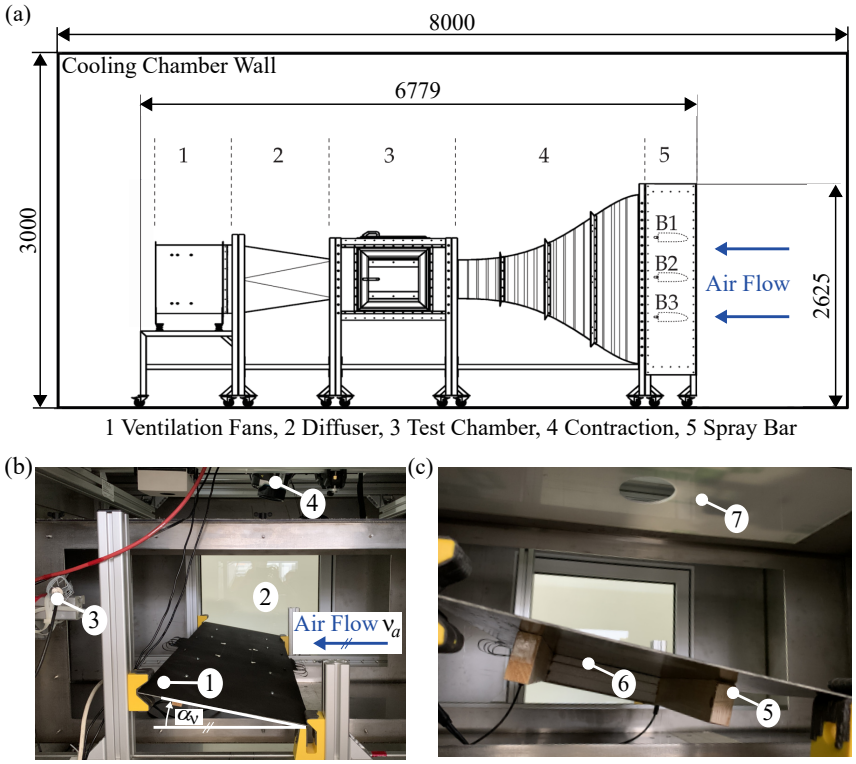

Figure 5.2: Test environment and setup: (a) De-Icing test bed (dimensions: [mm]), (b) Side-top view of flat plate test installation, (c) Detailed side-bottom view of flat plate; figures taken and adapted from [134]

The measurement and control system as well as the flat plate specimen are installed within the measurement volume of the De-Icing test bed. Figure 5.2 (a) shows the De-Icing

test bed which comprises an Eiffel type wind tunnel installed within a cooling chamber. The operational conditions of the De-Icing test bed are given in appendix A.5. Figures 5.2 (b) and (c) indicate the installed setup in which the flat plate specimen (1) is mounted with an angle of attack α_a with respect to the air stream direction. Furthermore, the flat plate is reinforced by two wood beams which are mounted before and behind the measured surface area A_m on the back side of the plate (5). It is assumed that this arrangement of the wood beams has no significant influence on the heat transfer at the measured surface area A_m on the top side. In addition, the surface on the back of the measured area is covered by a 40 mm thick polystyrene foam (6) to limit heat exchange. This is necessary to enable the assumption of an adiabatic condition on the backward boundary surface within the numeric model. The thermographic camera (4) is installed on top of the measurement volume (2) and is covered by a thin plate with a circular hole (7). The camera view angle on the surface is 90° in order to assure an undistorted measurement of the temperature θ_m. By the help of the thin plate, the air stream is not truncated and the hole enables a free view of the camera on the surface. An additional temperature sensor (3) measures the ambient temperature θ_a.

Table 5.2: Prescribed test conditions

Parameter	Intervall	Unit
Angle of attack α_a	$\{10, 30\}$	$^\circ$
Air velocity ν_a	$\{0, 15, 30\}$	$\frac{\mathrm{m}}{\mathrm{s}}$
Ambient temperature θ_a	$[258.15, 278.15]$	K
	increment: 5	K

For the investigation of the heat transfer behaviour of the MCM made flat plate specimen, different heat transfer conditions are set up to analyse the single influences on the convective HTC. Table 5.2 summarises the conditions of the angle of attack α_a, the air velocity ν_a which is horizontally aligned to the test bed and the ambient temperature range θ_a. The ambient temperature range corresponds to the typical aircraft icing conditions. A total of 25 environmental conditions are applied which cover free convection at $\nu_a = 0\ \frac{\mathrm{m}}{\mathrm{s}}$ as well as forced convection with respect to air speed and angle of attack. Once the ambient temperature is set, the power source is applied and controlled to provide a constant heating current of $\overline{I} = 2$ A. This current magnitude is used for all measurement conditions in order to indicate influences by the ambient conditions only. Accordingly, the supplied power is identical in all setups.

The next subsection provides the corresponding numerical model of the flat plate specimen and introduces the general assumptions for the computation of the convective HTC. Subsequently, the results of the experimental measurement and the numerical model are presented and discussed further.

5.1.2 Meso Scale Model of Heat Convection Setup

The numerical model of the flat plate is used to predict the measured temperature field and to identify the corresponding convective HTC h for all 25 environmental conditions (compare table 5.2). Thefore, the material volume comprising the measured surface area A_m and the material layers below is represented in a 3D geometry model (see figure 5.3 (a)). This meso scale representation applies homogenised material properties for the glass fibre composite and carbon fibre composite domains based on the homogenisation on the micro scale. To clearly indicate the domain definitions, figure 5.3 (b) shows a detail of the front surface, in which the single domains are distinguished. The passive (Ω_1) and active carbon fibre composite (Ω_2) are separated geometrically into two domains to provide the conducting part of the volume (carbon fibre volume fraction, active) and the not conducting part (matrix volume fraction, passive). This is necessary, since Joule heating depends on the absolute electrical resistance of the carbon fibre roving which in turn is volume dependent (compare equation 3.17 in subsection 3.1.3). Accordingly, the carbon fibre composite is separated into the two domains with respect to their fibre volume fraction as indicated in table 5.1. It should be noted that this separation within the model is needed to avoid a direct heat transfer from the heat source to the environment which would result in a zero heat flux within the material domain. This corresponds to the fact that the carbon fibres are not directly in contact with the environment since they are covered by the PE coating and are embedded in matrix material.

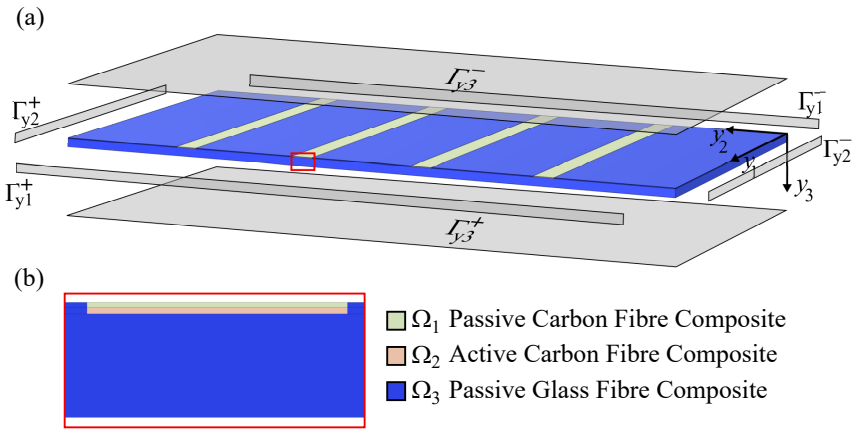

Figure 5.3: Geometry for virtual representation of measured flat plate volume and distinction of domains for the application of related material properties (compare table 5.3), figures taken and adapted from [134]

The carbon fibre composite domain is considered to be transversal isotropic with the transversal plane y_2, y_3. The glass fibre domain is considered to be transversal isotropic with the transversal plane y_1, y_2. The transversal isotropic plane of the glass fibre fabric is established by the glass fibre fabric which shows quasi isotropic properties in both directions. With respect to the ROM, this represents a parallel arrangement of the heat

conducting media in both directions. Accordingly, Voigt's solution (ROM ‖) is applied. Contrarily, the through thicknes direction is considered to be a series arrangement that leads to the application of Reuss' solution of the ROM (ROM ⊥). The applied effective material properties are indicated in table 5.3 with respect to the single domains and the homogenisation rule. The effective heat conductivity values are indicated with respect to the heat conductivity tensor elements (compare equation 3.47 in subsection 3.2.3). The electrical conductivity of the active carbon fibre composite domain equals the IMS65 specific electrical conductivity and is set to ∞ for the passive domains. The boundary

Table 5.3: Effective material properties applied in the flat plate model, domains are indicated in figure 5.3

Domain	Sym.	Value	Unit	Reference
Ω_1	$\overline{\Lambda}_1$	29.09	$\frac{\mathrm{W}}{\mathrm{mK}}$	ROM ‖
	$\overline{\Lambda}_2 = \overline{\Lambda}_3$	0.28	$\frac{\mathrm{W}}{\mathrm{mK}}$	ROM ⊥
	κ	$\rightarrow \infty$	Ωcm	**assumed
Ω_2	$\overline{\Lambda}_1$	29.09	$\frac{\mathrm{W}}{\mathrm{mK}}$	ROM ‖
	$\overline{\Lambda}_2 = \overline{\Lambda}_3$	0.28	$\frac{\mathrm{W}}{\mathrm{mK}}$	ROM ⊥
	κ	$1.45 \cdot 10^{-3}$	Ωcm	pure CF, Table 2.1
Ω_3	$\overline{\Lambda}_1 = \overline{\Lambda}_2$	0.11	$\frac{\mathrm{W}}{\mathrm{mK}}$	ROM ‖
	$\overline{\Lambda}_3$	0.11	$\frac{\mathrm{W}}{\mathrm{mK}}$	ROM ⊥
	κ	$\rightarrow \infty$	Ωcm	**assumed

**Assumed based on the fact that the electrical conductivity is much smaller compared to carbon fibre IMS65

conditions are chosen similar to modelling case C2 on the micro scale (see subsection 4.3.1). However, the periodicity conditions are not applied in y_2 directions on the meso scale but are replaced by temperature conditions:

$$\theta(\Gamma^+_{y2}) = \theta(\Gamma^-_{y2}) = \theta_a, \tag{5.1}$$

$$\theta(\Gamma^+_{y1}) = \theta(\Gamma^-_{y1}), \tag{5.2}$$

$$\mathbf{q}(\Gamma^+_{y3}) = 0 \ \frac{\mathrm{W}}{\mathrm{m}^2}. \tag{5.3}$$

The boundary temperatures $\theta(\Gamma^{+-}_{\mathrm{y2}})$ are set to ambient temperature, since this is indicated by recorded measurement data (see upcoming section 5.1.3 with results discussion). Furthermore, the boundary condition on the top surface is considered to be a combined

convective and radiative thermal heat transfer:

$$Q(\Gamma^{-}_{y3}) = Q_c + Q_r \quad \text{with} \tag{5.4}$$

$$Q_c = A_m(\Gamma^{-}_{y1}) \cdot h \cdot (\theta - \theta_a) \tag{5.5}$$

$$Q_r = s \cdot \varepsilon \cdot A_m(\Gamma^{-}_{y1}) \cdot (\theta^4 - \theta_a^4), \tag{5.6}$$

where ε is set to the indicated emissivity of the matt black surface of the flat plate (compare definition in equation 3.19 in subsection 3.1.3). The only unknown variable of these boundary conditions is the convective HTC h. The dual experimental and numerical approach of temperature measurements at the flat plate specimen and the temperature field prediction within the numerical model enables the back-calculation of the convective HTC.

Besides the thermal boundary conditions, the electrical boundary conditions are defined to enable the Joule heat source within the active carbon fibre composite domain Ω_2. The current density j is defined by the applied current within the experimental setup of $\overline{I} = 2$ A related to the corresponding cross section of four equivalent rovings. Therefore, a number of rovings $n_r = 4$ is applied in following equations. Each roving provides a total of $n_f = 24000$ fibres and each single fibre is assumed with a radius of $r_f = 2.5$ µm. Moreover, the surface inward normal $\mathbf{n}_{\mathrm{y1}}$ enables the definition of the inward pointing current density vector. Summarised, this holds:

$$Q_g = \kappa_f |\mathbf{j} \cdot \mathbf{j}| \qquad \text{with} \tag{5.7}$$

$$\mathbf{j}(\Gamma^{-}_{\mathrm{y1,j}}) = j \cdot \mathbf{n}_{\mathrm{y1}} \qquad \text{for } \Gamma^{-}_{\mathrm{y1,j}} \in \Omega_2 \text{ with} \tag{5.8}$$

$$j = \frac{\overline{I}}{n_r \cdot n_f \cdot \pi \cdot r_f^2} \qquad \text{and} \tag{5.9}$$

$$\phi(\Gamma^{+}_{\mathrm{y1},\phi}) = 0 \text{ V} \qquad \text{for } \Gamma^{+}_{\mathrm{y1},\phi} \in \Omega_2. \tag{5.10}$$

The FEM model is connected via Matlab Live Link with an iterative optimisation algorithm which compares the computed maximum temperature of the stationary field $\theta_{c,max} = max\left[\theta_c(y_1, y_2, y_3 = 0)\right]$ with the measured maximum stationary temperature $\theta_{m,max}$. The convective HTC h is optimised by an iterative computation until the accuracy of the numerical result achives an optimum. Therefore, a break up criterion is defined as $c = 0.5$ K for the maximum temperatures difference:

$$c_b \geq |\theta_{c,max} - \theta_{m,max}| \tag{5.11}$$

The identification of all convective HTC values for the 25 test cases is conducted and the results of either the experimental measurements, the numerical prediction as well as the

analysis of h change with environmental conditions is provided in the next subsection.

5.1.3 Discussion of Results and Model Validation

The discussion of measurement and modelling results is divided into three steps with the analysis of the

1. Measured temperature fields,
2. Numerically predicted temperature fields,
3. Influence of environmental conditions on the convective HTC.

The model validation is included in step 2, since the numerically predicted results are directly compared with the measured stationary temperature distributions from step 1 and conclusions are drawn towards the accuracy of the model. This directly contributes to the proof of hypothesis H2 which postulates an accurate representation of the thermal behaviour under De-Icing conditions by the help of the numerical model.

Analysis of measured temperature fields

As explained in subsection 5.1.1, the environmental conditions of all 25 test cases are set up within the De-Icing test bed. As soon as the heating current $\overline{I}$ is applied, the temperature starts to rise within the measured area A_m. The thermal behaviour and the corresponding convective HTC are analysed with respect to the stationary heat transfer case. Accordingly, a method is introduced to identify the *stationary temperature distribution* by means of a mathematical rule. Therefore, the maximum temperature within the measurement area A_m is identified for each time step and its rise over time is analysed. The stationary heat transfer case is related to a minimum change in maximum temperature. Consequently, the corresponding empirical variance (further denoted as variance) is computed as

$$\vartheta_{\mathrm{k}}(t_{\mathrm{i}}) = \frac{1}{\mathrm{n}-1}\sum_{\mathrm{i=k}}^{\mathrm{n}}(\theta_{m,max}(y_1, y_2, t_{\mathrm{i}}) - \overline{\theta}_{m,max})^2 \quad \text{with } \mathrm{n} = \mathrm{k} + 40, \tag{5.12}$$

where $\overline{\theta}_{m,max}$ denotes the average over the interval and n identifies the single time steps with respect to the time interval k that has a length of 40 steps. Accordingly, the complete measurement time span is divided in equal intervals with 40 time steps. The *stationary temperature distribution* is identified at that point in time t_s when the minimal variance is found. All stationary temperature fields are then related to the time point t_s.

Figure 5.4 (a) shows both, the maximum temperature versus time and the corresponding variance versus time. The red marker identifies the minimum in variance and the corresponding point in time t_s for measurement case K05. Furthermore, the environmental

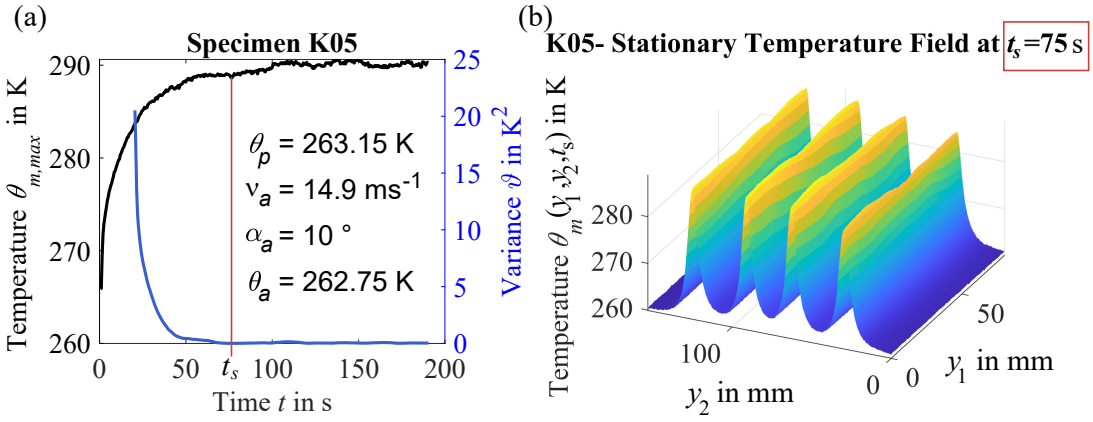

Figure 5.4: Measured transient heat up: (a) Maximum temperature over time and related variance, (b) Stationary temperature field at point in time t_s; figures taken and adapted from [134]

conditions angle of attack α_a, the prescribed temperature θ_p, the measured actual ambient temperature θ_a and the air speed ν_a are provided for each illustration. Figure 5.4 shows an example of the stationary temperature field on the measured surface area A_m at time point t_s. The following observations are made with respect to the temperature field:

1. The maximum temperatures are clearly located in the area of the heating CF rovings,
2. The maximum temperature varies along y_1 direction without a regular pattern,
3. The temperature drops in between the heating CF rovings significantly,
4. The temperature at $y_2 = 0$ mm and at $y_2 = 153$ mm drops nearly to ambient temperature.

The slight variation of the maximum temperatures along CF rovings in y_1 direction can be reduced to inaccuracies from production and material quality. It is mentioned that the specimen was made in a hand laminating process. Within this minor restriction, the maximum temperatures along the y_1 direction indicate that a homogeneous and constant heat transfer is present at the surface. This is important since a homogeneous air flow boundary is related to this heat transfer behaviour [140, 145]. Accordingly, a constant convective HTC can be expected for the measured area A_m. However, the quality of the temperature increase in the area of Joule heat sources is found to be very accurate to provide a significant temperature rise at the surface of the flat plate specimen. In a first attempt this is understood as a proof of concept for the De-Icing application scenario of MCM. The temperature drops in between are significant in a way that needs to be considered for material architecture optimisation. The drop is directly related to the low effective heat conductivity of the composite materials. This leads to an emphasis for convective heat transfer to the environment instead of a heat flux within the material

domain. Moreover, the optimisation of the CF roving distribution should be addressed with a minimum surface temperature condition. This is directly related to the expectation of a model based innovation potential towards the optimised application of MCM e.g. in the area of De-Icing (supporting hypothesis H3) which will be accounted for in section 5.2. The fact that the temperature at the outer boundaries drops towards ambient temperature is important for the corresponding boundary condition within the numerical model. This was already recognised by the BC definition in equation 5.1.

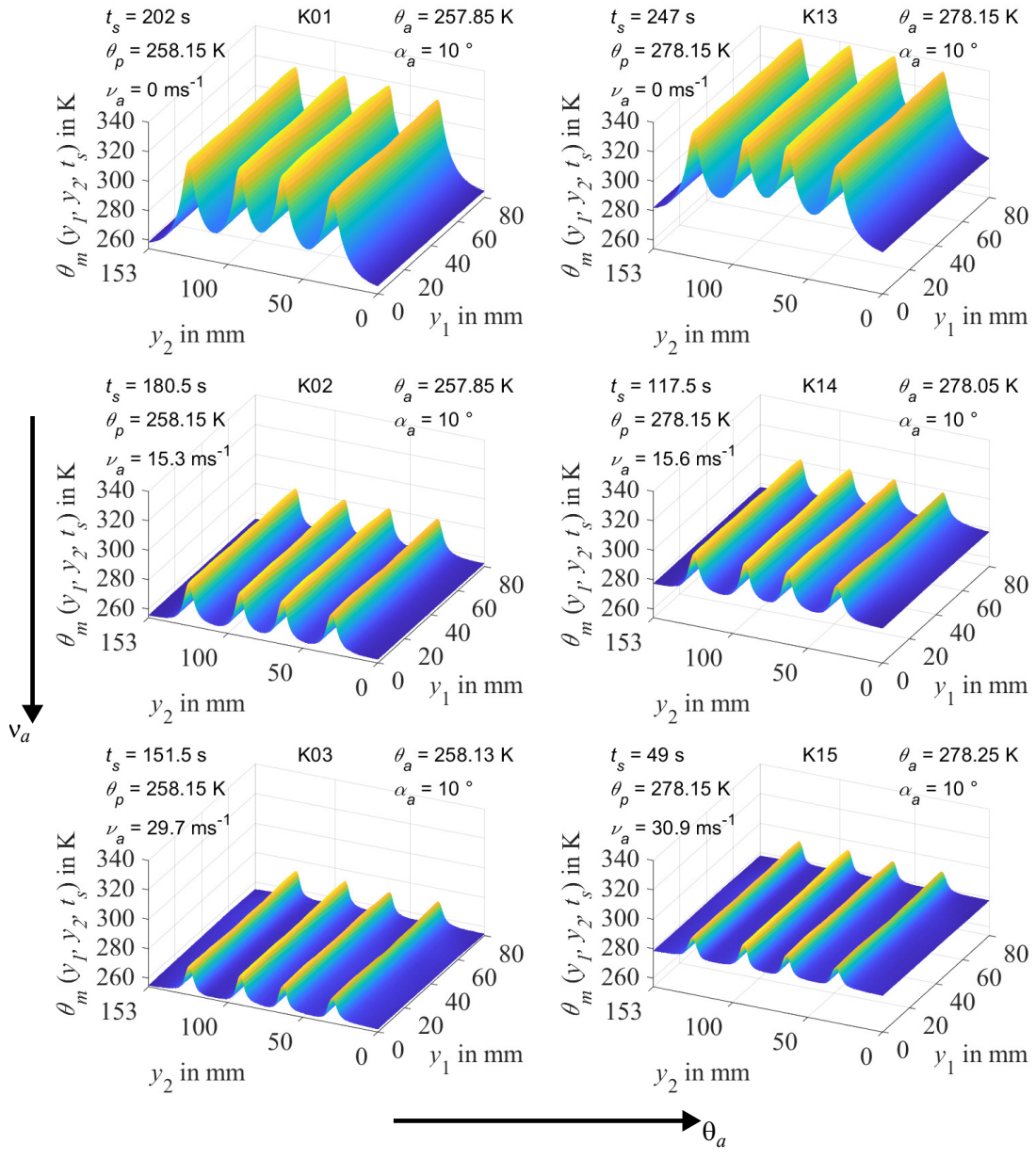

Figure 5.5: Stationary temperature fields for various ambient conditions (see individual label), figures taken and adapted from [134]

Besides the general characteristics of thermal heat transfer within the measured area, the influences by the different environmental conditions are analysed. Figure 5.5 provides

an overview of several stationary temperature distributions with indicated environmental conditions. The single plots are arranged with respect to an increasing air speed ν_a in vertical direction and with increasing ambient temperature θ_a in horizontal direction. All results are related to an angle of attack of $\alpha_a = 10°$. Within the comparison of the single stationary temperature fields $\theta_m(y_1, y_2, t_s)$ the following general observations are indicated:

1. All temperature fields show the general observations as stated with respect to test case K05,
2. The change in ambient temperature has a direct influence on the overall level of the temperature field but the temperature slope in the measured area A_m remains unchanged,
3. Conversely, the change from free to forced convection by increasing the air speed ν_a from 0 $\frac{\mathrm{m}}{\mathrm{s}}$ to 15 $\frac{\mathrm{m}}{\mathrm{s}}$ and 30 $\frac{\mathrm{m}}{\mathrm{s}}$ results in a significant decrease in maximum temperatures,
4. In addition, the temperature inbetween the heating CF rovings decreases down to ambient temperature θ_a for $\nu_a = 30$ $\frac{\mathrm{m}}{\mathrm{s}}$
5. The maximum temperature gradient $\frac{\partial \theta_m}{\partial y_2}$ increases with air speed ν_c,
6. The temperature variance in y_1 direction, which is related to manufacturing inaccuracies, becomes more pronounced with increased air speed ν_a.

The decrease in temperature for forced convection conditions was expected. However, the fact that the temperature in areas without active heating decreases significantly in forced convection conditions highlights that the internal heat transfer is minor compared to the convective heat transfer to the environment. This supports the aim for model based optimisation of the active CF roving distribution (approach for proof of hypothesis H3). Also the decrease of the maximum temperature for forced convection is important with respect to the energy consumption for the De-Icing function. Since most experimental and numerical investigations were considered under free convection conditions, the investigation here now quantifies the influence of forced convection on the resulting temperature field. This recognition again underpins the need for a model based optimisation with respect to energy consumption. Once the heat transfer behaviour is characterised, the system's energy input for Joule heating can be tailored with respect to the required De-Icing surface temperature. Another influence is the increased temperature gradient in y_2 direction for forced heat convection cases which is expected to affect the mechanical stress distribution within the material domain.

Besides air speed and ambient temperature, also the influence of the angle of attack α_a was analysed. Another overview with the related test cases is provided in appendix A.5 in figure A.9. The angle of attack shows a significant influence on the temperature

magnitudes. It is observed that the temperature level increases with increasing angle of attack which in turn leads to the conclusion that the forced convection is reduced. With respect to the possible application scenario of De-Icing for aircraft structures, this leads to the assumption that surface areas with high angle of attack need less energy for a proper temperature increase than those with small angle of attack. This general recognition should be emphasised in future research, e.g. under consideration of convective HTC distribution along an airfoil. This dependency could provide another requirement for the optimisation of the heating function of the MCM.

The numerical prediction of the flat plate's thermal characteristics is of high interest in this context. Once the experimentally identified behaviour can be represented by the model, the foundation for model based innovation is given (proofing hypothesis H2 and paving the way for the proof of hypothesis H3). Accordingly, the next analysis step concentrates on the predicted temperature fields and the model accuracy in comparison with the experimental results.

Numerically predicted temperature fields

The numerical model is used to represent the measured temperature field of the Joule heated flat plate. Therefore, the convective HTC h is optimised for all 25 test cases and the results are provided in a similar plot compared to the measured stationary temperature fields.

Figure 5.6 (a) shows the computed stationary temperature field $\theta_c(y_1, y_2, t_s)$ for test case K01 with indicated ambient conditions. The computationally predicted result appears appropriate in comparison with the measured temperature field in figure 5.5. The maximum temperature peaks are indicated with respect to the carbon fibre composite domains and also the characteristic temperature drop in between the rovings is given. In order to achive a more precise comparison, a 2D temperature plot at a fixed position y_1 shows the corresponding measured and computed temperature distribution along y_2. In figure 5.6 (a) on the right, this is provided for test case K01. Related to the direct comparison, the following observations are indicated:

1. The overal fit of the predicted temperature field is found to be accurate,
2. The maximum temperatures of the outer CF rovings is slightly overestimated,
3. The temperature decrease at $y_2 = 76.5$ mm is slightly underestimated,
4. The assumption of ambient temperature at the boundaries Γ_{y2}^{+-} lead to a reasonable temperature slope,
5. A general small geometric misalignment between the computational and the measured distribution is observed which is influenced by the actual, imperfect roving alignment within the specimen.

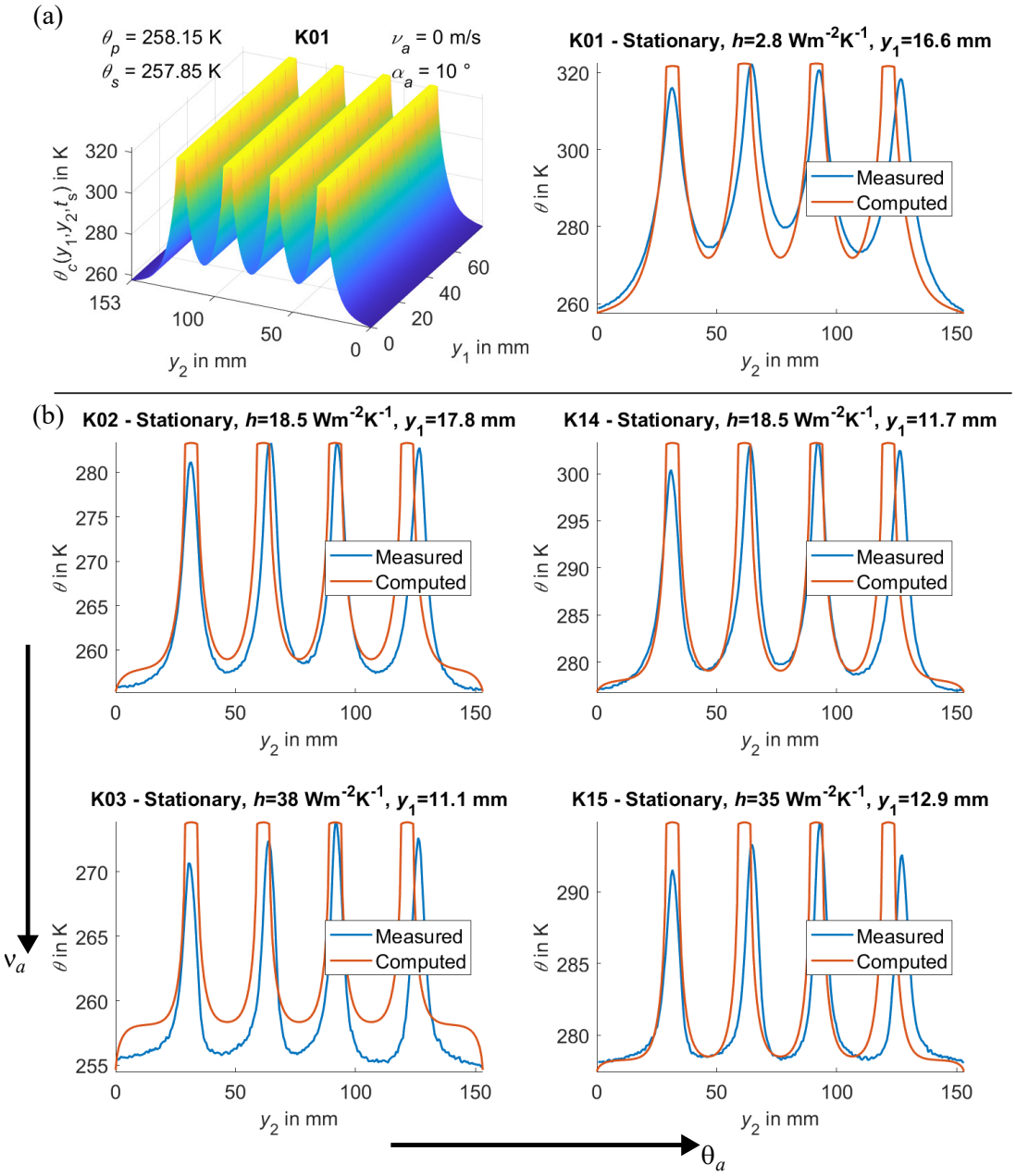

Figure 5.6: Overview of computed temperature distributions: (a) Exemplary 3D plot of temperature distribution and comparison with measured results for case K1, (b) Comparison of measured and computed stationary temperature distribution over y_2 with set y_1 position (as indicated); figures taken and adapted from [134]

The accuracy of the predicted temperature field is found to be high. This is an important indication in terms of model validation. The geometric misalignment between the experimentally measured and predicted temperature distribution is reduced to inaccuracies of the handmade specimen. The differences in the area of maximum and minimum temperatures are small compared to the absolute magnitude of the temperature range. Within the indicated range of accuracy, the model is in general assumed to predict a reliable temperature field. For test case K01, which represents a free convection case, the

convective HTC is found to hold $h = 2.8\ \frac{\mathrm{W}}{\mathrm{m^2K}}$. This magnitude is reliable with respect to typical free convection HTC numbers [136]. All in all, a proper representation of the heat transfer behaviour is indicated.

The comparison of experimental and numerical results is repeated for a choice of the remaining test cases in figure 5.4 (b). The general observations indicated for test case K01 can be transferred to all remaining cases. In addition, the model accuracy is increased for higher ambient temperature cases K13 and K15. However, the decrease of the temperature peaks at the outer CF rovings for forced convection conditions K03 and K15 can not be covered by the model. Since these temperature reductions are related to manufacturing inaccuracies, the ideal representation within the model can not cover this influence. Apart from these restrictions, the model shows a good accuracy for the different free and forced convection cases. In addition, the predicted forced convection HTCs lie in a typical range [137, 145] which is understood as a plausibility criterion. Further examples of test case comparisons are published in the related paper of the author of this thesis which support the observations and conclusions drawn in this section [134].

Summarising, the combined experimental and numerical approach enabled the validation of the model's accuracy and the computation of several convective HTCs for the different environmental conditions. In a third step, the quantitative analysis of the convective HTC related to the environmental conditions is conducted.

Influence of environmental conditions on convective HTC

The influences of the environmental conditions on the heat transfer behaviour were found to be significant with respect to the indicated temperature fields in the previous investigations. However, it was found that the convective HTC is very similar for the different ambient temperature cases. Since the change in convective HTC over temperature is minor, this influence is assumed to be negligible. All convective HTCs are recorded in tables A.6 and A.7 in appendix A.5. Consequently, the results of the convective HTC for different air velocities or angle of attacks are averaged over temperature to an effective convective HTC $\overline{h}$. In order to quantify the validity of this assumption, the scattering of the values around the average is indicated for all convective HTC values by the standard deviation. The single results for the convective HTC for all 25 test cases are provided in [134].

Figure 5.7 (a) presents $\overline{h}$ related to the single air speed configurations as a bar plot with an indication of the standard deviation by error bars. The standard deviation appears very small for all cases with respect to the overall magnitude. This supports the assumption that the convective HTC does not depend on the ambient temperature. However, the change from free to forced convection lead to an increase in $\overline{h}$ by the factor of 9 for an air speed of 15 $\frac{\mathrm{m}}{\mathrm{s}}$ and by a factor of 17 for an air speed of 30 $\frac{\mathrm{m}}{\mathrm{s}}$. This highly pronounced influence is important as a thermal requirement for the MCM. It is concluded that the

influence of forced heat convection needs to be considered for thermal modelling and optimisation of MCM.

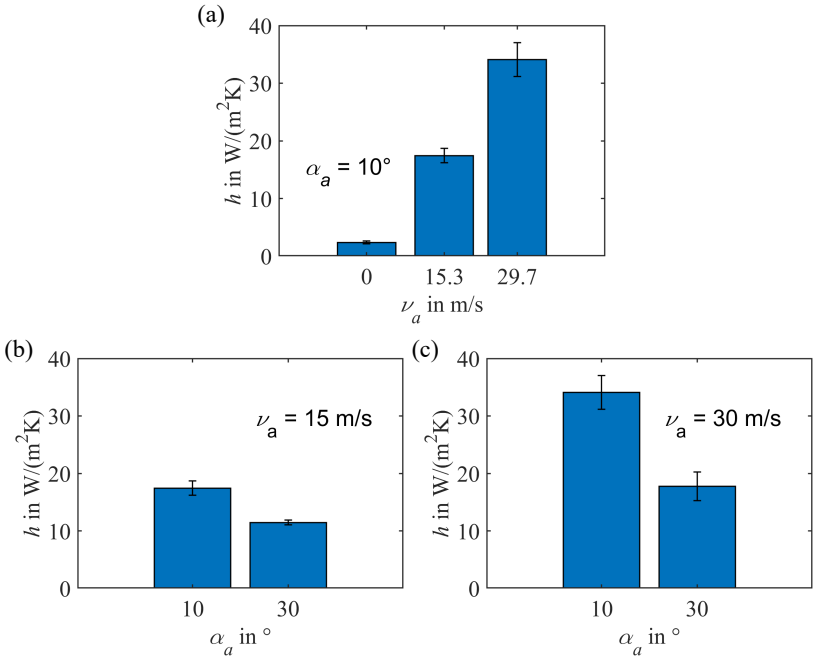

Figure 5.7: Overview of resulting heat convection coefficients: (a) For different air velocities, (b) For different angle of attacks at $\nu_a = 15\ \frac{\mathrm{m}}{\mathrm{s}}$ and (c) For different angle of attacks at $\nu_a = 30\ \frac{\mathrm{m}}{\mathrm{s}}$; figures taken and adapted from [134]

Furthermore, the influence of the angle of attack α_a is indicated by figures 5.7 (b) and (c). The standard deviation is found to be small also for these cases. However, an increase in standard deviation especially for $\alpha_a = 30°$ is expected to be induced by more increased air loads causing vibrations. This observation supports again the assumption of an invariance of the convective HTC with temperature, since the standard deviation seems to be more sensitive to the measurement chain. Apart from the standard deviation, the convective HTC is reduced by about 30 % and by about 50 % for the change from $\alpha_a = 10°$ to $\alpha_a = 30°$, respectively. This is indicated for both air speed configurations. Consequently, the conclusion drawn earlier that surface areas with a high angle of attack could need less thermal energy for the De-Icing function compared to surface areas with less angle of attack is reinforced. As already mentioned, this should be considered as an additional optimisation requirement for the MCM architecture in future research related to more complex structural geometries.

Summarised, a high influence of the air speed as well as of the angle of attack on the convective HTC h was identified. The model based prediction of the thermal field identified a high accuracy of the thermal model. This enables the general use of the model for a functional optimisation of the MCM design towards specific application scenarios like De-Icing and thus, model based innovation.

Besides the heat transfer behaviour analysis, the temperature drop within the material in y_3 direction was exemplary plotted in figure A.10, appendix A.5. The temperature drop on the meso scale was identified to hold $\Delta_{\theta c} = 1.5\ \frac{\mathrm{K}}{\mathrm{mm}}$. This is mentioned here as an additional validation of the micro scale model which predicted the temperature drop to hold a similar magnitude (see subsection 4.3.4). In addition, this supports the conclusion that the thin polymer coating considered in subsection 4.3.4 has only a minor influence on the effective heat transfer behaviour in the transversal isotropic plane. Accordingly, the applied effective heat conductivites are suitable to provide the material behaviour on the meso scale accurately.

The next section presents an engineering application of the electro-thermo-mechanically coupled multi scale model towards an ideal architecture for the De-Icing application. Couplings of the resulting thermal field on the mechanical behaviour are discussed and the system's performance is compared with standard De-Icing solutions from literature.

5.2 Model Based Innovation for De-Icing Systems

5.2.1 Measures for MCM Model Based De-Icing Optimisation

As already demonstrated for the characterisation of HTCs, a monofunctional laminate can be equipped with an actively heating MCM ply on the surface layer in order to enable a De-Icing function. However, the temperature distribution indicated by measurements in the De-Icing test bed (see subsection 5.1.3) highlighted that the active ply should be optimised for an ideal stationary surface temperature distribution. It is expected that the energy efficiency as well as the needed material mass can be minimised in order to provide a significant efficiency increase compared to industry De-Icing solutions (hypothesis H3). Furthermore, it is expected that the multiscale model developed in this thesis enables both a computational, geometrical and electrical performance optimisation (enabling the proof of hypothesis H3). In addition, the resulting laminate can be analysed towards electro-thermo-mechanical coupling effects.

In order to demonstrate an optimised, multifunctional De-Icing structure, a classical CFRP cross ply laminate was chosen as a reference structure. The laminate is equipped with an additional thin MCM ply on both surfaces for symmetry reasons. It is mentioned that this design is understood as an additional layer on top of an existing monofunctional structure, in order to demonstrate an efficiency increase compared to industry De-Icing solutions which are also installed on top of the primary structure (compare e.g. the electrical heater mats, described in subsection 2.4.3). A second option for an ideal use of the MCM in future designs is to consider the top layer as an integral part of the load bearing structure which even highlights the multifunctional use of the material.

Figure 5.8 (a) shows the chosen laminate configuration with $[0.0°, 90.0°, 0.0°]_s$ ar-

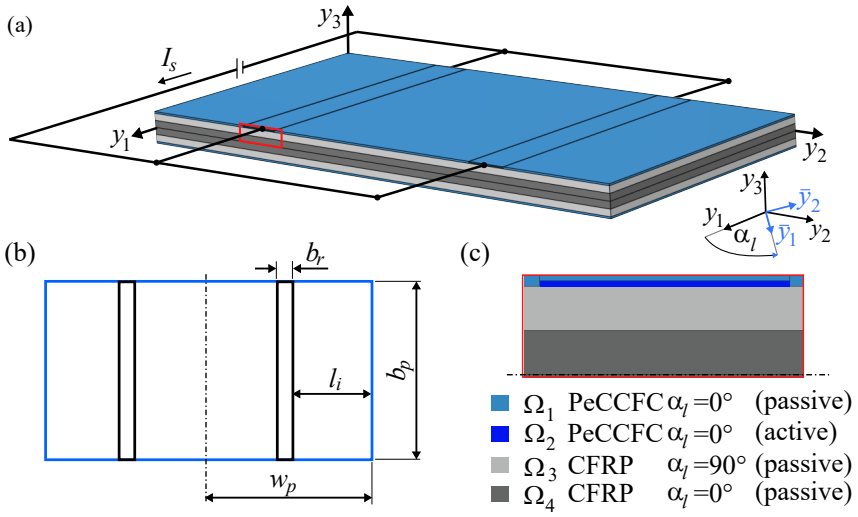

Figure 5.8: Overview of the multifunctional composite laminate, to be optimised for De-Icing: a) Laminate with indicated electrical circuit and transformed ply coordinate system with respect to α_l, b) Geometric definition and c) Material domains as defined in subsection 5.1.2, figure 5.3

chitecture (index s indicates symmetry to the middle plane y_1y_2 at $y_3 = 0$). The basic laminate is defined by unidirectional plies of which the 0° longitudinal direction is related to y_1. An additional ply coordinate system $[\overline{y}_1\ \overline{y}_2\ y_3]$ shows how the longitudinal direction in domain Ω_3 is defined, related to a ply orientation angle of $\alpha_l = 90°$ (see figure 5.8 (a) and (c)). The top (and bottom) layer is a PeCCF based MCM ply in which single sections of width b_r are chosen to represent the Joule heating domains. The general geometrical and modelling assumptions are applied similar to the definition in subsection 5.1.2. A complete overview of the volume fractions for all domains is given in table 5.4.

Table 5.4: Volume fractions of MCM composite ply and CFRP domains

Domain	Volume fraction	Symbol	Value	Reference volume
Ω_1, Ω_2	Carbon fibre IMS65	v_f	0.50	$V_{\Omega_1} + V_{\Omega_2}$
	Coating (see table 2.2)	v_c	0.22	$V_{\Omega_1} + V_{\Omega_2}$
	Epoxy Matrix	v_m	0.28	$V_{\Omega_1} + V_{\Omega_2}$
Ω_3, Ω_4	Carbon fibre IMS65	v_f	0.50	$V_{\Omega_3} + V_{\Omega_4}$
	Epoxy Matrix	v_m	0.50	$V_{\Omega_3} + V_{\Omega_4}$

In addition, table 5.5 provides the ply thicknesses t_{pl} in y_3 direction that are related to the single domains. For the MCM ply (Ω_1 and Ω_2), the PeCCF based composite material with epoxy resin matrix is chosen (as introduced in sections 4.2 and 4.3). The remaining domains are two phase compounds of IMS65 carbon fibres and epoxy resin matrix (material properties indicated in section 2.3).

Table 5.5: Single ply thickness t_{pl} related to material domains

Domain	Ω_1+Ω_2	Ω_3	Ω_4
t_{pl} in mm	0.22	0.88	0.88

The actively heating domain volume is considered to be a PeCCF roving with $n_f = 24000$ fibres. To distinguish the domains in which Joule heating is applied, the surface layer is divided into domains Ω_1 (passive - volume of matrix material) and Ω_2 (active - volume of carbon fibres) (see figure 5.8). The thickness of domain Ω_2 which is a fraction of the total thickness of the top ply (Ω_1 and Ω_2) is defined again by the fibre volume fraction of $v_{f,\Omega 2} = 0.5$ (compare subsection 5.1.2). This assures that the volume of Joule heating carbon fibres is identical with the volume of domain Ω_2 in which Joule heating is applied for the model. It should be noted that this separation is needed to avoid a direct heat transfer from the heat source to the environment, which would result in a zero heat flux within the material domain. For a future production of this laminate, domains Ω_1 and Ω_2 are not distinguished but are made from a PeCCF roving embedded within the epoxy matrix material. This corresponds also to the fact that the Joule heating carbon fibres are not in a direct contact to the environment, since they are fully covered by matrix material.

The MCM equipped flat plate laminate is subject to Joule heating by a prescribed current $\overline{I} = I_s$. Identical electro-thermal boundary conditions, as defined for experimental validation, are set (compare equations 5.1-5.10, subsection 5.1.2). Summarising, the developed electro-thermo-mechanical multi scale model, as defined in this thesis, is applied to this engineering example. Further definitions for the coupled model and the micro-meso scale interaction are provided in the following subsection.

In order to optimise the electro-thermo-mechanical performance of the MCM equipped flat plate, the following parameter are optimised (compare figure 5.8):

1. The prescribed current I_s,

2. The distance between active rovings l_i.

The applied Joule heating current I_s defines the maximum temperature θ_{max} on the laminates' surface and should be as small as possible to reduce energy losses by extensive heating. The distance between the rovings l_i defines the temperature drop, associated to the heat convection, radiation and the internal heat flux. Accordingly, the distance should be minimised to provide a minimum De-Icing temperature on the whole surface. Both parameter finally identify the temperature range on the surface area.

As a minimum temperature $\theta_{min} = 280$ K was chosen, for which De-Icing is assured. The maximum temperature on the surface is set to $\theta_{max} = 290$ K. Accordingly, a

maximum temperature drop of 10 K is allowed which again is beneficial for the mechanical performance of the laminate, since temperature changes are limited to this narrow range. Besides these optimisation criterions, a heat convection coefficient of $h = 38\ \frac{\mathrm{W}}{\mathrm{m^2K}}$ and an ambient temperature of $\theta_a = 258.15$ K are chosen as thermal boundary conditions. This configuration represents the most severe thermal load case that was applied to the flat plate specimen in the De-Icing test bed for $\nu_a = 30\ \frac{\mathrm{m}}{\mathrm{s}}$ and $\alpha_a = 10°$.

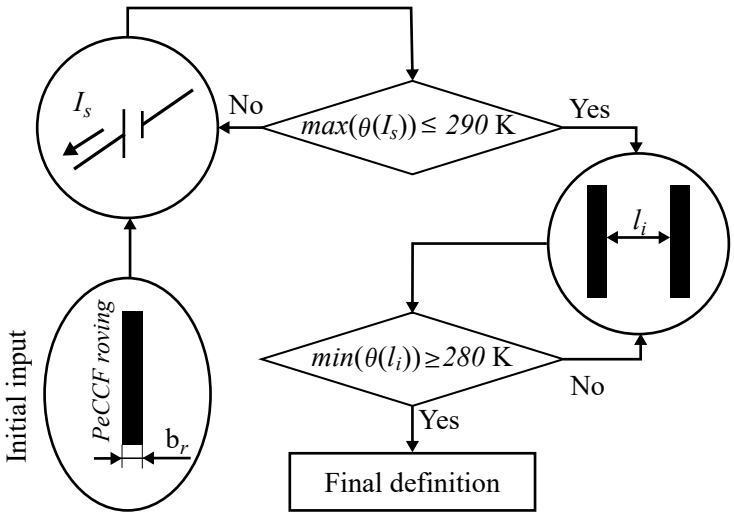

Figure 5.9: Overview of optimisation parameter and algorithm

Figure 5.9 illustrates the iterative process for the optimisation. Besides all static parameter of the model, a chosen width of the actively heating domains b_r is set before the optimisation is started. This parameter is motivated by the fact that carbon fibre rovings provide e.g. a standard number of fibres of $n_f = 24000$ which can have different roving widths (and corresponding thicknesses). Following observations from experimental testing, the most efficient use of Joule heat was found in the actively heated area. Accordingly, for this demonstrating optimisation a width of $b_r = 20$ mm was set which is motivated by actual industry spread tow rovings like TexTreme [146]. Starting the optimisation, the algorithm first optimises the prescribed current I_s to reach the desired maximum temperature and solves in a second iterative process for the minimum distance of l_i in order to assure the desired minimum temperature. For the model definition in each iteration, the edge length of the flat plate is defined to depend on b_r and l_i as:

$$w_p = 2 \cdot l_i + b_r \tag{5.13}$$

$$b_p = \frac{w_p}{2} \tag{5.14}$$

which enables a more efficient computation, since the volume is as small as possible.

The following subsection provides a detailed overview of the coupled electro-thermo-mechanical multi scale model and indicates which additional definitions and assumptions

are introduced compared to prior model parts described in earlier subsections. Finally, the results of the optimisation are discussed and conclusions are drawn towards energy efficiency and lightweight design benefits compared to industrial De-Icing solutions.

5.2.2 Electro-Thermo-Mechanical Multi-Scale Model of an MCM for De-Icing

The electro-thermo-mechanical multi scale model is enabled by a suitable micro scale homogenisation and by an iterative computation of scale related field variables. With respect to the optimisation process, the thermal field is solved for stationary heat transfer on the meso scale that was identified to be the governing thermal load case with maximum temperatures and temperature gradients. Accordingly, also the electrical and mechanical fields are solved for a stationary load case. To calculate all field variables on the meso scale in an efficient way, a micro scale homogenisation is used to estimate the effective material properties of the single domains.

For the representation of the MCM equipped flat plate laminate, the micro scale for domains Ω_1 and Ω_2 is modelled by a UC comprising the PeCCF embedded in an epoxy matrix (as analysed in subsection 4.2). All definitions like material properties, boundary conditions and homogenisation procedures are applied again. For the remaining domains of a two-phase CFRP, a second UC is defined which is similar to the PeCCF UC but without the PE coating phase. The effective stiffness tensor $\overline{\boldsymbol{C}}$, the effective thermal expansion tensor $\overline{\mathbf{A}}$ and the effective heat conductivity tensor $\overline{\mathbf{\Lambda}}$ are computed by the homogenisation methods described in subsections 4.2 and 4.3.1. The homogenisation strategy for the effective thermal heat conductivity is transferred from the RVE representation to the actual UC to simplify the computation. This is also motivated by the conclusion from subsection 4.3.4 that the actual, random distribution of the carbon fibres has no significant influence on heat transfer on the micro scale.

Figure 5.10 provides an overview of the two UCs for the micro scale model and the representation of the MCM equipped flat plate laminate on the meso scale. In order to introduce a coupling of the PE coating's modulus with temperature, a piecewise linear function is defined as

$$E_c = \begin{cases} -7.7\ \frac{\text{MPa}}{\text{K}} \cdot (\theta - \theta_0) + 820\ \text{MPa} & \text{for } \theta > 293.15\ \text{K} \\ 820\ \text{MPa} & \text{for } \theta \leq 293.15\ \text{K} \end{cases} \tag{5.15}$$

with $\theta_0 = 293.15$ K. Accordingly, the temperature induced stiffness change is approximated by a linear modulus function and is motivated from material properties indicated in table 2.2. This function represents the same stiffness drop which was assumed and discussed in subsection 4.2.

For the temperature coupling of the stiffness on the micro scale, which is given by the coating material's stiffness and by the thermal expansion, the actual temperature from the

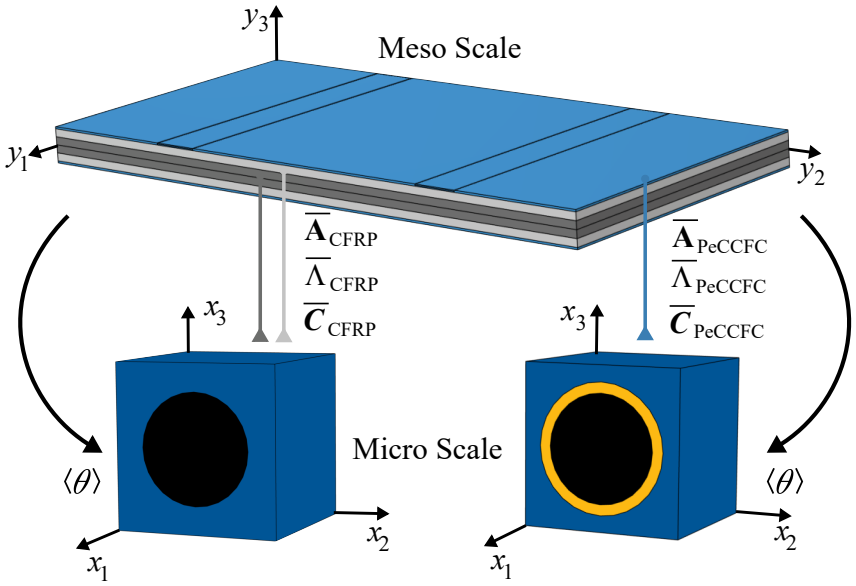

Figure 5.10: Overview of the multi scale model with indication of information transfer between scales

meso scale is needed. Therefore, the volume averaged temperature on the meso scale $\langle\theta\rangle$ (following equation 3.2.4) is computed and transferred to the micro scale (see figure 5.10). Then the effective stiffness tensor can be computed with respect to the actual temperature state on the meso scale.

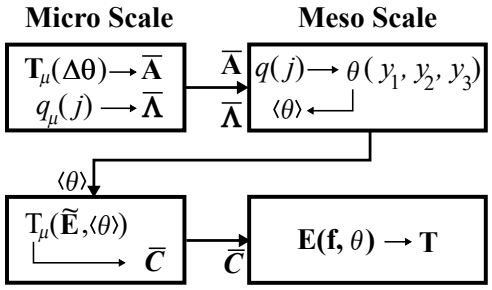

Figure 5.11: Overview of the computation order and the cross scale information transfer

Figure 5.11 shows the computational sequence with respect to the physical field variable which is solved and to the related scale level. First of all, the effective heat conductivity tensor $\overline{\Lambda}$ and the effective thermal expansion tensor $\overline{\mathbf{A}}$ are solved and transferred to the meso scale. This is possible, since these properties do not depend on the field variables on the meso scale. Then the computation of the meso scale stationary thermal field is enabled. The resulting volume averaged temperature $\langle\theta\rangle$ is transferred to the micro scale in order to solve for the temperature dependent stiffness tensor on the micro scale $\overline{\boldsymbol{C}}$. With this data, the meso scale model is enabled to solve for the mechanical field variables which could e.g. be the stress field $\mathbf{T}$.

The optimisation procedure prepared in subsection 5.2.1 is conducted based on this electro-thermo-mechanical multi scale model. The resulting optimised architecture of the

MCM equipped flat plate laminate is then analysed towards

1. The stationary temperature field on the meso scale for De-Icing,
2. The temperature induced effects on the stress field of the laminate in an exemplary mechanical load case,
3. The benchmark versus industrial De-Icing solutions in terms of lightweight design and energy efficiency.

The exemplary mechanical load case mentioned in (2) is defined as:

$$\mathbf{u}(y_1 = 0) = 0 \text{ mm} \tag{5.16}$$

$$\mathrm{u}_1(y_1 = b_p) = \frac{b_p}{1000} \tag{5.17}$$

which corresponds to a constant strain of 0.1 % in y_1 direction (compare figure 5.8). For this evaluation, the stress field is analysed for two cases of stationary temperature states:

1. Optimised temperature field with volume averaged temperature in the range of $\langle\theta\rangle = 286 \text{ K } \in [\theta_{min},\ \theta_{max}]$, corresponding to a set current of $I_s = 0.2$ A and
2. an temperature field of $\langle\theta\rangle = 368$ K, corresponding to a set current of $I_s = 0.4$ A.

These cases indicate a typical temperature range, associated with aircraft operation conditions (compare subsections 2.4 and 4.1). Besides the analysis of the temperature and stress field, the optimised MCM based De-Icing function is expected to provide a weight saving and an energy efficiency increase compared to industrial solutions. The results are presented in the following subsection and the expected benefits of an application of the new MCM for De-Icing are discussed.

5.2.3 Optimisation Results and Benchmark

The results from the optimisation procedure of the electro-thermo-mechanical multi scale model are presented in four steps: First, the temperature dependent effective stiffness tensor, obtained from the PeCCF UC homogenisation, is presented under consideration of the temperature dependent PE coating's modulus. Second, the optimised geometry and the resulting stationary temperature field are presented and discussed. Third, the corresponding mechanical behaviour is discussed based on an exemplary stress distribution. In a last step, the performance measures of the industrial De-Icing system *electrical heater mats* (as presented in subsection 2.4.4) are compared with the actual performance measures of the optimised MCM equipped flat plate laminate.

Temperature Dependent Effective Stiffness

Figure 5.12 indicates chosen effective stiffness tensor elements of the PeCCF composite material that are computed by homogenisation from the PeCCF based UC. All numbers are normalised by their corresponding matrix stiffness value (Young's modulus E_m and shear modulus G_m respectively) and distributed over the fibre volume fraction. Three different prescribed temperature cases are presented. First of all, it is found that the longitudinal stiffness $\overline{C}_{11}$ remains unaffected by the temperature dependent coating stiffness. All other elements show significant influences. The general trend is that the effective stiffness decreases with temperature rise. Since the defined stiffness function for the PE coating modulus $E_c(\theta)$ approximates the stiffness interval chosen for the mechanical micro scale analysis (subsection 4.2), the magnitudes and slopes of all curves are similar to the uncoupled results (compare figures 4.5 and A.4-A.6).

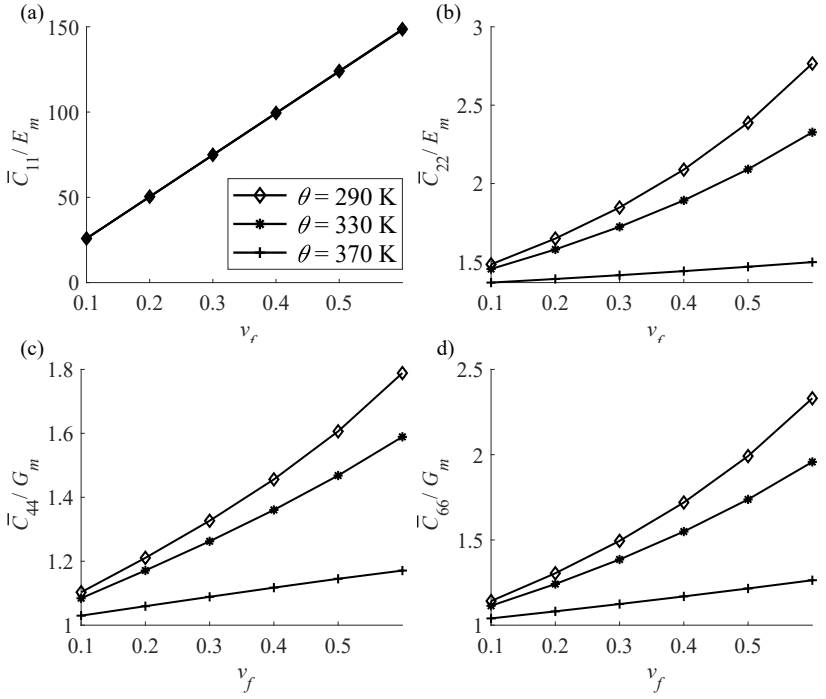

Figure 5.12: Overview of selected effective stiffness tensor elements, computed from the discrete PeCCF based micro scale UC homogenisation

With respect to the application scenario of De-Icing, the typical maximum operating temperature inside the material should not be much larger than $\theta = 290$ K. At this temperature level (or lower) the maximum effective stiffness is provided. If larger operating temperatures are expected, e.g. for a vehicle that operates in high temperature terrain, the stiffness reduction should be considered for the design of MCM laminates with respect to maximum compliance and failure.

Summarising, it is found that the introduction of the temperature dependent PE coating modulus as a function of temperature change resulted in plausible results for

the effective stiffness tensor elements of the PeCCF based MCM. This approach is also applied for the multi scale optimisation procedure as described in the previous subsection. Accordingly, the mechanical field will be computed under consideration of the temperature induced stiffness change of the MCM surface plies of the flat plate laminate.

Meso Scale Optimised Stationary Temperature Field

Based on the initial prediction of the effective heat conductivity on the micro scale, the meso scale stationary heat transfer problem can be solved. The optimisation procedure defined in subsection 5.2.1 is applied to the meso scale model and ideal settings for the prescribed current I_s and the distance between actively heating rovings l_i are computed. Figure 5.13 presents the resulting geometry and the 3D temperature field for the optimised

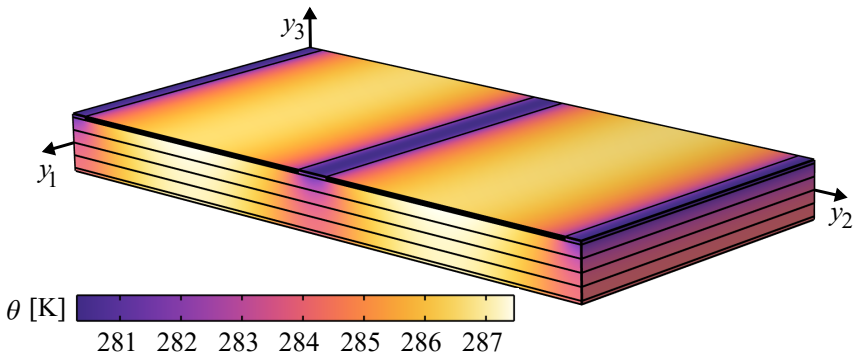

Figure 5.13: Overview of the 3D temperature distribution within the laminate after optimisation

parameter $I_s = 0.2$ A and $l_i = 2.5$ mm with respect to a heating roving width of $b_r = 20$ mm. The temperature range is within the limit of $\theta \in [\theta_{min}, \theta_{max}]$, as chosen. This is beneficial in terms of the De-Icing function which assures a complete heat up of the surface without any low temperature areas on which ice could remain. In addition the maximum temperature is only 10 K larger so that the effect on the mechanical field should be small. It is mentioned again that this result is obtained with respect to the lowest ambient temperature and the highest HTC considered in this thesis. Consequently, this result can be understood as the most severe thermal condition that is expected under the prescribed conditions.

To further indicate the temperature slope on the surface in this configuration, figure 5.14 provides the temperature field on the surface Γ^{+}_{y3}. It is again clearly indicated that the unheated surface area is exposed to the smallest temperatures. However, the temperature drop is much smaller compared to the De-Icing test bed examination, in which the flat plate specimen was unoptimised (compare subsection 5.1). The temperature on the surface is stable above 280 K that assures the De-Icing function on the complete surface. Besides this promising result, it is shown that not the complete surface needs to be heated although the

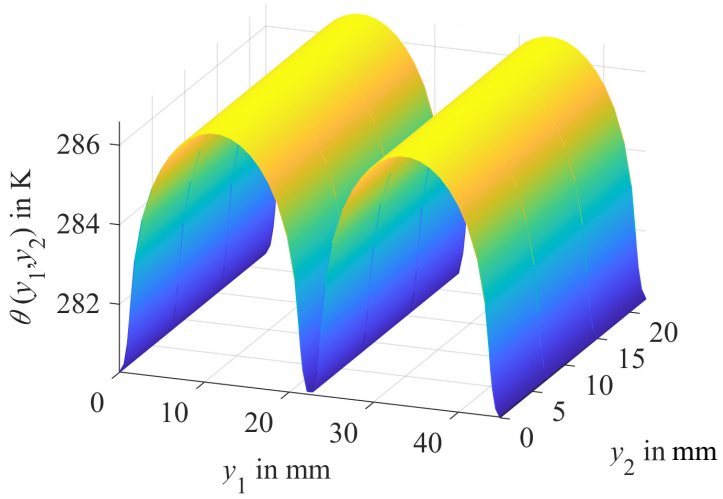

Figure 5.14: Overview of the 2D temperature distribution on the optimised laminate's surface

heat transfer within the material is small. In this context, the actively heating MCM can be understood as an electrical consumer. The less consumer volume is part of the electrical circuit, the less energy is needed to heat up the surface. In addition, the temperature gradient is found to be small compared to the unoptimised flat plate specimen. This is beneficial for homogeneous thermal stress distributions in the material domain.

Before the leightweight design and energy related performance of this optimised, MCM equipped flat plate laminate is discussed, the influence of the stationary temperature field on the mechanical behaviour is discussed in the next paragraph.

Thermo-Mechanical Effects on the Meso Scale

In order to indicate the effect of thermal expansion and temperature induced stiffness drop on the stress field, a static 0.1 % strain is applied in y_1 direction (as defined in subsection 5.2.2). Two cases of prescribed heating current I_s with associated volume averaged temperatures are evaluated: $I_s = 0.2$ A $\rightarrow \langle\theta\rangle = 286$ K and $I_s = 0.4$ A $\rightarrow \langle\theta\rangle = 368$ K. Figure 5.15 shows the resulting stress component T_1 (Voigt's notation) plotted over the laminate thickness. In addition, the temperature drop over thickness is indicated by the purple curve for the first case of $\langle\theta\rangle = 286$ K. The plot is associated with position $y_1 = w_p$ and $y_2 = b_p/2$, compare figure 5.8. In order to relate the curve sections with the single plies, the laminate is indicated on the left.

For the optimised De-Icing case under operational conditions, the stress distribution is typical for a cross ply laminate. The y_1 axis is within the symmetry plane of the laminate so that the stress distribution is symmetric to $y_1 = 0$. The core and surface plies (domains Ω_1, Ω_2 and Ω_4), of which the longitudinal direction $\overline{y}_1$ is parallel to the y_1 direction, show significant stresses for the given electro-thermo-mechanical load case. The stress in

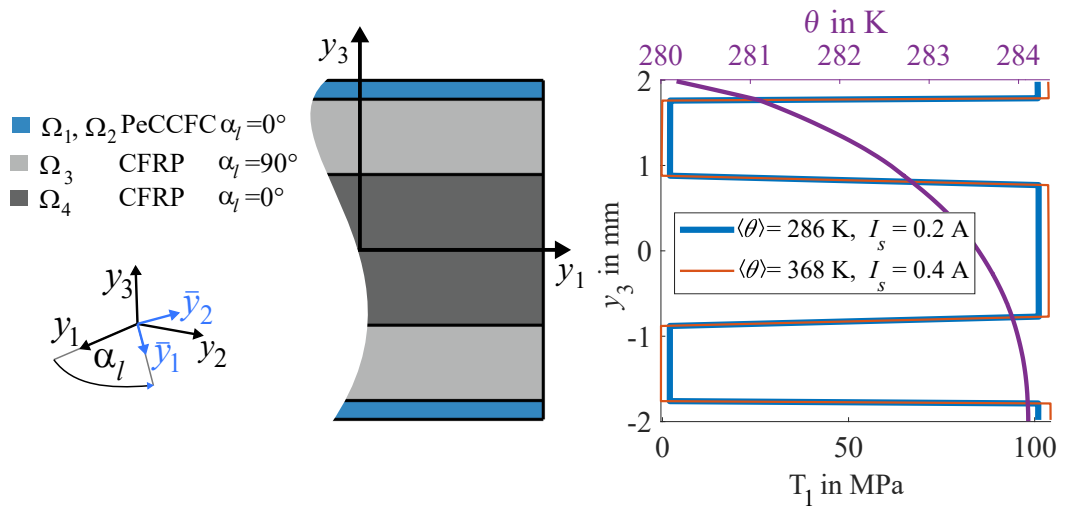

Figure 5.15: First principal stress and temperature over laminate thickness y_3 with respect to laminate architecture for $y_1 = w_p$ and $y_2 = b_p/2$

domain Ω_3 is much smaller which is related to the orientation angle of $\alpha_l = 90°$ (compare figure 5.15). Accordingly, the stiffness of domain Ω_3 in y_1 direction corresponds to the low transversal effective stiffnesses $\overline{E}_2 = \overline{E}_3$ of the CFRP. The influence of the temperature drop on the stress distribution over thickness is found to be minor with respect to the overall stress level.

When the temperature is increased to $\langle\theta\rangle = 368$ K, the principal stresses are increased in all plies of Ω_1, Ω_2 and Ω_4. Although the overall stress level is high, the effect of thermal expansion is significant if operating temperatures of up to $\theta = 370$ K are present. It should be noted that the effective TEC $\overline{\mathrm{A}}_1$ (corresponding to the y_1 direction) is negative in all plies of Ω_1, Ω_2 and Ω_4 for the chosen fibre volume fraction of $v_f = 0.5$. Consequently, this leads to a shrinkage of the volume, since the actual temperature is above the reference (thermal stress free) temperature of $\theta_0 = 293.15$ K. Therefore, the tensile stresses are increased. For the remaining ply of Ω_3 of which the longitudinal direction $\overline{y}_1$ is parallel to the y_2 direction by $\alpha_l = 90°$, the stress is decreased due to the temperature increase. This can be explained by the positive effective TEC $\overline{\mathrm{A}}_2 = \overline{\mathrm{A}}_3$ in the transversal-isotropic plane of domain Ω_3 that is related to the y_1y_3 plane. This results in a volume expansion in y_1 direction at the actual temperature. This leads to a decrease of the local stresses near to zero (compare figure 5.15).

Since a significant influence on the mechanical stresses is identified, the electro-thermo-mechanical coupling should be considered for structural design if high temperature applications are intended. It is mentioned that this example represents a simple mechanical load case in order to demonstrate the magnitude of the thermo-mechanical coupling effects. Other load cases like shear or bending loads could have additional coupling effects.

Apart from the analysis of the electro-thermo-mechanical coupling, the De-Icing optimised MCM equipped flat plate laminate is now evaluated in comparison to an industrial

De-Icing solution as a benchmark. In order to provide a reference to the model definition for all results in this thesis, a complete overview of the applied homogenisation methods with respect to the single physical fields and investigations in this thesis is provided by table A.8 in appendix A.6.

Performance of the MCM based De-Icing Function

Several reference De-Icing systems were examined by a systematic literature research and a subsequent approximation of specific system data was conducted. Thereby, a comparability between different system architectures and functionalities was achived (see subsection 2.4.4). Based on literature data and on first information about the PeCCF based MCM, the research hypothesis H3 was derived which states the expectation that a model based optimisation could lead to a new, competetitive De-Icing solution. The main drivers for innovation are the aim for leightweight design and the reduction of energy consumption for De-Icing.

One of the main drawbacks of traditional systems is the mass of the De-Icing system which adds substantial weight to the primary structure. This additional mass can be classified as *parasitic*, since for more than 50 % of a short distance flight and about 95 % of a long distance flight, the De-Icing functionality is not used (compare derivation in subsection 2.4.1). Accordingly, a significant mass reduction of the De-Icing system can contribute to a reduction of fuel burn in a commercial aircraft. The energy consumption is a second parameter which is expected to be decreased by the use of an optimised MCM.

The energy consumption of De-Icing systems is usually much higher than actually needed, since the safety factor for the applied heating power is high due to lack of information about heat transfer on the surface of iced structures. The approach presented in this thesis enables the optimisation of the energy consumption based on the thermal boundary conditions that the structure faces under operational conditions. Based on this information, the architecture and energy supply are optimised to reach the desired De-Icing temperature but to limit energy loss related to overheating. In addition, the MCM is able to provide a significant stiffness to the structure which can be used to decrease the amount of monofunctional CFRP material. However, the actual approach of a MCM equipped flat plate laminate is considered to have an extra layer of MCM on top of the standard CFRP cross ply laminate. This is done to indicate the performance for the MCM approach in comparison to traditional industry solutions that are usually installed on top of the load bearing primary structure.

One of these solutions is the *electrical heater mat* system that is chosen as a baseline, since it provides the best performance in the overall comparison of all industry solutions (see subsection 2.4.4). Table 5.6 presents the specific quantities of the optimised MCM based De-Icing system in a direct comparison with the baseline system. The results from

optimisation show that the performance is competitive with the industrial solution of electrical heater mats, although the MCM material was installed on top of the primary structure.

Table 5.6: Performance benchmark of MCM De-Icing system and electrical heater mats system

System	p in $\left[\frac{\mathrm{W}}{\mathrm{m}}\right]$	m_d in $\left[\frac{\mathrm{kg}}{\mathrm{m}}\right]$	Ref.
Heater Mats	[1] $[1.1,\ 5.0] \cdot 10^3$	0.71	Sec. 2.4
MCM installed	[2] $2.5 \cdot 10^1$	0.67	Sec. 5.2.3
MCM integrated	[2] $2.5 \cdot 10^1$	0.00	Sec. 5.2.3

(1) as estimated in subsection 2.4.3

(2) related to 1 m ice protected cord length

The energy consumption of the MCM De-Icing system is about two magnitudes smaller compared to the heater mats. In addition, the mass of the integrated MCM plies is lower compared to the mass added by the electrical heater mats. This means a power reduction of up to 97 % and a mass reduction of about 5 %. If the primary structure is originally designed by recognising the multifunctional capability of the MCM with respect to De-Icing and load bearing, no additional mass needs to be installed. For that case, the primary structure can directly be manufactured from the MCM and the structure is made from less monofunctional material. Then the mass reduction compared to the electrical heater mat system could be up to 100 %. With respect to these optimisation results, the expected optimisation capability and the aim for a model based innovation, as described by hypothesis H3, are demonstrated.

However, it should be noted that these performance measures are related to an ideal calculation based on the assumptions made for the presented electro-thermo-mechanical multi scale model and the resulting MCM structure optimisation. Additional influences for an application are expected due to power conducting installation material and generators to provide electrical energy. Research approaches have already been investigating such influences (see e.g. [147]). However, these influences were not considered for the scope of this thesis. The concept of a MCM application for De-Icing highlights important benefits and is a new example of a promising application scenario for MCMs. Future research and development work should consider this technology for further refinement and industrial adoption.

6 Summary

6.1 Conclusions

The conclusions that are derived from experimental and numerical investigations are summarised in the following table with respect to the hypotheses (as indicated in subsection 1.2) and the subsection, in which the foundation for the individual conclusions is provided. The conclusions are related to the coupled electro-thermo-mechanical multi scale model, the application scenarios with emphasis on De-Icing as well as the mechanical, thermal and electrical properties that are identified throughout all examinations.

Conclusions	Hypoth.	Section
Conclusions towards model accuracy		
The choice of micro (l = [1.0, 100.0] µm) and meso (l = [0.1, 100.0] mm) scale levels is appropriate for the multi scale model definition and application related simulation tasks.	H1	2.2, 4.2.2, 5.1.3
Linear thermo-elasticity is suitable for the prediction of the effective stiffness and thermal expansion tensors. UC based homogenisation is validated by a comparison to solutions from the ROM (Reuss, Voigt and refined approach).	H1	3, 4.1.2, 4.2.2
The choice of a UC or a RVE representation is found to be arbitrary, since small changes of heat transfer on the micro scale are negligible. Due to efficiency reasons, the use of the UC representation is suggested for future applications.	H1	3.1.1, 4.3.4
The influence of the PE coating on the mechanical and thermal behaviour of the MCM can be simulated, analysed and optimised by the indicated electro-thermo-mechanical multi scale model.	H1, H3	3.1, 4.2.2, 4.3.4, 5.1.3

The multi scale approach is needed due to the thermo-mechanical coupling on the micro scale which is induced by the PE coating. This leads to new strain and stress fields on the micro scale, depending on the meso scale mechanical and thermal load case. The homogenisation of the micro scale can be considered if the micro scale field must not be resolved.	H1, H2	4.2.2, 4.3.4, 5.1.3
The new Two-Level Lewis-Nielsen method enables a precise prediction of the effective thermal conductivity of the three-phase MCM. The more different the thermal conductivities of the single material phases are, the more increases the precision of the Two-Level Lewis-Nielsen approach compared to the TPLN method [112].	H1	3.3.2, 4.3.2, 4.3.4
The 2D representation of the micro scale model overestimates the temperature drop by $\Delta_{\theta,2D}(x_3) = 0.25\ \frac{\mathrm{K}}{\mathrm{mm}}$. With respect to the discrete solution of $\Delta_{\theta,3D}(x_3) = 1.00\ \frac{\mathrm{K}}{\mathrm{mm}}$, this inaccuracy is acceptable with respect to the significant decrease in computational cost of 99 %.	H1	4.3.4
The meso scale model underpinned by the micro scale homogenisation was found to be appropriate to cover the thermal behaviour under aircraft icing conditions. Safety factors should be considered to balance expected manufacturing inaccuracies when material architecture optimisation is conducted.	H1, H3	5.1.3
Conclusions towards applications of the MCM		
The PE coating is understood as functional interphase which enables the adaptive stiffness and influences the thermal expansion of the MCM significantly. The effective stiffness change of up to 48 % in the transversal plane should be considered for structural design in case of desired stiffness adoption (e.g. Morphing, Structural vibration control) or in case of a limitation need (e.g. De-Icing).	H3	4.2.2

A significant temperature increase on the surface of a flat plate specimen is demonstrated which enables the De-Icing function. The temperature field can be predicted by the developed multi scale model. By the help of this model, the mechanical and thermal performance can be optimised towards the multifunctional use as structural reinforcement and De-Icing system component.	H2, H3	5.1.2, 5.1.3, 5.2
The influence of the PE coating on the transient temperature rise is small. The newly proposed MCM can be applied for De-Icing of aircraft structures, since a fast and significant temperature increase at the surface can be established.	H2, H3	4.1.3, 4.3.4, 5.1.3
The condition of forced heat convection with respect to air speed ν_a and angle of attack α_a needs to be considered as important influence on the thermal field of the MCM. The fact that the energy dissipation increases by a factor of 17 for forced convection supports this conclusion. The predicted values of the convective HTC can be used for first functional optimisations of a flat plate like multifunctional structure.	H2, H3	5.1.3
The functional optimisation of the structural design must be informed by operational conditions like forced convective heat transfer and energy supply. For example establishing a homogeneous temperature field under forced convection conditions will improve both the thermal and mechanical performance. Internal temperature gradients and resulting temperature induced stresses are avoided then.	H2, H3	5.1.3, 5.2.3
The angle of attack α_a has a significant influence on the convective HTC. It is expected that airfoils can be optimised with respect to the needed energy supply under consideration of the surface's angle of attack.	H3	5.1.3
A significant increase in energy efficiency and a removal of additional mass from the De-Icing system was demonstrated by model based optimisation of the MCM towards operational conditions. It is expected that the new approach of MCM based De-Icing can provide a new, more efficient De-Icing solution for aircraft in the future.	H3	5.2.3

Conclusions towards mechanical properties of the MCM		
The stiff carbon fibre dominates the effective longitudinal stiffness C_{11} of the three phase MCM, irrespective of the coating material.	H2	2.3.1, 4.2.2
Depending on the load transfer path (e.g. shear loading of the coating phase), the effective Young's modulus of the PeCCF in longitudinal direction $\overline{E}_{PeCCF}$ is reduced by up to 14 % at room temperature $\theta = 293$ K (as measured by tensile tests and compared to standard IMS65 CF). Although the coating phase has a small volume fraction of $v_c = 16$ %, this influence is indicated.	H1, H2	4.1.2.
The choice of a fibre with a smaller transversal Young's modulus has a small influence on the effective transversal stiffness, since the weak coating phase dominates the effective transversal stiffness.	H2, H3	2.3.1, 4.2.2
The temperature induced drop of the PE coating's storage modulus E'_c of 94 % in a temperature range of $\theta = [293.0,\ 393.0]$ K results in an MCM effective transversal and shear stiffness drop Δ_C of 8 % for a fibre volume fraction of $v_f = 0.1$ and of 48 % for $v_f = 0.7$.	H2, H3	2.3.1, 4.2.2
The influence of the coating's thermal expansion coefficient (TEC) α_c on the effective transversal thermal expansion $\overline{\mathrm{A}}_{22}$, $\overline{\mathrm{A}}_{33}$ is significant. The effect can be reduced by minimising the coating's TEC in transversal direction. Due to this significant influence, the magnitude of thermal expansion of the coating material should be characterised physically for MCM applications with thermal heat exposure.	H2, H3	2.3.1, 2.3.2, 4.2.2
The influence of the coating's TEC on the effective thermal expansion in longitudinal direction $\overline{\mathrm{A}}_{11}$ is small. The fibre volume fraction can be tailored so that the effective TEC in longitudinal direction is minimised. This is an important option to reduce the thermo-mechanical coupling effects.	H2, H3	2.3.1, 2.3.2, 4.2.2

The static mechanical design can be related to the stationary heat transfer case, of which the largest temperature drop and the corresponding highest temperature level are found. However, in applications with a highly time dependent temperature field, the transient case could be relevant for durability and fatigue investigations.	H2, H3	4.3.4
Conclusions towards thermal properties of the MCM		
The choice of the carbon fibre's transversal thermal conductivity $\lambda_{\perp,f}$ has a small influence on the effective transversal thermal conductivity $\overline{\Lambda}_{22}$, $\overline{\Lambda}_{33}$, since the matrix material dominates the heat transfer in the transversal plane.	H2, H3	2.3.1, 2.3.2, 4.3.4
The thermal conductivity of the PE coating λ_c has a measurable influence on the heat transfer behaviour of the composite. However, combined with a typical polymeric matrix material in a MCM, the influence is negligible.	H2, H3	2.3.2, 4.3.4
The PeCCF based MCM provides a small effective heat conductivity which results in an effective temperature drop of up to 1 $\frac{\mathrm{K}}{\mathrm{mm}}$ in case of Joule heating via the carbon fibres and heat convection to the environment. This influence should be considered for modelling and optimisation of the MCM.	H2, H3	4.3.4
The increase of the MCM temperature gradient near to a surface with heat convection demonstrates that the heat transfer behaviour is governed by heat dissipation to the environment (especially for forced heat convection) and that the internal heat flux is small. This needs to be considered for MCM design optimisation towards a desired heat flux and temperature field.	H3	4.3.2, 4.3.4, 5.1.3
A precise solution for the homogenisation of the MC's thermal properties can be obtained by the Three-Phase Lewis-Nielsen Method ([105]) or the newly developed Two-Level Lewis-Nielsen Method. The more different the heat conductivities of single material phases are, the more precise is the Two-Level Lewis-Nielsen method.	H1, H2, H3	4.3.4

The homogenisation of the density and the specific heat has only a marginal influence on the transient thermal field of the MCM. Accordingly, the effective material properties are applicable on the meso scale without significant influence.	H1	4.3.4
Conclusions towards electrical properties of the MCM		
The carbon fibre's resistor type is characterised to be *constant ohmic*. Correspondingly, the Joule heating behaviour can be represented by a 0-D thermal model with respect to the assumption that the whole electrical energy is transferred to thermal energy.	H1	4.1.3
A PeCCF roving can be understood as a parallel circuit of single fibres. The corresponding absolute resistance is only dependent on the geometric properties of the single fibre, the specific electrical resistance κ_f and the number of fibres n_f.	H1	4.1.3

The proof of the research hypotheses H1, H2 and H3 is provided by the listed conclusions. It should be noted that the identified results and conclusions are only valid with respect to assumptions made for the modelling theory (e.g. linear thermo-elasticity) and experimental investigations with corresponding restrictions to measurement quality. If possible, the results are reflected based on literature references and were found to be suitable.

All in all, the model based analyses in this thesis contributed significantly to the identification of the electro-thermo-mechanical material behaviour of PeCCF based composite materials for multifunctional applications. It is found for the first time that Joule heat is a relevant effect for a broad range of application scenarios. Especially the structural battery, the De-Icing application as well as further applications like stiffness adaption and morphing are possible functionalities based on thermal actuation or at least based on thermal coupling effects. The highly affected effective shear and transversal-isotropic stiffnesses of the PeCCF based composite material can have a significant influence on the mechanical performance of structures made from it. In addition, it is identified for the first time that the thermal field is highly sensitive to the meso scale material architecture. This sensitivity should be considered for structural design, once temperature coupled physical effects are present. Related to the Joule heating effect, the micro and meso scale distribution of current conducting carbon fibres can provide efficient heat sources in positions where the heat generation is either desired (e.g. in case of De-Icing) or in

areas where heat can be dissipated best (e.g. in case of structural batteries). Especially, the high influence of forced convection on the internal temperature field is indicated by experimental and numerical analysis.

Based on the developed electro-thermo-mechanical multi scale model of PeCCF based MCM, the coupled characteristics can be analysed. In addition, it is demonstrated for the first time that the structure's geometry can be optimised towards an ideal performance for De-Icing. Besides the general characteristics of the material behaviour under this electro-thermo-mechanical load case, a significant decrease of energy consumption by 5 % as well as a weight decrease on system level by up to 100 %, compared to the industry baseline, is predicted by model based simulation. This quantitative benchmark is understood as a proof of the MCM based De-Icing which was already covered by the related industry patent [4].

The next subsection provides approaches for future research that could help to refine the presented results and modelling approaches. In addition, the transfer of approaches and observations on further multifunctional application areas is suggested.

6.2 Future Research

The following table summarises approaches and pathways for future research based on results and conclusions in this thesis. These approaches are considered to contribute to the refinement of the electro-thermo-mechanical model developed in this thesis, to the transfer of conclusions towards related applications of MCMs as well as to industry adoption.

Options for pursuing work	Section
The influence of the PE coating's TEC is identified to be significant. However, this characteristic is not yet identified physically and was assumed in this thesis. Accordingly, it needs to be characterised physically for accurate predictions of the coupled material behaviour.	4.2.2
The coating's TEC can be considered as a design factor for the development of new polymer coating systems in order to achive an ideal effective thermal expansion coefficient of a MCM.	4.2.2
The change of effective stiffness with temperature can be applied for the softening of shape adaptive structures or for the stiffness adoption in the area of structural vibration. A new, sophisticated material architecture design could enable the use of the temperature sensitive stiffness modes of the MCM.	4.2.2
For the application of the MCM in the area of De-Icing, the adaptive control of the heating current should be considered in order to decrease the heat up time. A fast heat up is required in the area of aircraft surface De-Icing and can be established, once the thermal heat transfer behaviour of a structure was characterised virtually or physically. In future works, the characterisation and the resulting adoption of the heating current should be standardised.	4.3.4
The 2D representation of the micro scale thermal model can be considered for future transient, coupled multi scale modelling, since it reduces the computational cost for calculations on the micro scale by 99 %. This high efficiency increase enables a time discrete update of the micro scale thermal heat transfer problem in each transient meso scale time step.	4.3.4

A new experimental investigation of MCM based De-Icing should be considered based on a standard airfoil geometry. As identified by the flat plate specimen measurements, the influence of the angle of attack α_a on the convective heat transfer behaviour could be utilised to optimise the distribution of the actively heating carbon fibre domains. This can contribute to an additional efficiency increase compared to the optimisation of the flat plate case.	5.1.3, 5.2.3
For the thermo-elastic behaviour of the PEC, a visco-elastic material model could be considered. This will enable a time-dependent analysis of creep or relaxation effects in the interphase. It is expected that especially for high temperature applications, creep effects could be significant. In addition, the relaxation of the interphase could be important for the durability and fatigue prediction of the composite material.	3.1.1, 4.2.2
The process of a continous coating procedure for the production of PeCCF needs to be investigated further in future research. The application of the PeCCF based MCM is dependent of the availability of huge amounts of PeCCF at low cost. The model based study of coating process parameter and its experimental validation could be a promising approach.	2.3.2
The results concerning convective heat transfer under operational conditions should be considered in further multifunctional material applications, such as stiffness adaptive structures [10] and structural batteries [2]. It is expected that the actual thermal field has a significant influence on the functional performance of these multifunctional materials and needs to be considered for functional performance optimisation.	1.2, 5.1.3

The indicated pathways for future work should be understood as a summary of further connections of the thesis to the research field. The objectives of these approaches highlight the strong demand for interdisciplinary research in the area of MCMs which characterised all examinations throughout this thesis.

Bibliography

[1] Airbus, "Special edition a350 xwb: Airbus technical magazine," *Flight airworthiness support technology (FAST)*, vol. 2013, 06-2013.

[2] L. E. Asp, M. Johansson, G. Lindbergh, J. Xu, and D. Zenkert, "Structural battery composites: a review," *Functional Composites and Structures*, vol. 1, no. 4, p. 042001, 2019.

[3] L. E. Asp, "Big breakthrough for "massless" energy storage: Structural battery that performs 10x better than all previous versions," 2021. https://scitechdaily.com/big-breakthrough-for-massless-energy-storage-structural-battery-that-performs-10x-better-than-all-previous-versions/, last accessed 16-06-2022.

[4] M. O. H. Schutzeichel and P. Linde, "Heatable leading edge apparatus, leading edge heating system and aircraft comprising them," 2019. Patent, US2019/0382119A1.

[5] D. Carlstedt, *On the multifunctional performance of structural batteries*. Licentiate thesis, Chalmers University of Technology, Gothenburg, 2019.

[6] L. E. Asp and E. S. Greenhalgh, "Structural power composites," *Composites Science and Technology*, vol. 101, pp. 41–61, 2014.

[7] A. Bismarck, A. F. Lee, A. S. Saraç, E. Schulz, and K. Wilson, "Electrocoating of carbon fibres: A route for interface control in carbon fibre reinforced poly methyl-methacrylate?," *Composites Science and Technology*, vol. 65, no. 10, pp. 1564–1573, 2005.

[8] S. Leijonmarck, T. Carlson, G. Lindbergh, L. E. Asp, H. Maples, and A. Bismarck, "Solid polymer electrolyte-coated carbon fibres for structural and novel micro batteries," *Composites Science and Technology*, vol. 89, pp. 149–157, 2013.

[9] A. Bachinger, J. Rössler, and L. E. Asp, "Electrocoating of carbon fibres at ambient conditions," *Composites Part B: Engineering*, vol. 91, pp. 94–102, 2016.

[10] C. Tridech, H. A. Maples, P. Robinson, and A. Bismarck, "High performance composites with active stiffness control," *ACS applied materials & interfaces*, vol. 5, no. 18, pp. 9111–9119, 2013.

[11] M. Papadakis and S.-H. Wong, "Parametric investigation of a bleed air ice protection system," in *44th AIAA Aerospace Sciences Meeting and Exhibit*, (Reston, Virigina), American Institute of Aeronautics and Astronautics, 2006.

[12] A. D. Shah, "Integrated thermal anti-icing and environmental control system: United states patent," 23-12-1974. Patent, US3981466.

[13] M. Sinnet, "787 no-bleed systems: Saving fuel and enhancing operational efficiencies," 2007. `https://www.boeing.com/commercial/aeromagazine/articles/qtr_4_07/AERO_Q407_article2.pdf`, last accessed 15-06-2022.

[14] J. Sloan, "787 integrates new composite wing deicing system: The composite wing leading edge on boeing's dreamliner features an integrated heating element that incorporates a sprayed metal conductive layer within the laminate stack.," 2008. `https://www.compositesworld.com/articles/787-integrates-new-composite-wing-deicing-system`, last accessed 15-06-2022.

[15] J. Schmidt, "Multifunktionale faserverbundstrukturen am beispiel einer strukturintegrierten, elektrothermischen vorderkantenenteisung," 2012. Deutscher Luft- und Raumfahrtkongress 2012, `https://elib.dlr.de/81175/`, last accessed 22-11-2022.

[16] D. Carlstedt and L. E. Asp, "Thermal and diffusion induced stresses in a structural battery under galvanostatic cycling," *Composites Science and Technology*, vol. 179, pp. 69–78, 2019.

[17] D. Carlstedt, K. Runesson, F. Larsson, and L. E. Asp, "On the coupled thermo–electro–chemo–mechanical performance of structural batteries with emphasis on thermal effects," *European Journal of Mechanics - A/Solids*, vol. 94, p. 104586, 2022.

[18] M. H. Kjell, E. Jacques, D. Zenkert, M. Behm, and G. Lindbergh, "Pan-based carbon fiber negative electrodes for structural lithium-ion batteries," *Journal of The Electrochemical Society*, vol. 158, no. 12, p. A1455, 2011.

[19] C. Liang and C. A. Rogers, "Design of shape memory alloy springs with applications in vibration control," *Journal of Intelligent Material Systems and Structures*, vol. 8, no. 4, pp. 314–322, 1997.

[20] P. Ladpli, R. Nardari, F. Kopsaftopoulos, Y. Wang, and F.-K. Chang, "Design of multifunctional structural batteries with health monitoring capabilities," in *European Workshop on Structural Health Monitoring Series*, vol. 8.

[21] S. C. Roberts and G. S. Aglietti, "Satellite multi-functional power structure: Feasibility and mass savings," *Proceedings of the Institution of Mechanical Engineers, Part G: Journal of Aerospace Engineering*, vol. 222, no. 1, pp. 41–51, 2008.

[22] L. E. Asp, K. Bouton, D. Carlstedt, S. Duan, R. Harnden, W. Johannisson, M. Johansen, M. K. G. Johansson, G. Lindbergh, F. Liu, K. Peuvot, L. M. Schneider, J. Xu, and D. Zenkert, "A structural battery and its multifunctional performance," *Advanced Energy and Sustainability Research*, vol. 2, no. 3, p. 2000093, 2021.

[23] Z. L. Wang and Z. C. Kang, eds., *Functional and Smart Materials*. Boston, MA: Springer US, 1998.

[24] M. Rakotondrabe, ed., *Smart Materials-Based Actuators at the Micro/Nano-Scale*. New York, NY: Springer New York, 2013.

[25] Federal Aviation Administration, "Ac 20-107b - composite aircraft structure," August 24, 2010. `https://www.faa.gov/documentLibrary/media/Advisory_Circular/AC20-107B.pdf`, last accessed 19-08-2022.

[26] D. J. Johnson, "Structure-property relationships in carbon fibres," *Journal of Physics D: Applied Physics*, vol. 20, no. 3, pp. 286–291, 1987.

[27] T. Carlson, *Multifunctional Composite Materials: Design, Manufacture and Experimental Characterisation*. Phd thesis, Luleå University of Technology, Luleå, 2013.

[28] G. Fredi, S. Jeschke, A. Boulaoued, J. Wallenstein, M. Rashidi, F. Liu, R. Harnden, D. Zenkert, J. Hagberg, G. Lindbergh, P. Johansson, L. Stievano, and L. E. Asp, "Graphitic microstructure and performance of carbon fibre li-ion structural battery electrodes," *Multifunctional Materials*, vol. 1, no. 1, p. 015003, 2018.

[29] Y. Fang, K. Peuvot, A. Gratrex, E. V. Morozov, J. Hagberg, G. Lindbergh, and I. Furó, "Lithium insertion in hard carbon as observed by 7 li nmr and xrd. the local and mesoscopic order and their relevance for lithium storage and diffusion," *Journal of Materials Chemistry A*, vol. 10, no. 18, pp. 10069–10082, 2022.

[30] A. Bertram and R. Glüge, *Solid Mechanics*. Springer International Publishing, 2015.

[31] R. M. Jones and R. M. Jones, *Mechanics of composite materials*. Taylor & Francis, 2. ed., 1999.

[32] Z. Hashin, B. W. Rosen, E. A. Humphreys, C. Newton, and S. Chaterjee, *Fiber Composite Analysis and Design: Composite Materials and Laminates, Volume 1*. 1997.

[33] L. M. Manocha, "Carbon fibers," in *Encyclopedia of Materials: Science and Technology*, pp. 906–916, Elsevier, 2001.

[34] D. D. Edie, "The effect of processing on the structure and properties of carbon fibers," *Carbon*, vol. 36, no. 4, pp. 345–362, 1998.

[35] N. Athanasopoulos and V. Kostopoulos, "Resistive heating of multidirectional and unidirectional dry carbon fibre preforms," *Composites Science and Technology*, vol. 72, no. 11, pp. 1273–1282, 2012.

[36] M. Weber and M. R. Kamal, "Microstructure and volume resistivity of composites of isotactic polypropylene reinforced with electrically conductive fibers," *Polymer Composites*, vol. 18, no. 6, pp. 726–740, 1997.

[37] Y. Shen, Y. Lu, S. Liu, and X. Hao, "Temperature distribution analysis of carbon fiber reinforced polymer composites during self-resistance electric heating process," *Journal of Reinforced Plastics and Composites*, p. 073168442110734, 2022.

[38] M. O. H. Schutzeichel, T. Kletschkowski, P. Linde, and L. E. Asp, "Experimental characterization of multifunctional polymer electrolyte coated carbon fibres," *Functional Composites and Structures*, vol. 1, no. 2, p. 025001, 2019.

[39] M. H. Kjell, T. G. Zavalis, M. Behm, and G. Lindbergh, "Electrochemical characterization of lithium intercalation processes of pan-based carbon fibers in a microelectrode system," *Journal of The Electrochemical Society*, vol. 160, no. 9, pp. A1473–A1481, 2013.

[40] E. Jacques, *Lithium-intercalated Carbon Fibres: Towards the Realisation of Multifunctional Composite Energy Storage Materials*, vol. 2014:07 of *TRITA-AVE*. KTH Royal Institute of Technology, 2014.

[41] Teijin Carbon, "Tenax filament yarn - datasheet." `https://www.teijincarbon.com/fileadmin/PDF/Datenbl%C3%A4tter_dt/Product_Data_Sheet_TSG01de__EU_Filament___DE_.pdf`, last accessed 08-07-2022.

[42] Toray Composite Materials America, "T800h technical data sheet." `https://www.toraycma.com/wp-content/uploads/T800H-Technical-Data-Sheet-1.pdf.pdf`, last accessed 08-07-2022.

[43] Toray Composite Materials America, "M60j technical data sheet." `https://www.toraycma.com/wp-content/uploads/T800H-Technical-Data-Sheet-1.pdf.pdf`, last accessed 08-07-2022.

[44] S. Duan, F. Liu, T. Pettersson, C. Creighton, and L. E. Asp, "Determination of transverse and shear moduli of single carbon fibres," *Carbon*, vol. 158, pp. 772–782, 2020.

[45] J. Hagberg, S. Leijonmarck, and G. Lindbergh, "High precision coulometry of commercial pan-based carbon fibers as electrodes in structural batteries," *Journal of The Electrochemical Society*, vol. 163, no. 8, pp. A1790–A1797, 2016.

[46] A. E. Zantout and O. I. Zhupanska, "On the electrical resistance of carbon fiber polymer matrix composites," *Composites Part A: Applied Science and Manufacturing*, vol. 41, no. 11, pp. 1719–1727, 2010.

[47] Toray Composite Materials America, "T300 technical data sheet." `https://www.toraycma.com/wp-content/uploads/T300-Technical-Data-Sheet-1.pdf.pdf`, last accessed 18-08-2022.

[48] N. Angelidis, C. Y. Wei, and P. E. Irving, "The electrical resistance response of continuous carbon fibre composite laminates to mechanical strain," *Composites Part A: Applied Science and Manufacturing*, vol. 35, no. 10, pp. 1135–1147, 2004.

[49] L. E. Asp, A. Bismarck, G. Lindbergh, S. Leijonmarck, and M. H. Kjell, "Structural battery half cell, a structural battery and their manufacture," 2015. Patent, US 2015/0180028A1.

[50] S. Gabriel, R. Jérôme, and C. Jérôme, "Cathodic electrografting of acrylics: From fundamentals to functional coatings," *Progress in Polymer Science*, vol. 35, no. 1-2, pp. 113–140, 2010.

[51] J. R. MacCallum and D. H. MacKerron, "Electropolymerisation of methyl methacrylate on carbon fibre surfaces," *European Polymer Journal*, vol. 18, no. 8, pp. 717–724, 1982.

[52] G. E. F. Brewer, "Electrophoretic painting," *Journal of Applied Electrochemistry*, vol. 13, no. 3, pp. 269–275, 1983.

[53] M. Willgert, M. H. Kjell, and M. Johansson, "Effect of lithium salt content on the performance of thermoset lithium battery electrolytes," in *Polymers for Energy Storage and Delivery: Polyelectrolytes for Batteries and Fuel Cells* (K. A. Page, C. L. Soles, and J. Runt, eds.), vol. 1096 of *ACS Symposium Series*, pp. 55–65, Washington, DC: American Chemical Society, 2012.

[54] M. Willgert, M. H. Kjell, E. Jacques, M. Behm, G. Lindbergh, and M. Johansson, "Photoinduced free radical polymerization of thermoset lithium battery electrolytes," *European Polymer Journal*, vol. 47, no. 12, pp. 2372–2378, 2011.

[55] S. Alessi, E. Caponetti, O. Güven, M. Akbulut, G. Spadaro, and A. Spinella, "Study of the curing process of dgeba epoxy resin through structural investigation," *Macromolecular Chemistry and Physics*, vol. 216, no. 5, pp. 538–546, 2015.

[56] I. Oral, H. Guzel, and G. Ahmetli, "Determining the mechanical properties of epoxy resin (dgeba) composites by ultrasonic velocity measurement," *Journal of Applied Polymer Science*, vol. 127, no. 3, pp. 1667–1675, 2013.

[57] J. E. Mark, *Physical Properties of Polymers Handbook*. Springer New York, 2007.

[58] H. Maples, *Composites with Controllable Stiffness*. PhD thesis, Imperial College London, London, 2014.

[59] A. Bismarck, J. J. Blaker, D. B. Anthony, H. Qian, H. A. Maples, P. Robinson, M. S. Shaffer, and E. S. Greenhalgh, "Development of novel composites through fibre and interface/interphase modification," *IOP Conference Series: Materials Science and Engineering*, vol. 139, p. 012001, 2016.

[60] D. Carlstedt, E. Marklund, and L. E. Asp, "Effects of state of charge on elastic properties of 3d structural battery composites," *Composites Science and Technology*, vol. 169, pp. 26–33, 2019.

[61] D. Carlstedt, *Computational modelling of structural battery composites*. Phd thesis, Chalmers University of Technology, Gothenburg, 2022.

[62] Federal Aviation Administration, "Aviation maintenance technician handbook - chapter 15: Ice and rain protection." `https://skybrary.aero/sites/default/files/bookshelf/4452.pdf`, last accessed 13-07-2022.

[63] European Aviation Safety Agency, "Certification specifications for large aeroplanes (cs-25)." `https://www.easa.europa.eu/sites/default/files/dfu/CS-25_Amdt%203_19.09.07_Consolidated%20version.pdf`, last accessed 13-07-2022.

[64] W. R. Sand, W. A. Cooper, M. K. Politovich, and D. L. Veal, "Icing conditions encountered by a research aircraft," *Journal of Climate and Applied Meteorology*, vol. 23, no. 10, pp. 1427–1440, 1984.

[65] W. Lewis, "A flight investigation of the meteorological conditions conducive to the formation of ice on airplanes." `https://apps.dtic.mil/sti/pdfs/ADA800737.pdf`, last accessed 19-08-2022.

[66] Boeing, "Statistical summary of commercial jet airplane accidents."

[67] Airbus Industrie, "Getting to grips with cold weather operations - a flight operations view." `https://www.cockpitseeker.com/wp-content/uploads/goodies/ac/a320/pdf/data/ColdWeatherOps.pdf`, last accessed 13-07-2022.

[68] A. Heinrich, R. Ross, G. Zumwalt, J. Provorse, V. Padmanabhan, J. Thompson, and J. Riley, *Aircraft Icing Handbook - Volume 1 of 3*. 1991.

[69] A. Heinrich, R. Ross, G. Zumwalt, J. Provorse, V. Padmanabhan, J. Thompson, and J. Riley, *Aircraft Icing Handbook - Volume 2 of 3*. 1991.

[70] Airbus, "Ice and rain protection: Flight crew operating manual." `https://www.smartcockpit.com/docs/A320-Ice_and_Rain_Protection.pdf`, last accessed 13-07-2022.

[71] J. Shin, T. H. Bond, and G. A. Mesander, "Results of a low power ice protection system test and a new method of imaging data analysis: Nasa technical memorandum 105745."

[72] P. K. C. Rudolph and G. Dezso, "Anti-icing system for aircraft," 1992. Patent, US5114100.

[73] T. Strobl, *Modellbasierter Entwurf eines hybriden Systemansatzes zur Eisentfernung von den Oberflächen einer Flugzeugkonfiguration*. Phd thesis, Technical University Munich, Munich, 2016.

[74] A. C. Hoffmann, I. G. Hansen, R. F. Beach, R. M. Plencner, R. P. Dengler, K. S. Jefferies, and R. J. Frye, "Advanced secondary power system for transport aircraft." `https://ntrs.nasa.gov/api/citations/19850020632/downloads/19850020632.pdf`, last accessed 13-07-2022.

[75] C. Zilio and L. Patricelli, "Aircraft anti-ice system: Evaluation of system performance with a new time dependent mathematical model," *Applied Thermal Engineering*, vol. 63, no. 1, pp. 40–51, 2014.

[76] N. Alegre, *Full-Scale Runback Ice: Accretion and Aerodnymic Study*. Phd thesis, Cranfield University, Cranfield, 2008. `https://dspace.lib.cranfield.ac.uk/handle/1826/5547`, last accessed 13-07-2022.

[77] K. Al-Khalil, "Effect of mixed icing conditions on thermal ice protection systems: Faa specialists' workshop mixed phase and glaciated icing conditions." `https://www.coxandco.com/assets/files/FAA-D9688.pdf`, last accessed 13-07-2022.

[78] S. M. Lewis, P. English, and N. J. Winter, "Electrothermal heater mats," 2011. Patent, WO2011/092483.

[79] Boeing, "787, airplane characteristics for airport planning." cloudfront.net, last accessed 26-07-2022.

[80] ATSB, "Tyre failure and flap asymmetry event involving boeing 787, vh-vka." https://reports.aviation-safety.net/2017/20170513_B788_VH-VKA.pdf, last accessed 26-07-2022.

[81] Interglas, "Glass fibre fabric interglas 92110." http://www.ezentrumbilder.de/rg/pdf/td_de_style%2092110.pdf, last accessed 26-07-2022.

[82] Cox & Company, "Low power ice protection systems." https://www.coxandco.com/low_power_ips.htmlCox%20&%20Company, last accessed 26-07-2022.

[83] CAV Systems Ltd, "Tks ice protection." https://www.cav-systems.com/tks/, last accessed 26-07-2022.

[84] K. Al-Khalil, T. Ferguson, and D. Phillips, "A hybrid anti-icing ice protection system." https://citeseerx.ist.psu.edu/viewdoc/download?doi=10.1.1.472.5193&rep=rep1&type=pdf, last accessed 26-07-2022.

[85] K. Al-Khalil, "Thermo-mechanical expulsive deicing system - tmeds," in *45th AIAA Aerospace Sciences Meeting and Exhibit* (Aerospace Research Central, ed.), (Reston, Virigina), American Institute of Aeronautics and Astronautics, 2007.

[86] VDI e. V., *VDI Heat Atlas*. Springer Berlin Heidelberg, 2 ed., 2010.

[87] M. O. H. Schutzeichel, T. Kletschkowski, and H. P. Monner, "Microscale thermal modelling of multifunctional composite materials made from polymer electrolyte coated carbon fibres including homogenization and model reduction strategies," *Applied Mechanics*, vol. 2, no. 4, pp. 739–765, 2021.

[88] P. A. Tipler, G. Mosca, and J. Wagner, *Physik*. Springer Berlin Heidelberg, 2015.

[89] M. Kästner, *Skalenübergreifende Modellierung und Simulation des mechanischen Verhaltens von textilverstärktem Polypropylen unter Nutzung der XFEM*. Dissertation, Technische Universität Dresden, 2009.

[90] R. Hill, "Elastic properties of reinforced solids: Some theoretical principles," *Journal of the Mechanics and Physics of Solids*, vol. 11, no. 5, pp. 357–372, 1963.

[91] R. Hill, "On constitutive macro-variables for heterogeneous solids at finite strain," *Proceedings of the Royal Society of London. A. Mathematical and Physical Sciences*, vol. 326, no. 1565, pp. 131–147, 1972.

[92] C. Karch, "Micromechanical analysis of thermal expansion coefficients," *Modeling and Numerical Simulation of Material Science*, vol. 04, no. 03, pp. 104–118, 2014.

[93] N. Lombardo, "Effect of an inhomogeneous interphase on the thermal expansion coefficient of a particulate composite," *Composites Science and Technology*, vol. 65, no. 14, pp. 2118–2128, 2005.

[94] Z. H. Karadeniz and D. Kumlutas, "A numerical study on the coefficients of thermal expansion of fiber reinforced composite materials," *Composite Structures*, vol. 78, no. 1, pp. 1–10, 2007.

[95] H.-g. Kim and W. Ji, "Thermal conductivity of a thick 3d textile composite using an rve model with specialized thermal periodic boundary conditions," *Functional Composites and Structures*, vol. 3, no. 1, p. 015002, 2021.

[96] V. V. Vasiliev and E. V. Morozov, *Advanced Mechanics of Composite Materials and Structures: Third Edition*. Elsevier, 2018.

[97] K. Knothe and H. Wessels, *Finite Elemente*. Springer Berlin Heidelberg, 2017.

[98] O. C. Zienkiewicz, R. L. Taylor, and J. Z. Zhu, *The finite element method: Its basis and fundamentals*. Elsevier Science, 7th ed. ed., 2013.

[99] S. Ebnesajjad, *Handbook of Adhesives and Surface Preparation: Technology, Applications and Manufacturing*. Plastics Design Library, William Andrew, 2010.

[100] J. C. Halpin, "Stiffness and expansion estimates for oriented short fiber composites," *Journal of Composite Materials*, vol. 3, no. 4, pp. 732–734, 1969.

[101] L. E. Nielsen, "Generalized equation for the elastic moduli of composite materials," *Journal of Applied Physics*, vol. 41, no. 11, pp. 4626–4627, 1970.

[102] A. Einstein, "Über die von der molekularkinetischen theorie der wärme geforderte bewegung von in ruhenden flüssigkeiten suspendierten teilchen," *Annalen der Physik*, no. 17, pp. 549–560, 1905.

[103] J. M. Burgers, "On the motion of small particles of elongated form. suspended in a viscous liquid," in *Selected Papers of J. M. Burgers* (F. T. M. Nieuwstadt and J. A. Steketee, eds.), pp. 209–280, Dordrecht: Springer Netherlands, 1995.

[104] M. Loos, *Carbon nanotube reinforced composites: CNR polymer science and technology*. Plastics Design Library, Elsevier, first edition ed., 2015.

[105] R. Kochetov, A. V. Korobko, T. Andritsch, P. H. F. Morshuis, S. J. Picken, and J. J. Smit, "Three-phase lewis-nielsen model for the thermal conductivity of polymer nanocomposites," in *2011 Annual Report Conference on Electrical Insulation and Dielectric Phenomena*, pp. 338–341, IEEE, 2011.

[106] L. E. Asp, L. A. Berglund, and R. Talreja, "Effects of fiber and interphase on matrix-initiated transverse failure in polymer composites," *Composites Science and Technology*, vol. 56, no. 6, pp. 657–665, 1996.

[107] N. Pagano, "The significance of effective modulus theory (homogenization) in composite laminate mechanics," *Composites Science and Technology*, vol. 60, no. 12-13, pp. 2471–2488, 2000.

[108] F. Danzi, D. Fanteria, E. Panettieri, and M. Palermo, "A numerical micro-mechanical study of the influence of fiber–matrix interphase failure on carbon/epoxy material properties," *Composite Structures*, vol. 159, pp. 625–635, 2017.

[109] J. Karger-Kocsis, H. Mahmood, and A. Pegoretti, "All-carbon multi-scale and hierarchical fibers and related structural composites: A review," *Composites Science and Technology*, vol. 186, p. 107932, 2020.

[110] F. Thuselt, *Physik der Halbleiterbauelemente*. Springer Berlin Heidelberg, 2011.

[111] American Society for Testing and Materials, "Standard test methods for properties of continuous filament carbon and graphite fiber tows," *ASTM D4018-11*, 2017.

[112] M. O. H. Schutzeichel, T. Kletschkowski, and H. P. Monner, "Effective stiffness and thermal expansion of three-phase multifunctional polymer electrolyte coated carbon fibre composite materials," *Functional Composites and Structures*, vol. 3, no. 1, p. 015009, 2021.

[113] H. S. Choi and Y. H. Jang, "Micro-mechanical behavior of a unidirectional composite subjected to transverse shear loading," *Applied Composite Materials*, vol. 18, no. 2, pp. 127–148, 2011.

[114] H. W. Wang, H. W. Zhou, R. D. Peng, and L. Mishnaevsky, "Nanoreinforced polymer composites: 3d fem modeling with effective interface concept," *Composites Science and Technology*, vol. 71, no. 7, pp. 980–988, 2011.

[115] Y. Cheng, H. Cheng, K. Zhang, K. K. Jones, J. Gao, J. Hu, H. Li, and W. K. Liu, "A sequential homogenization of multi-coated micromechanical model for functionally graded interphase composites," *Computational Mechanics*, vol. 64, no. 5, pp. 1321–1337, 2019.

[116] P. C. Varelidis, R. L. McCullough, and C. D. Papaspyrides, "The effect on the mechanical properties of carbon/epoxy composites of polyamide coatings on the fibers," *Composites Science and Technology*, vol. 59, no. 12, pp. 1813–1823, 1999.

[117] K. Wang, Y. Lu, Y. Rao, N. Wei, J. Ban, Y. Peng, S. Yao, and S. Ahzi, "New insights into the synergistic influence of voids and interphase characteristics on effective properties of unidirectional composites," *Composite Structures*, vol. 255, p. 112862, 2021.

[118] C. L. Tucker III and E. Liang, "Stiffness predictions for unidirectional short-fiber composites: Review and evaluation," *Composites Science and Technology*, vol. 59, no. 5, pp. 655–671, 1999.

[119] P. Pitchai, H. Berger, and P. J. Guruprasad, "Investigating the influence of interface in a three phase composite using variational asymptotic method based homogenization technique," *Composite Structures*, vol. 233, p. 111562, 2020.

[120] B. Raju, S. R. Hiremath, and D. Roy Mahapatra, "A review of micromechanics based models for effective elastic properties of reinforced polymer matrix composites," *Composite Structures*, vol. 204, pp. 607–619, 2018.

[121] S. C. Cowin and M. M. Mehrabadi, "Anisotropic symmetries of linear elasticity," *Applied Mechanics Reviews*, vol. 48, no. 5, pp. 247–285, 1995.

[122] S. Li, "On the unit cell for micromechanical analysis of fibre-reinforced composites," *Proceedings of the Royal Society of London. A. Mathematical and Physical Sciences*, vol. 455, no. 1983, pp. 815–838, 1999.

[123] J. Hughes, "The carbon fibre/epoxy interface—a review," *Composites Science and Technology*, vol. 41, no. 1, pp. 13–45, 1991.

[124] J. Jancar, "Review of the role of the interphase in the control of composite performance on micro- and nano-length scales," *Journal of Materials Science*, vol. 43, no. 20, pp. 6747–6757, 2008.

[125] L. Riaño, L. Belec, J.-F. Chailan, and Y. Joliff, "Effect of interphase region on the elastic behavior of unidirectional glass-fiber/epoxy composites," *Composite Structures*, vol. 198, pp. 109–116, 2018.

[126] H. Zhang, X. Zhang, Z. Fang, Y. Huang, H. Xu, Y. Liu, D. Wu, J. Zhuang, and J. Sun, "Recent advances in preparation, mechanisms, and applications of thermally conductive polymer composites: A review," *Journal of Composites Science*, vol. 4, no. 4, p. 180, 2020.

[127] J. Venetis and E. Sideridis, "The thermal conductivity of periodic particulate composites as obtained from a crystallographic mode of filler packing," *Journal of Composites Science*, vol. 2, no. 4, p. 71, 2018.

[128] E. T. Swartz and R. O. Pohl, "Thermal boundary resistance," *Reviews of Modern Physics*, vol. 61, no. 3, pp. 605–668, 1989.

[129] Y. Benveniste, "Effective thermal conductivity of composites with a thermal contact resistance between the constituents: Nondilute case," *Journal of Applied Physics*, vol. 61, no. 8, pp. 2840–2843, 1987.

[130] B. He, B. Mortazavi, X. Zhuang, and T. Rabczuk, "Modeling kapitza resistance of two-phase composite material," *Composite Structures*, vol. 152, pp. 939–946, 2016.

[131] I. A. Tsekmes, R. Kochetov, P. H. F. Morshuis, and J. J. Smit, "Thermal conductivity of polymeric composites: A review," in *2013 IEEE International Conference on Solid Dielectrics (ICSD)*, pp. 678–681, IEEE, 2013.

[132] C.-W. Nan, R. Birringer, D. R. Clarke, and H. Gleiter, "Effective thermal conductivity of particulate composites with interfacial thermal resistance," *Journal of Applied Physics*, vol. 81, no. 10, pp. 6692–6699, 1997.

[133] M. Kamiński and P. Ostrowski, "Homogenization of heat transfer in fibrous composite with stochastic interface defects," *Composite Structures*, vol. 261, p. 113555, 2021.

[134] M. O. H. Schutzeichel, T. Strübing, O. Tamer, T. Kletschkowski, H. P. Monner, and M. Sinapius, "Experimental and numerical investigation of a multifunctional cfrp towards heat convection under aircraft icing conditions," *Applied Mechanics*, vol. 3, no. 3, pp. 995–1018, 2022.

[135] A. Baumert, S. Bansmer, P. Trontin, and P. Villedieu, "Experimental and numerical investigations on aircraft icing at mixed phase conditions," *International Journal of Heat and Mass Transfer*, vol. 123, pp. 957–978, 2018.

[136] C.-P. Feng, L.-B. Chen, G.-L. Tian, S.-S. Wan, L. Bai, R.-Y. Bao, Z.-Y. Liu, M.-B. Yang, and W. Yang, "Multifunctional thermal management materials with excellent heat dissipation and generation capability for future electronics," *ACS applied materials & interfaces*, vol. 11, no. 20, pp. 18739–18745, 2019.

[137] P. S. Ghoshdastidar, *Heat transfer*. Oxford Univ. press, 2. ed. ed., 2012.

[138] R. J. Goldstein and E. Eckert, "The steady and transient free convection boundary layer on a uniformly heated vertical plate," *International Journal of Heat and Mass Transfer*, vol. 1, no. 2-3, pp. 208–218, 1960.

[139] F. L. Test and R. C. Lessmann, "An experimental study of heat transfer during forced convection over a rectangular body," *Journal of Heat Transfer*, vol. 102, no. 1, pp. 146–151, 1980.

[140] D. C. McCormick, F. L. Test, and R. C. Lessmann, "The effect of free-stream turbulence on heat transfer from a rectangular prism," *Journal of Heat Transfer*, vol. 106, no. 2, pp. 268–275, 1984.

[141] J. Xu, Z. Geng, M. Johansen, D. Carlstedt, S. Duan, T. Thiringer, F. Liu, and L. E. Asp, "A multicell structural battery composite laminate," *EcoMat*, vol. 4, no. 3, 2022.

[142] R&G Composite Technology, "Epoxydharz l 20: Technical datasheet," 2022. `http://www.ezentrumbilder.de/rg/pdf/td_de_Harz%20L+H%C3%A4rter.pdf`, last accessed 05-05-2022.

[143] Chemtronics, "Technical data sheet tds cw2460," 2022. `https://www.chemtronics.com/content/msds/TDS_CW2460.pdf`, last accessed 25-09-2022.

[144] D. Cárdenas-García, "Emissivity measurement of high-emissivity black paint at cenam," *Revista Mexicana De Física*, vol. 60, no. 4, pp. 305–308, 2014.

[145] R. G. Sam, R. C. Lessmann, and F. L. Test, "An experimental study of flow over a rectangular body," *Journal of Fluids Engineering*, vol. 101, no. 4, pp. 443–448, 1979.

[146] ACP Composites, "2.36 oz uni spread tow carbon fiber tape," 2022. `https://store.acpcomposites.com/SSP%20Applications/NetSuite%20Inc.%20-%20CMS/CMS/Site-2/files/Data%20Sheets%20(PDS)/Carbon-Fiber-Spread-Tow-Tape-Textreme-5018-PDS.pdf`, last accessed 25-10-2022.

[147] P. Krammer and D. Scholz, *Estimation of Electrical Power Required for Deicing Systems*. 2009. Hamburg University of Applied Sciences, `https://www.fzt.haw-hamburg.de/pers/Scholz/Aero/Aero_TN_Deicing_09-07-14.pdf`, last accessed 26-10-2022.

[148] R&G Composite Technology, "Glas fibre fabric technical data sheet fk144," 2022. `http://www.ezentrumbilder.de/rg/pdf/td_de_style%2005507.pdf`, last accessed 05-05-2022.

[149] M. Endres, *Autonomes Enteisen mittels resonanter Strukturanregung*. PhD thesis, Institute of Adaptive Systems and Function Integration, Technical University Braunschweig, Germany, 2019.

A Appendix

A.1 Mathematical Definitions in Continuum Mechanics

In order to clarify special mathematical definitions for the application of the theory of continuum mechanics, the following equations are presented. For the double scalar product, e.g. of the stiffness tetrade $\boldsymbol{C}$ with the strain tensor $\mathbf{E}$ the following relation relations are indicated with respect to an ONB with base vectors $\mathbf{x}_\mathrm{i}$:

$$\mathbf{x}_\mathrm{i} \cdot \mathbf{x}_\mathrm{j} = 0 \quad \wedge \quad \mathbf{x}_\mathrm{i} \cdot \mathbf{x}_\mathrm{i} = 1 \qquad \text{for} \quad \mathrm{i,j} = 1,2,3 \quad \text{and} \tag{A.18}$$

$$\boldsymbol{C} \cdot\cdot \mathbf{E} = C_\mathrm{ijkl} \mathbf{x}_\mathrm{i} \otimes \mathbf{x}_\mathrm{j} \otimes \mathbf{x}_\mathrm{k} \otimes \mathbf{x}_\mathrm{l} \cdot\cdot \mathrm{E}_{mp} \otimes \mathbf{x}_\mathrm{m} \otimes \mathbf{x}_\mathrm{p} \tag{A.19}$$

$$= C_\mathrm{ijkl} \mathbf{x}_\mathrm{i} \otimes \mathbf{x}_\mathrm{j} \left(\mathbf{x}_\mathrm{k} \cdot \mathbf{x}_\mathrm{m}\right) \left(\mathbf{x}_\mathrm{l} \cdot \mathbf{x}_\mathrm{p}\right) \mathrm{E}_{mp} \tag{A.20}$$

$$= C_\mathrm{ijkl} \mathbf{x}_\mathrm{i} \otimes \mathbf{x}_\mathrm{j} \delta_\mathrm{km} \delta_\mathrm{lp} \mathrm{E}_{mp} \tag{A.21}$$

$$= C_\mathrm{ijkl} \mathrm{E}_{kl} \mathbf{x}_\mathrm{i} \otimes \mathbf{x}_\mathrm{j}. \tag{A.22}$$

This definition of the double scalar product is applied to other tensor based double contractions with other ONB definitions in the same way.

A.2 Thermographic Measurements on PeCCF Specimens

This appendix section provides additional data on thermographic measurements of PeCCF specimens. Figures A.1-A.3 provide the measured transient temperature curves for coated and uncoated surface areas of several sepcimens in order to complete the choice provided in subsection 4.1.3 of this thesis. In addition, table A.1 indicates all electrical properties of the single specimens.

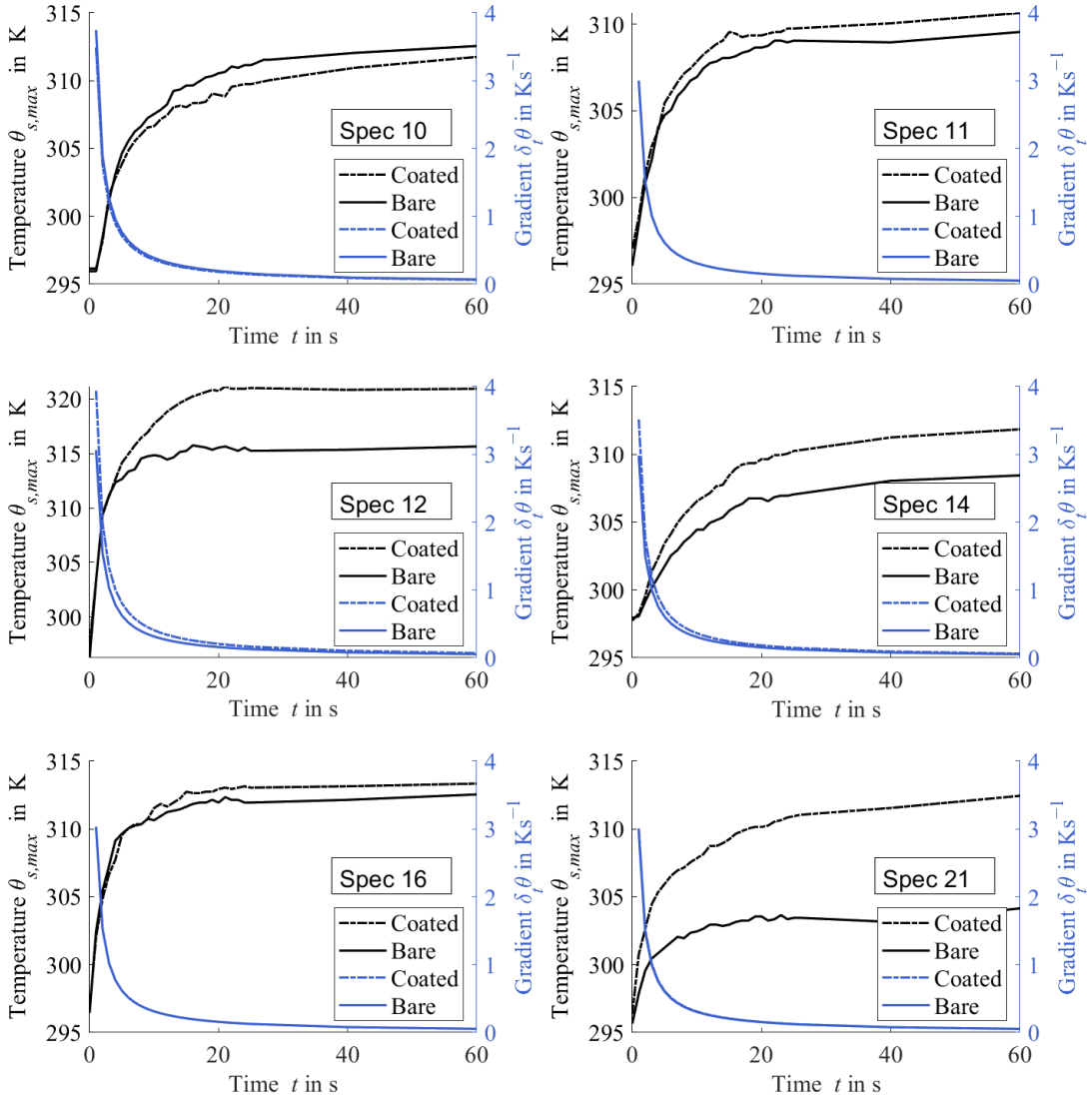

Figure A.1: Choice of results from transient temperature rise measurements related to a stationary temperature of $\theta_s = 312$ K

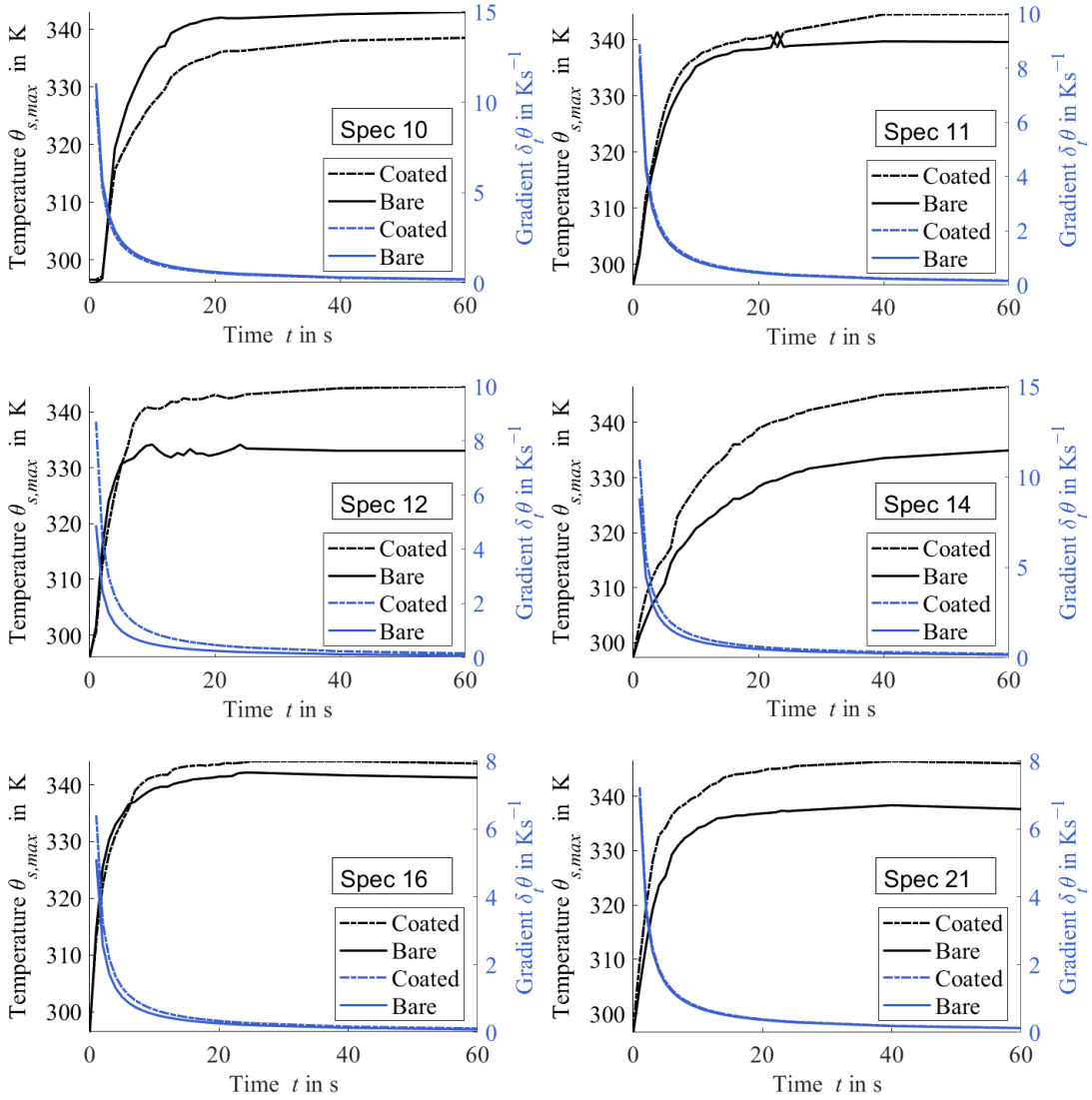

Figure A.2: Choice of results from transient temperature rise measurements related to a stationary temperature of $\theta_s = 342$ K

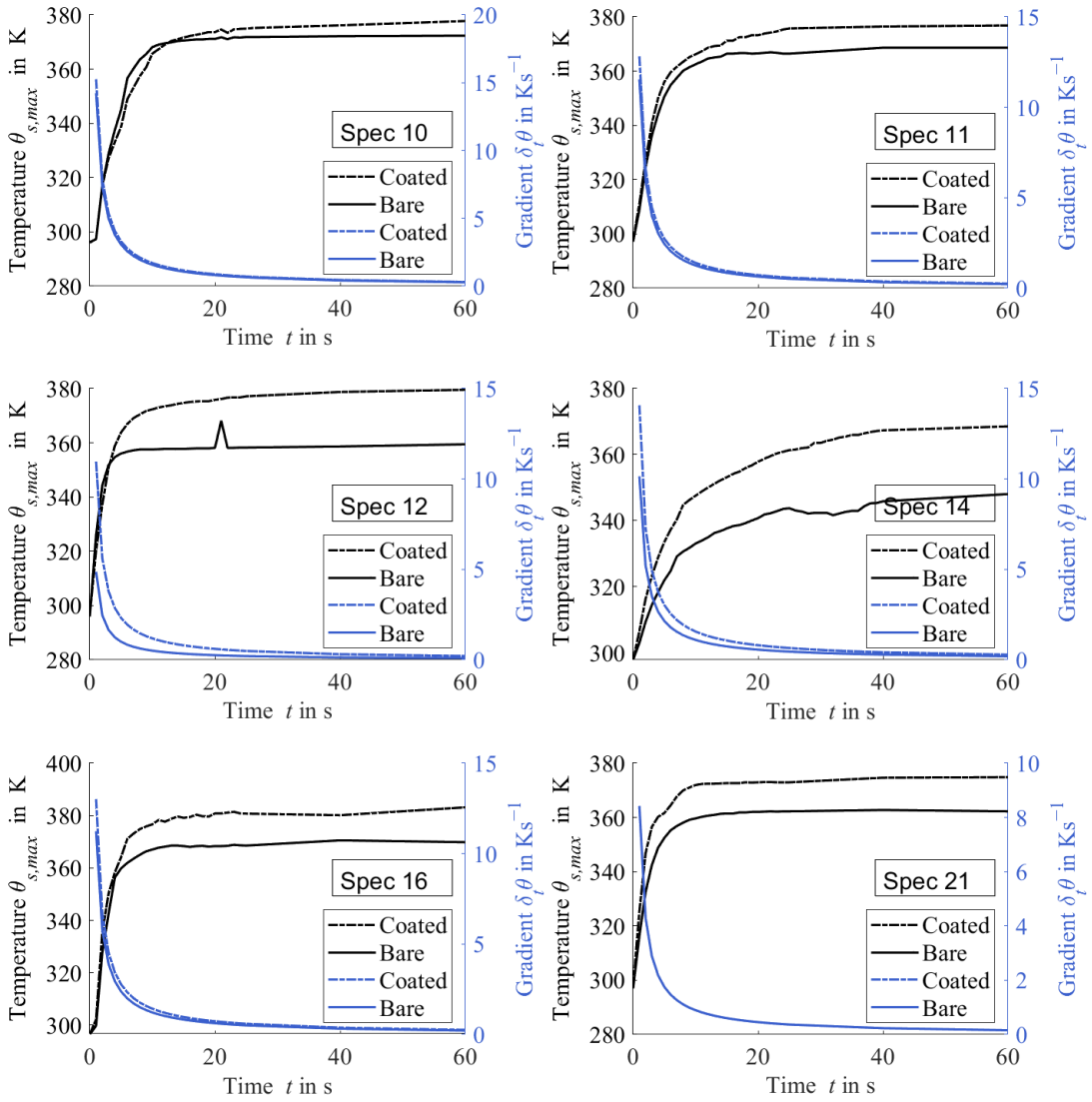

Figure A.3: Choice of results from transient temperature rise measurements related to a stationary temperature of $\theta_s = 372$ K

Table A.1: Electrical resistance K of PeCCF specimens and related measurement length l_m, related to distance between contacting clamps

Nr.	l_m [mm]	K [Ohm]	Nr.	l_m [mm]	K [Ohm]
Spec 1	55	40.2	Spec 12	89	37.5
Spec 2	50	93.1	Spec 13	99	24.6
Spec 3	60	36.3	Spec 14	112	7.8
Spec 4	60	25.7	Spec 15	110	21.3
Spec 5	60	110.2	Spec 16	95	39.9
Spec 6	55	61.0	Spec 17	90	29.0
Spec 7	45	73.3	Spec 18	95	30.8
Spec 8	50	25.7	Spec 19	89	87.5
Spec 9	60	33.8	Spec 20	89	33.3
Spec 10	110	17.2	Spec 21	97	45.5
Spec 11	115	19.9	Spec 22	105	75.4
Ref	60	1.7			

A.3 Overview of Effective Stiffnesses Data

This appendix section provides additional figures and data of the effective stiffness tensor elements which are predicted and discussed within subsection 4.2.2. Therefore figures A.4 - A.6 indicate the influence of various fibre volume fractions as well as PE coating stiffnesses on the effective stiffness tensor elements. Figure A.7 and table A.2 provide an overview of different FE mesh configurations that were used for the homogenisation procedure on the micro scale. Since no significant change was found for both mesh definitions, the standard mesh definition was used for all results in this thesis.

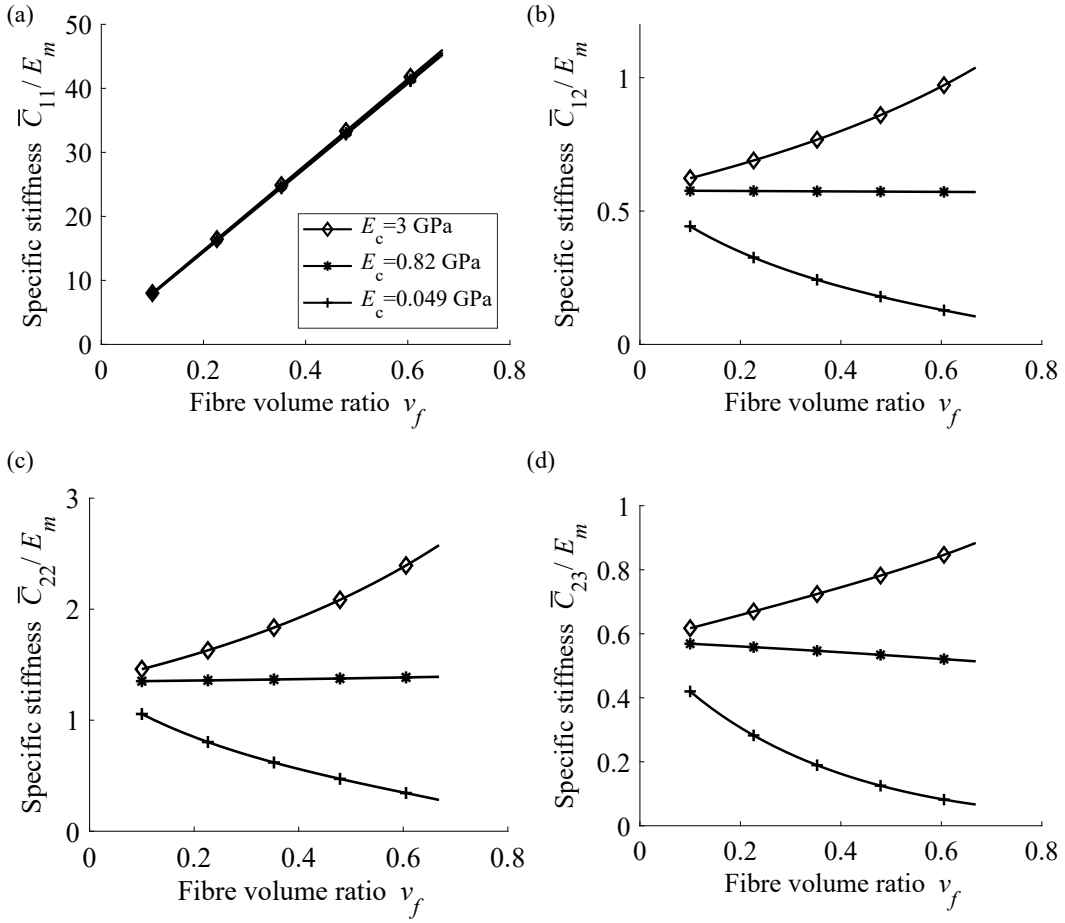

Figure A.4: Specific effective stiffnesses of effective stiffness tensor $\{\overline{C}_{ij}\}$

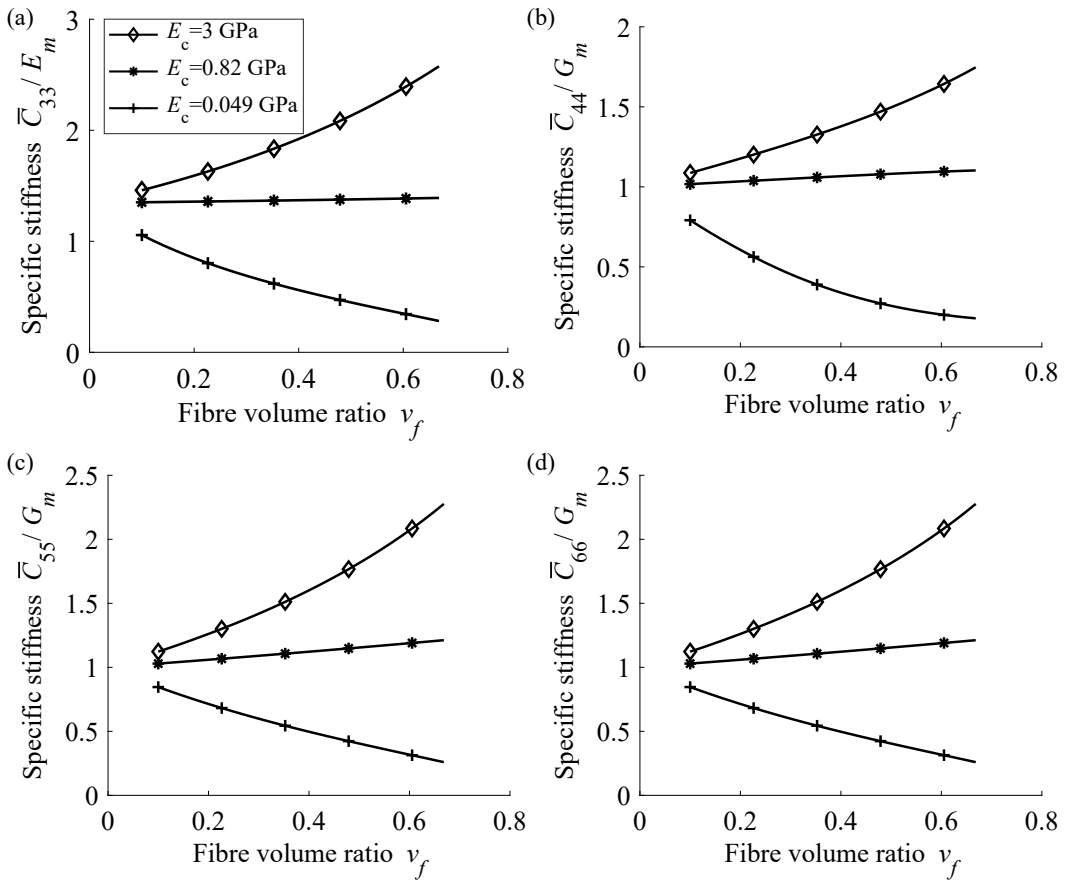

Figure A.5: Continued: Specific effective stiffnesses of effective stiffness tensor $\{\overline{C}_{\mathrm{ij}}\}$

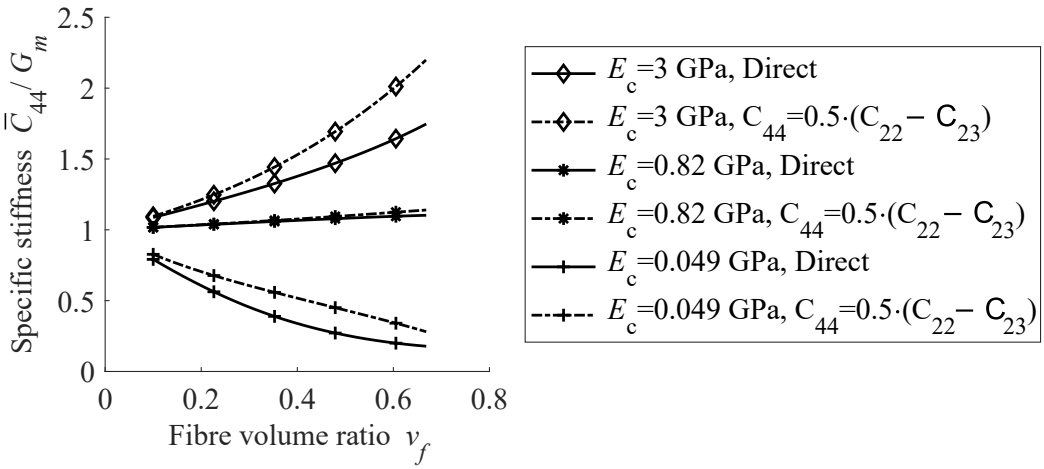

Figure A.6: Overview of effective stiffness tensor element C_{44} direct calculated from FEM in comparison with calculation from tensor elements C_{22} and C_{23}

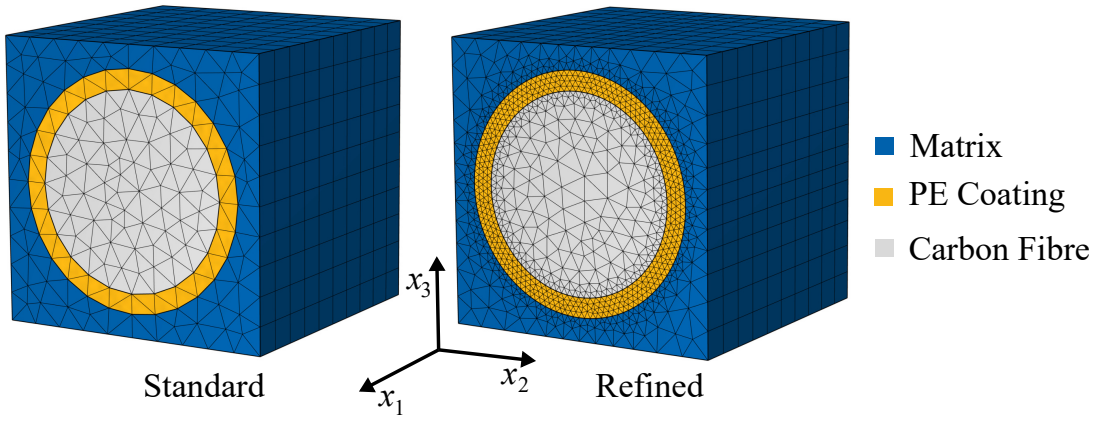

Figure A.7: Illustration of standard and refined FE mesh configuration for stiffness computation

Table A.2: Configurations of finite element meshes a) and b), see figure A.7

Properties	Mesh a)	Mesh b)
Element types	Prisma	
Shape functions	Quadratic serendipity*	
Reference fibre volume fraction v_f	0.55	
Nr. of elements domain 1	1260	5140
Nr. of elements domain 2	520	8680
Nr. of elements domain 3	1380	6100
Total nr. of elements	3160	19920
Total degrees of freedom (DOF)	30141	178890

*as defined in COMSOL MULTIPHYSICS v6

A.4 Overview of Effective Heat Transfer Data

This appendix section provides additional figures and data related to the effective heat transfer behaviour of the PeCCF composite, as presented and discussed in subsection 4.3.4. Figure A.8 and table A.3 provide additional info about the FE meshes that were applied for heat transfer modelling on the micro scale. Since no significant influence by the mesh definition was found, the coarse mesh was used for the computation of all micro scale heat transfer results related to the 3D RVE.

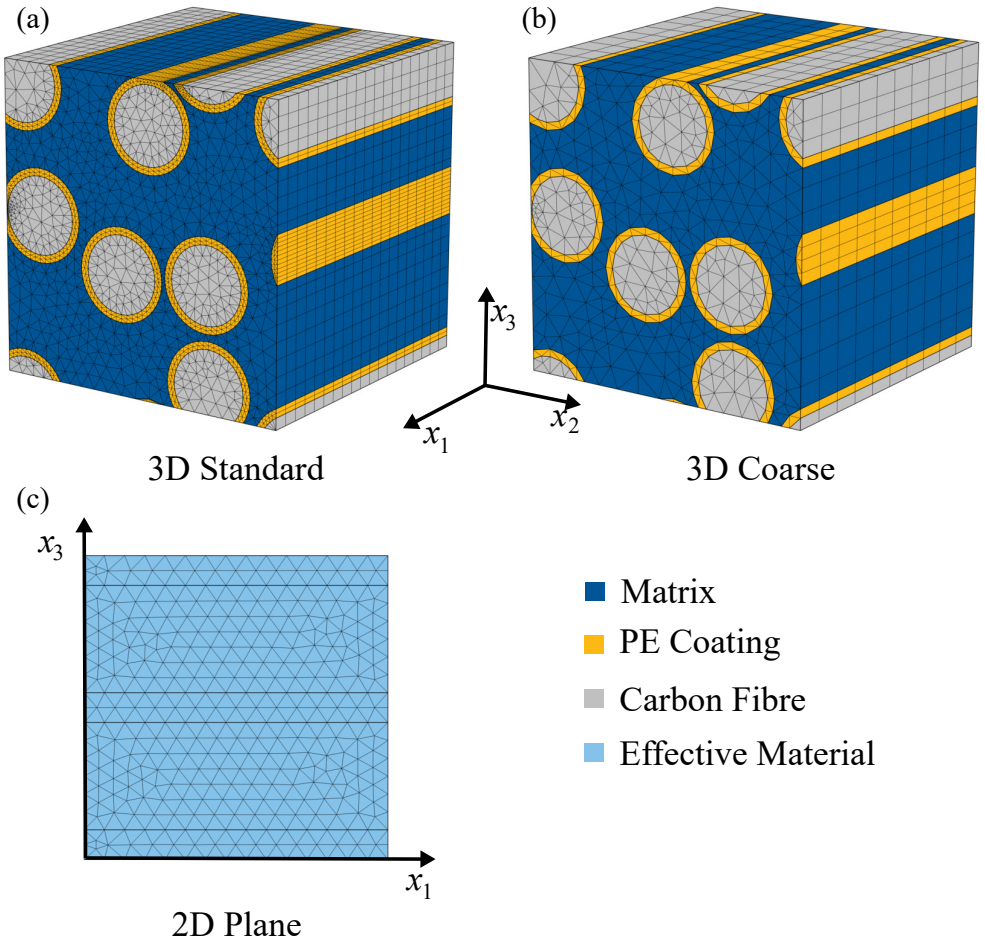

Figure A.8: Illustration of FE mesh configurations for heat transfer prediction

Table A.3: Technical details of FE meshes compare figure A.8

Properties	Refined	Coarse	2D Hom.
Element types	Prisma		Triangle
Shape functions	Quadratic serendipity*		
Reference fibre volume fraction v_{cf}	0.42		-
Nr. of elements Carbon Fibre	13243	2490	-
Nr. of elements PE Coating	23636	2200	-
Nr. of elements Matrix	17936	3840	-
Total nr. of elements	54815	8530	646
Total degrees of freedom (DOF)	377985	61600	1844

*as defined in COMSOL MULTIPHYSICS v6

A.5 Additional Overview of Convective Heat Transfer Measurements

In this appendix section, additional figures with data from heat transfer measurements and numerical predictions are provided, as discussed in subsection 5.1.3. Therefore figure A.9 provides additional heat transfer cases and measured stationary temperature distributions. In addition, figure A.10 indicates the computed temperature drop over the thickness of the flat plate specimen. Moreover, the tables A.4 and A.5 provide properties of the flat plate specimen materials and of the De-Icing test bed, respectively. Finally, all predicted free and forced convective HTCs are presented in tables A.6 and A.7 with respect to the corresponding environmental conditions.

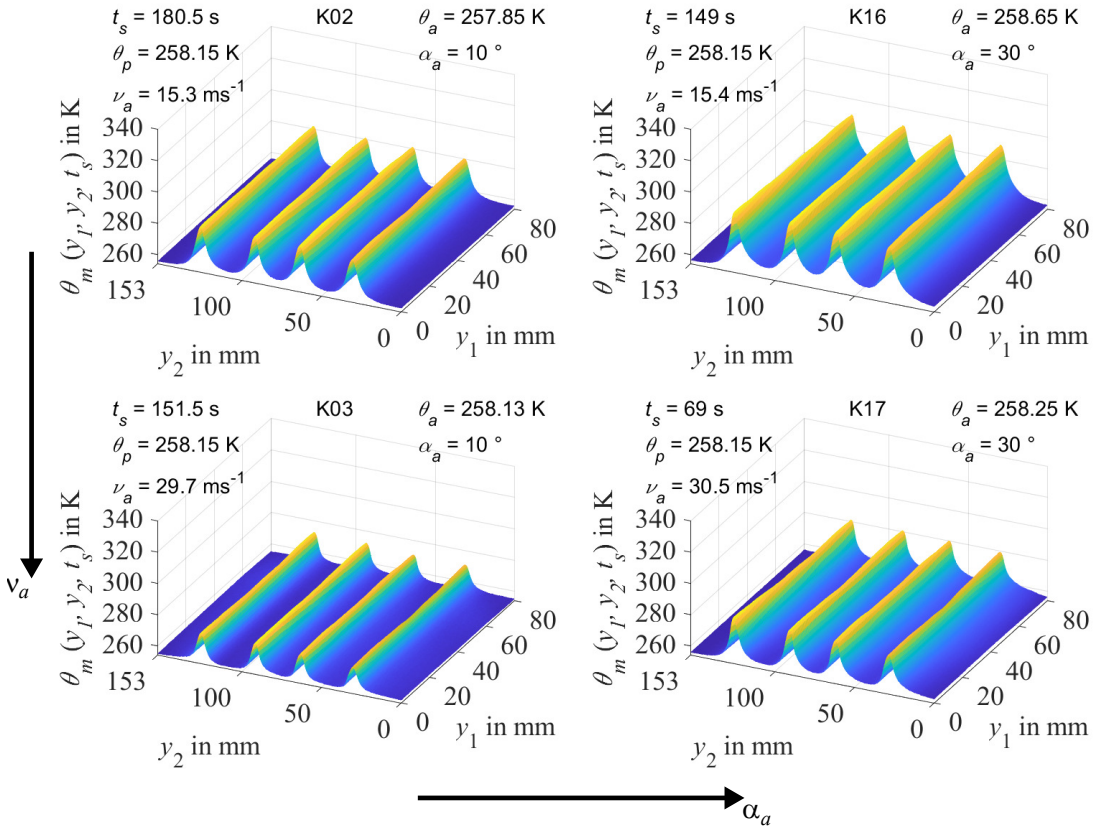

Figure A.9: Overview of the angle of attack's influence on measured temperature distributions under aircraft icing conditions

Table A.4: Glas fibre fabric properties

Property	Sym.	Value	Unit	Reference
Thermal conductivity	λ_g	0.10	$\frac{\mathrm{W}}{\mathrm{mK}}$	[32]
Specific electrical resistance	κ_g	$\rightarrow \infty$	Ωcm	[32]
Thickness (dry)	t_g	0.24	mm	[148]
Density	ρ_g	0.83	$\frac{\mathrm{g}}{\mathrm{cm}^3}$	[148]

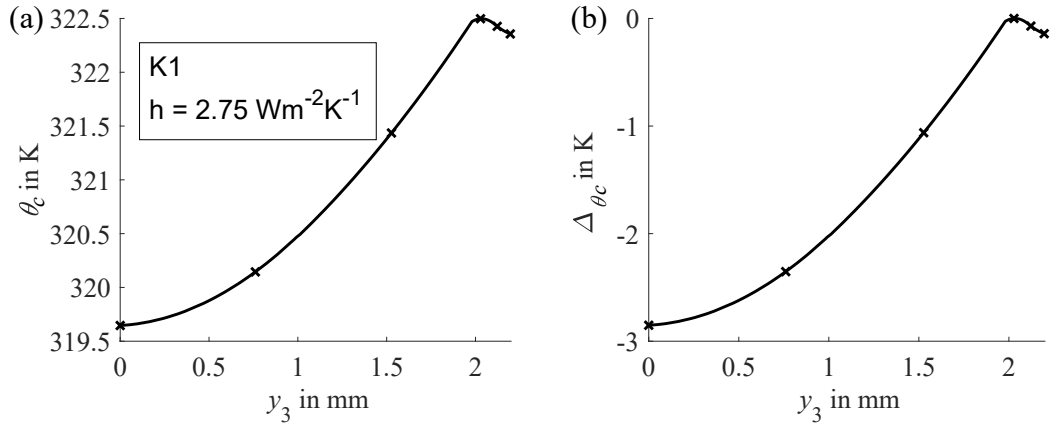

Figure A.10: Overview of the computed temperature distribution in flat plate thickness direction y_3: (a) Absolute temperature and (b) Temperature drop as defined in equation 4.37

Table A.5: De-Icing test bed properties [149]

Parameter	Value	Unit
Test chamber dimensions	450x450x1000	mm^3
Max. air speed	[0, 35]	$\frac{m}{s}$
Temperature range	[253.15, θ_r]	K
Air humidity	[60, 80]	%

Table A.6: Computed free convection coefficients

θ_s	[K]	258.15	263.15	268.15	273.15	278.15
h	$[\frac{W}{m^2K}]$	2.8	2.4	2.2	2.4	2.2

Table A.7: Computed forced convection coefficients

ν_a $[\frac{m}{s}]$	α_a [°]	θ_p [K]	258.15	263.15	268.15	273.15	278.15
15	10	h $[\frac{W}{m^2K}]$	18.5	17.8	17.0	15.5	18.5
15	30		11.0	11.8	11.8	11.8	11.0
30	10		38.0	35.0	30.5	32.0	35.0
30	30		18.5	21.5	14.8	17.0	17.0

A.6 Additional Overview of Applied Methods

The following table A.8 provides a section or subsection related overview of homogenisation methods which are applied to the single calculations. It is mentioned that some properties are calculated based on FEM models (with UC or RVE geometries) and analytical methods (e.g. ROM) from literature for comparison reasons.

Table A.8: Overview of applied homogenisation methods with respect to the single sections or subsection in this thesis

	Physical			Theory	
Section	field	Property	Methods	page nr.	Geom.
4.2	Mechanical	$\overline{\boldsymbol{C}}$	VMT	30	UC
	field		ROM	38	-
		$\overline{\mathbf{A}}$	VMT	34	UC
			ROM	38	-
4.3	Thermal	$\overline{\boldsymbol{\Lambda}}$	VMT	35	RVE
	field		ROM	38	-
			TPLN	39	-
			TLLN	65	-
		$\overline{\rho}$	VA	34	RVE
			ROM	38	-
		$\overline{c}_p$	VA	34	RVE
			ROM	38	-
5.1, 5.2	Mechanical	$\overline{\boldsymbol{C}}$	VMT	30	UC
		$\overline{\mathbf{A}}$	VMT	34	UC
	Thermal	$\overline{\boldsymbol{\Lambda}}$	TLLN	65	-
	field	$\overline{\rho}$	ROM	38	-
		$\overline{c}_p$	ROM	38	-
		$\langle\theta\rangle$	VA	34	UC

VMT: Virtual material testing based on unit load cases and volume averages, solved by FEM